Human Body-Enabled Methods for the Implicit Synchronization of Distributed Wearable Systems

Dissertation

zur Erlangung des Grades eines Doktors
der Ingenieurwissenschaften

vorgelegt von M.Sc.
Florian Wolling

eingereicht bei der Naturwissenschaftlich-Technischen Fakultät der
Universität Siegen

Siegen 2023

Betreuer und erster Gutachter

Prof. Dr. Kristof Van Laerhoven
Universität Siegen

Zweiter Gutachter

Prof. Dr. Oliver Amft
Albert-Ludwigs-Universität Freiburg

Mitglieder der Promotionskommission

Prof. Dr. Roman Obermaisser
Universität Siegen

Prof. Dr. Roland Wismüller
Universität Siegen

Tag der mündlichen Prüfung

26. Mai 2023

Digital Object Identifier

https://doi.org/10.25819/ubsi/10490

Þetta reddast

to my family

Zusammenfassung

Das Thema Wearable Computing erlebte in den letzten drei Jahrzehnten eine beeindruckende Entwicklung. Bisher werden Wearables meist als Einzelgeräte am Handgelenk getragen. In letzter Zeit entwickeln sie sich jedoch zunehmend zu einem Konglomerat gleichzeitig an verschiedenen Körperstellen platzierter Einheiten, die mit spezialisierten Sensoren komplementäre Perspektiven erfassen können. Die Anwendung moderner Techniken der Sensorfusion und des maschinellen Lernens auf die Messdaten mehrerer Geräte ermöglicht Rückschlüsse auf das Gesamtbild des Nutzers. Die so erreichte Genauigkeit ist die der eines einzelnen Sensors überlegen. Sie leiden jedoch erheblich unter den Ungenauigkeiten der internen Taktgeber, der manuellen Justierung der Sensorkanäle und somit den nicht übereinstimmenden Zeitbasen der Aufzeichnungen. Verfügbare funkbasierte Online- wie auch ereignisbasierte Offline-Synchronisationsmethoden beeinträchtigen entweder erheblich die Batterielaufzeit oder erreichen nicht die erforderliche Genauigkeit. Darüber hinaus erfordern beide Methoden die explizite Interaktion des Nutzers, um die verteilten Geräte zu vernetzen oder bestimmte Aktionen zur Synchronisierung durchzuführen.

Diese Dissertation stellt die Hypothese auf, dass die Anbringung von Geräten am menschlichen Körper Technologien und Methoden ermöglicht, die ohne ihn nicht umsetzbar wären. Es werden zwei implizite Methoden vorgestellt, die den Bedarf tragbarer Systeme an genauer und gleichzeitig effizienter Synchronisation bedienen sollen. Dafür werden zwei Perspektiven untersucht, die den Körper zum einen als Quelle natürlicher Signale und zum anderen als Übertragungsmedium künstlicher Signale sehen. Die Übertragung der medizinischen Sensormodalitäten Elektrokardiographie und Photoplethysmographie in ein tragbares Format ermöglicht den ständigen Zugang zu den Vitaldaten des Nutzers. Die erste Methode PulSync nutzt den unregelmäßigen Rhythmus des Herzschlags, der auf der gesamten Körperoberfläche gleichzeitig detektierbar ist. Moduliert durch physiologische Prozesse bilden die Intervalle zwischen den Herzschlägen Muster, die in der abgeleiteten Intervallfunktion der Herzratenvariabilität einzigartig wie ein Fingerabdruck wiedererkennbar sind und in einem datengesteuerten Offline-Nachbearbeitungsschritt als wichtige Orientierungspunkte für die Ausrichtung von Aufzeichnungen dienen. Das neuartige Prinzip der körpergebundenen Kommunikation lässt sich zwischen den traditionellen kabelgebundenen und drahtlosen Techniken ansiedeln, weist jedoch ihnen gegenüber Vorteile auf. Die zweite Methode IBSync basiert auf künstlichen Markierungssignalen, die entweder bewusst oder implizit und zufällig durch Berührung oder Passieren von mit Sendebaken ausgestatteten Flächen oder Gegenständen in die Haut des Nutzers induziert werden. Die vom augmentierten menschlichen Körper gewonnenen Markierungen können mit Daten angereichert werden, um die Zeitreihen offline eindeutig auszurichten oder sogar die Positionen der Markierungen einer absoluten Zeit zuzuordnen. Beide Methoden erreichten eine Genauigkeit in der Größenordnung eines Samples und zeigen eine vergleichbare Leistung: PulSync mit -0.714 ± 3.440 Samples und IBSync mit 0.800 ± 1.792 Samples. Mit einer Genauigkeit von 2.86 ms bei 250 Hz und 6.25 ms bei 128 Hz sind die zwei Methoden PulSync und IBSync daher den meisten verfügbaren Offline-Synchronisationsmethoden überlegen und können sogar mit den gängigen Online-Methoden mithalten.

Stichworte: Tragbare Computer, implizite Synchronisierung, Elektrokardiographie, Photoplethysmographie, drahtlose Körpernetzwerke, körpergebundene Kommunikation, kapazitive Kopplung

Abstract

During the last three decades, wearable computing has experienced an impressive evolution. While single all-round devices, worn at familiar and convenient locations such as the wrist, have been standard for many years, wearables are recently evolving rather into a conglomerate of simultaneously deployed, specialized sensing units that can be attached to various sites with complementary perspectives. Applying cutting-edge sensor fusion and machine learning techniques on the collected multi-device data allows inferring the user's bigger picture with an accuracy superior to that from a single site. However, the applied techniques suffer significantly from the inaccuracies of the devices' internal clocks, the manual temporal alignment of their sensor channels, and hence the recordings' unmatched time bases. The available radio-based online or event-based offline synchronization methods either considerably affect the devices' battery life or often do not achieve the required accuracy. Moreover, both methods demand for the user's explicit interaction to either network the distributed devices or perform specific synchronization actions.

This dissertation hypothesizes that attaching devices to the human body can enable technologies and methods that would not be possible without its presence. Two implicit methods are presented to address the lack of accurate and efficient synchronization principles for distributed wearable systems. Therefore, two perspectives are investigated in which the human body is considered first as a source of natural signals and second as a transmission medium to provide artificial signals throughout the body surface. The transfer of the medical sensing modalities electrocardiography and photoplethysmography to a wearable form factor has enabled constant access to the user's vital signs. The first method PulSync leverages the irregular rhythm of the heartbeat, ubiquitously and simultaneously detectable throughout the entire body surface. Modulated by various physiological processes, the inter-beat intervals form patterns in the derived heart rate variability interval function that are unique like a fingerprint and, therefore, can serve as significant landmarks for the offline alignment of recordings in a data-driven post-processing step. The novel communication principle of intra-body communication is somewhat located between traditional wired and wireless techniques while showing advantages over both. The second method IBSync is based on artificial landmark signals that are either consciously or implicitly and incidentally induced into the user's skin by touching or passing areas or objects equipped with transmitter beacons. Obtained from the augmented human body, the detected landmarks are enriched with data, allowing to uniquely align the recordings offline or even allocate landmark positions in the absolute time. Both methods achieved an alignment accuracy in the order of a single sample and show a comparable performance: PulSync with -0.714 ± 3.440 samples and IBSync with 0.800 ± 1.792 samples. Therefore, with the achieved temporal accuracy of 2.86 ms at 250 Hz and 6.25 ms at 128 Hz respectively, the two methods PulSync and IBSync are superior to most available offline synchronization methods and can even keep up with common online methods.

Keywords: Wearable Computing, Implicit Synchronization, Electrocardiography, Photoplethysmography, Wireless Body-Area Networks, Intra-Body Communication, Capacitive Coupling

Contents

1 Introduction

Initiated by the release of the first activity tracker in 2009, the market of wearable devices has seen an "explosive growth" [BDD16]. As a result, a vast number of devices are released each year, ranging from low-priced no-name to precious lifestyle products. According to a market survey of PricewaterhouseCoopers (PwC) in 2016 [BL16], at that time already 49 % of the 1000 respondents owned at least one wearable and 36 % even two or more. Thereby, the wrist is the most common position for commercial wearable devices, which mostly come in the shape of watches (35.0 %) or jewelry such as bracelets and rings (29.1 %) [BDD16]. While these positions are familiar, e.g. from traditional wristwatches [Seh+22], there is a perceptible trend toward more "fashionable" [SH15; Kou18] and even invisible "none products" [BL22]. Devices are becoming less obtrusive in the shape of finger rings [Rhe+98; LVH16], in-ear devices [Kaw+18; Röd+22; Fer+22], and skin-friendly adhesive patches [LPS17; AMK20; Ate+22] to improve the long-term wearability in everyday life.

After the term "ubiquitous computing" was coined by Mark Weiser in 1988 [Wei93], the pioneers Steve Mann and Thad Starner [Man97; Sta+97] proceeded with portable devices that consider the human body as a habitat, thus shaping the beginnings of modern wearable computing [AL09]. With gradually smaller devices worn closely or even directly attached to the body surface, the following generations of wearables began to consider the body not only as a physical carrier but, beyond that, also as a source of valuable information about the user. The emergence of accelerometers made simple pedometers possible, paved the way for human activity recognition (HAR) [VG04], and changed the devices' perspective from an external, observing to an internal, egocentric view. The adaption of sensing modalities from medical settings [KCS84] and their transfer to the familiar wrist of the users eventually enabled the continuous self-monitoring and ambulatory health assessment, initiating the breakthrough of today's fitness trackers [KA21; Ome+21].

While "Privacy is the most often-cited criticism of ubiquitous computing" [HL04], especially when dealing with health-related data, many of these weaknesses are associated with wireless communication. In 1995, Zimmerman [Zim95] found that the human body itself can serve as a confined medium which is not only "physically secure" [Nat+21] but can also considerably improve the energy efficiency of signal transmission [Nar+18; Mai+20a]. Since then, intra-body communication (IBC) promises to improve wireless body area networks (WBANs), but applications remain underinvestigated due to the absence of commercially available transceiver modules or integrated circuits (ICs). Nevertheless, IBC is presumably the first step toward a new generation of wearables that consider the human body as a crucial part of the system, looking at it from a very technical perspective and thus enabling new methods and technology.

Foreseen by Feynman in 1959 and promoted by Moore since 1965 [Moo65], the miniaturization of semiconductors is successively allowing for smaller circuits [Lei+20]. This way, the gradually smaller devices are imaginable to be attached to almost arbitrary body positions, only constrained by aspects of wearability and social acceptance [Gem+98; Zea17; Seh+22]. However, present "wearables are just scratching the surface of what is possible" [ADD21] while not all desired information can be obtained from a single site. Therefore, they are successively evolving into a conglomerate of simultaneously deployed hardware

units rather than into a single all-round device [AV17; ADD21; Ome+21]. The distributed, multi-device systems comprise specialized sensor nodes that allow to cover complementary perspectives [LL22], thus capturing the user's bigger picture. Applied to the multi-modal data, cutting-edge sensor fusion and machine learning techniques allow, for instance, to recognize human activities [Agu+19] or to infer a wearer's emotional state and stress level [Sch+18]. Thereby, the inference on data from multiple devices tends to be "significantly more accurate than [from] a single device worn on either wrist" [Agu+19; Lu+20].

However, these modern techniques substantially suffer from the inaccuracy of the devices' internal clocks, the manual temporal alignment of sensor channels, and, therefore, the recordings' unmatched time bases [Ohm+06; Xu+17; Wan+19; Goo+22]. In order to regularly update and adjust the local clocks, conventional online synchronization methods usually rely on wireless radio communication to negotiate a common time base between the networked devices at runtime. However, "The cost of communicating is high" [Luc+17] and tends to exceed the comparatively small energy budget of wearable devices [BGJ15a], as it can easily make up to 50 % of a typical device's consumption [AMH19]. Originated in research on HAR, offline synchronization methods aim to avoid this load by deferring the alignment of signal channels to a data-driven post-processing step. External, simultaneously detectable events such as significant motion are exploited to correlate and automatically match predefined templates [BAL09; BGJ15b], distinct signal patterns [BGJ15b; Wan+19], or derived statistical measures such as entropy [BGJ15a] and standard deviation [HOV19] in indeterminate, relative time. However, the available methods typically result in a low accuracy of tens to hundreds of milliseconds and "in realistic scenarios achieving high synchronization performance is not trivial" [BAL09].

This dissertation hypothesizes that attaching devices to the human body can enable technologies and methods that would not be possible without its presence. Therefore, the human body is seen from a very technical perspective, as a central and crucial part of a system of distributed wearable devices. As illustrated in **Figure 1.1**, the dissertation investigates two perspectives considering the human body first as a source of natural signals (**RQ 1**) and second as a transmission medium to provide artificial signals throughout the body surface (**RQ 2**). Inspired by the vision of "Augmented Interaction" by Rekimoto and Nagao [RN93], the human body is interpreted as a kind of augmented object that devices are discretely and unobtrusively attached to and from which they can obtain information and data. With the proposed application of implicit synchronization (**RQ 3**), illustrated in **Figure 1.2**, the synchronization of wearable devices is turned from an active decision by the user to an incidental process allowing for better signal quality and classification due to better timing and a more accurate alignment of coincident events. It implements the idea of "implicit human-computer interaction" which "aims to reduce computer manipulations by using environmental information as implicit input" [SGM00] and, therefore, supports "seamlessly bridging the gulf between physical and virtual worlds" [Wan+99].

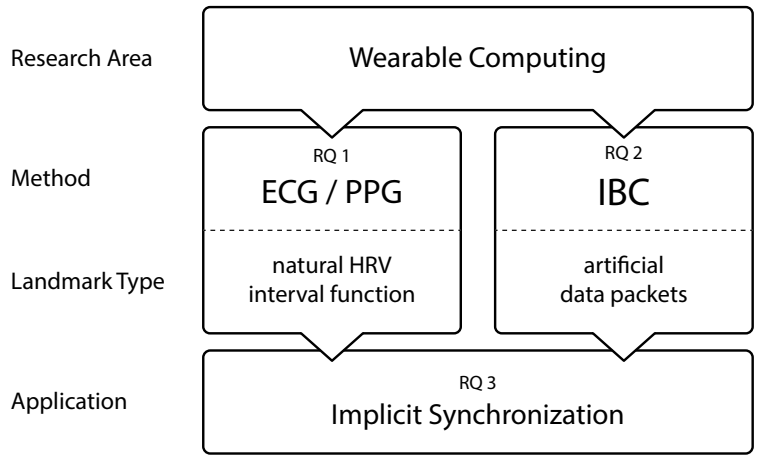

Figure 1.1: Overview of the three research questions answered by this dissertation in the research area of wearable computing: **RQ 1** investigates wearable sensing on the example of electrocardiography (ECG) and photoplethysmography (PPG) for the detection of the natural heartbeat and the derivation of the unique heart rate variability (HRV) interval function, **RQ 2** investigates intra-body communication (IBC) to induce artificial signals and provide data throughout the human body surface, and **RQ 3** implements and evaluates the concept of implicit synchronization as an example of human body-enabled technology.

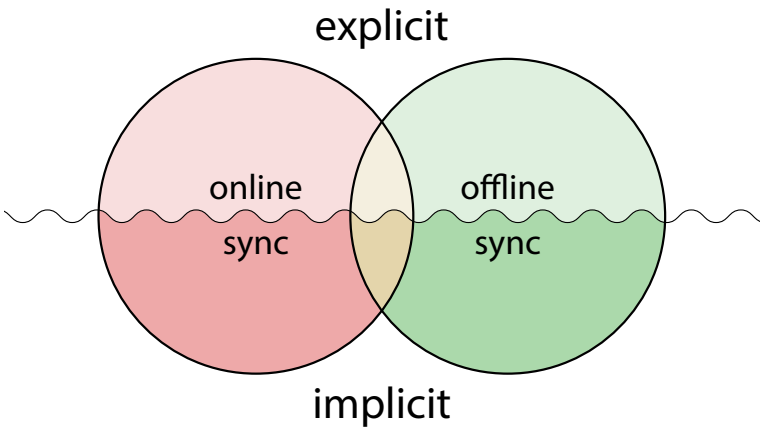

Figure 1.2: Illustration of the proposed implicit synchronization concept, which follows the idea of implicit human-computer interaction (HCI) by Schmidt et al. [SGM00]. The concept allows to apply both online and offline synchronization techniques that unobtrusively provide information but do not require the user's explicit and intentional interaction.

1.1 Problem Formulation

Datasets collected with distributed systems of wearable devices with complementary perspectives allow for capturing a bigger picture. However, applied sensor fusion and machine learning techniques suffer significantly from the devices' unmatched time. The inaccurately aligned signal patterns of coincident events result in blurry models and weak classification. To solve this problem, conventional, radio-based online synchronization techniques negotiate common time during operation, hence loading the resource-constrained hardware units with an energy-intensive overhead. Alternatively, offline techniques defer the data-driven alignment to a post-processing step, typically achieving insufficient accuracy.

This dissertation aims to investigate the human body's potential to enable the implicit synchronization of multiple body-attached devices. Although viewed from a very technical perspective, the human body is seen beyond its simple use as a physical carrier of wearable devices and interpreted as the central element of the system. Two perspectives are explored, one considering the human body as a source of natural information and the other as a transmission medium for artificial information provided throughout its surface.

The content of this dissertation answers the following research questions:

RQ1 Which natural signals are available at the human body surface and suitable for use in implicit synchronization?

- **a)** Which natural signals can be detected at the body surface?
  Section 2.1
- **b)** How can they be captured and how do they need to be processed?
  Section 2.2 & 2.4
- **c)** Which available datasets are suitable for evaluating wearable techniques?
  Section 2.3

RQ2 How can the human body be used as a transmission medium to provide artificial signals that enable implicit synchronization?

- **a)** How can artificial signals be provided throughout the body surface?
  Section 3.2
- **b)** How can commercially available, off-the-shelf devices detect these signals?
  Section 3.3
- **c)** How can custom devices detect these signals?
  Section 3.4 & 3.5

RQ3 How can wearable devices implicitly be synchronized using either the natural signals identified in RQ1 or the artificial signals from RQ2?

- **a)** What is implicit synchronization?
  Section 4.2
- **b)** How can this synchronization concept be implemented?
  Section 4.3 & 4.4
- **c)** How can the natural signals from RQ1 be used for this purpose?
  Section 4.3
- **d)** How can the artificial signals from RQ2 be used for this purpose?
  Section 4.4
- **e)** Which signal source is more suitable for this purpose?
  Section 4.5

1.2 Methodology

This dissertation aims to investigate the human body's potential beyond its simple use as a physical carrier to enable the implicit synchronization of multiple wearable devices. A collection of case studies will present approaches made possible by using the human body as the central object the devices are connected to by attaching.

The research will be based on a broad, interdisciplinary literature review covering various disciplines, ranging from computer science, communication technology, and digital signal processing to adjacent topics in the biomedical field. Relevant research areas will then be intensified with a focused search in depth. The case studies will be designed to demonstrate the feasibility of specific aspects of the research problem formulated in the previous section. Their evaluation is intended to discover benefits, raise remaining research questions for future work, and identify potential drawbacks compared to common techniques. Public datasets will be used to benchmark the approaches against comparable or adjacent research whenever available and appropriate. Considering safety and ethical standards, empirical experiments will be conducted to generate new datasets for further data analysis or obtain measurements to characterize custom prototypes. The prototypes will be developed and implemented when there are no commercially available, off-the-shelf devices that would provide the desired functionality, sensing modality, or signal quality and, thus, cannot answer the research question. The case studies' evaluation will primarily rely on quantitative metrics such as a device's power consumption or a method's performance, e.g. in terms of temporal accuracy. The measurements will be collected using suitable devices with sufficient accuracy or compared against an appropriate reference that ideally can serve as ground truth. Conducting the studies with several subjects or at least with several runs is intended to provide reliable statistical evidence.

Two distinct perspectives are identified, allowing the case studies to be grouped thematically and their fundamental concepts to be investigated independently. Thereby, the first perspective considers **the human body as a source of information** (**RQ1**) that is inherently unique. Physiological signals, such as the primary vital signs, have been found to be influenced by various physiological processes and to show a certain degree of randomness and chaos. It is assumed that these unique signal patterns can be exploited to enable implicit synchronization throughout the human body. Furthermore, it is hypothesized that the wearer's irregular heartbeat will best meet the signal source requirements. After theoretical reasoning, diverse modalities are assessed, and different strategies for energy-efficient and optimal signal processing are developed, evaluated, and discussed. The second perspective considers **the human body as a transmission medium** (**RQ2**) for intra-body communication, a novel yet commercially unestablished technique that allows providing information throughout the body surface without relying on fixed cable joints or energy-intensive radio communication. The technique of capacitive coupling, on which the different approaches are based, will be chosen attempting to enable the detection and reception of artificial information. These are intended to be received consciously or implicitly and incidentally by touching, approaching, or passing certain areas, surfaces, or objects with embedded transmitters. Based on the findings from the two perspectives of RQ1 and RQ2, the **implicit synchronization of wearable devices** (**RQ3**) will be implemented as a relevant and meaningful example of human body-enabled methods and applications. The implemented methods will be evaluated in terms of their performance and applicability in real life, and compared to each other as well as to existing techniques.

1.3 Contributions

This dissertation contributes to public research in the following areas:

1) Wearable Photoplethysmography

- **a)** Investigation and a better understanding of raw signals and their necessity to ensure the validity of algorithm benchmarks. [**W20a; C21c**]
- **b)** Review of publicly available datasets that pretend to contain raw reflective mode signals but often turn out to contain considerably preprocessed signals with limited information value, validity, and generalizability. [**W20a; C21c**]
- **c)** Review of different active sampling schemes and strategies applied in both research prototypes and commercial wearable devices. [**A19**]
- **d)** Investigation and determination of the minimum sampling rate required to reliably derive the heart rate from raw, regularly sampled signals. [**W18**]
- **e)** Review of methods for the analysis, interpretation, and derivation of features from raw signals in time and frequency domain. [**W18; J20b; C21c**]
- **f)** Investigation of the optimal preprocessing strategies to preserve fiducial points, i.e. pulse peak positions, and optimize algorithms' performance. [**C21c**]
- **g)** Benchmark of popular algorithms to detect fiducial points, i.e. pulse peak features, in time series of differently preprocessed signals. [**C21c**]
- **h)** Provide a dataset with manually annotated pulse peak labels to allow for future benchmarks on actual raw signals. [**C21c**]

2) Intra-Body Communication

- **a)** Development and evaluation of a prototype to combine conductive textiles with capacitive coupling for a simplified transmission channel with local ground reference potential, achieving significantly better signal-to-noise ratio and symbol rate. [**C17**]
- **b)** Development and evaluation of a novel pulse-width modulation scheme for a simple yet effective symbol representation and data transmission. [**C17**]
- **c)** Development and evaluation of a novel approach repurposing analog electrocardiography sensor front-ends of commercial off-the-shelf wearable devices for the detection and reception of artificially induced signals. [**C21b; J22b**]
- **d)** Evaluation of a novel technique to provide situational context identifiers through the electrocardiography sensor of commercial, off-the-shelf wearable devices by touching surfaces or objects equipped with transmitter beacons. [**C21b; J22b**]
- **e)** Development of a prototype to measure and characterize the inter-electrode capacitance in diverse settings, furthermore enabling to detect hand-washing. [**W22a**]
- **f)** **OpenIBC**: Development and evaluation of an open-source platform that uses analog RFID / NFC front-ends to enable faster prototyping, aiming at developing potential applications and concepts, e.g. in human-computer interaction. [**C22c**]

3) Synchronization of Wearable Devices

- **a)** Introduction of the novel concept of implicit synchronization, which can use both online and offline methods, is intended to be unobtrusive, and does not require any intentional interaction by the user. [**W21a; C21b; C21c**]

b) PulSync: A novel synchronization method is proposed and evaluated, which exploits the wearer's heartbeat and unique patterns in the slightly varying inter-beat intervals for the data-driven offline alignment of time series. **[W21a]**

c) IBSync: A novel synchronization method, based on intra-body communication, is proposed and evaluated that uses artificial landmark signals to transport data segments, enabling both the unique offline alignment of time series and even their exact temporal allocation online and in respect to absolute time. **[C21b; J22b]**

These contributions have already been published in the following original and peer-reviewed publications, listed in the order of their release and marked with the prefixes J for journal articles, C for conference papers, W for workshop papers, and A for magazine articles:

[C17] **Florian Wolling**, Philipp M. Scholl, Leonhard M. Reindl, and Kristof Van Laerhoven. "Combining Capacitive Coupling with Conductive Clothes: Towards Resource-Efficient Wearable Communication". In: *Proceedings of the 2017 ACM International Symposium on Wearable Computers*. ISWC '17. Maui, Hawaii, USA: ACM, 2017, pp. 146–149. ISBN: 978-1-4503-5188-1. DOI: 10.1145/3123021.3123059.

[W18] **Florian Wolling** and Kristof Van Laerhoven. "Fewer Samples for a Longer Life Span: Towards Long-Term Wearable PPG Analysis". In: *Proceedings of the 5th International Workshop on Sensor-based Activity Recognition and Interaction*. iWOAR '18. Berlin, Germany: ACM, 2018, 5:1–5:10. ISBN: 978-1-4503-6487-4. DOI: 10.1145/3266157.3266209.

[A19] **Florian Wolling**, Simon Heimes, and Kristof Van Laerhoven. "Unity in Diversity: Sampling Strategies in Wearable Photoplethysmography". In: *IEEE Pervasive Computing* 18.3 (2019). Ed. by Oliver Amft, pp. 63–69. ISSN: 1536-1268. DOI: 10.1109/MPRV.2019.2926613.

[W20a] **Florian Wolling** and Kristof Van Laerhoven. "The Quest for Raw Signals: A Quality Review of Publicly Available Photoplethysmography Datasets". In: *Proceedings of the 3rd Workshop on Data: Acquisition To Analysis*. DATA '20. Virtual, Japan: ACM, 2020, pp. 14–19. ISBN: 9781450381369. DOI: 10.1145/3419016.3431485.

[J20b] Elina Kuosmanen, **Florian Wolling**, Julio Vega, et al. "Smartphone-Based Monitoring of Parkinson Disease: Quasi-Experimental Study to Quantify Hand Tremor Severity and Medication Effectiveness". In: *Journal of Medical Internet Research (JMIR), mHealth & uHealth* 8.11 (2020), e21543. ISSN: 2291-5222. DOI: 10.2196/21543.

[W21a] **Florian Wolling**, Kristof Van Laerhoven, Pekka Siirtola, and Juha Röning. "PulSync: The Heart Rate Variability as a Unique Fingerprint for the Alignment of Sensor Data Across Multiple Wearable Devices". In: *Proceedings of the 2021 IEEE International Conference on Pervasive Computing and Communications Workshops, PerHealth Workshop*. Virtual, Germany: IEEE, 2021, pp. 188–193. ISBN: 978-1-6654-0424-2. DOI: 10.1109/PerComWorkshops51409.2021.9431015.

[C21b] **Florian Wolling**, Cong Dat Huynh, and Kristof Van Laerhoven. "IBSync: Intra-body Synchronization of Wearable Devices Using Artificial ECG Landmarks". In: *Proceedings of the 2021 ACM International Symposium on Wearable Computers*. ISWC '21. Virtual, USA: ACM, 2021, pp. 102–107. ISBN: 9781450384629. DOI: 10.1145/3460421.3478815.

[C21c] **Florian Wolling**, Sudam Maduranga Wasala, and Kristof Van Laerhoven. "Optimal Preprocessing of Raw Signals from Reflective Mode Photoplethysmography in Wearable Devices". In: *Proceedings of the 43rd Annual International Conference of the IEEE Engineering in Medicine & Biology Society*. EMBC '21. Virtual, Mexico: IEEE, 2021, pp. 1157–1163. ISBN: 978-1-7281-1179-7. DOI: 10.1109/EMBC46164.2021.9630955.

[W22a] **Florian Wolling**, Kristof Van Laerhoven, Jonas Bilal, Philipp M. Scholl, and Benjamin Völker. "WetTouch: Touching Ground in the Wearable Detection of Hand-Washing Using Capacitive Sensing". In: *2022 IEEE International Conference on Pervasive Computing and Communications Workshops, WristSense Workshop*. Virtual, Italy: IEEE, 2022, pp. 769–774. ISBN: 978-1-6654-1647-4. DOI: 10.1109/PerComWorkshops53856.2022.9767345.

[J22b] **Florian Wolling** and Kristof Van Laerhoven. "IBSync: Intra-body synchronization and implicit contextualization of wearable devices using artificial ECG landmarks". In: *Frontiers in Computer Science* 4 (2022). DOI: 10.3389/fcomp.2022.915448.

[C22c] **Florian Wolling**, Florian Hauck, Günter Schröder, and Kristof Van Laerhoven. "OpenIBC: Open-Source Wake-Up Receiver for Capacitive Intra-Body Communication". In: *Proceedings of the 2022 International Conference on Embedded Wireless Systems and Networks*. EWSN '22. Linz, Austria: ACM, 2022, pp. 186–191.

1.4 Outline

The remainder of this dissertation is structured as follows. This **Chapter 1** introduces to the research topic, describes the applied methodology, and motivates the presented research contributions. **Chapter 2** first considers the human body as a source of natural signals. After an overview of sensing modalities available at the body surface, the focus is on heart rate (HR) monitoring with electrocardiography (ECG) and photoplethysmography (PPG). Specifically for the latter, sampling strategies are investigated and discussed, available datasets are reviewed, the minimum required sampling rate is determined in the frequency domain, optimal preprocessing of raw signals is evaluated, and two algorithms are benchmarked in the time domain. The natural signals available at the body surface are compared and discussed in terms of the target application. **Chapter 3** then considers the human body as a transmission medium for artificially induced signals. After an introduction to intra-body communication (IBC) based on capacitive near-field coupling, five case studies examine various aspects of this novel technique. The first approach simplifies the transmission channel by using conductive textiles, the second repurposes ECG sensor front-ends, the third characterizes the electrode setup used, and the fourth uses RFID / NFC front-ends to receive data. The different approaches are compared and discussed in terms of the target application. Eventually, **Chapter 4** applies the findings of **Chapter 2** and **3** to enable the synchronization of wearable devices. The concept of implicit synchronization is explained, formalized, and then applied to evaluate and demonstrate its benefits. **Chapter 5** finally summarizes the findings and discusses the presented approaches and case studies to conclude the work.

2 | Wearable Sensing

The last three decades have shown an impressive evolution of wearable devices, from bulky portable devices to lightweight and convenient companions in everyday life. The ongoing miniaturization allows for smaller and more fashionable devices which successively become unobtrusive and, to a certain extent, invisible. Worn close or even attached to the skin, these have access to multifaceted information. Since such small devices can be placed on almost arbitrary body positions, they foster the trend from the single all-round wearable to multiple distributed, simultaneously deployed, and specialized sensor units with complementary perspectives to capture the bigger picture. The sensing modalities electrocardiography and photoplethysmography are available in virtually every modern wearable. The transfer of these from medical settings to the user's wrist requires, however, diverse adaptions of the original principles. Furthermore, the resource constraints of wearable devices require for diverse trade-offs and the application of efficient algorithms.

In this Chapter, the human body is considered as a valuable source of information. Primarily focusing on the monitoring of vital signs, **Section 2.1** introduces to the fundamentals of electrocardiography (**Section 2.1.1**) and photoplethysmography (**Section 2.1.2**), which give access to versatile secondary information (**Section 2.1.3**). Wearable photoplethysmography sensors, such as the prototype presented (**Section 2.1.4**), enable to detect the heartbeat throughout the body surface. Although photoplethysmography is standard in modern wearable devices, there are still many questions unanswered, which is why the remainder of this Chapter specifically focuses on the fundamentals of photoplethysmography sensing. First, the sampling mechanisms of passive and active sensors are described (**Section 2.2**) and then studied by investigating the sampling strategies of commercial devices (**Section 2.2.1.2**). The resource constraints of wearables demand for a trade-off between the achieved performance and battery life. To minimize the power consumption of active photoplethysmography sensors, an experimental study investigates the minimum sampling frequency required (**Section 2.2.2**). The development and benchmark of efficient algorithms and the training of machine learning models need large and especially suitable datasets, which are reviewed in **Section 2.3**. The findings have additionally led to guidelines for the recording of fruitful datasets (**Section 2.3.3**). By introducing methods for the frequency and time domain, **Section 2.4** describes the typical processing of photoplethysmography signals. A particular focus is set on the optimal preprocessing of raw signals, which significant influence on algorithms' performance is demonstrated in a benchmark study in **Section 2.4.4**. In the end, **Section 2.5** summarizes all findings and discusses these with regard to the research intent of **Chapter 4**.

Contributions by the Author

[W18] **Florian Wolling** and Kristof Van Laerhoven. "Fewer Samples for a Longer Life Span: Towards Long-Term Wearable PPG Analysis". In: *Proceedings of the 5th International Workshop on Sensor-based Activity Recognition and Interaction*. iWOAR '18. Berlin, Germany: ACM, 2018, 5:1–5:10. ISBN: 978-1-4503-6487-4. DOI: 10.1145/3266157.3266209.

[A19] **Florian Wolling**, Simon Heimes, and Kristof Van Laerhoven. "Unity in Diversity: Sampling Strategies in Wearable Photoplethysmography". In: *IEEE Pervasive Computing* 18.3 (2019). Ed. by Oliver Amft, pp. 63–69. ISSN: 1536-1268. DOI: 10.1109/MPRV.2019.2926613.

[W20a] **Florian Wolling** and Kristof Van Laerhoven. "The Quest for Raw Signals: A Quality Review of Publicly Available Photoplethysmography Datasets". In: *Proceedings of the 3rd Workshop on Data: Acquisition To Analysis*. DATA '20. Virtual, Japan: ACM, 2020, pp. 14–19. ISBN: 9781450381369. DOI: 10.1145/3419016.3431485.

[J20b] Elina Kuosmanen, **Florian Wolling**, Julio Vega, et al. "Smartphone-Based Monitoring of Parkinson Disease: Quasi-Experimental Study to Quantify Hand Tremor Severity and Medication Effectiveness". In: *Journal of Medical Internet Research (JMIR), mHealth & uHealth* 8.11 (2020), e21543. ISSN: 2291-5222. DOI: 10.2196/21543.

[C21b] **Florian Wolling**, Cong Dat Huynh, and Kristof Van Laerhoven. "IBSync: Intra-body Synchronization of Wearable Devices Using Artificial ECG Landmarks". In: *Proceedings of the 2021 ACM International Symposium on Wearable Computers*. ISWC '21. Virtual, USA: ACM, 2021, pp. 102–107. ISBN: 9781450384629. DOI: 10.1145/3460421.3478815.

[J22b] **Florian Wolling** and Kristof Van Laerhoven. "IBSync: Intra-body synchronization and implicit contextualization of wearable devices using artificial ECG landmarks". In: *Frontiers in Computer Science* 4 (2022). DOI: 10.3389/fcomp.2022.915448.

[C21c] **Florian Wolling**, Sudam Maduranga Wasala, and Kristof Van Laerhoven. "Optimal Preprocessing of Raw Signals from Reflective Mode Photoplethysmography in Wearable Devices". In: *Proceedings of the 43rd Annual International Conference of the IEEE Engineering in Medicine & Biology Society*. EMBC '21. Virtual, Mexico: IEEE, 2021, pp. 1157–1163. ISBN: 978-1-7281-1179-7. DOI: 10.1109/EMBC46164.2021.9630955.

2.1 Heart Rate Monitoring

As probably the most important primary vital sign of human beings, the pulse was already of interest in ancient times (200 B.C.) when doctors palpated it to derive the heart rate (HR) and to draw conclusions about the patient's state of health [Cou11]. Today, modern medical instruments take over the task of continuously monitoring and analyzing cardiac muscle activity for the diagnosis of heart diseases. Over the last two decades, miniaturization has gradually brought these capabilities into everyday life [Zhe+14]. While most wearable devices allow the ambulatory measurement of HR, the applied sensing modalities and methods differ significantly from those used in medical settings due to constraints in the possible budget, energy supply, and computing power [Lei+20; Qai+20].

The heartbeat can be detected by means of different sensing modalities. Each contraction of the cardiac muscle (myocardium) is initiated through electrical action potentials, which accumulated electric field can be captured and monitored at the body surface by means of electrocardiography (ECG: **2.1.1**). With its development in the late 19^{th} century, electrocardiography (ECG) has established itself as today's 'gold standard' in medical care. Besides the electrical signal, the contraction also generates a mechanical pulse wave that travels through the blood vessels and is, therefore, ubiquitously accessible at the surface of all sufficiently perfused tissues [Tur+83; Li+10]. In this way, the heartbeat can manually be palpated with fingers at the skin surface above an artery that expands according to the percussion wave [Cou11]. For the continuous monitoring of non-critical, regular ward patients, medical instruments typically use photoplethysmography (PPG: **2.1.2**), an optical measurement principle to detect the pulsating blood volume by means of changing light absorption characteristics of perfused tissue [AP81]. In recent years, the technique has undergone a revival and miniaturization finally made it available as a standard in modern wearable devices for the continuous self-monitoring, health care, and fitness tracking.

Besides ECG and photoplethysmography (PPG), there are methods for specific medical examinations, but also ones that are still under development. According to Pinho Ferreira et al. [PGM21], these can be divided into electric, plethysmographic, and ballistocardiograpic methods. Electric methods are mostly associated with ECG and usually resemble a single standard lead [Cas+08; Klu+19; Li+22]. However, recent research attempts to enable the detection of the heartbeat at a single spot or even from a distance. Often termed as bio-potential sensing [Ha+14], the signal is captured from tiny potential differences along small tissue intervals, e.g. with three or two electrodes on the upper arm [VME19] or forearm close to the wrist [RC16], with a single electrode and the environmental ground as a fragile reference potential [Pra+00; Gar+13; SY16], or remotely in the electric far field [HCP02]. Plethysmographic methods cover PPG but also impedance cardiography (ICG), which analyzes the electrical conductivity of the thorax [She+90] or blood vessels [He+16; Kus+19], magneto-cardiography (MCG), and magnetic resonance imaging (MRI). Lastly, ballistocardiographic methods sense the mechanical percussion wave [Cou11], use microphones to capture the heart sound in phonocardiography (PCG), or measure the blood flow velocity in doppler ultrasonography (DUS). Furthermore, research in ballistocardiography (BCG) and seismocardiography (SCG) revealed that the heartbeat can be detected with sensitive acceleration sensors at the chest [Pha+08; Ver+15] due to the expansion of the thorax, or even at the wrist [Hae+15; McC+18] due to tiny movements of the subjacent perfused tissues. Accelerometers are interesting for this purpose as they do not require direct skin contact and are already available in virtually every wearable device by default. Moreover, they are assumed to be more energy-efficient than active sensing modalities (**Section 2.2**) such as PPG [Hae+15]. [PGM21]

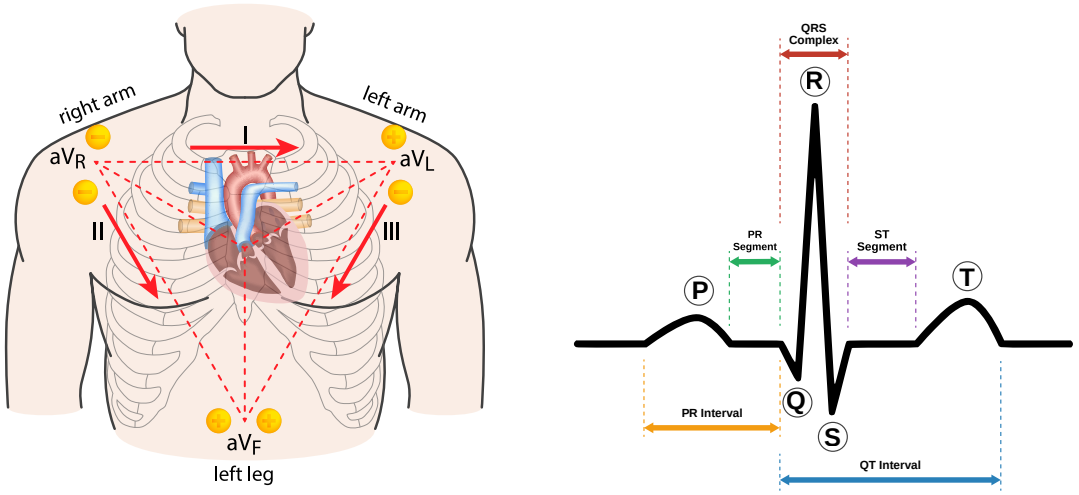

(a) Einthoven's triangle. c.f. [Ad24] (©alfa md) **(b)** The ECG wave pattern. Fig. from [Wik22]

Figure 2.1: (a) Einthoven's triangle with the three bipolar leads I to III, formed through electrodes at the three measurement sites aV_R (right arm), aV_L (left arm), and aV_F (left leg). Figure c.f. [Ad24] (©alfa md, Adobe Stock) **(b)** The well-known ECG wave pattern with its unique attributes, labeled with P, Q, R, S, and T, derived from standard leads such as lead I. The pointed R peak of the prominent QRS complex commonly serves as unique fiducial point and significant feature. Figure from [Wik22] (CC0 1.0).

2.1.1 Electrocardiography

First experiments and the actual invention of electrocardiography (ECG) can be traced back into the end of the 19th century [AL12]. In today's medical care, it is an essential instrument and the 'gold standard' for the analysis of heart activity, to diagnose heart diseases, and to reliably monitor HR. Every contraction of the heart is initiated through electrical action potentials which polarize the myocardal muscle. The electric field accumulates, spreads in tissue, and is eventually detectable at the skin. Since electric potentials cannot be measured without a reference, multiple electrodes are placed at specific locations on the body surface and combined into pairs. Termed as leads, these enable to measure the difference of local potentials, e.g. across the limbs or torso [AL12].

Several lead systems exist which allow to analyze the beating of the heart from different directions and, hence, action potentials of the cardiac muscle's different areas. In 1888, the early ECG instruments of Waller [Wal88] applied "five electrodes, one on each of the four extremities and the mouth" to derive 10 leads. In 1950, Einthoven et al. [EFW50] were able to reduce the number of electrodes to three bipolar ones by excluding those with the "lowest yield". Furthermore, they formulated the important concept known today as Einthoven's triangle (**Figure 2.1a**), illustrating the use of leads I – III to cover the frontal plane with 60° increments [EFW50]. In 1954, the American Heart Association recommended the standardization of the 12-lead ECG with 10 wired, unipolar wet gel electrodes, 6 at the chest (V1 – V6) and 4 peripheral ones of which one is the "indifferent" neutral (aV_L and aV_R at the arms, aV_F at the left and N at the right leg), to cover the frontal plane with 30° increments [Wil+54]. Even more fine-grained, with a grid of tens to hundreds of electrodes worn as a vest, body surface potential mapping (BSPM) enables the detailed analysis of the electric field on the torso [Med+02; Ber+21]. In 1961, Holter [Hol61] presented a lead system with only 5 electrodes, placed over bones to avoid

signal artifacts from muscle activity. This reduced number is less obtrusive and disturbing, yet still sufficient to allow HR monitoring in everyday life and the observation of occasional arrhythmias over a long term. [AL12]

Standard leads, such as lead I, allow to derive the typical, well-known ECG wave pattern (**Figure 2.1b**) with its unique attributes, labeled with P, Q, R, S, and T [Wil+54]. The high reliability and accuracy of ECG originates from the pointed R peak of the prominent QRS complex, a unique fiducial point that commonly serves as a significant feature. The R peaks enable to determine HR by either counting their number per unit time or by calculating the individual R-R interval's reciprocal for an instantaneous measure [CBR91].

The progress in miniaturization does not only enable more convenient but also more energy efficient wearable sensing devices [Zhe+14]. Nevertheless, the conventional ECG leads remain inapplicable and too uncomfortable for the continuous monitoring in long-term ambulatory assessments. The first wearable devices for single-lead ECG, by Karvonen et al. in 1984 [KCS84], had the shape of a chest strap and used dry electrodes to resemble lead I across the heart. Since 2013, these devices have successively been pushed out of the market by wrist-worn devices that primarily apply the optical PPG (**Section 2.1.2**). However, PPG cannot yet compete with ECG in terms of accuracy [Cas+18]. As a result, the wrist-worn devices gradually offer the special feature of a supplementary single-lead ECG sensor to enable the monitoring of heart activity at a medical grade [IM20]. To form lead I with potentials from "either side of the heart" [Bea+18], the user has to touch an electrode with a finger from the opposite arm [Tho+16; Bea+18]. Moreover, by placing the device on the abdomen, the derivation of the leads II and III is also possible [Avi19].

In the recent years, diverse wearable ECG devices in form of skin-compatible adhesive patches have been presented [Cas+08; Klu+19; Li+22] which are expected to improve long-term wearability and comfort. However, they have to be placed accurately to span lead I and cannot be attached to arbitrary body locations due to a phenomenon termed as line of zero potential [Wal88]. It describes that, due to the polarization of the myocardal muscle, no signal is available along a diagonal line across the torso.

The use of dry electrodes inevitably results in a considerably weaker signal [CJC10] that typically ranges from tens to hundreds of µV [Cas14; Ha+14]. The used differential amplifier hence requires a high input impedance in the order of several MΩ to not load the fragile signal [HCP02; CMC11]. Introduced by Neuman and Webster [NW78], detailed by [WW83], a prevalent technique to improve the common-mode rejection ratio (CMRR) is an actively driven electrode, usually termed as driven-right-leg (DRL) circuit or body bias, that allows to suppress common-mode interference such as 50 or 60 Hz humming noise from power line [SY16]. Nevertheless, the single-spot measurement of ECG at the wrist, without closing the wide lead I, remains a challenge [INJ17]. It requires the reference electrode to be omitted by parasitic coupling to the environmental ground [Pra+00; Gar+13; SY16]. This approach requires highly sensitive analog front-ends (AFEs) with a very high input impedance beyond several GΩ and a very high common-mode rejection ratio (CMRR) beyond 80 dB [HCP02; CMC11]. However, with the off-the-shelf AFEs available today, the signal-to-noise ratio (SNR) at the wrist quickly drops to less than 0 dB, which makes the differentiation of the desired signal from the noise floor de facto impossible [Bea+18]. Fortunately, the last two decades have shown promising circuits [Pra+00; HCP02; CMC11; Gar+13; RC16; SY16] that are said to enable "the very highest quality ECG at any point on the body surface, even from the fingertips" [HCP02]. In this way, the electric field would quasi simultaneously be detectable throughout the entire body surface.

2.1.2 Photoplethysmography

With its fundamentals investigated in the late 19th century, the principle of photoelectric plethysmography was introduced by Hertzman in 1937 [Her37] and is today referred to as photoplethysmography (PPG). The optical measurement principle enables to non-invasively monitor the pulsating blood volume flow in the microvascular bed of the tissue beneath the skin [TMS+14; Par+21]. In clinical settings, PPG is regularly applied as pulse oximetry, a proven method to monitor not only HR, but also to determine the peripheral oxygen saturation (SpO_2) of regular ward patients [All07; Alh+19]. The transmission mode is typically applied embracing a fingertip or an earlobe, with light-emitting diodes (LEDs) on one side illuminating the translucent tissue, while a photodetector on the opposite side measures the changes in the detected light intensity, modulated through the increased absorption of a larger blood volume [Her37; NDM81].

Initiated by the crowdfunded Mio Alpha and the Scosche Rhythm in 2013 [KA21], the technique has undergone a revival and is nowadays standard in wearable devices [Cho+22]. Those primarily apply the more convenient, easy-to-implement, and cheap reflective mode at the dorsal wrist, where both illuminating LEDs and detecting photodiodes (PDs) are placed nearby and in the same orientation on the skin surface [TMS+14]. In this way, the non-absorbed light is measured, reflected or scattered by the perfused superficial layers of the skin [AP81; All07; Aba16; MSH18; Bis+19; Par+21].

In both modes, short light flashes are emitted from an intensive light source to actively sample (**Section 2.2**) the blood volume of the moment. There is a broad consensus on the origin of the signal in transmission mode, in which an increasing blood volume absorbs a larger amount of light [Man07; Aba16; Par+21]. In contrast, the origin of signal modulation in reflective mode PPG "is still a matter of debate" [KM17] and "PPG-based techniques and applications have developed more than the opto-physiological knowledge pertaining to the origin of the signal" [MSH18]. This vagueness causes confusion among researchers regarding the phase or 'direction' of the original signal's course [Aba16; KM17; Svi+18; MSH18]. There is a general consensus that signals from the received light intensity of both modes are in phase to each other by nature, but inversely proportional to the captured blood volume variations [NDM81; Aba16; Par+21]. However, even the recently proposed physical models conflict with observations, for example, an amplitude inversion due to wrist rotation [Cho+17; KM17; LC22] and an increased amplitude when "pressing the skin against a glass plate" [MSH18]. Moreover, it is common practice to flip the filtered and normalized signal amplitude during preprocessing (**Section 2.4.4**) to be consistent with and comparable to invasive arterial blood pressure (ABP) measurements [Aba16; Cho+17; KM17]. In commercial devices, this is common practice, but the recordings are, nevertheless, sold as raw signals [Aba16; Cho+17].

In contrast to the well-known ECG signal, the course of the typical PPG wave is less abrupt and has a rounder contour (**Figure 2.3b**). Nevertheless, the systolic and diastolic phases of the cardiac cycle can be identified through the systolic and diastolic points which respectively appear as local minimum and maximum in the raw, non-stationary PPG signal [Cha+22a; Loh+22]. Besides these peaks, the dicrotic notch and peak can appear for healthy subjects due to inflections, wave reflections from lower extremities and the aortic valve [DH41; Mil+06; All07; Elg12; Loh+22]. The definition of a fiducial point P, analog to the R peak of the QRS complex in ECG, then allows to likewise determine the HR [CBR91]. The most commonly used reference point is the diastolic onset, which tends to be more abrupt, pointed, and thus more accurate than the round systolic peak [Gil+10]. Also other feature points, e.g. from tangent intersections [Chi+91] or the signal's second derivative with the attributes a, b, c, d, and e [Tak+98], have been subject to investigation and have both pros and cons [Pos+13; Jey+15; HP16; Per+19; Cha+22a].

2.1.2.1 Light Wavelength

LEDs are used as intensive light source to illuminate the skin as they are small, inexpensive, and can be turned on and off at high speeds, showing an immediate optical response with negligible transient time. This enables fast active sampling (**Section 2.2**) with a low duty cycle to save power. However, the selection of the LED color has large effects on what is actually measured. Depending on the applied wavelength, the human skin shows different absorption, reflection, and scattering characteristics [AP81; Man07]. Coming from pulse oximetry, wearable PPG sensors initially attempted to apply principles of the transmission mode to the reflective mode and often used red and infrared (IR). However, the emitted light penetrates the skin differently and captures information from different dermal layers [San+10; Vol+17]. Short wavelengths of blue and green light measure the blood volume changes in the superficial capillaries of the epidermis, the outermost layer. The medium-wavelength yellow light reaches the arterioles in the dermis, the layer below. Long wavelengths of red and IR are found to even reach the smaller arteries in the hypodermis below. While the pulsating blood vessels modulate the reflected light, the smaller veins and other nearby tissues just add a direct current (DC) component, which typically constitutes about 98 % of the detected light. [COL90; Jin+16; Vol+17]

Several studies attempted to model and simulate the interaction of light in tissue for a better understanding and an optimized sensor placement, mostly based on the Beer-Lambert law for light attenuation [van+89; Man07; Rei+08] and Monte Carlo methods for its scattering. They demonstrated that incident light scatters and is reflected back in a curved optical path which flux envelope resembles the shape of a "banana" [RK10; Aba16; KCW19; CBK20; RBA23]. Longer wavelengths increase its span, penetrate the skin deeper, and attenuate along the path due to scattering and absorption of the tissues, vessels, and blood [KCW19]. Therefore, the optimal distance of each LED from the PD also depends on the applied light wavelength to achieve the maximum signal quality and amplitude [CBK20]. The 'banana' models the cross section, but on the skin's plane, the optimal distance between LED and PD forms a circular optimum around the isotropic light source. To capture a maximum amount of reflected light and to eliminate directivity, a special ring-shaped PD with a single LED in its center has been proposed and evaluated [Kan+12]. Notwithstanding, modern wearables usually use multiple LEDs of at least two different wavelengths, placed around one or few PDs [Cha+19b; Yan+20].

The amplitude of the desired signal also largely depends on the used wavelength while its pulsatile alternating current (AC) component comprises only about 1 to 10 % of the total scope [KM17; KCW19]. To be able to represent the signal sufficiently, the analog-to-digital converter (ADC) of the sensor AFE has to provide a high resolution, typically ranging from coarse 12 up to granular 24 bit [Sch17].

While the origin of the signal modulation at green light, and shorter wavelengths in general, is still subject to research [KM17; MSH18; LC22], its advantages are manifold. Recent PPG sensors tend to use green or even yellow lights, which exhibit the largest modulation depth in the detected signal [TMS+14]. The blood constituents oxyhaemoglobin (O_2Hb) and deoxyhaemoglobin (HHb) absorb about seven (7) times more green than red light [Man07; Vol+17; Alh+19]. However, the signal from green light shows even a factor of 13.1 larger amplitude and a factor of 7.5 better signal-to-noise ratio (SNR) than red light due to a shallower penetration and less attenuation by the tissue layers passed [COL90]. In addition, the signal correlates better with the measurements from ECG than IR light and it is less affected by ambient temperature [Mae+08; MST11b]. With physical activity causing sensor displacement and soft tissue deformation (**Section 2.4.1**), green light has also proven to be more motion tolerant than light with wavelengths that penetrate

the skin deeper and pass through more complex and inhomogeneous textures [COL90; San+10] with different reflection and scattering behavior [Vol+17] that "produce a much more complex signal" [MST11b]. Nevertheless, IR and red light are still regularly used to measure the peripheral oxygen saturation (SpO_2) [Bra+20], which is difficult to be reproduced with shorter wavelengths. IR is also still used to inconspicuously detect proximity to the skin to verify that devices are actually being worn by the user.

Under the hashtag "#tattoogate" users in 2015 complained that tattoos interfered with their devices' HR and contact sensor [Ros15]. More recently, there has also been a debate about a racial bias in fitness trackers, criticizing that the HR measurements are wrong for people with darker skin color [Hai19; Woo22]. The used light wavelengths are naturally absorbed differently by different skin tones with different levels of melanin [Yan+17; Ben+20; Got+22; ACK22]. However, "Skin pigmentation is seen to attenuate reflectance rather than altering the character of the modulation spectra" because melanin "occurs only in epidermis where no blood supply exists", which "suggests that a weak reflected light due to dark skin pigmentation can be compensated by using a stronger light source without compromise to the signal-to-noise (physiological noise) ratio" [COL90]. Nevertheless, it was found that this fact was not sufficiently taken into account in commercial pulse oximeters which recently still showed a considerable error bias [BFS05; Sjo+20]. As a consequence, "Black patients had nearly three times the frequency of occult hypoxemia that was not detected by pulse oximetry as White patients." [Sjo+20].

One promising way to solve this issue is the simultaneous use of multiple wavelengths. To achieve the best signal quality for the individual, either the most suitable LEDs are chosen from a sequentially sampled array of LEDs with single wavelengths each [Yan+17; Yan+20], or a single LED, covering a broad light spectrum, is used in combination with a spectrometer chip, e.g. set up from multiple PDs with attached filters [Cha+19b]. This way, the synchronous use of 15 wavelengths improved the SNR by 50 % and the accuracy of HR by 15 % [Cha+19b]. Moreover, the use of multiple wavelengths enables to prevent occlusion in tissue due to contact pressure and to estimate SpO_2 and ABP.

2.1.2.2 Measurement Location

Considerably constrained by the used transmission mode PPG, conventional pulse oximeters are only applicable at certain peripheral sites that enable to embrace translucent tissue such as a fingertip, toe, or earlobe [Man07; Aba16]. For modern wearable devices, the wrist is the most common measurement location to apply the reflective mode [BDD16]. While the step from the fingertip to the wrist was just an intuitive consequence that resulted from the familiar watches, recent trends show, however, that this is not the only location that is accepted by the customers [Kaw+18]. Today, miniaturization allows for smaller devices that are imaginable at almost arbitrary body positions, only constrained by aspects of wearability and social acceptance [Gem+98; Zea17; Seh+22]. Therefore, especially for long-term deployment, also other body locations are considered as they might be more convenient than the wrist [Cas+18]. In general, there is a perceptible trend toward less obtrusive, more "fashionable" [SH15; Kou18], and even invisible products [BL22].

A dense net of capillaries spans the body surface, therefore it is likely that the positions under consideration provide access to the wearer's pulse. While the PPG signal can be captured from any site with sufficiently perfused tissue, the location is still an important design issue and decides on the signal quality, modulation depth of the signal [Tur+83], and the robustness against motion [TMS+14]. A total of 52 anatomical sites of healthy subjects have been characterized and examined for their degree of blood perfusion using IR PPG and laser Doppler velocimetry (LDV), and the regions face, ears, fingers, and

palms are identified to show the highest average perfusion [Tur+83]. Regions in vicinity of arteries show a good modulation, except for the brachial artery at the upper arm that has relatively poor pulse [TMS+14]. Nevertheless, the application of shorter wavelengths (**Section 2.1.2.1**) allows to obtain signals from almost any location as only the superficial blood vessels are captured and no arteries have to be within reach beneath the skin.

Although popular, the lower arm and especially the wrist are not ideal since they have a comparatively low density of capillaries and low blood flow concentration. Therefore, the two main arteries in a depth of about 5 – 10 mm remain the primary signal source [Cou11] with good signal quality when using IR light to directly measure at the radial or ulnar arteries, only at rest however [TMS+14]. While conventionally placed between the two forearm bones, the distal radius and the head of the ulna, experiments with IR, red, and green light have shown better signal quality if the sensor is located around the distal radius on the left hand [LSH16]. In contrast, the fingertips show a very high blood perfusion and, therefore, provide optimal signal quality with large signal amplitudes [TMS+14]. Because they are already familiar, more comfortable, and "probably, the only thing that the majority of people will accept to wear at all times" [RYA01], smart rings attracted attention in research and have already been available as commercial products for a few years [RYA01; Kin+20; Umm+20; Fio+21]. The fingernail represents a mechanically stable window to well-perfused tissue. A sensor glued to the nail tip, therefore, enables the continuous monitoring in everyday life for several weeks without causing discomfort due to sweating or steaming and the need for sanitary cleaning [IH20]. At the foot, embedded into the sole of a sensing sock and combined with temperature and force-sensitive pressure sensors, PPG showed the best quality below the thumb (hallux) [Gar+18].

The human skull is covered by a thin skin along with a high density of blood vessels, the cranium bone structure directs incident light back which leads to a higher sensitivity, even under conditions of lower perfusion, and motion has minor effect due to little soft tissue deformation, a more homogeneous texture, and rare muscular activity [Cas+18]. In recent research, besides finger and ear, sensors have also been attached to the forehead to detect blood loss (hypovolemia) in trauma patients [Rel+18]. Similarly added to a head-worn virtual reality mask, green-light PPG is applied to the forehead to derive the respiratory rate (RR) [Sta+22] (**Section 2.1.3.2**). Embedded into a surgical eye protection mask, an array of IR and red light PPG sensors is used to monitor HR and to derive secondary measures (**Section 2.1.3**) such as SpO_2 and ABP [Rut+20]. Most recently, PPG is embedded into a face mask to identify and monitor COVID-19 suspects [Yam+22]. Embedded into the nose bridge of eyeglasses, the signal showed to be more resistant to motion during exercises [Zhe+12]. As a part of smart glasses, extended with multi-modal sensors to support context-aware applications, the pulse is incidentally detected at the temple [WFA15]. Aiming at the detection of swallowing, research measured PPG at the throat, showing that the best quality is available "in the mid-throat region over the thyroid gland" while the lower throat is an "excellent choice" to monitor respiratory-induced modulations [Yiz+16] (**Section 2.1.3.2**). A similar approach used IR and green light in the neck to "extract and enhance the laryngeal motion component introduced by swallowing activities" [Zha+22].

The ear turned out to be particularly interesting for PPG as it mainly consists of cartilage, covered with a highly perfused tissue and arteries close to the surface. Furthermore, it is relatively steady and, thus, robust against motion artifacts (**Section 2.4.1**). Prototypes have been developed to measure at locations next to, behind, on, or in the ear. Apparently, the ear canal is the perfect location to shield the sensor from influences of ambient light. The optical coupler can be positioned against the tragus to sense the subcutaneous blood vessels in the region or inside the ear canal which leads to more accurate

signals [BK14; Fio+21]. The earlobe is already familiar from pulse oximetry clips and, due to no cartilage and a large amount of blood vessels, it provides the largest perfusion value [Tur+83] but is far less vulnerable to motion artifacts. [TMS+14; Cas+18; Röd+22]

Diverse body positions have been evaluated for IR and red light PPG and especially the chest showed to be challenging as it tends to be "covered by thick muscle tissue" that shadows the arteries and induces respiratory-related artifacts [Kra+17; Lin+21]. In general, this region is more susceptible to motion-induced deformation due to a concentration of soft tissue with a comparatively large seismic mass. Again, shorter wavelengths have shown to obtain signals even from suboptimal locations such as the chest using skin-compatible adhesive patch sensors [Alh+19; Lee+21; Li+22].

Although the inner blood vessels of dental pulp in teeth, brain in skull, and tissue in bones are naturally enclosed in a ragid envelope, impeding blood volume changes of the inner vessels, these show a weak but detectable PPG signal [NO21; KA21].

In recent years, various approaches have attempted to move "from contact to non-contact and from point to imaging" [Hu+09], with the goal of developing remote, camera-based imaging PPG [McD+15; SY16; Wan+17]. Originated in medical applications such as hemodynamic imaging and the visualization of the blood perfusion in limbs, mostly external, controllable IR or visible light sources have been used to ensure proper illumination and thus a stable SNR [Zhe+08a; Zhe+08b; Hu+09; MSH16; MSH18]. Later on, the user's face attracted interest for applications outside the medical context [Sug+20; Sel+22] and research attempted to use the available ambient light, with considerably lower SNR however [VSN08; Lew+11; Tar+14]. The selection of a suitable region of interest (ROI) [Kwo+15], advanced face tracking techniques [Nag+20; Wei+22], and sophisticated algorithms to extract the desired PPG signal [PSP10; HJ13; Hv14; WSH16; Wan+17; Gud+19; Boc+20] successively enable to derive even secondary measures such as SpO_2, RR, or temporal delays (PAT and PTT: **2.1.3.1**) [Kam+16].

2.1.3 Secondary Information

Both ECG and PPG are fruitful modalities that allow to derive supplementary information, secondary measures beyond the basic HR. The best known one is pulse oximetry that is based on conventional transmission mode PPG and the standard to continuously monitor regular ward patients at the hospital. Besides reading the HR, the use of two different light wavelengths allows to determine the peripheral oxygen saturation (SpO_2). While conventional SpO_2 in transmission mode normally uses IR and red light [Man07], the principle is successively transferred to wearable sensors which apply the reflective mode instead [LKL16]. Recent approaches also demonstrated the derivation of SpO_2 from green and orange light [Alh+19] and using multi-wavelength PPG [Ray+21].

While the electrical field of the cardiac muscle is almost immediately available across the body, the mechanical percussion wave travels more slowly through the arteries until it is detectable at the measurement site. This delay is measured as pulse arrival time or pulse transit time (PAT & PTT: **2.1.3.1**) and allows, for example, to estimate the arterial blood pressure (ABP). In recent years, especially the slightly varying distance between consecutive heartbeats has gained attention as it contains a wealth of information. The analysis of the heart rate variability (HRV: **2.1.3.2**) enables to derive the respiratory rate (RR) but also reflects activity in the autonomic nervous system (ANS).

2.1.3.1 Pulse Arrival and Pulse Transit Time

The electrical stimuli of the cardiac muscle spread in the dielectric of inhomogeneous tissues in different ways [GLG96; Kel+10]. Nevertheless, the conduction velocity is often assumed to be the speed of light ($c = 299\,792\,458\,\mathrm{m\,s^{-1}}$) [Ges89; MP95]. First experiments could only demonstrate a lower-bound propagation velocity of at least $250\,\mathrm{m\,s^{-1}}$ [BG15]. The recent revision with better equipment and improved statistical evidence still showed a comparatively poor mean propagation velocity of $1500\,\mathrm{m\,s^{-1}}$ [Buc+22]. This velocity is in admittedly multiple orders away from the speed of light, but it, nevertheless, makes the signal virtually simultaneously detectable throughout the body surface.

In contrast, the mechanical percussion wave is traveling through the vascular system much slower with a pulse wave velocity (PWV) of about 5.2 to $14.6\,\mathrm{m\,s^{-1}}$ [FAG+10]. It mainly depends on the blood vessel's diameter and the subject's age, which is associated with parameters such as arterial stiffness and blood pressure [Kim+07; CM+19]. Because the diameter of blood vessels decreases with increasing distance from the heart, also the PWV increases. The actual blood flow velocity (BFV) is inversely related to the total cross-section area of the human's vessel network and comparatively slow. It ranges from about $30\,\mathrm{cm\,s^{-1}}$ in the typically $2.0 - 2.5\,\mathrm{cm}$ wide aorta to only about $0.026\,\mathrm{cm\,s^{-1}}$ in the $2 - 12\,\mu\mathrm{m}$ narrow capillaries [Cle21; MGR21].

The pulse arrival time (PAT) describes the time that a pulse wave travels through the vessels from the heart to a peripheral measurement site. It is determined by measuring the location-dependent delay between the detection of the R peak in ECG and the arrival of the pulse wave, e.g. the diastolic onset detected in PPG as fiducial point P. This way, PAT is the sum of the cardiac pre-ejection period (PEP), which is the period of the isovolumetric ventricular contraction of the heart, and the vessel transit time (VTT), the actual time the wave requires to travel from the aortic opening to the sensor location [Che+00; Joh+06]. However, the distance respectively path length from the heart to the measurement site is not directly determinable. Instead, usually the lag between the detection of the same feature P in the PPG signals from two different locations is measured to determine the pulse transit time (PTT), which is inversely proportional to the local PWV of that interval [Che+00]. Therefore, the PAT is a special case of PTT that relies on the R wave in ECG as a reference, virtually located in the heart as the origin of the heartbeat, but includes the PEP time. Typical PATs between the R wave in ECG and the diastolic / systolic point P in PPG are respectively 0.133 s / 0.397 s at the ears, 0.199 s / 0.436 s at the thumbs, and 0.301 s / 0.515 s at the toes [AM00]. Consequently, the position of the sensor on the body surface has a significant impact on the timing of pulse detection.

In medical settings, oscillometric, inflatable blood pressure cuffs (sphygmomanometers) are applied to non-invasively measure the ABP. However, these allow only for intermittent samples in $3 - 5\,\mathrm{min}$ intervals [Cha+19a; Rut+20]. Since PAT and PTT are proportional to ABP [Cha+19a], they are examined to enable its continuous estimation, thus serving as a proper surrogate for the long-term ABP monitoring in everyday life [Wel+20]. Most approaches are based on the combination of ECG and another modality such as PPG to determine PAT [Che+00; Wel+20] or the use of multiple PPG sensors separated from each other to measure PTT [Cha+19a]. The use of multi-wavelength PPG allows to detect the pulse in different skin layers and, therefore, to determine PTT on a very short interval of the blood vessels, thus enabling the single-site estimation of ABP [Liu+16; Cha+19b].

2.1.3.2 Heart Rate Variability

The pointed ECG signal shows a pseudo-periodic run [Bas+87], influenced by diverse physiological processes, illustrated in **Figure 2.2**. The predominating variations are originated in the phenomenon respiratory sinus arrhythmia (RSA) [Moo+85]. Accordingly, breathing modulates the signal in three ways, termed as respiratory-induced intensity (RIIV), amplitude (RIAV), and frequency (RIFV) variations, which allow to derive RR from the ECG time series [Cha+18; AM00]. These variations are, however, different for women and men [Li+10] and in particular RIAV and RIIV are also very sensitive to dehydration and hypovolemia [Deh+18]. The breathing mechanism is controlled by respiratory neurons which regulate the activity of the respiratory muscles of which the diaphragm takes over the major control in breathing control. During inhalation, it moves downward to make more room in the thorax and causes the heart volume to increase. Informed of the increased volume by the sinoatrial node, then the ANS orders to accelerate the HR. The exhalation reverses this process and results in a relaxing diaphragm, a shrinking thorax, a decreasing heart volume, and, therefore, a deaccelerating HR. The variations in intensity and amplitude are, however, originated in "mechanical distortion of the atria due to changes in thoracic pressure" [Bil11]. [Bar+18; Sta+22]

In general, the quasi-random modulation of the R-R inter-beat intervals (IBIs) between consecutive R peaks is termed as heart rate variability (HRV) and contains a wealth of health-related information that have already been interpreted for more than three centuries [Bil11]. In healthy subjects, the interval variations between consecutive heartbeats can be remarkable and contain periodic as well as aperiodic frequency components with medical relevance. A low HRV is generally associated with higher cardiovascular mortality while the resting HRV is an indicator of cardiovascular and autonomic health as well as general fitness, and at night, HRV reflects the sleep quality and reacts to the sleep phases [Kin+20]. While the span of HRV already provides valuable information, usually the HRV interval function is analyzed in frequency domain. An overview of the metrics and standards as well as guidelines for the physiological and clinical interpretation are available [MC96; SG17]. The ANS of the human consists of two parts which regulate the body's unconscious activity and act complementary to each other. While the parasympathetic nervous system with a slower response controls the body at rest and is responsible for the 'rest and digest', the sympathetic nervous system with a faster response controls the shortening reactions of 'fight or flight' in case of a threat. Commonly termed as Mayer wave, a low frequency (LF) oscillation has been observed at about 0.1 Hz which spontaneously occurs in conscious subjects and is assumed to be "tightly coupled with [...] sympathetic nervous activity" [Kam+05; Jul06; Láz+19]. Also the HRV reflects the sympathetic and parasympathetic activity in the ANS, such as the body's thermoregulation [Bas+87; AM00]. Also the effect of sauna was examined, indicating improvements in HRV and arterial health [HMR20].

Similar to the HRV in ECG, a signal modulation is observable in the blood flow and hence in any heartbeat-related modality such as PPG [Kar+13; Cha+18]. Analog to the HRV analysis for ECG, the pulsatile PPG signal shows P-P IBIs which can be taken for a pulse rate variability (PRV) analysis [CS17; Pos+13]. To derive the PRV, it is required to identify robust and reliable features which are preserved throughout the entire body and result in a signal preferably identical to the HRV. The relationship of HRV and PRV has been verified with a "high correlation" [Akd+13] in diverse studies, which conclude that for most applications PRV from PPG can serve as a proper surrogate for HRV from ECG [Gil+10; Pos+13; Mej+20]. The observable differences in the quality of obtained information, usually from the frequency spectrum, are hypothesized to be originated in "technical aspects" [MMK22] and largely depend on the quality of the feature point detec-

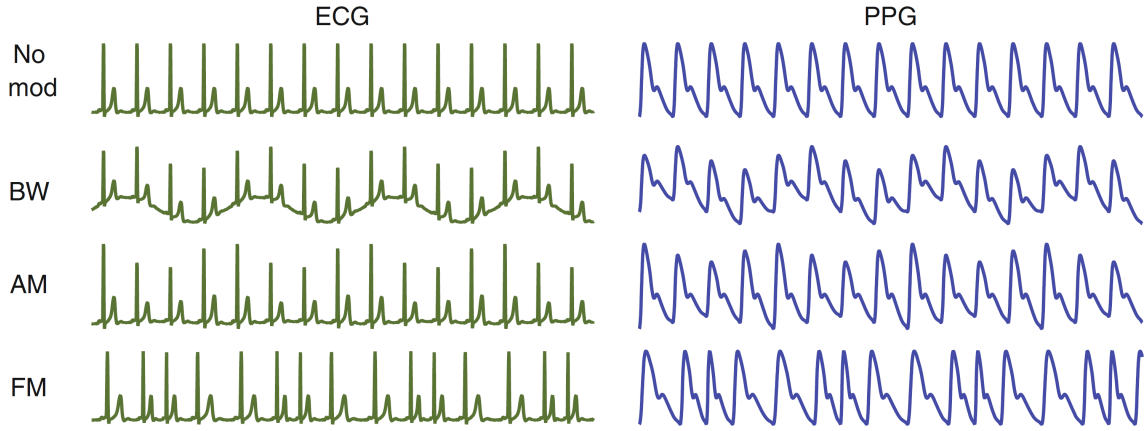

Figure 2.2: Illustration of typical influences on the ECG (left) and PPG (right) signals, induced by physiological processes: no modulation present (top); low-frequency baseline wander (BW), e.g. RIIV; amplitude modulation (AM), e.g. RIAV; frequency modulation (FM), e.g. RIFV. Figure from [CVS16] (CC BY-NC 4.0)

tion and the applied preprocessing [Akd+13; Pos+13; Rib+18; MMK21; MMK22]. While the pointed R peak in ECG is very significant, the pulse morphology tends to be rounder and, moreover, changes considerably with the measurement site as the branching of the blood vessels – from arteries to arterioles and finally into capillaries – influence the blood flow through superimposing reflections and inflections [DH41; Mil+06; All07; CM+19; Har+19]. Nevertheless, the diastolic onset is shown to be not considerably affected and to provide reliable, preserved landmarks throughout the entire body surface [CM+19; MMK22]. It is the most commonly used fiducial point P, but also other features have been evaluated and showed slightly different applicability and accuracy [Pos+13; Per+19; MMK22]. Therefore, the IBIs enable a reliable and relatively noise-resistant analysis as the pulse position identification is less affected by noise and motion artifacts than the directly measured signal amplitudes or intensity variations [Kar+13; Deh+18].

Interval Function

In medical context, the HRV is often plotted in an interval tachogram [Bas+87], a discrete visualization of enumerated IBIs $t_x - t_{x-1}$ from a set of heartbeat-related timestamps T:

$$Tacho(T) := \langle \{t_x - t_{x-1}\}, \ldots \rangle_{x=1}^{\|T\|-1} \tag{2.1}$$

However, as signals from wearable devices tend to be affected by motion artifacts, erroneously detected, spurious peaks can misalign and distort these simple sequences. In contrast, the HRV interval function [Bas+87] is a function of time, based on the timestamps t_x themselves, that is less and, in case of artifacts, only locally disturbed.

$$HRV(T) := \langle \{t_x,\ t_x - t_{x-1}\}, \ldots \rangle_{x=1}^{\|T\|-1} \tag{2.2}$$

Because the HRV interval function is sampled by means of the irregular heartbeat at a finite but varying rate, the obtained information largely depend on the average HR. Standard methods to transform the HRV signal from time to frequency domain, such as the primarily applied fast Fourier transformation (FFT), require, however, regularly sampled sampled time series [LRZ19]. Therefore, the sequence of detected T are first interpolated and then resampled at a certain sampling rate f_{hrv} [Bas+87], with 4 – 10 Hz

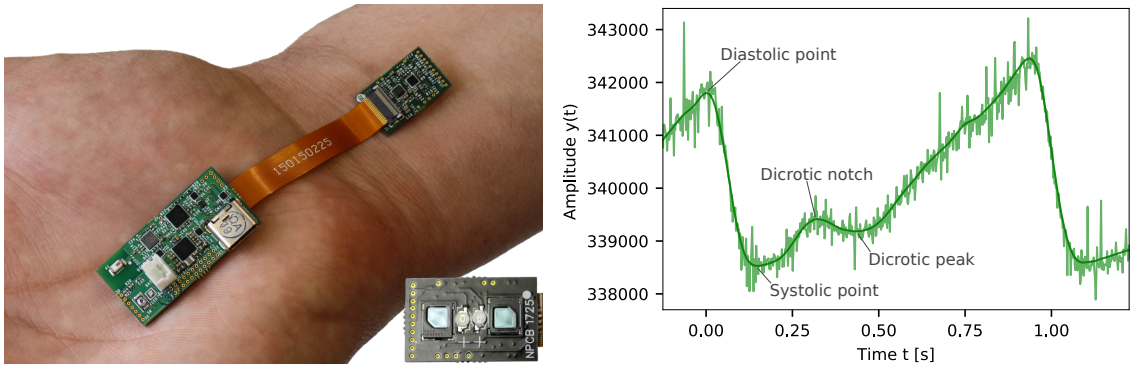

(a) Evaluation system of the MAX86140 / 41. **(b)** Raw PPG signal of a single cardiac cycle.

Figure 2.3: (a) The employed wearable PPG sensor module uses the evaluation board of the MAX86140 / 41 [MAX8]. It combines a low-power microcontroller, a Bluetooth LE transceiver, and a sensing unit with two PDs, a green, and a yellow LED (bottom right). Facing to the skin surface, the sensor unit measures the reflected light to infer the blood volume changes in the microvascular bed of tissue beneath the skin. **(b)** Excerpt from a raw PPG signal covering a single cardiac cycle, measured with green light at a sampling rate f_s of 512 Hz and showing an inverse course. Note the characteristic features: diastolic and systolic point, dicrotic notch and peak of the reflected wave from aorta and lower extremities, as well as the spikes of interfering noise. **[W18]**

found to be useful [Gil92; Cha+18; Mor+19]. Different types of interpolation functions can be applied $intp(HRV(T_X))$, e.g. linear or cubic spline interpolation [Mor+19; MK22]. The discontinuity of linearly interpolated data causes high frequency (HF) noise that is usually eliminated by applying a low-pass (LP) filter to avoid their aliases to show up in the frequency bands of interest.

Due to the rich spectrum of information, features derived from HRV or PRV are often used as the underlying characteristic in novel approaches for the biometric identification of individuals [Isr+05; Akh+15]. Especially the location-independence, stability, and uniqueness of the derived features enable the application in a similar way as the biometric identification through the fingerprint [Isr+05].

2.1.4 Wearable Prototype

The conduction of the intended experiments and the evaluation of the low-level approaches requires hardware that delivers raw PPG signals of a high quality, also considering the recent findings regarding suitable light wavelengths (**Section 2.1.2.1**). The choice was made for the MAX86140 / 41 [MAX8] and its evaluation board as an integrated optical data acquisition system (DAQ) system. It is a state-of-the-art low-power platform that is suitable as a light-weight and wearable PPG-sensing system, as presented in **Figure 2.3a**.

Its central microcontroller is a MAX 32620 ARM Cortex-M4 with floating point unit. It includes 2 MB of flash memory and 256 kB of SRAM to collect the measurements. Readings can also be transmitted via the nRF52832 Bluetooth LE transceiver for intermittent further processing and long-term offline storage. The MAX86140 itself provides three programmable 8 bit LED driver digital-to-analog converters (DACs) for pulse modulation and a low-noise AFE with a single input channel to a 19 bit sigma-delta ADC with integrated filter for 50 / 60 Hz interference from ambient light. It provides sampling rates f_s from 4096 Hz down to 8 Hz. Furthermore, the manual triggering enables individual sequences,

thus even lower than 8 Hz. The option of using a low f_s in combination with diverse energy saving modes and a proximity function to detect skin contact enables the use of this hardware design in research for low power applications. The influence of ambient light is compensated and abrupt changes can, if activated, be rejected by a picket fence detect and replace algorithm for value estimation. As a result, the modules provide stable signals, but still allow to obtain unfiltered, raw PPG measurements which is important for the research intent. They allow for the unconstrained offline analysis of recorded signals, including the application of possible filters without anticipating the necessity of preprocessing stages such as a LP filter for the elimination of baseline wander.

The use of a suitable light source (**Section 2.1.2.1**) is essential. The prototype provides a green LED (LT PWSG) with $\lambda_g = 528\,\text{nm}$ and a yellow, amber-colored LED (LY P47F) with $\lambda_y = 590\,\text{nm}$. To detect the small variations in the detected light, the system uses two PDs (VEMD5010X01) with a sensitivity suitable for visible and near infrared light. In the conducted experiments, the following measuring parameters have been applied: During each sample, the LEDs are successively turned on, driven with a current of 4.9 mA. After a settling time of 12 µs the reflected light is integrated for 14.8 µs and, finally, measured by the ADC. Although the measurement time can be extended up to 117.3 µs, resulting in a higher SNR, the default configuration is used due to a significant lower energy consumption, nevertheless, still providing a sufficient modulation depth for most skin types.

However, the duty time of 14.8 µs already results in a time-averaged current of about $262.6\,\text{nA}\,\text{Hz}^{-1}$. Thus, the activation of each discrete LED incorporates a relevant portion of the prototype's energy consumption: about 1.1 mA at 4096 sps, 134.5 µA at 512 sps, 16.8 µA at 64 sps, 2.1 µA at 8 sps. Therefore, not only the LEDs' demand increases linearly with the applied f_s, also the AFE consumes a rising current, ranging from a few µA up to about 1.2 mA. Just the PPG module's sensor AFE with a single LED hence consumes about 2 mA at the maximum f_s of 4096 sps, compared to less than 5 µA at about 10 sps. In addition, a higher f_s has also large impact on the microcontroller's busyness, resource and memory usage, again resulting in a larger dissipation.

2.2 Sampling Strategies

Sampling is the fundamental principle that allows physical quantities to be captured from the analog real world and the continuous input signals to be represented by a sequence of discrete data values. Theoretically, the signal is sampled by Dirac unit impulses of infinite amplitude, infinitesimal width, and discrete time to capture the value of the exact moment. However, the imperfections of reality affect this mechanism and thus limit the achievable accuracy. In general, analog-to-digital converter (ADC) circuits serve as an interface between the analog and the digital domains and digitally quantize the continuous analog signal, usually provided by the sensor as a voltage. The different ADC types have different pros and cons regarding power consumption, accuracy, noise-immunity, and conversion time. The conversion time describes a non-negligible period of time needed for the conversion while the input signal may still change, e.g. due to noise. Therefore, sample and hold amplifiers (SHAs) are used to capture the voltage of the moment, store it and hence to ensure a constant level for a certain period of time and eliminate the unwanted fluctuations. Storing a sufficient amount of energy to enable the conversion process requires a storage element such as a hold capacitor. Consequently, the charging characteristics of capacitors apply to the circuit's input and, although the flowing current is comparatively small, it can load the sensor and affect its delivered signal. Limiting the flowing current by a high input impedance reduces this load but requires a more sophisticated ADC and usually a longer sampling time to charge the hold capacitor. Therefore, it is essential to harmonize the ADC and its SHA with the sensor being read to keep leakage current low and not affect its signal beyond a certain degree. [Lyo11; Zum11]

2.2.1 Passive and Active Sampling

Passive sensors measure the energy emitted by an external source, which can either directly reach the sensor or take a more complex path. The intensity of sunlight, for example, can be measured directly with a photodetector, but it can also serve as a means of measuring the reflectivity of an object that reflects the incident sunlight to the sensor. In contrast, active sensors themselves emit energy, such as radio waves or light, that is backscattered and reflected by the objects and environment under investigation. The changes in the detected signal can then be analyzed, interpreted, and, if necessary, calibrated.

Thus, ECG is a typical example of a passive sensing modality that detects the electric field generated by the myocardial muscle. In contrast, PPG requires the active emission of light at specific wavelengths to capture the changes in blood volume beneath the skin. Recent approaches in remote PPG attempt to use ambient light to detect the pulse in camera images. Unfortunately, the extracted signal tends to be weak and shows a rather low SNR. Furthermore, sunlight introduces large natural fluctuations in both intensity and wavelength spectrum, depending on day time, altitude of the sun, and cloud coverage. Artificial light even exhibits continuous flickering at 50 / 60 Hz, causing significant interference. A reliable HR measurement might, therefore, be possible in illuminated rooms with constant and bright light conditions. For wearable devices, worn close to the body surface and in changing environments, frequently affected by motion, natural light is most likely not sufficient and a supplementary light source is required.

Therefore, PPG actively illuminates the skin with LEDs of specific wavelengths and simultaneously measures the intensity of the backscattered and reflected light with one or multiple PDs. The sampling rate f_s is one of the key parameters as it decides about the the energy dissipation and the device's battery life on the one hand, but also on the temporal resolution and the signal's details on the other hand. A patent application by

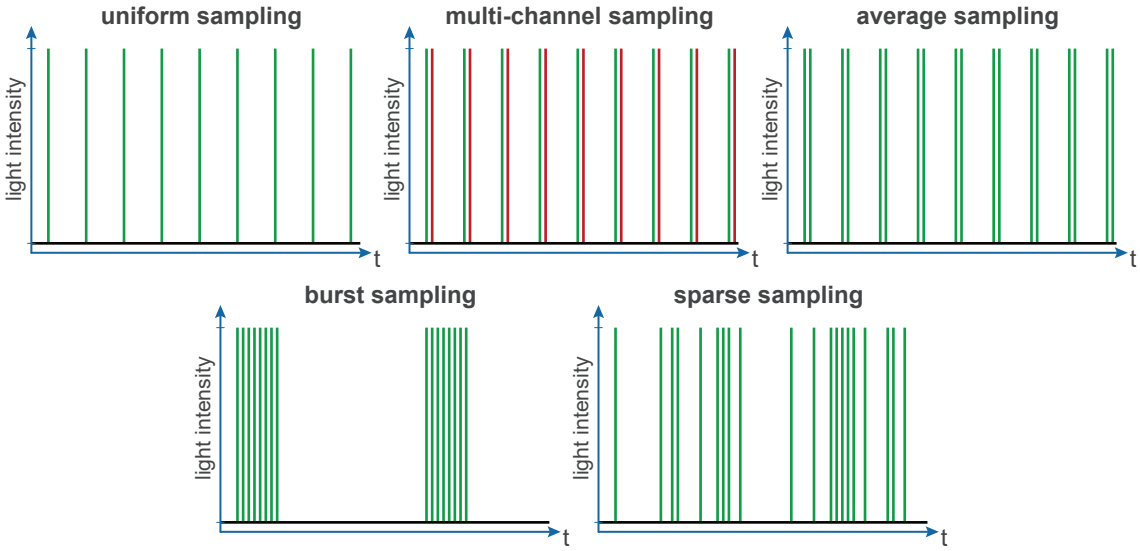

Figure 2.4: Typical sampling schemes applied in wearable PPG sensing devices. From left to right: **a)** uniform sampling with constant frequency, **b)** multi-channel sampling with multiple subsequent pulses of different wavelengths, **c)** average sampling with multiple samples per captured value, **d)** burst sampling with a burst frequency and duty cycle which window captures samples with a specific pulse repetition frequency (PRF), and **e)** sparse sampling for compressed sensing with a randomized sampling pattern. [**A19**]

Intel mentions that "the LED pulsing consumes approximately 80 % of system power in a conventional 32 Hz PPG design" [NDR17]. With regard to the characteristics of the light source, photodetector, and the AFE, several other parameters have to be considered when sampling PPG. These are mainly the LEDs' colors, settling and transient time, and intensity on the one hand, and the PD's sensitivity, dimensions, and the applied ADC's SHA on the other hand. The dimensions of the PD with its inherent capacitance and the sample and hold time influence the quality of the captured measurement and the resulting SNR. A longer sample time extends the integration time, which means that the induced signal of the incident light is accumulated and HF distortions are neglected by averaging. However, the peak current for the illumination can be tens of mA and powering the high-intensity LEDs over extended periods puts a large dent into a wearable's energy budget. Therefore, the LEDs are switched on only for a short flash period of several ms down to tens of µs for each sample, thus significantly limiting the required power.

Although diverse advanced sampling strategies have been proposed, most research in PPG still relies on conventional uniform, regular sampling. In contrast, commercial devices are following very different approaches and use different sampling strategies to save energy and yet obtain good readings. This begs the question: How often, and in which sampling scheme, should these measurements take place?

2.2.1.1 Present Strategies

In traditional uniform sampling (**Figure 2.4a**), which is still the most common scheme, samples are taken continuously at a particular frequency. However, if the device is not worn, many devices resort to a reduced sampling rate with single intermittent samples. Such proximity measurements are often performed with IR light as it is not visible for the human eye and, thus, not distracting. If multiple channels with different wavelengths

are available (**Figure 2.4b**), those are triggered subsequently with a little gap to permit the PD to recover. This gap should not to be too large, otherwise the physiological signal would change during the measurement and the samples would no longer be comparable and quasi simultaneously taken. For example, determining SpO_2 requires the ratio of measurements from two different wavelengths, ideally taken at the same moment (**Section 2.1.3**). Sampling can also be reduced in other situations, such as when the user is moving too much to deliver a clean PPG signal.

Sampling improvements have been achieved by capturing multiple adjacent samples that are averaged (**Figure 2.4c**) either in software or, more efficiently, in hardware. This method decimates the amount of data throughput, but also reduces the influence of HF noise due to the implementation of a simple moving-average LP filter. This increases the number of samples per averaged value, and consequently the cost of illumination is increased as well, but the derived values stay at a lower rate and do not require more resources or larger efforts in processing. Another approach reduces the energy consumption through non-averaged, intermittent burst measurements (**Figure 2.4d**) at which the duty cycle determines the power dissipation. Similar to continuous sampling, the samples are taken at a specific sampling rate, the so-called pulse repetition frequency (PRF), but the measurement is limited to a certain time interval. The minimization of this duty cycle reduces the energy demands, but at the same time reduces the gathered information, as well. Diverse approaches make the devices only record samples if the user is at rest for a certain time, thus avoiding distortions through motion artifacts.

Yet another strategy uses non-uniform sampling, which is applied for compressed sensing approaches (**Figure 2.4e**). Raw PPG signals are pseudo-periodic pulse signals which are superimposed by non-stationary, chaotic low-frequency baseline wandering and HF noise. Because the desired signal exhibits low activity and diversity, uniform sampling delivers redundant data that is largely predictable. To reduce the dissipation through needless light flashes of the high-intensity LEDs, the samples are partially omitted and a sparse sampling scheme in a random pattern is applied. Due to the reduced number of samples, also less data has to be processed. However, the missing information of the fewer samples has to be reconstructed and estimated through suitable methods, which in turn require computational efforts and energy again. Whereas such algorithms are usually running on larger platforms and result in highly accurate estimates, the performance of wearable devices is limited and such algorithms would need to be highly efficient to outperform conventional uniform sampling. An example for hardware-implemented compressed sensing, a input-dependent integrate and fire sampler is proposed that avoids "redundant sampling" by capturing only specific ROIs such as the pulse peaks by predicting their locations and intensifying the sample density accordingly [NPE15].

2.2.1.2 Strategies of Commercial Wearables

In **[A19]**, the sampling strategies of seven (7) commercial wrist-worn devices are analyzed, specifically not addressing their accuracy and the success of the approaches, but instead investigating what types of sampling schemes and strategies are used in current PPG-based wearables. The set of devices covers the entire price spectrum, from low-cost wristbands up to expensive lifestyle devices that have appeared over the past years. The oldest device, commonly used in research studies, is the Empatica E4 [EmE4], released in November 2014. Next is the consumer product Samsung Gear S3 from November 2016. The fitness tracker Polar OH1 has been released in September 2017, and the devices Mobvoi TicWatch E and Xiaomi Amazfit Bip have been released late 2017. The most recent devices are the Fitbit Versa from March 2018 and the Apple Watch 4 from September 2018.

Table 2.1: Overview of the pulse repetition frequency (PRF) and group frequency (GF) of the 7 analyzed commercial PPG sensing devices, sampling either in the continuous or the sporadic modes. **Figure A.3** and **A.4** provide excerpts from the measurements. [**A19**]

		Continuous		Sporadic	
Product	Release	PRF	GF	PRF	GF
Empatica E4	Nov. 2014	5 kHz	64 Hz		
Samsung Gear S3	Nov. 2016	1.3 kHz	20 Hz	20 Hz	0.5 Hz
Polar OH1	Sep. 2017	4.8 kHz	135 Hz		
Mobvoi TicWatch E	Nov. 2017	3.8 kHz	20 Hz		
Xiaomi Amazfit Bip	Dec. 2017		25 Hz		
Fitbit Versa	Mar. 2018	2.7 kHz	256 Hz	25 Hz	unknown
Apple Watch 4	Sep. 2018	7.5 kHz	25 Hz	2.5 kHz	8 Hz

The PPG sampling of all wearables is monitored in two conditions. **Figure A.1** shows the continuous sampling that is actively triggered through the user interface, for example to monitor physical exercises, whereas **Figure A.2** shows the incidental measurements that are applied sporadically during normal operation to save energy. Each device's LED activity is captured with a PD and recorded by a digital oscilloscope. The amplitude is normalized and the pulses are identified using a threshold-based peak detector to enable the characterization of all sampling parameters. **Table 2.1** summarizes the insights.

With one or two PDs placed near multiple LEDs, the physical appearance of the sensing setup looks similar for most wearables. An elaborate configuration with Fresnel lenses seems to be used by the Apple Watch 4 while all other devices place the PDs directly on the skin surface. The Empatica E4 and the Mobvoi TicWatch E provide a shielded window to the sensor, but the other devices, such as the Xiaomi Amazfit Bip, place the sensor closer to the skin by making it protrude from the case. All tested wearables apply green light. However, the Empatica E4 and Fitbit Versa apply green and red light, and the Apple Watch 4 uses green and IR light to support the derivation of SpO_2.

The sampling schemes show a large diversity. Straightforward uniform sampling is used by the Xiaomi Amazfit Bip which simultaneously samples two green LEDs at 25 Hz. The Samsung Gear S3 and Polar OH1 also use two green LEDs, but differently. The Samsung Gear S3 consecutively flashes at 1.3 kHz pulse repetition frequency (PRF) and 20 Hz group frequency (GF). The Polar OH1 uses 4.8 kHz pulse repetition frequency (PRF) and 135 Hz group frequency (GF), presumably in an averaging strategy. The most recent devices, the Fitbit Versa and the Apple Watch 4, are following the approach of multi-channel sampling and utilize green light in combination with either red or IR light. The two channels are likely used to determine SpO_2. The PRF and GF are 7.5 kHz and 25 Hz respectively for the Fitbit Versa and 2.7 kHz and 256 Hz for the Apple Watch 4. The Empatica E4 has two green and then two red LEDs flashing subsequently, with likely two readings of the same wavelength averaged and then likely used to enable the SpO_2 determination. It is the only device that actively regulates the light intensity according to the present body surface. The Mobvoi TicWatch E surprisingly applied a fundamentally different scheme at which three pulses are followed by 25 larger pulses and a terminating larger pulse of presumably green light. While the PRF is about 3.8 kHz, the GF is only about 20 Hz.

Sporadic sampling modes were only applied by three devices, the Samsung Gear S3, the Fitbit Versa, and the Apple Watch 4. The latter one uses three consecutive samples from the green LEDs at about 2.5 kHz PRF and 8 Hz GF while the IR LEDs seem to be inactive. The Samsung Gear S3 applies a burst measurement with a PRF of about 20 Hz instead, repeated at a GF of about 0.5 Hz. Finally, the Fitbit Versa applies an interesting sampling scheme with a PRF of about 25 Hz in which the amplitudes of the green LEDs are

gradually decreasing. In the first time period, the two treads exhibit four pulses, followed by 42 pulses with a constant amplitude, then followed by a second time period with 30 adjacent double pulses. The latter ones consist of two flashes, alternatingly emitted either from the green or the red LED.

To get an idea of what is possible by optimizing the sampling strategy and measurement duty cycle, one can experience the Oura ring, a small and comparatively unobtrusive sleep tracker that successively turns into a fully-featured fitness tracker. While the second generation was sampling with IR light only at night and at comparatively high 250 Hz [Tur19], the third generation, released in 2022, has two PDs and samples only at 50 Hz [Our22a]. During the day, it measures every five (5) minutes for a period of one (1) minute with two green LEDs [Our22b], at night, it also determines the SpO_2 with a red and IR multi-chip LED [Ste22], and during exercises like running, activated by the user, it measures again with green light. This way, the tiny device achieved an accuracy comparable to that of medical grade ECG [Kin+20]. Although the battery has only a capacity of 16 mA h [Ste22], tiny compared to the capacity of a wrist-worn device with typically about 200 – 350 mA h, it nevertheless lasts for about one week.

2.2.2 Minimum Sampling Rate

As discovered in the previous **Section 2.2**, commercial devices tend to use a significantly higher sampling rate f_s to obtain more detailed signals with a high temporal resolution. The trend to inconsiderately increase f_s prevailed for a while. On the one hand, it has been motivated by the filter-based stabilization of the average, statistically representing the expected value, smooths the slope, and suppresses occurring noise. On the other hand, the interpretation of the HRV requires a higher f_s to precisely locate the pulse peaks and to measure the IBIs between consecutive peaks. **Figure 2.5** illustrates the relation between f_s and the temporal resolution which is required for an accurate HRV derivation [CS17].

Due to the high energy consumption and the desire for small and long-lasting wearable devices, research again concentrates on the reduction of f_s, to reach its necessary minimum. Thus, the fundamental Nyquist-Shannon sampling theorem [Sha49] returns to mind, which defines the possible minimum f_s necessary to reliably represent the desired signal. However, in the raw measurement data, the interfering noise is not filtered and the signal thus not band-limited. Consequently, a higher f_s would be required to not violate the guideline and unwittingly cause aliasing. However, at a certain point, the benefits of a higher f_s will stagnate while the energy consumption will still increase constantly.

The approach of Giovanni et al. [Gio+16] examines the energy-efficient estimation of HR based on a single-sided amplitude spectrum, applying the FFT on short windows of PPG signals. The algorithm removes existing motion artifacts without the reconstruction of a noise-free signal or adaptive filtering. Additionally, by lowering the f_s from 125 Hz to 31.5 Hz it was able to reduce the required memory to 5.8 kB. At the same time, the average absolute error increases only from 1.27 ± 0.91 bpm to 2.24 ± 1.01 bpm.

A similar approach is examined by Choi and Shin [CS17] which evaluates the required minimum f_s to reliably analyze the HRV. The original 10 kHz PPG signal is sampled down by decimation to the range of 5 kHz to 5 Hz. Afterwards, the signal sequences are analyzed in time and frequency domain, and then compared to the reference ECG measurements with a f_s of 10 kHz. As a result, it is stated that a f_s beyond 25 Hz does not show significant difference to the lower ones and, thus, a higher f_s does not contribute to the reliability of PPG for the HRV derivation.

The following study **[W18]** argues for using wearable PPG sensors to observe slower trends, across longer stretches of time, by evaluating data that span minutes rather than

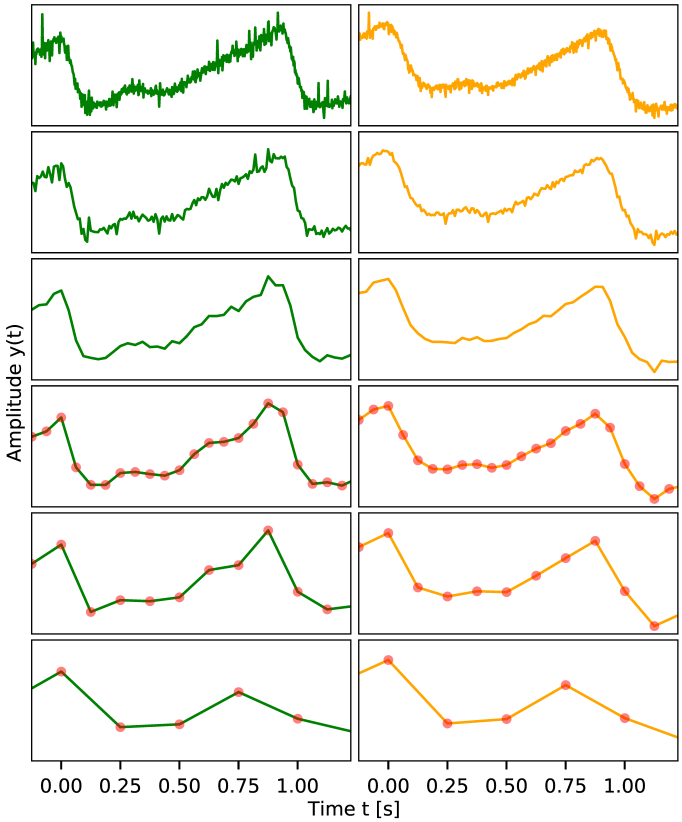

Figure 2.5: Illustration of the effect of downsampling through decimation on the PPG signal, with the channels of green light (left) and yellow light (right), from 512 Hz (top) down to 128, 32, 16, 8, and 4 Hz (bottom). With lower frequency, the temporal resolution decreases and an accurate localization of the pulse peaks is not possible anymore. **[W18]**

seconds. Using spectral analysis of minute-long signals, it is intended to extract the different oscillations present in the PPG signal that correspond to HR, RR, and a third range which has been identified to represent sympathetic nervous activity (SNA). Specifically the effect of the PPG sensor's sampling frequency f_s on such estimates is investigated, since the LED-driven measurements are a major hurdle for wearable long-term deployments. Therefore, two experiments are presented: One on a clinical benchmark dataset of 42 individuals and a second one on experimental recordings from 6 individuals taken with the wearable PPG system presented (**Section 2.1.4**).

2.2.2.1 Analysis on a Public Dataset

The approach is first validated regarding the effect of f_s on the spectral analysis of PPG data with a publicly available dataset that has been recorded from a highly variable set of 42 users. As will be discussed in the following section (**Section 2.3.2**), raw PPG data is not as easily found. The popular CapnoBase IEEE TBME dataset [Kar+10; Kar+13] with recordings from a fingertip pulse oximeter is used. It is one of the few publicly available clinical datasets that contain synchronized ECG, PPG, and CO_2 RR recordings from a large variety of persons. The dataset was originally devised for examining RR estimation algorithms from presumably raw PPG signals of 42 persons, for a duration of eight (8) minutes each and sampled at 300 Hz. The PPG readings are complemented with reference CO_2 readings, ECG readings, and artifact labels validated by an expert rater. **Figure 2.6a** shows a one-minute segment of raw ECG, CO_2 RR, and PPG data from this

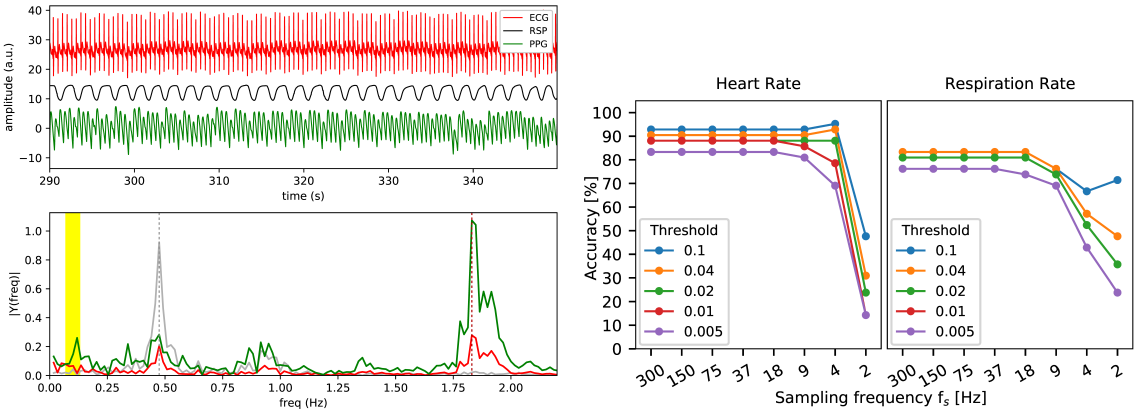

(a) Analysis of the CapnoBase IEEE TBME. **(b)** Results for the CapnoBase IEEE TBME.

Figure 2.6: (a) Analysis of an excerpt from the popular CapnoBase IEEE TBME dataset [Kar+10; Kar+13] with fingertip pulse oximeter readings taken from 42 individuals. Original time series over 1 minute from wearable ECG, CO_2 RR, and PPG sensors, all sampled at 300 Hz (top). Frequency spectrum of PPG data, annotated with frequencies and dominant frequency in ECG and CO_2 RR (bottom). Occurrence of LF processes typical for SNA. **(b)** Accuracy for the detection of HR (left) and RR (right) from the PPG readings, while varying f_s from the sensor's original 300 down to 2 Hz. The different lines represent the results using different thresholds to establish whether a correct prediction was made. They are measured in Hz as the maximum absolute distance between prediction and ground truth. Note that reducing f_s to as low as 18 Hz or 9 Hz has a moderate to minor effect, with a more severe impact for the estimates of RR. **[W18]**

repository, and our frequency analysis for the said segment.

In a first pass, possible artifacts in the dataset are eliminated by selecting, for each person, a one-minute subset of data for which no artifacts are present in the ECG, RR, or PPG signals. These artifacts are annotated in the benchmark, using the incremental-merge segmentation (IMS) algorithm [Kar+12], which detects short-term artifacts by identifying abnormally large and clipped pulses. Subsequently, the DC component in raw PPG data is removed through a high-pass (HP) filter with a cutoff frequency of 0.01 Hz. Spectral analyses is performed based on Welch's method of an averaged periodogram [Wel67]: The PPG time series are divided into 50 % overlapping 60 s segments, computing a modified periodogram for each segment, and averaging the resulting periodograms. The segments are Hanning-windowed, to minimize the first sidelobe of the frequency response, and Fourier-transformed using the FFT. The range of the expected RR and HR frequencies is as in [Kar+13] defined as 0.067 – 1.08 Hz or 4 – 65 cpm for RR and for the HR a similar search window that reaches up to 3 Hz or 180 cpm. For the calculation of the average frequencies for both HR and RR, the frequencies with maximum power within the respective ranges are then identified. For SNA, the area under the power spectrum is computed for the LF range from 0.04 to 0.15 Hz [AA06].

To study the effect of the f_s on the detection of HR, RR, and SNA, intermittent samples are systematically removed from the original 300 Hz data, down to 2 Hz. **Figure 2.6b** shows the results for the recovery HR and RR, using a range of distance thresholds from 0.005 Hz up to 0.1 Hz. The predicted frequency is marked as correct if it is within this threshold from the ground truth, and false otherwise. Overall, the detection of the RR around 80 % is lower than the HR around 90 % for the same thresholds. The detection for the HR and RR accuracy can also be seen to deteriorate rapidly after reducing f_s to 4 Hz.

2.2.2.2 Analysis on Experimental Data

After the evaluation of the fundamental approach, in a second experiment, experimental data from the previously presented wearable PPG sensor system (**Section 2.1.4**) are analyzed and evaluated. For the experiments, besides the PPG sensors themselves also other sensors have been utilized to provide ground truth information about the actual RR, but also to detect mechanical disturbances. The recordings have been analyzed offline on a computer. To provide a matched data base, the sensors have been synchronized with specific gestures as will be discussed in the remainder of this dissertation (**Chapter 4**).

Primary device is the wearable sensor module based on the MAX86140 / 41 [MAX8] that has been employed to record raw PPG data at the subjects' right wrist. Further, the onboard accelerometer BMA280 is used to support the identification of occurring disturbances. Besides the elimination of motion artifacts, this even enabled to examine the mechanical influence of breathing, as the arm is slightly displaced with every thorax movement. To gather ground truth information about RR, a secondary sensor module has been attached below the chest's left pectoral muscle, close to the heart. It focuses on the acceleration that is changing due to the direct thorax expansion and, consequently, enables to infer RR. The position was chosen to additionally test the PPG principle at this position in foresight for the use in smart patches. However, the chest strap of the second device has been perceived as unhandy and uncomfortable, and was not applied in later experiments. Instead, a time-of-flight (ToF) depth camera has been used to remotely measure the respiratory movements of the thorax. This measurement principle has been validated in detailed respiratory experiments and showed high accuracy and reliability [Kv18] (**Figure 2.7**). The two wearable modules recorded the measurements of the two PPG channels, green and yellow light, the ambient light intensity, and the acceleration in three axes at a f_s of 512 Hz. For both PPG channels, the influence of ambient light has automatically been detracted. Due to the slower frame rate of the depth camera, the RR reference signal is recorded at about 30 Hz.

The PPG sensors and accelerometers are synchronized onboard. However, the two wearable devices, attached to wrist and chest, as well as the external depth camera still had to be synchronized among each other. To link the wearable modules, their casings are tapped against each other to generate significant peaks in the acceleration. Subsequently, a fast waving gesture, of the arm with attached sensor module, through the measurement window, spanning the chest of the detected subject, enabled to link the depth camera signals with the acceleration channels of the wearables. By executing this procedure at the beginning and the end of the recordings, also the clock drift of the particular devices can be rectified which is important for longer time spans.

Diverse filters and algorithms are applied to extract the desired parameters HR, RR, and SNA from the recorded signals. At first, the parameters are estimated according to the approach of this research, based on the frequency spectra of the FFT (**Section 2.4.2**). Those are then compared to the estimates that have been extracted the conventional way, using established and widely accepted standard techniques. The most fundamental value derived from PPG is the HR. To extract this parameter from the measured signals, a standard peak detection algorithm has been applied. It is common even though not efficient, but ensures the independency from specific concepts and algorithms. Thus, it returns not only the count of peaks per window length, but also their position which is basic requirement for the subsequent parameters. To achieve a reliable locating of the pule peaks, the algorithm has been configured considering the standard HR frequency range between 0.67 Hz and 3.67 Hz respectively 40 bpm and 220 bpm [Gio+16] (**Figure 2.13**). Due to optimal conditions of the selected data windows without motion artifacts, this approach

is sufficient. Before the peak detection is executed, the signal is filtered with a forward-backward, linear phase, 2nd order band-pass (BP) filter to reject baseline wandering and noise below 0.025 Hz and beyond 10.0 Hz.

Due to RIIV (**Section 2.1.3.2**), it is possible to extract RR directly from the fluctuations in the raw PPG signals. However, because this feature is very sensitive to motion artifacts, the measurement of the related phenomenon RSA through HRV is currently the mostly applied way. The slope of HRV is derived from the positions of the pulse peaks which have been used to generate the envelope function of the raw PPG signal. The maxima respective the diastolic base points represent an irregularly sampled sequence of peak-features that is resampled using linear interpolation [Kar+13; Cha+16].

2.2.2.3 Results and Discussion

Figure 2.6a shows a typical time series of the first experiment's benchmark dataset which provides the three channels of ECG, RR CO_2, and PPG. Although the patients are not artificially ventilated at a specified frequency, the respiratory signal still shows a uniform, continuous signal and a pointed, significant peak in the frequency spectrum. The heart beat is distinctively observable in both, the ECG and the PPG signals. The superimposing RIIV is simultaneously observable in both channels, however, its amplitude is clearly lower than the primary pulses. As a result, the frequency and power spectra show significant peaks at the fundamental frequencies of HR and RR within the mentioned frequency bands. The peak of the RR CO_2 measurement is congruent with the RR-associated peaks in the ECG and PPG channels, but those are less distinct. In contrast, the dominant frequency peak of HR is several times larger than the one of RR due to its smaller amplitude of the superimposing RIIV. The results of the downsampling are presented in **Figure 2.6b** and show a relatively stable accuracy down to a f_s of about 9 Hz for both HR and RR with about 90 % and 80 % correctly identified dominant components.

In contrast to the first experiment, the subjects of the second experiment performed paced breathing at 0.25 Hz. As is observable in **Figure 2.7**, all three reference measurements, either from the ToF depth camera or of the on-board accelerometers, show a similar signal, resulting in a significant peak at the desired RR frequency in the spectra. Thus, the ToF depth camera provides reliable reference measurements and is a valid replacement for the obtrusive chest strap that has been used in preliminary experiments. Although still observable at the wrist, the influence of the respiratory motion due to thorax displacement is expected to have negligible influence on the quality of the PPG signal. The **Figures 2.8** and **2.9** show excerpts from the time series of the PPG sensors attached to wrist and chest. Apparently, the chest sensor's signal is considerably superimposed by respiratory-induced intensity variations (RIIV). Because the pulse peaks are clearly visible and no harsh motion artifacts are observable, direct mechanical influence of the thorax displacement on the signal can be excluded. In contrast, the PPG signal at the wrist does not contain similar superimposition. Instead, a LF component is visible, which is not noticeable at the chest. Analog to the observations in time domain, the frequency spectra of the sensors show significant peaks for RR at the chest and for LF at the wrist. Both spectra show scattered peaks around the actual HR, but their distributions are neither similar nor comparable in width and shape. Due to the phenomenon of the RSA, the analysis of the feature-based HRV reveals the RR signal at both measurement positions, at the wrist as well as at the chest. Both curves swing around the average inter-beat distance, about 1 s in this case, but exhibit a different phase. The resulting peak of the RR dominant frequency is significantly observable in both HRV spectra. In contrast, the HR frequency band is not occupied at all. While the spectrum of the wrist's raw data showed a distinct increase within the LF range, this frequency band is just unremarkable in the

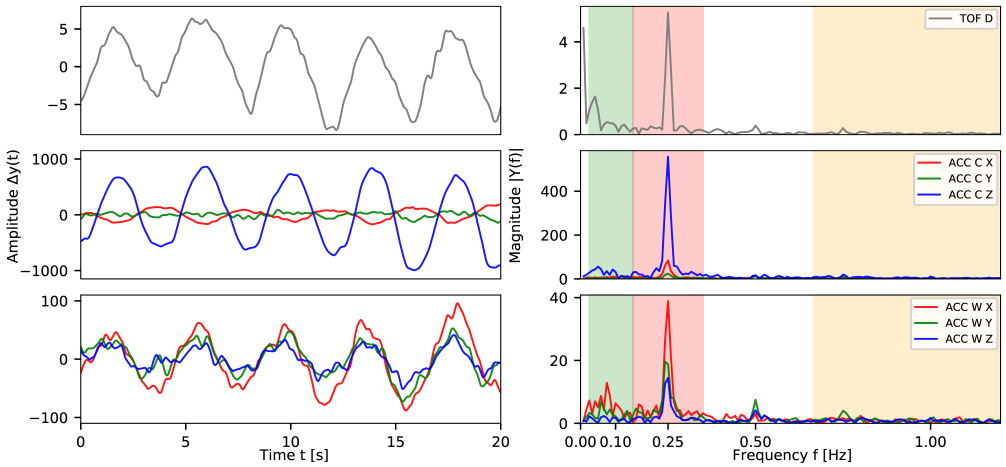

Figure 2.7: Validation of paced breathing at 0.25 Hz (15 cpm). Measurement of the thorax expansion with ToF depth camera (top), accelerometer at the chest (middle), and accelerometer at the wrist (bottom). Signal segment of 20 s (left) and frequency spectra of full 120 s (right). Depth camera BP filtered (0.5 – 50 Hz) time series and unfiltered frequency spectrum. Acceleration signals BP filtered (0.025 – 2.0 Hz) in both cases. **[W18]**

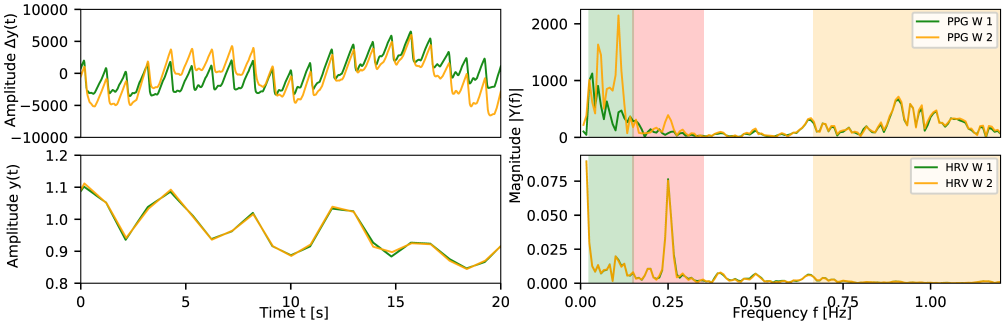

Figure 2.8: Analysis of PPG signals from the wrist during paced breathing. Time series of 20 s raw data (top left), frequency spectrum of full 120 s raw data (top right), linearly interpolated HRV from irregularly sampled maximum peak-features (bottom left), and respective frequency spectrum (bottom right). Top right: significant SNA (green), observable RR (red), and HR (yellow). Bottom right: significant RR (red). **[W18]**

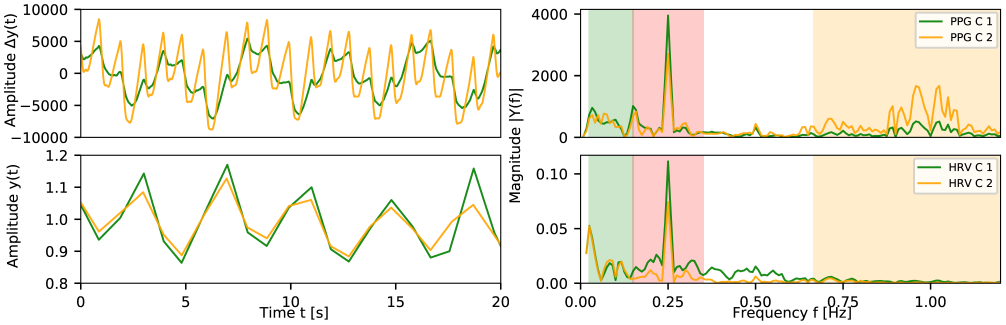

Figure 2.9: Analysis of PPG signals from the chest during paced breathing. Time series of 20 s raw data (top left), frequency spectrum of full 120 s raw data (top right), linear interpolated HRV from irregularly sampled maximum peak-features (bottom left), and respective frequency spectrum (bottom right). Top right: observable SNA (green), significant RR (red), and HR (yellow). Bottom right: significant RR (red). **[W18]**

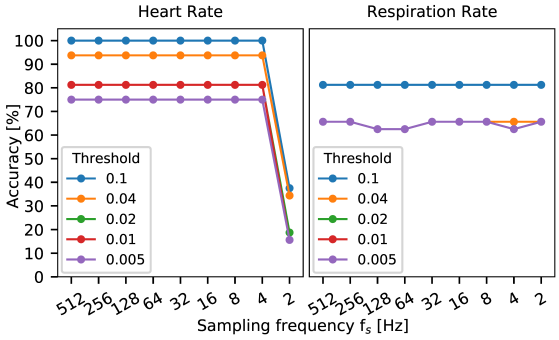

Figure 2.10: Accuracy for the detection of HR (left) and RR (right) from the experimental PPG readings, while varying f_s from the sensor's original 512 down to 2 Hz. The different lines represent the results using different thresholds to establish whether a correct prediction was made. They are measured in Hz as the maximum absolute distance between prediction and ground truth. Note that reducing f_s has only minor to no effects for RR and a more severe impact on HR. **[W18]**

HRV spectra of both sensor positions. The results of the downsampling are presented in **Figure 2.10** and show a relatively stable accuracy down to about 4 Hz SR for both HR and RR. The average accuracy spreads around 80 % for HR and 70 % for RR.

The wearer's HR and RR are essentially calculated by observing dominant frequencies in their respective frequency bands. Although the presented method does not provide detailed, peak-specific identification and segmentation, which is what many state-of-the-art approaches currently aim for, it does lend itself well for energy-efficient PPG monitoring and solutions that need to be light-weight and wearable over longer stretches of time. This way, both experiments showed the feasibility of inferring HR and RR from frequency spectra at reduced f_s without losing reliability and accuracy. Of course, the aggregation of the information in a minute-long measurement window and the calculation of its average results in a coarsening, but the resulting resolution is usually sufficient for long-term observations. In general, the RR frequency can be extracted from both spectra, based on the raw measurements or the HRV information. Instead, the HR itself can only be derived from the raw signal's spectrum. Due to the paced and, therefore, constant RR frequency in the second study, the dominant frequency was extraordinary significant and easy to extract. Variations in breathing and the change of the fundamental RR frequency within a measurement window would spread the frequency components and, thus, flatten the peaks. This behavior is observable for HR at which the slight frequency variations of RSA generate a wide distribution with sidebands according to the HRV's swing.

2.3 Wearable Photoplethysmography Datasets

The development and benchmark of efficient algorithms and the training of machine learning models requires large datasets from numerous individuals with different constitutions. However, obtaining recordings from long-term deployment is difficult and hence most publicly available databases, such as MIMIC-II / -III [Sae+11; Joh+16] of the notable platform PhysioNet [Gol+00], are originated in large medical studies with a clinical background and stationary devices. Although these datasets often provide PPG readings, the compiled findings cannot directly be transferred to wearable devices and their typical challenges emerging when worn in everyday life.

In medical settings, often the standard pulse oximeters are applied while commercial wearable devices are common for in-the-wild studies. For both kind of devices the raw signal, directly obtained from the AFE, is usually not accessible. The devices apply filters to remove the predominant DC component, LF baseline wandering, and HF noise to obtain a detrended and smooth signal. Due to their limited memory, especially wearable devices condense the signal down to its required essence, e.g. readings of SpO_2, HR, and features derived from HRV. Only devices intended for the use in research, such as the popular Empatica E4 [EmE4], provide pretended raw data which, however, are also preprocessed to ease the interpretation and to save valuable memory. Consequently, the signals are already filtered, often rescaled or normalized, and flipped to be consistent with the associated ABP that is already known and easier to analyze by physicians.

In contrast, researchers developing innovative sensing concepts and hardware, primarily test their proper working, but usually do not focus on the recording of measurements over long term and under different conditions. Typically, only a few individuals are testing the prototypes in a lab and rarely in real-life settings. Furthermore, the recordings are exclusively evaluated and presented as consolidated results, but the gathered data are then not documented and made publicly available.

Hence, in research focusing on algorithms that are applied close to the hardware level, either available datasets from a clinical origin or self-recorded datasets with a limited evidence and reproducibility have to be used. As stated by Charlton et al. [Cha+18], there are only few studies applying their approach to more than two datasets or even comparing multiple approaches to each other, tested on the same, larger benchmark dataset, but their comparison is important as the "performance may differ significantly between datasets". Also Reiss et al. [Rei+19] describe the problem that "existing approaches are highly parametrised and optimised for specific scenarios of small, public datasets". Pimentel et al. [Pim+17] also emphasize that "Future studies should concentrate on the use of [...] raw data sources as a benchmark for comparison". However, the immense variety of possible parameters has an essential impact on the recorded signals. The selection of light color (**Section 2.1.2.1**) and sampling scheme (**Section 2.2**), but also the hardware's individual characteristics make it even harder to generate a universal dataset which novel approaches such as compressed sensing and spectral estimation could be tested with.

2.3.1 Raw Signals

In digital signal processing, datasets of original, raw signals are preferred over preprocessed ones which naturally limit the possible use right from the start. Raw data are considered to be universal and to still provide all inherent information, the noise spectrum as well as the desired signals and even hidden secondary information. Although these datasets tend to become very large quickly, it is still reasonable to record the direct measurements, if possible, as today's computers are usually capable of handling them.

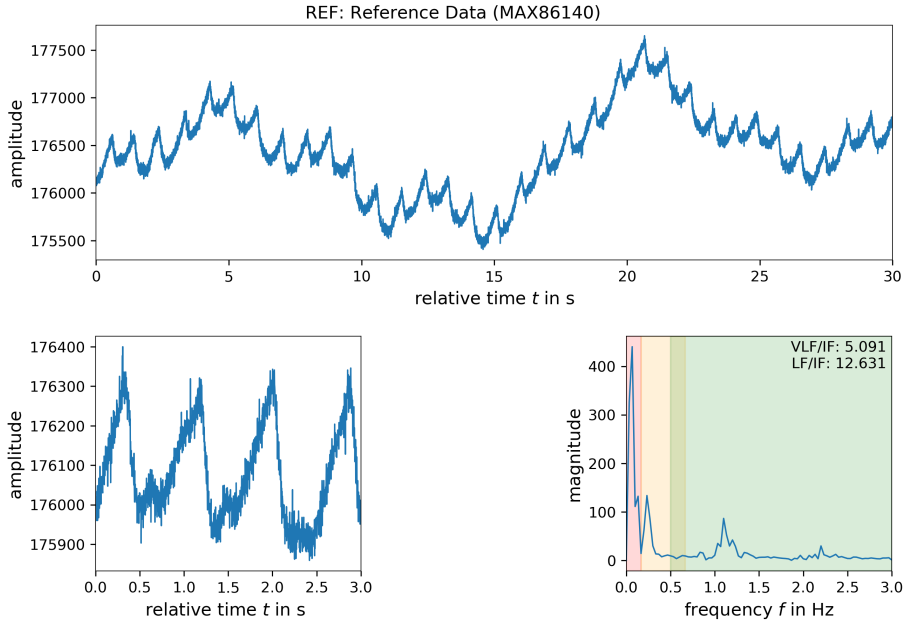

Figure 2.11: Excerpt from the raw reference PPG signal, the green light channel of the MAX86140 / 41 [MAX8] evaluation system. A short close-up (bottom left), a 30-second window (top), and the respective frequency spectrum (bottom right). The pulsatile heartbeat signal is inversely proportional to the blood volume, superimposed by LF baseline wandering and HF noise. Note also the large DC offset. **[W20a]**

However, Gitelman [Git13] states that "raw data is an oxymoron" as "data are always already 'cooked' and never entirely 'raw' ". Although rather philosophic, this statement is also valid for PPG sensing. The definition of the term raw is strongly related to the perspective and interest of the researcher. It mainly depends on the research domain and hence the intended level of abstraction, from the highest one of the devices' consumer via the medicals' view on HR or SpO_2 measurements down to the engineers' bits, amperes, and volts or even the physicists' luminous flux, absorption, and reflectivity.

In this dissertation, raw signals are defined to contain the maximum possible information by applying the minimum necessary preprocessing. In case of PPG this means that the recordings contain the values directly captured from the ADC which receives the amplified analog signal from the photodetector, usually via a transimpedance amplifier. **Figure 2.11** shows an excerpt from such raw signals of the MAX86140 / 41 (**Section 2.2.2**).

2.3.2 Systematic Review

Table 2.2 provides an overview of the ten (10) datasets reviewed, their related publications, information about the length, number of subjects, and contained recordings as well as links to their public repositories. **Table 2.3** summarizes additional information about the used sensing devices, technical details, and applied preprocessing as stated in their documentation. **Figure A.3 and A.4** show characteristic excerpts from the signals.

The recording of a suitable reference dataset with multiple subjects has been prohibited by the COVID-19 pandemic. Hence, recordings from preliminary experiments with the evaluation system of the Maxim MAX86140 **[W18]** (**Section 2.2.2**) serve as a reference (**REF**) for the quality review. However, the set of just a few experimental recordings is not itself suitable for a full research dataset, as the number of participants is too small.

2.3.2.1 Decision Metrics

The suitability and applicability of a dataset is difficult to quantify in a universal way. The following seven (7) decision metrics are developed to support the selection of a suitable, publicly available dataset, either from the list of the reviewed ten (10) references or from a different source by applying the developed analytic tool.

Time Base

The sampling frequency f_s is often assumed to be constant. Hence, the individual samples' timestamps are usually omitted to save valuable memory and only the desired rate is specified. However, due to internal processes, devices tend to show a deviating sampling period Δt and consequently a jittering frequency. The rate's mean $\bar{f}_s$ is preferably close to the desired value and the standard deviation σ_{f_s} ought to be negligible. Despite that, it is beneficial to know the exact time of a sample taken, to be able to consider deviations and omitted samples, to generate a regularly sampled time series by means of interpolation.

$$\bar{f}_s = \frac{1}{n}\sum_{i=1}^{n}\frac{1}{\Delta t_i} \quad \text{and} \quad \sigma_{f_s} = \sqrt{\frac{1}{n}\sum_{i=1}^{n}\left(\frac{1}{\Delta t_i} - \bar{f}_s\right)^2} \quad \text{with } \Delta t_i = t_{i-1} - t_i \tag{2.3}$$

Signal Mean

The raw signal y naturally contains a very large DC component. Consequently, its mean $\bar{y}$ already tells a lot about the applied preprocessing. A mean around 0 exposes that the signal has potentially been shifted to get a zero-centered signal or even a HP filter was applied for a detrended signal, causing the signal to drop back to the origin. For practical reasons an error margin ϵ_z of 1.5 % is added as the filtered values might not hit exact 0.

$$\bar{y} : \begin{cases} |\bar{y}| \gg 0 & \text{, } \textbf{natural DC component} \\ |\bar{y}| \leq 0 + \epsilon_z & \text{, detrended, zero-centered} \end{cases} \tag{2.4}$$

Signal Scope

The signal's scope represents only a minor fraction of the overall signal's extent and is often cropped at its minimum to reduce the memory demands. In many cases, the signals are even scaled and normalized to the range of $[0, 1]$. In other cases the signal is fit into the range of $[-1, 1]$, but if the signal has been zero-centered beforehand, then either the $min(y)$ or the $max(y)$ might not reach the lower -1 or upper 1 boundary.

$$y : \begin{cases} 0 \ll min(y) < max(y) & \text{, } \textbf{normal scope} \\ min(y) \gtrsim 0 \ \wedge \ max(y) > 1 & \text{, cropped} \\ min(y) \gtrsim 0 \ \wedge \ max(y) \leq 1 & \text{, } [0, 1] \text{ normalized} \\ min(y) \geq -1 \ \wedge \ max(y) \leq 1 & \text{, } [-1, 1] \text{ normalized} \end{cases} \tag{2.5}$$

Granularity

The granularity Δ of the signal y is ideally identical to its amplitude resolution if f_s is sufficiently high to quantize and reconstruct the signal slopes. It is determined from the sorted list of unique values without duplicates by seeking the minimum Euclidean distance.

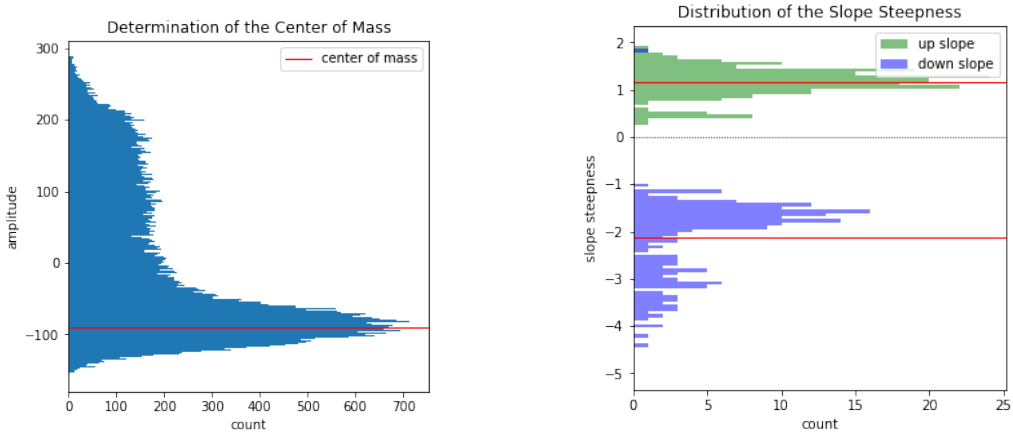

(a) Sample distribution and center of mass. **(b)** Slope steepness distribution.

Figure 2.12: (a) Distribution of the amplitude samples and determined center of mass and **(a)** distribution of the determined slope steepnesses for raw, uninverted PPG signals.

The granularity helps to unveil applied preprocessing as the values directly obtained from the ADC are binary integers by nature.

$$\Delta = min(y_i - y_{i-1}) \, \forall \, y_i \in sort(unique(y)) \tag{2.6}$$

$$\Delta : \begin{cases} \Delta \in \mathbb{N} \wedge \Delta = 1 & \text{, } \textbf{integer of 1 digit} \\ \Delta \in \mathbb{N} \wedge \Delta > 1 & \text{, integer, small } f_s \text{ or short } t \\ \Delta \in \mathbb{R} & \text{, floating-point} \end{cases} \tag{2.7}$$

Clipping

If the signal has been normalized to either $[0, 1]$ or $[-1, 1]$, clipping artifacts can occur at the boundaries, cutting the caps of the lowest and highest peaks. Those flat tops are detectable by means of multiple successive samples staying constant at the boundary value for a minimum period t_c. These are then counted and averaged over 30 s windows along the entire time series.

Flipping

Traditional pulse oximetry sensors monitor the PPG signal proportional to the run of ABP and, therefore, often flip it to enable this analogy. However, the raw signals of both PPG modes originally show an inversely proportional course (**Section 2.1.2**). To determine the pulse direction, two measures are determined, illustrated in **Figure 2.12**. The first one determines the pulses' center of mass which is usually originated at the systolic onset while the diastolic peak is much lighter. Then, based on the approach of Choi et al. [Cho+17], the second measure compares the steepness of the down and up slopes which tend to be steeper for the systolic than for the diastolic phase.

Frequency Spectral Ratio

As all physiological signals, raw PPG signals are non-stationary and dominated by LF baseline wandering. Therefore, most approaches apply a high-pass (HP) or band-pass (BP)

filter to remove the LF components and to limit the pulsatile signal in a constant boundary envelope. This filtering, however, prevents the option of analyzing these frequency components, associated with activity in the ANS and RSA (**Section 2.1.3.2**).

The frequency spectrum is split up into four bands. The very low frequency VLF band (0.0 to 0.167 Hz) predominantly contains random baseline wandering. The low LF band (0.167 to 0.667 Hz respective 10 to 40 bpm) mainly contains respiratory signals, but is overlapping with the intermediate IF band (0.5 to 3.0 Hz respective 30 to 180 bpm) which mainly contains the HR signal [Deh+18; Fle+11]. The high frequency HF band (>3.0 Hz) is associated with noise, but can also contain higher harmonics of the pulse. Disturbances through daily motion are mainly located in the 1.0 to 2.5 Hz band [TMS+14] and, consequently, might affect the metrics. Those are derived from firstly the ratio of the dominant peak in the VLF versus the dominant peak in the IF band and secondly the dominant peak in the LF versus the mean of the IF band. They are covering the most common corner frequencies applied to detrend the raw PPG signal.

$$\frac{max(VLF)}{max(IF)} : \begin{cases} \gg 1 & \text{, if } \textbf{very low frequencies present} \\ \leq 1 & \text{, if high-pass filtered, } f_c \geq 0.167\,\text{Hz} \end{cases} \tag{2.8}$$

$$\frac{max(LF)}{\overline{IF}} : \begin{cases} \gg 1 & \text{, if } \textbf{low frequencies present} \\ \leq 1 & \text{, if high-pass filtered, } f_c \geq 0.667\,\text{Hz} \end{cases} \tag{2.9}$$

2.3.2.2 Results and Discussion

Table 2.4 summarizes the output from the multi-varied quality analysis tool applying the presented seven (7) decision metrics. Most of the reviewed datasets have benn recorded at a sampling rate f_s of more than 100 Hz, except for the two datasets **S02** and **S03** based on the wearable Empatica E4 [EmE4] with fixed 64 Hz. The time bases are provided for **S01**, **S06**, and **S07**. However, as no jitter was detectable for **S01**, its samples' timestamps have probably been added subsequently, based on the desired f_s, but the real $\bar{f}_s$ according to the device's internal clock is not traceable anymore. In contrast, **S06** and **S07** provide real timestamps of the samples' moments which enables the subsequent resampling and interpolation to a regular rate. **S01** and **S05** showed a granularity of 1 which allows the conclusion that those contain actual raw signals directly obtained from the ADC. However, while the other metrics of **S01** indicate that it was not preprocessed at all, the ones of **S05** indicate a flipped signal course. The majority of the flipped time series are originated in a transmission mode measurement (**S05**, **S06**, **S08**, and **S10**) while only the wearable Empatica E4 devices' signals **S02** and **S03** are also flipped, presumably to conform with the measurements from traditional pulse oximeters. For **S07** it was not possible to validate the detected direction. Although most time series were filtered, only **S02**, **S03**, **S09**, and **S10** are actually zero-centered. While **S06** is ideally fitted into $[0, 1]$, **S04** is rather $[-1, 1]$-but probably intended to be also $[0, 1]$-normalized. The metrics VLF and LF reliably distinguish the unfiltered (**S01**, **S04**) from the little (**S07**, **S10**) and the strongly (**S08**, **S09**) HP filtered datasets. However, they are inapplicable for **S05** as it contains only very short signal snippets of 2.1 s, which result in a very coarse and inadequate frequency spectral resolution. Only **S10** showed clipping artifacts which are typical for aged data from CapnoBase. In general, the results of **S02** and **S03**, originated in the same research team, show a high similarity and accordance although the datasets contain independent recordings from different studies with different research questions. Therefore, accompanied by **REF**, only the most recent dataset **S01** proved itself to contain entirely raw signals, **S01** without providing real timestamps, however.

The most important criteria are related to filtering as it significantly affects the signal and limits suitable applications. If the signal mean is close to zero, most likely a HP filter has been applied which removes the LF components and hence shifts the signal. Although it is an artifact of aged datasets, also clipping considerably affects the signal quality by cutting the lowest and highest peak caps and thus impedes their accurate positioning. In contrast, the granularity as well as the $[0, 1]$ and $[-1, 1]$ normalizations do not affect the signal itself, but indicate that the raw signals from the ADC have been relabeled according to a physical value or even rescaled. In case of an interpolation process, e.g. due to regularization, the granularity is assumed to show rather a floating point than an integer value. In general, the transition from integer to floating point values is unfavorable as the calculation with those often results in rounding errors and inaccuracies. The awareness of flipping allows to repeatedly inverse the signal as most algorithms are less effective with slopes in an unexpected direction.

Limitations

We assume that the characteristics of a single time series are valid for the entire dataset. As the two datasets **S02** and **S03** show, this assumption applies not only within the same series, but also for the same device type applied. Therefore, recordings were carefully selected to represented a meaningful cross section of the entire dataset. Of course the tool can be applied to all kind of data and serve as a basis for a statistical analysis, but a general validity would have gone beyond the scope and intention.

2.3.3 Guidelines

The following guidelines are provided to supplement the general requirements on quality datasets, e.g. [BBS14; Sch+18; YFM19], with a specific focus on PPG datasets. Unprocessed, raw measurements are prefereable and do not limit the research in signal processing and algorithms for wearable PPG sensing right from the start. As the performance of wearables tends to be limited, their long-term deployment in-the-wild is not easy. Hence, the sensor configuration is always a trade-off between universality and reusability of the data on the one hand, but required memory and battery life on the other hand.

These guidelines are intended to encourage **1)** to utilize PPG sensors that are capable of recording raw or just slightly filtered signals; **2)** to record synchronized reference signals such as ECG and RR; **3)** to use the maximum possible sampling rate as long as it does not limit and terminate the experiment early; **4)** to save the unaggregated samples of all particular measurement channels, also the ambient light intensity, if available; **5)** to enable the recording of timestamps for each sample taken. These configurations consume higher amounts of valuable memory and energy, thus a balancing of the parameters according to the research interests and the mitigation of others for long-term monitoring is required.

Furthermore, **6)** access to all technical details of the applied sensing device as well as its configuration is essential. This includes not only the desired sampling rate and the number of measurement channels, but also the components' names, e.g. of LEDs and PDs, their light wavelength and drive current or peak sensitivity, sampling time, and the applied sampling scheme. Also **7)** the setup, attachment, and measurement location of the sensor needs to be described. The location 'wrist' can for example be described more precisely by adding 'volar' for the palm side or 'dorsal' for the back side.

A **8)** detailed documentation with a brief description of the author's research domain and questions will help fellows to appraise whether the conducted experiments and recorded data are compatible to their research intent.

Table 2.2: Overview of the reviewed publicly available datasets. **[W20a]**

id	dataset		authors	year	origin	data format	#subjects	#recordings	length	link
S01	MAXREFDES100	[Bia+20]	Biagetti et al.	2020	recording	*.mat	7	105		https://www.sciencedirect.com/science/article/pii/S2352340919314003
S02	PPG-DaLiA	[Rei+19]	Reiss et al.	2019	recording	*.pkl / *.csv	15			https://ubicomp.eti.uni-siegen.de/home/datasets/sensors19/index.html.en
S03	WESAD	[Sch+18]	Schmidt et al.	2018	recording	*.pkl / *.csv	15 (12m, 3f)		~36 min	https://ubicomp.eti.uni-siegen.de/home/datasets/icmi18/index.html.en
S04	BloodLossSvm	[Rel+18]	Reljin et al.	2018	recording	*.csv / *.txt	9 (trauma) / 27 (healthy)	67 / 27	2 min	https://figshare.com/articles/NR_bloodlosssvm_zip/5594644
S05	PPG-BP	[Lia+18]	Liang et al.	2018	recording	*.txt	219	657	3 × 2.1 s	https://figshare.com/articles/PPG-BP_Database_zip/5459299
S06	BIDMC	[Pim+17]	Pimentel et al.	2017	MIMIC II [Sae+11]	*.mat / *.csv	53	53	8 min	https://physionet.org/content/bidmc/1.0.0/
S07	Wrist PPG During Exercise	[JC17]	Jarchi et al.	2017	recording	wfdb data	8 (5f, 3m)			https://physionet.org/content/wrist/1.0.0/
S08	Cuff-Less Blood Pressure Estimation	[Kac+15]	Kachuee et al.	2015	PhysioNet [Gol+00]	*.mat				https://archive.ics.uci.edu/ml/datasets/Cuff-Less+Blood+Pressure+Estimation
S09	IEEE SPC 2015 (TROIKA)	[ZPL15]	Zhang et al.	2015	recording	*.mat	12 (training) / 8 (test)	12 / 8		https://sites.google.com/site/researchbyzhang/ieeespcup2015
S10	IEEE SPC 2013	[Kar+13]	Karlen et al.	2013	CapnoBase [Kar+10]	*.mat	42	42	8 min	http://www.capnobase.org/index.php?id=857

#: number of

Table 2.3: Overview of the applied PPG sensor setups and configurations. **[W20a]**

id	sensing device	location	mode	illumination	f_S	ADC resolution	preprocessing
REF	MAX86140 (EVSYS#)	wrist (dorsal)	reflective	green (2x 528 nm), yellow (2x 590 nm)	512 Hz	19 bit	BS 50 / 60 Hz (hardware)
S01	MAXREFDES100#	wrist	reflective	infrared (880 nm), red (660 nm), green (537 nm)	400 Hz	16 bit	
S02	Empatica E4	wrist (non-dominant)	reflective	red (2x), green (2x)	64 Hz	0.9 nW/dig	BW removal, MA removal (combines different light waves)
S03	Empatica E4	wrist (non-dominant)	reflective	red (2x), green (2x)	64 Hz	0.9 nW/dig	BW removal, MA removal (combines different light waves)
S04		finger, forehead, ear	reflective	infrared, red	80 Hz		
S05	SMPLUS SEP9AF-2	earlobe, fingertip (?)	transmission	infrared (905 nm), red (660 nm)	1000 Hz	12 bit	BP 0.5 to 12.0 Hz
S06		wrist (dorsal) (?)	transmission (?)		125 Hz		
S07	Shimmer 3 GSR+	left hand's finger (?)	reflective	green (510 nm)	256 Hz	12 bit	Shimmer's on-board filter / cycling: LP 15 Hz (2nd order Butterworth)
S08		fingertip	transmission (?)		125 Hz		
S09		wrist (dorsal)	reflective	green (2x 515 nm, 2 cm distance)	125 Hz		BP 0.4 to 4.0 Hz (2nd order Butterworth)
S10			transmission (?)		300 Hz		

(?): ambiguous information; BP: band-pass filter; BS: band-stop filter; BW: baseline wondering; MA: motion artifact

Table 2.4: Results of the multi-varied quality analysis. Color highlighted indicators for the output of the 7 decision metrics with green: positive, red: negative, orange: vague declaration, blue: unverifiable. Additionally, overview of subsidiary measures. **[W20a]**

		sampling rate f_s (Hz)			signal characteristics						time domain				frequency domain		artifacts
id	dataset	desired	real	jitter	mean	min	max	span	#values	gran. Δ	ZC	[0, 1]	[−1, 1]	flip	VLF / IF	LF / IF	clipping
REF	Reference Data (MAX86140)	512.0	511.750	0.001	176529.1	174920.0	178594.0	3674.0	3477	1	No	No	No	No	76.9	103.0	No
S01	MAXREFDES100#	400.0	400.000		6054.6	5661.0	7387.0	1726.0	1553	1	No	No	No	No	109.5	55.3	No
S02	PPG-DaLiA	64.0			-0.002	-1647.390	1557.6	3205.0	59323	0.010	Yes	No	No	Yes	0.150	1.783	No
S03	WESAD	64.0			-0.000	-873.670	988.080	1861.8	45440	0.010	Yes	No	No	Yes	0.044	1.947	No
S04	BloodLossSVM	200.0			0.475	-0.013	0.998	1.011	1011	0.001	No	Quasi	Yes	No	246.6	15.7	No
S05	PPG-BP	1000.0			2036.9	1682.0	2587.0	905.000	511	1	No	No	No	Yes	[2]0.009	[2]0.047	No
S06	BIDMC	125.0	125.000	3.559	0.466	0.224	0.698	0.474	407	0.001	No	Yes	No	Yes	0.018	1.884	No
S07	Wrist PPG During Exercise	256.0	255.882	0.575	1378.3	1269.8	1498.1	228.372	23744	0.003	No	No	No	[1]No	0.066	31.0	No
S08	Cuff-Less Blood Pressure Estimation	125.0			1.840	0.000	4.002	4.002	2792	0.001	No	No	No	Yes	0.009	0.590	No
S09	IEEE SPC 2015 (TROIKA)	125.0			-0.708	-270.000	208.500	478.500	840	0.500	Yes	No	No	No	0.088	0.781	No
S10	IEEE SPC 2013	300.0			-0.215	-9.840	10.240	20.080	754	0.020	Yes	No	No	Yes	0.059	0.927	Yes

#: number of; ZC: zero-centered; VLF / IF: very low to intermediate frequency ratio; LF / IF: low to intermediate frequency ratio; 1: too noisy signal; 2: too short recordings

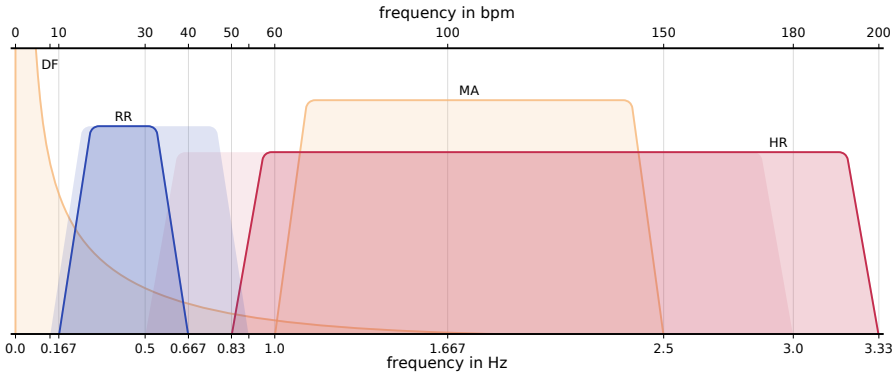

Figure 2.13: Frequency components present in raw PPG signals. Frequency bands: fundamental frequencies of HR and RR according to [Deh+18; Fle+11]; DC offset and $1/f$ fluctuations (DF) [KM82; Bil11; Ern17]; general noise and disturbances through daily motion (MA) [TMS+14]. Natural limits of HR and RR change with the age from infants and children to adults (solid lines). Overlapping areas are critical since they are hard to distinguish and to assign [TMS+14]. Y-axis unspecified. **[C21c]**

2.4 Digital Signal Processing

For ECG there exist standards for the preprocessing and well-established algorithms to identify the prominent R peaks of the consecutive QRS complexes. A still commonly used one is the Pan-Tompkins algorithm from 1985 [PT85], but there are also more recent and specialized ones as summarized by Köhler et al. [KHO02]. These algorithms are usually also applicable for readings from wearable ECG sensors, as long as they resemble the standard lead I. However, depending on the wearing location and orientation of the wearable device, the vector of the R peak changes and can even invert its polarity. Therefore, depending on the resembled lead (e.g. aV_R or V1 – V3, introduced in **Section 2.1.1**), the algorithm has to detect and consider the direction of the significant R peak.

The raw PPG signal is not affected by the device's orientation, but instead shows a large intrinsic diversity of the pulse contour. The pulse waveform depends not only on the subject's physiological conditions, HR, and ABP, but also on the measurement site (**Section 2.1.2.2**) and applied light wavelength (**Section 2.1.2.1**). **Figure 2.13** illustrates the spectrum of raw PPG signals, composed of diverse superimposing frequency components. Besides the diverse physiological signals of interest, PPG measurements also contain a certain amount of physiological noise [COL90] and chaos [Svi+18]. Moreover, wearable PPG significantly suffers from motion artifacts (**Section 2.4.1**). This superposition of desired signals and interference makes the careful filtering of the desired components necessary [CPK22]. However, the filtering of raw PPG signals also has an effect on the pulse contour and thus on the derived features and secondary signals such as HRV [Liu+21; MMK21]. The typical processing pipeline for PPG signals is illustrated in **Figure 2.14** and consists of five stages: signal sampling, preprocessing, motion artifact treatment, fiducial point detection, and secondary measure derivation [Fis+17; IAS21].

Although the frequency bands of HR and RR are limited by nature, it is not advisable to apply filters with fixed passband limits to extract the components [TMS+14]. The plausibility of frequencies' occurrence highly depends on the individual and there is no consensus on optimal, generalized ranges [Cha+18]. For adults, the bands typically range from about 0.833 to 3.333 Hz (50 – 200 bpm) for HR and about 0.133 to 0.667 Hz (8 – 40 bpm) for RR. In the age of infants to young adults, the spectra for HR and RR range from 0.5 to 3.0 Hz

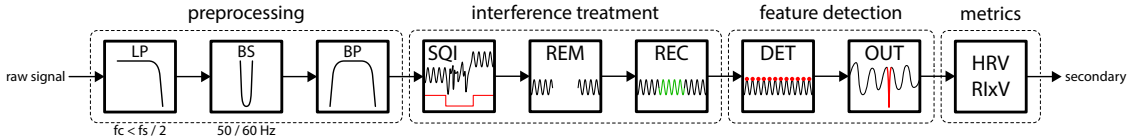

Figure 2.14: Typical processing pipeline for the extraction of infromation from raw PPG signals: Active sampling to obtain the raw signal; preprocessing: consecutive filter stages of LP, BS, and BP to extract the desired; interference treatment: signal quality index estimation (SQI), artifact removal (REM), signal recovery (REC); feature detection: fiducial point detection (DET) and outlier removal (OUT); secondary signal derivation applying metrics such as RIIV, RIAV, or RIFV / HRV. c.f. [Fis+17; IAS21]

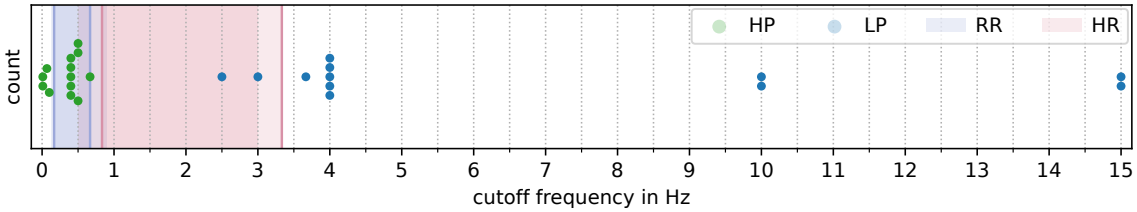

Figure 2.15: Review of 14 publications. Distribution of applied filter cutoff frequencies: lower corner (HP) and upper corner (LP), in respect to RR and HR bands (**Figure 2.13**). Publications: [ZPL15; Fis+17; Kam+89; Zon+03; Cha+16; Gio+16; LSH16; Dao+17; Tem17; CR18; Xie+18; CLL19; HS20; WP20]. **[W20a]**

(30 – 180 bpm) and 0.667 to 0.9 Hz (40 – 54 bpm) respectively [Deh+18; Fle+11]. Consequently, the universal cardiac and respiratory frequency bands, for both infants and adults, overlap. The separation of the desired signal components from in-band noise, especially motion artifacts from daily activities such as walking and jogging (typically 1.0 to 2.5 Hz), becomes even more challenging [TMS+14; IAS21].

The artifact-free raw PPG signal (**Figure 2.11**) is dominated by a large DC offset while the AC signal amplitude comprises only about 1 – 10 % of the total scope [KM17; KCW19]. Depending on the ADC's resolution, typically ≥ 16 bit, the digital representation and storage of measurements requires a lot of memory. The simple elimination of the DC offset, often taken as unnecessary, easily reduces the extent.

In addition to the DC offset, the raw PPG signal contains also other frequency components that are usually not of interest and removed through signal conditioning and preprocessing techniques. It is general standard to limit the signal's spectral bandwidth by any type of BP filter, of which the Butterworth is the most common one. The passband's lower $f_{c,hp}$ and upper $f_{c,lp}$ cutoff frequencies are defined through successive HP and LP filter stages, as depicted in **Figure 2.20**. The LP stage rejects HF noise which hinders the accurate detection and localization of the small AC pulse peaks. At the same time, the natural baseline wander of the physiological signal contains LF components [KM82; Bil11; Bas+87] which blur and smear the pulses along steep and large slopes. Thus, the HP filter stage is applied to detrend the signal and to remove for example the RR variations [Pim+17; Deh+18; Cha+16]. Particularly the first ten harmonics of the fundamental HR shape the pulse waveform and need to be preserved [Kam+89; SN12]. **Figure 2.15** illustrates the widespread distribution of utilized cutoff frequencies from 14 publications. Previous research has reviewed commonly applied conditioning and preprocessing strategies **[W20a]** (**Section 2.3.2**) and investigated the influence of the sensor's sampling rate f_s on the HR determination **[W18]** (**Section 2.2.2**).

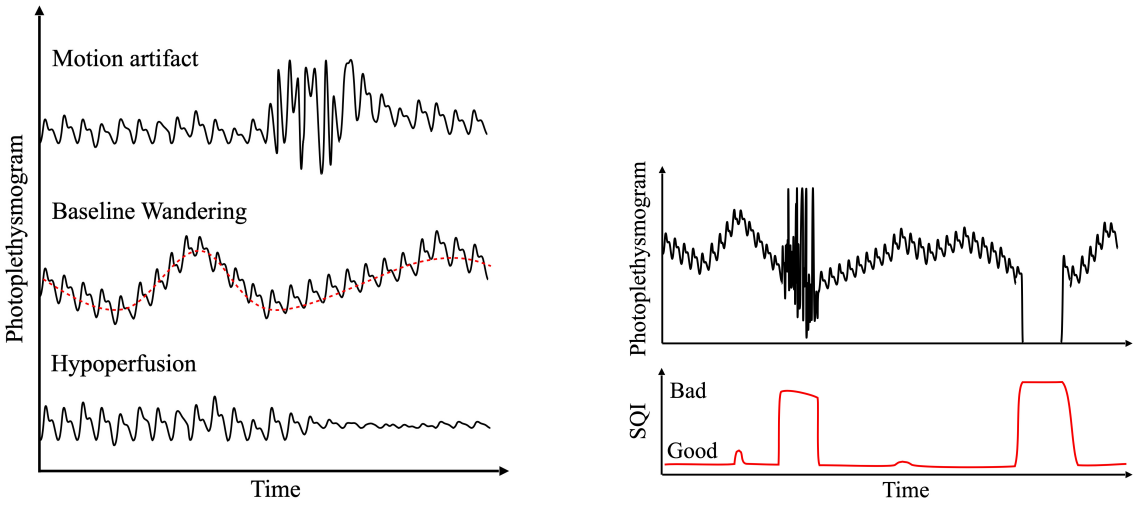

(a) Motion artifacts in raw PPG signals.

(b) The signal quality index (SQI).

Figure 2.16: (a) Illustration of the diverse appearances of motion artifacts and interference occurring in raw PPG signals and **(b)** the derived SQI to estimate the signal quality and decide whether to skip an interval. Figures from [Par+21] (CC BY 4.0)

Common preprocessing stages for PPG signals include traditional filters such as high-pass (HP), band-pass (BP), and band-stop / notch (BS) filters. HP filters are applied to detrend the raw signal, to remove the predominating DC component and the baseline wandering, to obtain a zero-centered signal. The use of a BP filter adds a LP filter stage to smooth the signal contour, to suppress HF noise and therefore prevent aliasing (**Section 2.2.2**). A notch band-stop filter is often used to eliminate power line noise around 50 / 60 Hz and is usually implemented on-board, in the sensor's AFE hardware. The aforementioned filters are usually implemented in software as Butterworth FIR or IIR filter of 2^{nd} order, as higher orders tend to degrade the signal [CR18]. The Savitzky-Golay [SG64] FIR is a linear-phase smoothing filter which conserves the pulsatile shape of the desired waveform on top of the non-stationary signal and non-Gaussian noise, but does not show a constant, predictable transfer function [CR18]. [Elg12]

2.4.1 Motion Artifacts

In any application for the conscious human, especially during physical activity, the loosely attached wearable PPG sensor captures motion-induced distortions. This way, "The signal quality [...] is affected by a multitude of artifacts" [Böt+22] which are mostly originated in slight sensor displacements, varying contact pressure [Mae+13], a possible air gap between sensor and skin, hemodynamic effects, and soft tissue deformation [All07; Man07; PBG07; Wij+12; Böt+22] (**Figure 2.16a**). Particularly the skin at the wrist envelops moving muscles, tendons, and bones which make reliable attachment and measurements difficult as intrinsic effects cause artifacts and can even invert the signal amplitude according to a pronation or supination twist [Cho+17; Cha+22a]. However, also a change of pose and, therefore, a "dynamic redistribution of venous blood in response to external pressure or gravity" has an influence on the signal [HS01]. In addition, any sensor displacement and tissue deformation changes the path of the light in the tissue. The light scans the inhomogeneous textures [COL90; San+10] whose different reflection and scattering behavior [Vol+17] thus modulates the reflected light (**Section 2.1.2.1**). Also the slow step

response of filters can cause problems, when motion causes abrupt baseline changes and the filter stage smears the offset along the continuing signal **[C21c]** (**Section 2.4.4.2**).

Motion-induced interference tends to occur in a regular rhythm, e.g. induced by continuously performed motion patterns such as walking. To a certain degree, these distortions are usually separable and removable from the desired signal. In contrast, spontaneous motion causes artifacts that are typically observable rather as abrupt changes. These disrupt the desired yet fragile pulsatile signal and thus impede the application of simple algorithms. The relationship between different measurement locations and the reliability of the signal [Jar+18] as well as the occurrence of motion artifacts [MST11a; Lon+19; Cha+22a] has been investigated. Nevertheless, the biggest challenge remains the identification, exclusion, and removal of motion artifacts and the reconstruction of the desired signal. The recent advances have been reviewed by Castaneda et al. [Cas+18] and Ismail et al. [IAS21]. Diverse approaches apply adaptive filtering, signal decomposition, statistics, spectrum subtraction, and diverse heuristics to detect and remove motion-related signal components [IAS21]. Since the typical pulse waveform is known from previous measurements, its morphology or extrema are assessed and the application of a predefined threshold common to identify signal steps caused by motion [Kar+12; Fis+17; vGe+19]. Also the peak recovery and spectral reconstruction of the pulse waveform has shown good progress [Mas+21]. Others approaches analyze signals from auxiliary sensors, mostly accelerometers [Gio+16; WP20], but also from piezoelectric pressure sensor [Lee+19], optical flow sensors known from computer mouses [FGM20], or even the ambient light [PGM20]. Research has also attempted to automatically evaluate signals and derive a signal quality index (SQI) (**Figure 2.16b**) that can be used to estimate the reliability of the signal and decide whether to consider or skip the assessed interval [SYZ12; Par+21; Böt+22].

2.4.2 Frequency Domain

The pseudo-periodic PPG signal can be analyzed in two different ways of which one is operated in the frequency domain. As previously presented and applied in **Section 2.2.2**, the raw, detrended, or even filtered PPG signal can be transformed into its spectral representation. Approaches in this domain [Gio+16; SMZ17; Bis+19; Mas+21] often aim for the application in very resource-constrained systems. They collect the signal over a longer period of several seconds to minutes, then aggregate the data and analyze the spectrum generated through a decomposition method or transformation function. Besides advanced techniques for spectral estimation [BG09; NPE15; ZPL15; Dao+17; Ahm+19], the most frequently applied ones are FFT algorithms [CT65; DV90] and Welch's method [Wel67] for a smooth periodogram from overlapping, windowed FFTs. **[W18]**

Essential for the FFT are the window parameters of time span T and number of samples N, joined in the sampling frequency $f_s = \frac{N}{T}$. According to the sampling theorem of Nyquist-Shannon [Sha49], the representable frequency band cannot exceed $f_{max} = \frac{f_s}{2}$. If the sampled signal is not band-limited and contains frequencies beyond f_{max}, the components are, therefore, mirrored at this boundary and reflected as aliases. To avoid the aliasing effect, usually a LP anti-aliasing filter is applied to the signal. In addition, certain window functions are applied to the signal segments before their transformation to limit spectral leakage, frequency components occurring due to the window's finite duration and the step response of its abrupt boundaries. For a single-sided spectrum, N results in the respective number of bins $\frac{N}{2}$. Those collect frequency components within a certain range, defined by the frequency resolution $\Delta f = \frac{1}{T}$. The limit f_{max} does usually not affect the desired signal components of HR, RR, and SNA as it gets larger easily by increasing f_s adequately. However, the achieved resolution Δf is crucial for the accurate estimation

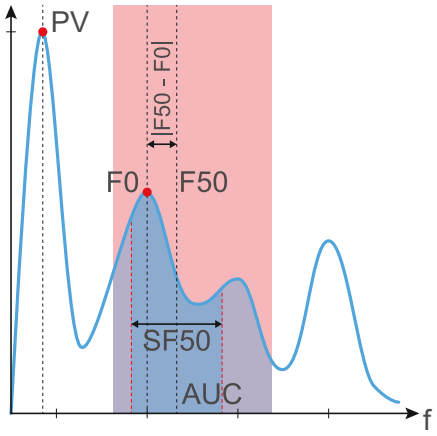

Figure 2.17: Overview of the features derivable from a physiological signal in frequency domain. PV: maximum value of a PSD; F0: predominant frequency component within a certain frequency band of interest; AUC: area under the curve, total power of the signal in the band; F50: central frequency between two equally divided parts of the spectrum; SF50: frequency dispersion, width around F50 containing σ of 68.2 % of the signal's power; |F50−F0|: distance between central frequency (F50) and fundamental frequency (F0).

and discrimination of the desired measures since their frequency components are located relatively close to each other, have partly overlapping frequency bands (**Figure 2.13**), and show only slight variations. Consequently, for a better Δf, the measurement time T has to be increased already in time domain, during the recording. [Lyo11]

The FFT responds quickly to changes but also tends to be disturbed. In contrast to the direct application of the FFT, Welch's method [Wel67] generates a non-parametric estimation of the power spectral density (PSD) and reduces the variance with increasing number of samples by averaging multiple sub-spectra of overlapping window intervals. This way, the method highlights continuously present frequency components while stochastic, irregularly occurring ones, such as noise interference, are suppressed. **[J20b]**

Figure 2.17 illustrates the diverse features that can be derived from the signal's spectral representation, enabling e.g. the inference on HR, RR, and SNA. Usually, these features are derived from certain frequency bands that are associated with the desired measures. The F0 is the most common feature and related to the predominant frequency component of maximum power within the band of interest. It is important to note that it does not represent the average of the desired signal but the frequency component that predominates during the time period of the analyzed window. Additional features can support the validation and adjustment of the estimate by means of different heuristics. Such features are the area under the curve (AUC) that describes the total power of the signal within its band, the peak value (PV) that represents the maximum value of the entire PSD, the F50 which is the central frequency between two equally divided parts of the spectrum, the frequency dispersion (SF50) which describes the standard deviation σ around F50 containing of 68.2 % of the signal's total power, and the distance between central and fundamental frequency (|F50−F0|). **[J20b]**

However, the shortcut of analyzing the signal in the frequency domain prevents applications from deriving secondary information such as HRV metrics [Bil11; SG17], the tachogram, or the interval function [Bas+87]. Since modern applications demand for these values, most HR tracking algorithms are applied in the time domain.

2.4.3 Time Domain

The analysis of the pulsatile PPG signal in the time domain allows deeper insights and the interpretation of secondary signals derived from the consecutive pulses. However, the applied algorithms tend to be more sophisticated and, since they have to identify each individual pulse, they require significantly more processing power and resources. As illustrated in **Figure 2.14**, the preprocessing stage applies diverse filters to remove undesired signal components such as the DC offset, the LF baseline wander, and HF noise.

Eventually, the individual pulses of the heartbeat are identified by means of significant fiducial points. As elaborated in **Section 2.1.2**, most algorithms identify the diastolic onset, but also other feature points have been subject to investigation with both pros and cons [Chi+91; Tak+98; Pos+13; Jey+15; HP16; Per+19; Cha+22a]. The HR can then be determined by counting and averaging the number of pulses per unit time, or by directly calculating the individual reciprocal of the IBI for an instantaneous measure [CBR91].

In case of absence of motion artifacts, simple, threshold-based approaches can achieve good results using derivatives, moving averages, or the archaic slope sum function [Zon+03] and relics from ECG analysis such as the popular Pan-Tompkins algorithm [PT85] to detect the fiducial points [NPE15]. In recent years, diverse pulse detection and segmentation approaches have been presented in [Kar+12; SBW12; Fis+17; CLL19; vGe+19; HS20; WP20] and reviewed in [Obi21]. Two very different yet well-known representatives are the algorithms or Karlen et al. [Kar+12] from 2012 and van Gent et al. [vGe+19] from 2019, therefore benchmarked in the following **Section 2.4.4.3**. Also machine learning techniques have been applied to reliably detect the pulses in PPG signals which appear in very different shapes [Bas+19a; Rei+19; Kwo+22; RCP22]. **[C21c]**

2.4.4 Optimal Preprocesing

In research, and especially in field studies with numerous devices, the Empatica E4 [EmE4] has been established as a popular and commercially available tool for the monitoring of vital signs over long term [McC+16]. Besides the early detection and diagnosis of heart diseases in medical studies, secondary features from the HRV (**Section 2.1.3.2**), derived from the pseudo-periodic heartbeat, have shown to be linked to the wearer's emotions and affective state. The evidence of the findings is, however, biased and limited to signals from specific devices such as the aforementioned E4.

For researchers, it is comfortable to obtain the measurements from such embedded sensors. The signals are usually straightforward to interpret and analyze, since they come already conditioned and preprocessed (**Figure A.3**, **S02** and **S03**). To the inexperienced observer from disciplines other than signal processing, the sensing devices seem to deliver proper raw signals because they come directly from them. However, the embedded software of commercial wearables is usually closed, not adaptable, and hence limits the signal's information content as well as possible applications. The use of actual raw sensor data would demand for more knowledge and effort from the researcher, but also allows for customization to meet individual, research-specific requirements.

In context of the extraction of the RR from PPG signals, Pimentel et al. [Pim+17] emphasize that "Future studies should concentrate on the use of [...] raw data sources as a benchmark for comparison". The previous review of public datasets (**Section 2.3.1**) has, however, revealed that, although advertised as such, most datasets do not actually contain raw but conspicuously filtered signals. For this reason, most large and promising datasets are not suitable to benchmark available algorithms or even to determine optimal preprocessing parameters. Likewise, Reiss et al. [Rei+19] state that "State-of-the-art

publications rely mostly on the two datasets introduced for the IEEE Signal Processing Cup" [Kar+13; ZPL15] (**Figure A.4**, **S10**), which do not contain actual raw PPG signals, and found that "existing approaches are highly parametrised and optimised for specific scenarios of small, public datasets". **[W20a]**

The following study **[C21c]** aims at the deeper understanding of the raw PPG signal's characteristics, directly obtained from the sensor, to pave the way for more universal, reliable, and accurate sensor-integrated algorithms, running on modern wearable devices. In recent years, there has already been research aiming at the identification of optimal techniques and filter parameters for the preprocessing of PPG signals. Those studies did, however, not lead to a clear consensus. They either targeted specific applications or exhibited weaknesses that this work aims to address.

In 2012, Stuban and Niwayama [SN12] evaluated the optimal filter bandwidth for pulse oximetry, which traditionally applies transmission mode PPG. The research concentrated on the estimation of SpO_2 from the ratio of measurements at two different wavelengths, red and IR light, sampled at 40 Hz. The DC and very low frequency (VLF) components have been removed by a 2^{nd} order infinite impulse response (IIR) HP filter. The lower cutoff frequency was set to 0.1 Hz and "must be lower than the fundamental frequency of the pulse". Noise and harmonics of the pulse have then been removed by a 100^{th} order finite impulse response (FIR) LP filter with five different upper cutoff frequencies at 0.66, 1.0, 1.5, 3.0, or 15.0 Hz. From their findings they conclude that the "harmonics of the pulse signal do not contribute to the accuracy of pulse oximetry" and consequently "filtering out the harmonics [...] does not degrade the accuracy".

In 2018, Liang et al. [Lia+18] published an impressively large dataset of 657 PPG snippets, captured at the left index fingers of 219 subjects. Since the recordings are very short, just 2.1 s long, the dataset's applicability is however limited. Based on a selection of 219 pulses, classified as "excellent", "acceptable", and "unfit", they determined the 4^{th} order Chebyshev II to be the optimal filter technique – at least for these short signals.

Most recently, in 2020, Cassani et al. [CTF20] analyzed the spectral coherence and the signal-to-noise ratio between "isolated" and the original, "raw" pulses. They determined the optimal filter passband to be 0.6 to 3.3 Hz for adults and 1.0 to 2.7 Hz for children. The spectral analysis revealed an optimal bandwidth from 0.8 to 2.4 Hz for adults and from 0.9 to 2.7 Hz for children. The study analyzed 27 000 pulses from the well-known CapnoBase IEEE TBME [Kar+10; Kar+13] (**Figure A.4**, **S10**) dataset containing signals from a fingertip pulse oximeter, but not raw, reflective mode PPG signals.

In 2019, Bastos et al. [Bas+19b] investigated the optimal parameters for Butterworth and maximal overlap discrete wavelet transform (MODWT) filters which are "widely employed" in resource-constrained wearables. Considering very few cutoff frequencies, again the dataset from [Kar+10] and the MIMIC-II BIDMC [Pim+17] (**Figure A.4**, **S06**) are applied, both unfortunately not containing actual raw signals from reflective mode PPG.

2.4.4.1 Dataset

Public datasets with actual raw signals from reflective mode PPG sensors are scarce **[W20a]** (**Section 2.3.1**). The adequate benchmark of available algorithms and preprocessing techniques requires, however, large datasets of such kind. The following two studies are based on the recent dataset of Biagetti et al. [Bia+20] from 2020. It is originally intended for the application of machine learning techniques in scope of HAR. With in total 286 min of raw PPG measurements (**Figure A.3**, **S01**), it provides a set of 105 recordings from seven (7) subjects wearing the MAXREFDES100# [MAX1a], a commercially available reference design. Simultaneous PPG and acceleration signals, sampled at

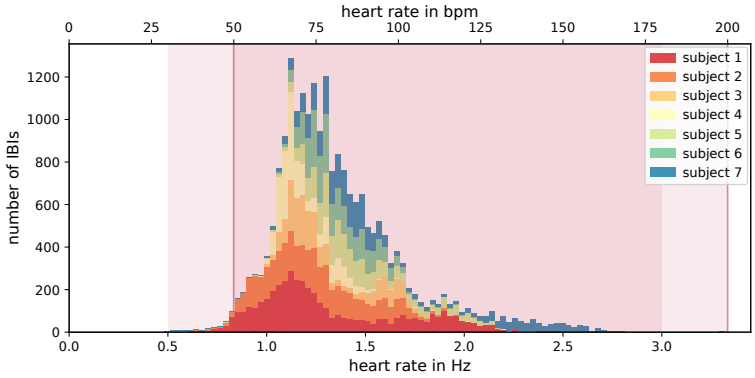

Figure 2.18: Distribution of the seven (7) subjects' instantaneous HR, derived from the IBIs of the manually labeled pulses. Limited cardiac frequency band (red, see **Figure 2.13**). HR on the x-axes and counted number of IBIs on the y-axis. **[C21c]**

a rate f_s of 400.0 Hz, are provided for subjects performing three exercises: "rest", "squat", and "step". Hence, the time series are not entirely clean but also contain motion artifacts that do affect the applied algorithms.

An ideal dataset would uniformly cover the entire range of the natural HR (30 – 200 bpm [Deh+18; Fle+11]). This requirement would, however, hardly be possible without a health risk for the volunteers as they might exceeded their individual limits. As illustrated in **Figure 2.18**, the used dataset covers a broad HR spectrum of at least 40 to 160 bpm, with a strong core area ranging from 50 at rest to 110 bpm at light exercise. The three exercises exhibit the mean HR of 72.9 ± 11.1 bpm (1.22 ± 0.18 Hz) for rest, 98.6 ± 16.0 bpm (1.64 ± 0.27 Hz) for squat, and 106.2 ± 21.2 bpm (1.77 ± 0.35 Hz) for step.

Ground Truth

For every recording in daily life, the supply of ground truth tends to be the major issue. Usually, a second sensing device or even a second sensing modality is used to provide the information with, at best, a higher degree of reliability and precision. In case of the HR, wearable long-term ECG devices are mostly employed since the electrodes are directly attached to the skin and hence enable the reliable and robust measurement, at cost of comfort, however. Unfortunately, the selected dataset does not provide ECG as ground truth. The PPG signal is, therefore, manually analyzed and annotated by a human expert rater with year-long experience. The performance of the applied algorithms is not compared against a reference device but the labels accurately set by the expert. Consequently, the theoretical limits are demonstrated by means of the human and their ability to interpret PPG signals.

Data Annotation

For the purpose of the comfortable and reliable annotation, a graphical tool has been developed (**Figure 2.19**), which allows the expert rater to label the fiducial points within the raw time series. The decision against an automatic labeling or preselection was made deliberately to avoid the expert being influenced and biased in their decision. Without a doubt, this decision resulted in more and monotonous manual work – reams of clicks to select the in total 21 806 peaks. To prevent faults due to fatigue, the expert split the work up into one subject per day, first the larger but easier-to-label data of rest and, after a break, the shorter but ambitious recordings of the squat and step exercises. In total

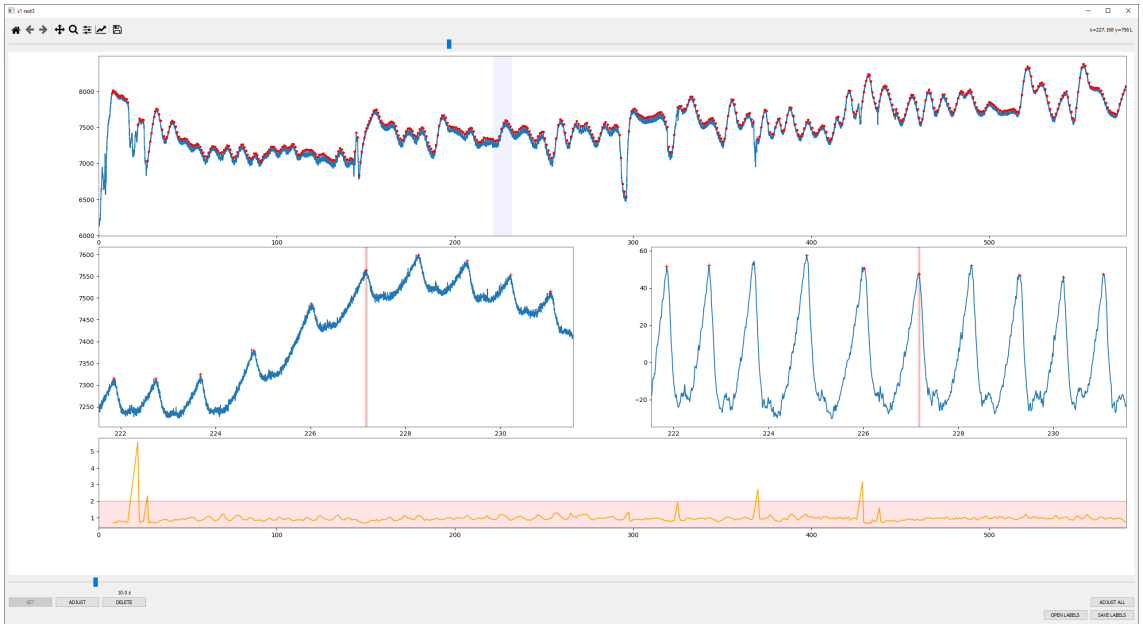

Figure 2.19: Screenshot of the developed graphical tool for the comfortable and reliable annotation of fiducial points within raw PPG time series. Overview of the entire recording (top), excerpt of the unfiltered signal (middle left), the detrended and smoothed respective excerpt (middle right), and the derived HRV interval function to indicate outliers (bottom).

104 of 105 time series, 278 of 286 min (97.3 %) are annotated with 21 806 peak labels. Only 7.73 min do not show distinguishable signals or are considerably affected by motion artifacts and hence excluded. 88 of 105 time series are entirely labeled. The subset squat 3 of subject 5 is rejected since it does not contain any clearly distinguishable pulses.

While the ECG's characteristic R peak (**Section 2.1.1**) is pointed and hence relatively 'easy' to identify, even in noisy signals, the typical PPG waveform is rather smooth and round. Recorded at a higher sampling rate **[W18]** (**Section 2.2.2**), the raw PPG signal also shows a large portion of noise and baseline wander which blurs the optimal pulse peak and makes the identification of its exact position ambiguous (**Figure 2.20a**). Consequently, the very top of the pulse is not always distinct but often subject to interpretation. In contrast to deterministic algorithms, the expert has, however, intuition, grounded in experience, to 'see' which tiny wave is an actual pulse onset and which one is just negligible noise or motion-induced distortion.

To exclude the influence of filtering from the beginning, the labels are set within the raw signal before applying any filter. A second panel allows the expert, however, to have a glance at the detrended and smoothed signal for orientation and validation, to avoid the selection of any invalid pulses. A 4^{th} order ($2 \times 2^{\text{nd}}$) `filtfilt` forward-backward zero-phase [Liu+21] BP filter with a passband from 0.5 to 30.0 Hz is applied. Unnaturally short or long IBIs have automatically been labeled as invalid and were subject to revision by the expert. The remaining uncertain intervals are finally excluded from the studies.

2.4.4.2 Peak Displacement

Filtering considerably changes the trend and morphology of the raw PPG signal [Liu+21]. By narrowing down the passband, the feature positions are conspicuously affected, smeared, and blurred (**Figure 2.20**). The first study investigates the influence of filtering on the

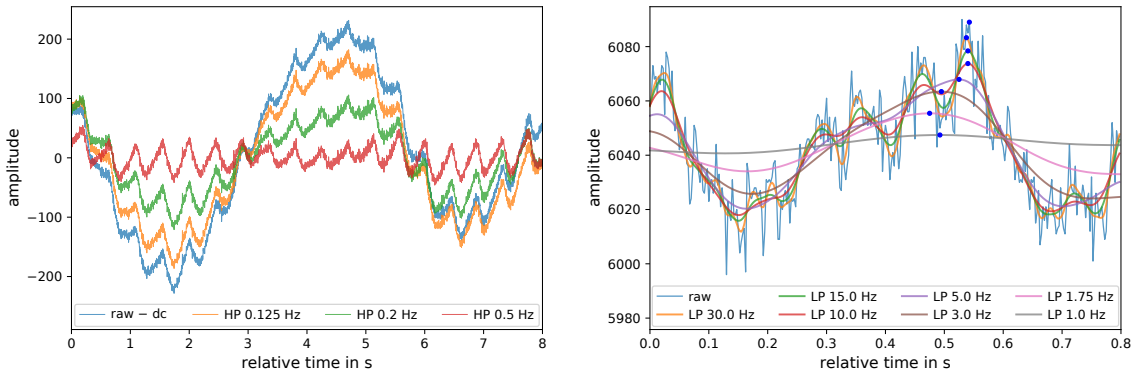

(a) Effect of HP filtering on raw PPG signals. **(b)** Effect of LP filtering on raw PPG signals.

Figure 2.20: (a) Effect of diverse HP filters for detrending on the raw PPG signal. **(b)** Illustration of the pulse peak position (blue) displacement due to the application of diverse LP filters. Conspicuously affected, smeared, and blurred pulse contour, vanishing with the baseline wander, due to eliminating the HR's higher harmonics. **[C21c]**

positions of pulse onsets [Pos+13; HP16; Per+19; Cha+22a], the maximum peaks in raw signals respectively. A 4^{th} order ($2 \times 2^{\text{nd}}$) Butterworth BP filter is applied with 40×40 non-equidistant lower $f_{c,hp}$ and upper $f_{c,lp}$ cutoff frequencies: $\{\,/\,, 0.005, \ldots, 2.5\,\text{Hz}\} \times \{\,/\,, 199.0, \ldots, 2.5\,\text{Hz}\}$. The applied `filtfilt` forward-backward filter method with zero phase allows to protect and preserve the signal's original phase [Liu+21]. To track the peak displacement $\varepsilon_d = |p_0 - \hat{p}|$, a simple hill climbing algorithm is applied to follow the original position p_0 up to the closest local maximum of the filtered signal at $\hat{p}$, implemented as a function $\hat{p}(\, f_{c,hp}\,,\, f_{c,lp}\,)$. Any $\varepsilon_d > 250\,\text{ms}$ is excluded as a slipped outlier.

Figure 2.21 illustrates the mean ε_d results for the individual exercises (left) which sum up to the averaged overall results (right). The boundaries of the minimum error plateaus with $\varepsilon_d \leq 0.5\,\text{samples}$ (blue) are shifted (red arrows) due to the increasing HR (vertical line) from rest (1.22 Hz) via squat (1.64 Hz) to step (1.77 Hz). Accordingly, an extended $f_{c,lp}$ (y-axis) is required to cover a sufficient number of harmonics, for an adequate contour and peak reconstruction, but it also allows for a higher $f_{c,hp}$ (x-axis).

2.4.4.3 Benchmark of Algorithms

The results from the previous study on peak displacement serve as the upper boundary of maximal achievable accuracy from filtered PPG signals. To benchmark available algorithms and to investigate the effect of preprocessing on their performance, two popular algorithms are taken as examples and are applied on the differently filtered time series: **1)** Karlen et al. [Kar+12] from 2012 and **2)** van Gent et al. [vGe+19] from 2019. Those apply two fundamentally different principles to identify the pulse peaks in time domain.

To assess the algorithms' performance, every position p_0 from the manual annotations is assigned to its closest counterpart $\hat{p}_a$ from the detected peaks. If the error distance $|p_0 - \hat{p}_a| \leq 250\,\text{ms}$, the pair $(p_0, \hat{p}_a)$ is classified as true positive (TP). All missed p_0 without a counterpart $\hat{p}_a$ within reach are classified as false negative (FN) while the surplus of erroneously detected peaks falls into false positive (FP). This approach allows to apply the popular performance metrics F1-score (**Equation 2.10**), the harmonic mean of precision (PPV) and recall (TPR) (**Equation 2.11**), to measure peak detection performance:

$$F1 := 2 \cdot \frac{PPV \cdot TPR}{PPV + TPR} \tag{2.10}$$

$$PPV := \frac{TP}{TP + FP}\,,\; TPR := \frac{TP}{TP + FN} \tag{2.11}$$

For all pairs in true positive (TP), the average error distance $\varepsilon_a = |p_0 - \hat{p}_a|$ is determined analog to the displacement error ε_d of the previous study (**Section 2.4.4.2**). In case of an algorithm's ideal performance, the F1-score would hit 1.0 and ε_a would match the theoretical limit ε_d. Since the local optima of F1-score and ε_a can be conflicting (**Figure 2.22** and **2.23**), a simple parameter optimization is applied to find a trade-off by multiplying the two normalized metrics.

1) Karlen et al. [Kar+12]

Intended for usage on resource-constrained devices, the algorithm consists of two stages. First, the IMS algorithm extracts the morphological features by segmenting and compressing the signal into straight lines. It is implemented as a sliding window of size m, which is the only parameter that requires tuning, but also depends on f_s. With a larger m the algorithm is faster and less susceptible to noise, but the determined peak positions are also less precise. Subsequently, the extracted lines with positive gradient are classified as artifact or valid pulse using simple adaptive thresholds. The authors state that "No other filtering than the standard BP filter applied by pulse oximeter manufacturers to remove the DC component [...] is necessary", but they do not specify proven values. Before, the algorithm has been evaluated using two datasets of which one is from CapnoBase [Kar+10], hence from transmission mode pulse oximeters. Since the algorithm expects the inverted pulse direction, consistent with the ABP, the time series need to be flipped before its application (**Section 2.3.2**).

2) van Gent et al. [vGe+19]

The open-source HeartPy toolkit aims for the computational efficient but particularly reliable pulse detection independent from the utilized sensor. Besides a comfortable Python library, an implementation for embedded devices in C is also available. First, a moving average, with a default window size w of 750 ms (300 samples at f_s), is used to identify local maxima as a first selection of candidate peaks. Since an excessive or missing single peak significantly increases the standard deviation of successive differences (SDSD), this measure is combined with the constraint of the natural HR limits (40 – 180 bpm by default) to successively adjust the threshold and, hence, to find the optimal peak selection of minimal SDSD. To compare the algorithms' performance, its validation heuristic is set to the previously discussed natural HR limits from 30 to 200 bpm [Deh+18; Fle+11].

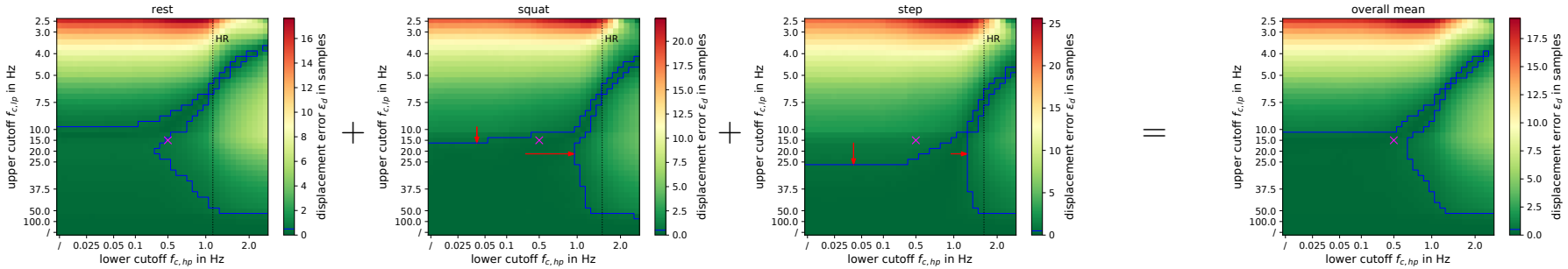

Figure 2.21: Evaluation results of the displacement error ε_d due to filtering at diverse lower $f_{c,hp}$ (x-axis) and upper $f_{c,lp}$ (y-axis). Left to right: results of subsets *rest*, *squad*, *step*, and their overall mean. Shifting (red arrows) boundaries of minimum error plateau $\varepsilon_d \leq 0.5$ samples (blue) due to increasing HR (vertical). Proposed filter passband (magenta mark): 0.5 to 15.0 Hz. **[C21c]**

2.4.4.4 Results and Discussion

The optimal cutoff frequencies largely depend on the subjects' HR. At rest it is low while the frequency band tends to be narrow (rest: 1.22 ± 0.18 Hz). With increasing activity, the HR increases and the frequency band widens (squat: 1.64 ± 0.27 Hz; step: 1.77 ± 0.35 Hz).

Accordingly, the first study demonstrates that the most universal and effectual filter passband ranges from the theoretical minimum 0.5 Hz of the natural HR to appropriate 15.0 Hz. As illustrated in **Figure 2.21**, it is applicable for HR at rest as well as during exercise such as squat and step. While the lower $f_{c,hp}$ can be 'easily' estimated and tied to the minimum HR to be expected, the upper $f_{c,lp}$ is more critical and difficult to specify. A generous $f_{c,lp}$ allows to cover more harmonics of the fundamental HR, which eventually refine the pulse contour. However, at a HR of 0.5 Hz (30 bpm), the covered 29^{th} harmonic is not very gainful. Nevertheless, the upper 15.0 Hz cutoff is required to cover at least three (3) harmonics of a HR at 3.3 Hz (200 bpm) – ten (10) harmonics would be ideal [Kam+89; SN12]. A wider passband of up to 25.0 Hz would result in slightly more pointed and accurate peak contours but also gives unnecessary space for HF noise (**Figure 2.20b**).

The second study demonstrates the very different character of the applied algorithms: **1)** The algorithm of Karlen et al. [Kar+12] performed best with a small window m of 34.236 samples (85.589 ms) and a filter passband from 0.9375 to 25.0 Hz. The configuration results in an F1-score of 0.958 and an ε_a of 3.037 samples (7.594 ms). **Figure 2.22** shows that the F1-score is optimal close to the fundamental HR but remains constant along a varied upper $f_{c,lp}$. The ε_a stays relatively steady along the lower $f_{c,hp}$ until it passes the HR but increases considerably along with a decreasing upper $f_{c,lp}$. The m is homogeneous and plane until it passes the HR along the lower $f_{c,hp}$. **2)** The algorithm of van Gent et al. [vGe+19], in contrast, performed best with a large window w of 270.426 samples (676.065 ms) and a narrower passband from 1.125 to 10.0 Hz. The configuration results in an F1-score of 0.970 and an impressively small ε_a error of 0.051 samples (0.127 µs). Due to the immense increase of peak candidates in raw and noisy signals, accompanied by increasing processing efforts, the evaluation in **Figure 2.23** is limited to $f_{c,hp} \geq 0.5$ Hz.

Limitations

Because the used dataset does not provide ground truth information, the assessment relies on an experienced expert rater to annotate the PPG data afterwards, which inadvertently introduces some bias as well. In case of peaks vanishing with the baseline, the identification can be rather subject to interpretation than a distinct recognition. Inaccuracies due to imperfect label placement are, however, statistically compensated through the large number of labels. The use of an ECG reference channel would, without question, be expedient. Very low as well as very high HR are underrepresented in this dataset. Follow-up studies should focus on a broader HR diversity that spans the entire range of the natural HR from 0.5 to 3.3 Hz (30 – 200 bpm [Deh+18; Fle+11]). However, this is not easily possible, as it entails a possible health risk for the subjects. Also, since PPG at the wrist shows a location-specific composition (**Section 2.1.2.2**), the harmonics may contribute differently to the pulse peak at other measurement locations. Although skin pigmentation has shown to have an effect on the received signal amplitude (**Section 2.1.2.1**), the applied algorithms are unlikely to discriminate against certain skin tones per se. However, this does not preclude other algorithms, and especially approaches based on machine learning, from being biased. The aforementioned aspects highlight the need for further benchmark studies based on measurements from a larger set of subjects with different age, constitution, and diverse skin tones.

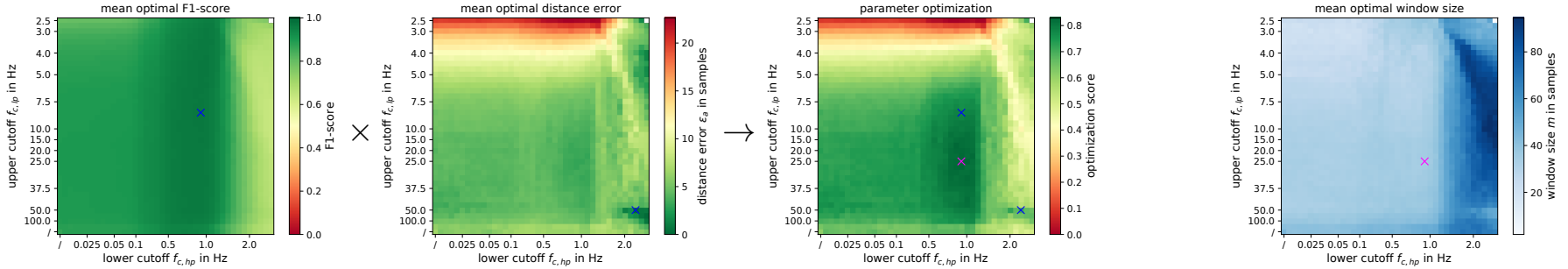

Figure 2.22: Evaluation chain and results for the algorithm of Karlen et al. [Kar+12]. Left to right: mean optima of F1-score, distance error ε_a, fused parameter optimization, and window size m versus lower $f_{c,hp}$ and upper $f_{c,lp}$. Local optima of F1-score and ε_a (blue). Optimal configuration (magenta): $f_{c,hp}$ of 0.9375 Hz, $f_{c,lp}$ of 25.0 Hz, and m of 34.236 samples resulting in an F1-score of 0.958 and ε_a of 3.037 samples. Relatively homogeneous plateau of possible parameters of similar quality. **[C21c]**

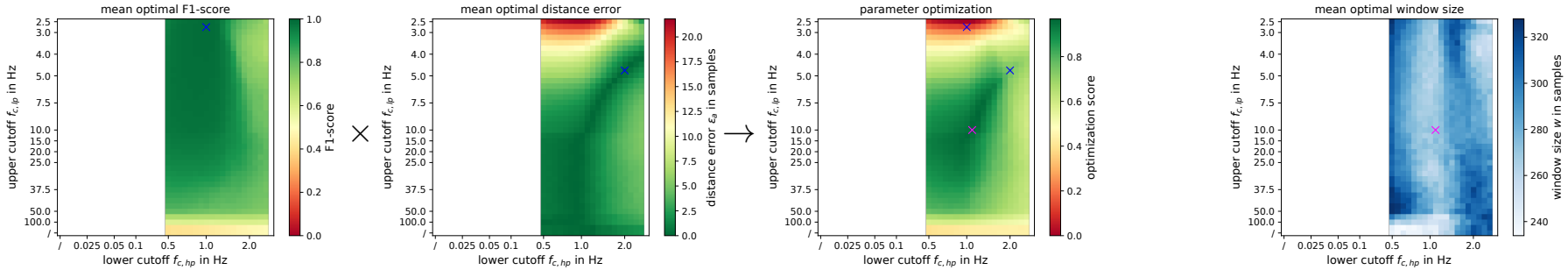

Figure 2.23: Evaluation chain and results for the algorithm of van Gent et al. [vGe+19]. Left to right: mean optima of F1-score, distance error ε_a, fused parameter optimization, and window size m versus lower $f_{c,hp}$ and upper $f_{c,lp}$. Local optima of F1-score and ε_a (blue). Optimal configuration (magenta): $f_{c,hp}$ of 1.125 Hz, $f_{c,lp}$ of 10.0 Hz, and m of 270.426 samples resulting in an F1-score of 0.970 and ε_a of 0.051 samples. Rather complex texture with abruptly falling peak of optimal parameters. **[C21c]**

2.5 Summary and Discussion

During the last three decades, wearables have shown an impressive evolution from bulky portable to convenient wearable devices used by many people. While the first devices considered the human body only as a habitat and physical carrier, nowadays, more comfortable wearables appear as designed lifestyle products that consider the human body a source of valuable information. The ongoing miniaturization allows these devices to be attached to almost arbitrary body positions, fostering the trend from single all-round wearable devices to the simultaneous deployment of multiple sensor units.

The first MEMS accelerometers enabled the introduction of pedometers that allow to count the user's steps and track their physical activity in everyday life. The transfer of the standard modalities ECG and PPG from medical settings to user's wrist has finally led to the breakthrough of modern wearables. The sensors either detect the electric field generated by the cardiac muscle or the mechanical percussion wave traveling through the blood vessels. However, the continuous ambulatory monitoring of the wearer's primary vital signs at the wrist required the adaption of the modalities' fundamental working principle. The approach of wearable ECG is relatively close to that of conventional single-lead ECG by resembling the standard lead I. In contrast, the revival of PPG in the reflective mode differs fundamentally from the conventional transmission mode still applied in pulse oximeters at regular wards of hospitals.

ECG is still considered as the gold standard for measuring cardiac activity. The derivation of the significant and well-known signal pattern of the QRS complex is, however, still limited by the attachment of multiple electrodes at different specific body positions. For the continuous monitoring in a wearable form factor, only the chest provides comfortable access to the signal. However, the phenomenon of the line of zero potential [Wal88] further limits the possible locations. To establish the lead I for wrist-worn devices, the user has to touch an electrode with a finger from the opposite arm [Tho+16; Bea+18], thus impeding the monitoring during physical activities. Therefore, it is still impractical for wearable devices to detect the electrical signal at a single spot. Even the differential signal captured at wrist vanishes with an SNR of about 0 dB [Bea+18]. However, recent advances in the development of sensors with very high input impedances are promising and demonstrated that the heartbeat can be detected not only at arbitrary body positions but even remotely at a distance [Pra+00; HCP02; Gar+13; SY16]. Considering the pace of developments in recent years, the required ECG sensor front-ends will likely become available and standard in wearables soon, hence enabling the methods presented in the remainder of this work.

During the last decade, PPG has established as the primary sensing modality and standard in wearable devices to non-invasively and continuously monitor cardiac activity. In contrast to the transfer of ECG to wearable devices, the adaption of the conventional transmission mode to the reflective mode PPG on the skin was more difficult and is still subject to research. Nevertheless, the optical measurement principle enables to detect the pulse in any sufficiently perfused tissue throughout the body surface. In contrast to the passive ECG principle, the active sampling of PPG requires an intensive LED which puts a dent into the devices energy budget. Diverse sampling schemes and strategies, implemented in commercial devices and proposed by researchers, aim at minimizing the power consumption and at the same time providing reliable data. Nevertheless, motion artifacts and interference induced during physical activity remain one of the key challenges of wearable PPG. Especially green light has proven to be more robust and tolerant against motion than the conventionally applied IR and red light, which, however, allow to estimate SpO_2. While the origin of the PPG signal from green light is still vague, the preprocessing

and undocumented flipping of the signal amplitude, to conform with ABP, have caused even more confusion. The development and benchmark of efficient algorithms and the training of machine learning models, intended to catch up with clinical ECG, require large datasets from numerous individuals with different constitutions. The approaches are, however, usually benchmarked on either available datasets from a clinical origin or self-recorded datasets with a limited evidence and reproducibility. Although advertised as such, most datasets do not actually contain raw but conspicuously filtered signals, often from transmission mode PPG. Despite these issues, PPG is undoubtedly capable of detecting the heartbeat rhythm at almost arbitrary body positions and, therefore, similarly to ECG, provides access to the natural information required for the proposed methods.

Several approaches have attempted to apply seismocardiography at the body surface and detect the heartbeat with sensitive but energy-efficient accelerometers, available in virtually every wearable device. However, the methods require complex filters and the achieved reliability, especially when moving, is not satisfying yet. Therefore, the predominating modalities for wearable HR monitoring are still ECG at rest, consciously forming lead I across the arms with a medical-grade accuracy, and PPG even during physical activity. However, future developments may allow the use of other sensor technologies.

Naturally yet irregularly sampled by the rhythm of the heart, the derived HRV contains a large spectrum of superimposing physiological signals, e.g. RSA, related to RR, and SNA. The secondary signal shows a high degree of intrinsic variation and temporal uniqueness [Isr+05], superimposed by physiological noise [COL90] and chaos [Svi+18]. While the raw ECG and PPG signals look very differently along the body surface, the derived HRV interval functions are very similar yet ideally identical.

The mean propagation velocity of the cardiac muscle's electrical field in tissue has been determined to be about $1500\,\mathrm{m\,s^{-1}}$ [Buc+22]. Therefore, the ECG signal is virtually simultaneously detectable throughout the body surface. In contrast, the mechanical pulse wave is traveling through the vascular system much slower with a PWV of about 5.2 to $14.6\,\mathrm{m\,s^{-1}}$ [FAG+10]. The resulting PATs delays between the R wave in ECG and the diastolic / systolic point P in PPG are respectively 0.133 s / 0.397 s at the ears, 0.199 s / 0.436 s at the thumbs, and 0.301 s / 0.515 s at the toes [AM00]. Taking these delays into account, the continuously available signal from the human heart is perfectly suitable for the synchronization of wearable devices.

Case Studies on Wearable Photoplethysmography

PPG sensing has undergone a revival and became standard in modern devices to unobtrusively obtain information about the wearer's vital signs, enabling continuous self-monitoring, health care, and fitness tracking. In recent years, the variety of light wavelengths used in current wrist-worn PPG devices has settled on primarily using green light since it is robust against motion artifacts and provides a larger signal amplitude. However, all other parameters that one might consider in sampling PPG measurements are less settled. The inspection of commercial wearables showed that some devices apply traditional uniform sampling at a fixed sampling frequency, but many others follow different strategies as a trade-off to achieve a good signal while dissipating a minimum of energy. They seem to follow different variations of multi-channel sampling, average sampling, and burst sampling strategies at various frequencies, yet the need for different qualities of readings can explain only part of this diversity. Even though PPG has been integrated into many commercially available wrist-worn devices, their sampling strategies have thus not yet converged to a single solution and still demand for more research. **[A19]**

The insights into commercial products underline the importance of efficient sampling strategies for the long-term deployment of wearable devices. However, developing and benchmarking algorithms and training machine learning models requires large datasets with recordings from suitable sensing modalities. However, most of the publicly available are originated in extensive medical studies. The sensors of stationary clinical equipment, therefore, tend to be incomparable to those applied in wearable devices, and the findings of studies based on such data are lacking evidence. The presented analytical tool for the quality review of PPG signals is based on seven (7) multi-varied decision metrics. The conducted review of ten (10) publicly available PPG datasets was rather disappointing. All datasets were advertised to contain raw data, which are defined by this work as signals containing the maximum possible information by applying the minimum necessary preprocessing. Nevertheless, the characteristics of the PPG data look quite diverse. Besides the reference data (**REF**), recorded with the evaluation system of the MAX86140 / 41 [MAX8], only one dataset (**S01** of Biagetti et al. [Bia+20]) proved itself to contain the desired quality of raw measurements. The results highlight the need for more quality datasets that actually contain raw PPG readings and do not limit their further use right from the start. Hence, guidelines for future datasets are provided with a focus on recordings of reflective mode PPG for research in digital signal processing and the development of algorithms for resource-limited wearable devices. **[W20a]**

The resource constraints of wearable devices demand for high efficiency. Obtaining the information through the spectral analysis of PPG data in the frequency domain promises to be particularly suitable for the long-term monitoring as it allows sampling at considerably lower frequencies. The wearer's HR and RR are determined by observing dominant frequency components in their respective frequency bands. Additionally, the activity of the SNA is inferred by capturing the area under the curve in the characteristic LF band. Although the presented methods do not provide detailed, peak-specific identification and signal segmentation, they lend themselves well for energy-efficient PPG monitoring and solutions that need to be lightweight and wearable over longer stretches of time. Despite features such as detecting motion artifacts, the high sampling rate f_s represents a considerable bottleneck for such systems. The spectral analysis can be implemented on current systems, as it depends largely on the FFT to transform a window of PPG data into its frequency components. Even for minutes of data, as required to observe LF components associated with SNA, this is achievable in off-the-shelf hardware. Two experiments are conducted to demonstrate that f_s can indeed be reduced to 10 Hz, without significant deterioration of the detection performance of HR and RR as well as the inferring of SNA. In the first experiment, the approach is applied to the popular CapnoBase IEEE TBME dataset [Kar+10; Kar+13] with PPG recordings from a fingertip pulse oximeter of 42 highly variable individuals and a wide variety of HR and RR. It turned out that RR was accurately detected in around 80 % of all cases, even when varying the f_s from originally 300 Hz down to 9 Hz. The HR was accurately detected at almost 90 % of all cases under the same conditions. The second experiment used data from the MAX86140 / 41 [MAX8] evaluation system, from 6 individuals that performed paced breathing at 0.25 Hz (15 cpm). Similar accuracy performance was detected for these data as well, with slightly better performance for the lower f_s down to 4 Hz. In both experiments, no significant indication of SNA has been observed, however, this specific topic demands for more detailed research. While the second experiment particularly confirmed the feasibility of our approach for the implementation on wearable systems, the first study showed its reliability and accuracy for similar data recorded from real patients without paced breathing. It is important to note, however, that the influence of motion has been excluded in both cases. **[W18; J20b]**

However, besides the basic HR reading, modern applications also demand for reliable and accurate pulse detection to derive the secondary HRV signal, which makes the detection of fiducial points in the time domain necessary. Most available algorithms have been evaluated and benchmarked on either the few available datasets from a clinical origin and of conspicuously filtered signals or self-recorded datasets with limited evidence and reproducibility. The conducted experiments on actual raw PPG signals highlight the importance of benchmarking. Based on the dataset of Biagetti et al. [Bia+20] and 21806 peak labels, manually annotated by an expert rater, the impact of preprocessing on pulse peak positions and the performance of peak detection algorithms have been evaluated. The filter passband of 0.5 Hz to 15.0 Hz showed the best universality by preserving the HR's harmonics for distinct and precise pulse peak positions. Applying 40×40 filter configurations, also the two popular algorithms of **1)** Karlen et al. [Kar+12] from 2012 and **2)** van Gent et al. [vGe+19] from 2019 are benchmarked. Despite their very different concepts, both algorithms show very good performances with **1)** an F1-score of 0.958 and ε_a of 3.037 samples and **2)** an F1-score of 0.970 and ε_a of 0.051 samples. In summary, algorithm **2)** is more complex than **1)** but, in the absence of LF baseline wonder, its concept results in significantly better accuracy and precision. **[C21c]**

Data Availability

The raw reference data, recorded with the MAX86140 / 41 [MAX8] (**Section 2.1.4**), as well as the implemented Python tool, based on the presented seven (7) decision metrics, are available for download to support the reproducibility and the review of new datasets: https://ubicomp.eti.uni-siegen.de/home/datasets/data20/

Researchers are encouraged to use the publicly available dataset of Biagetti et al. [Bia+20] in combination with the supplementary annotations from this research to benchmark their own algorithms and machine learning approaches. The annotation files, provided as `*.pkl` and `*.csv`, of the 21 806 diastolic pulse onset labels are available for download from: https://ubicomp.eti.uni-siegen.de/home/datasets/embc21/

3 Intra-Body Communication

Today, most wearable devices regularly upload their collected measurements to the wearer's smartphone, which hence serves as a gateway to the internet and the manufacturer's cloud. There is, however, a perceptible trend from wearing single all-round devices toward distributed and continuously networked hardware units to establish an internet of wearable things. Unfortunately, wireless communication loads the resource-constrained devices with a considerable power dissipation of the radio modules. These suffer from the omnidirectional radiation of cost-efficient antennas and shadowing effects caused by the water-rich body in close proximity. In 1995, a novel yet promising communication principle was introduced that uses the confined human body as the transmission medium. Intra-body communication is somewhat located between the traditional wired and wireless techniques while showing advantages over both. Research has presented numerous approaches that leverage different physical effects and techniques, all aiming at more energy-efficient and secure communication in wireless body area networks. While a few notable research teams continue to push the boundaries of what is possible, none of the presented approaches ever reached the market, the implementations remained closed-source and are not turned into commercial products to make them available. Due to the absence of commercially available transceiver modules with low cost and complexity, research into potential applications is lagging behind. Especially concepts for more intuitive human-computer interaction and their impact on the user experience, therefore, cannot be explored yet.

In this Chapter, the human body is considered as a physical medium for the transmission of artificial signals. First, **Section 3.1** introduces to WBANs in general and then focuses more on the novel IBC principle, also giving examples of applications based on it (**Section 3.1.1**). Subsequently, the applied capacitive coupling principle (**Section 3.1.2**) is introduced in depth, describing the issues of grounding, the diverse frequency ranges, available channel models, and the design of electrodes. Based on these fundamentals, four case studies are presented. The first study (**Section 3.2**) is a hardware-based approach that simplifies the transmission channel by using conductive textiles to form a reliable local reference potential. It also demonstrates the application of a novel modulation scheme based on pulse-width modulation for an efficient signal transmission. The second study (**Section 3.3**) is a software-based approach that repurposes the electrocardiography sensor front-ends of commercially available wearable devices to receive information about the situational context by touching surfaces or objects equipped with transmitter beacons. The third study (**Section 3.5**) is again hardware-based and discovers the effect of environmental changes on the intrinsic inter-electrode capacitance. This way, not only the fluctuating electrode capacitance is characterized, but also the detection of hand-washing due to grounding effects is investigated. The fourth study (**Section 3.5**) uses the previously characterized electrodes for an open-source project that repurposes an RFID / NFC receiver front-end to implement a low-power wake-up receiver. Finally, **Section 3.6** summarizes the findings and discusses these with regard to the research intent of **Chapter 4**.

Contributions by the Author

[C17] **Florian Wolling**, Philipp M. Scholl, Leonhard M. Reindl, and Kristof Van Laerhoven. "Combining Capacitive Coupling with Conductive Clothes: Towards Resource-Efficient Wearable Communication". In: *Proceedings of the 2017 ACM International Symposium on Wearable Computers*. ISWC '17. Maui, Hawaii, USA: ACM, 2017, pp. 146–149. ISBN: 978-1-4503-5188-1. DOI: 10.1145/3123021.3123059.

[C21b] **Florian Wolling**, Cong Dat Huynh, and Kristof Van Laerhoven. "IBSync: Intra-body Synchronization of Wearable Devices Using Artificial ECG Landmarks". In: *Proceedings of the 2021 ACM International Symposium on Wearable Computers*. ISWC '21. Virtual, USA: ACM, 2021, pp. 102–107. ISBN: 9781450384629. DOI: 10.1145/3460421.3478815.

[W22a] **Florian Wolling**, Kristof Van Laerhoven, Jonas Bilal, Philipp M. Scholl, and Benjamin Völker. "WetTouch: Touching Ground in the Wearable Detection of Hand-Washing Using Capacitive Sensing". In: *2022 IEEE International Conference on Pervasive Computing and Communications Workshops, WristSense Workshop*. Virtual, Italy: IEEE, 2022, pp. 769–774. ISBN: 978-1-6654-1647-4. DOI: 10.1109/PerComWorkshops53856.2022.9767345.

[J22b] **Florian Wolling** and Kristof Van Laerhoven. "IBSync: Intra-body synchronization and implicit contextualization of wearable devices using artificial ECG landmarks". In: *Frontiers in Computer Science* 4 (2022). DOI: 10.3389/fcomp.2022.915448.

[C22c] **Florian Wolling**, Florian Hauck, Günter Schröder, and Kristof Van Laerhoven. "OpenIBC: Open-Source Wake-Up Receiver for Capacitive Intra-Body Communication". In: *Proceedings of the 2022 International Conference on Embedded Wireless Systems and Networks*. EWSN '22. Linz, Austria: ACM, 2022, pp. 186–191.

3.1 Wireless Body Area Networks

Today, only a few wearable devices are entirely self-contained. Although these are often equipped with simple displays that provide basic information to the user, a closer look at the collected data requires opening either a smartphone application or even the manufacturer's website. Therefore, most sensing devices upload the preprocessed and often compressed readings to the wearer's smartphone, which serves as a gateway to the internet and the manufacturer's cloud [AV17; Ome+21]. For this type of device, conventional radio communication, and in particular Bluetooth with its diverse low-power modes, is the most commonly used wireless technology [AOD20]. In general, the use of wireless standards such as Bluetooth, ZigBee (based on IEEE 802.15.4, LR-WPAN), and Wi-Fi (IEEE 802.11) is convenient because of the availability of a plethora of fully developed, standardized, small, and affordable modules that can be easily embedded into research prototypes and commercial devices.

Radio communication is also suitable for body-worn systems of distributed hardware units. However, the energy is often radiated by cost-efficient antennas in an isotropic manner and thus omnidirectionally into free space, the large, quasi-infinite medium air. This way, the radio modules, attached to or at least worn close to the skin, suffer significantly from the close proximity to the water-rich body, resulting in shadowing effects due to absorption and varying channel losses due to motion [Don09; AB13]. Therefore, depending on the application and duty cycle, communication can make up to 50 % of a typical device's consumption [AMH19], considerably limit battery life, and impede long-term deployment. However, recent research aims for even more communication to make the devices "networked beyond pure connectivity" [Wil+14] and at establishing the internet of wearable things (IoWT) [JVR20]. This objective necessitates and drives research into a more efficient communication technology.

For decades, wired networks have been the standard in stationary local area networks (LANs). In wearable applications, however, fixed cable joints, but also thin wires or coated threads embedded and woven into clothing [Ort+98; Pou+16], are promising but not yet a serious alternative. Wiring within the clothing would be washable and comfortable to wear, but the individual and fixed signal and supply lines of the distributed components are inflexible in positioning. More flexibility could be achieved by two separated conductive layers within the clothing, which the nodes are connecting to via special pins [VVG03]. Wires do not only have the advantage of the simple distribution of data, but also easily allow to supply the deployed devices with power. Nevertheless, the attachment and linking of devices tends to be interference-prone, inflexible, and perceived uncomfortable by the user. Therefore, tends in research have recently "shown a different emphasis, away from garment-based forms" [BDD16].

In 1995, the thesis [Zim95] and the ensuing publication [Zim96] of Zimmerman for the first time described the fundamentals of a novel yet promising communication principle, today termed as intra-body communication (IBC). It is somewhat located between the traditional wired and wireless techniques while showing advantages over both. By using the confined human body as the transmission medium, it likewise enables to provide information throughout the user's skin. However, it does not require a wired infrastructure and, in contrast to the busy air, the body channel is still 'free' while the limited distribution volume considerably improves the energy efficiency of signal propagation [Don09; KTL14]. Moreover, by coupling or inducing the signals to or even into the human body, depending on the transmission principle applied, they are only detectable at or close to the body surface, which makes IBC less susceptible to eavesdropping.

Originally, the principle was termed as personal area network (PAN), relating to the "evolutionary progression in the development of computer networks [...] towards very personal computing [...] worn on and near the body" [Zim95]. In subsequent research, PAN was regularly referred to as body-coupled or body channel communication (BCC) as well as intra-body communication (IBC). Since 2012 it is, designated as human body communication (HBC), included in the IEEE 802.15.6 standard [IEE12] for WBAN. Nevertheless, IBC is still the term most often used in publications.

In IBC, the signals are intentionally induced to or even into the user's confined and therefore limited body volume. Depending on the applied principle, signals either penetrate the tissue or travel along the skin surface. Seen from a technical perspective, the human body enables diverse ways of inducing and transmitting signals. As surveyed by Naranjo-Hernández et al. [Nar+18], there exist two primary principles for the signal induction: the original capacitive coupling [Zim95; Zim96] and galvanic coupling [Han+97; Lin+98; Weg+07]. Reviewed by Tomlinson et al. [Tom+19], other approaches using electromagnetic fields [KYK12; PM15] and transdermal ultrasound, as discussed in [Gal+12], remain exotic and rather unpopular. Today, most research focuses on capacitive coupling (**Section 3.1.2**), the original approach of Zimmerman [Zim95; Zim96], and so here.

Since its invention, IBC evolved into a promising alternative for WBAN and research aimed at the development of optimal electrode setups, modulation schemes, and models for the simulation of the channel characteristics. As stated by Donker [Don09], "simple experimentation [...] can be done by graduate students with limited budgets", but "more advanced implementations currently require integrated circuit manufacturing". According to this, the developed prototypes range from implementations on an experimental PCB-level [Gro+14; MAK15] to high-level, chip-casted ASICs [Son07; CCL15; Cho+16; Mai+20a; Cha+22b], achieving a very high data rate of 80 Mbit/s at 8.9 mW [Cho+16], 2 Mbit/s at 0.2 mW [Son07], or even an outstanding efficiency of 1 – 20 kbit/s at 415 nW [Mai+20a]. Large teams continuously push the boundaries of what is possible by developing high-performance transceiver circuits, accompanied with advances in reliability, energy efficiency, and data throughput. Nevertheless, none of the presented approaches ever reached the market, the implementations remained closed-source and are not turned into commercial products to make them available. With the discontinued attempt BodyCom [Pop11], Microchip provided the specialized AFE MCP2035 which, however, quickly disappeared. In general, it seems that companies are very hesitant and cautious with investing.

Diverse commercial devices have been repurposed for IBC and similar concepts. On the one hand, fingerprint sensors of smartphones and touchpads of laptops have been utilized as transmitters in [HIG16], achieving a data rate of up to 50 bps by triggering the active sensors' operation, and hence the generation of electromagnetic interference (EMI). On the other hand, touchscreens of tablet computers have been used as receivers to distinguish users at 4 bps in [Vu+12] and for the continuous user authentication at 12 bps in [HK15] by means of wrist-worn transmitters. This dissertation demonstrates that also the AFEs of conventional, wearable ECG sensors can be repurposed to detect artificial signals, achieving about 20 bit/s **[C21b; J22b]** (**Section 3.3**).

Due to the absence of commercially available IBC transceiver modules with low cost and complexity, research into potential applications is lagging behind. Especially concepts for more intuitive human-computer interaction (HCI) and their impact on the user experience (UX) have, therefore, no yet been thoroughly explored.

3.1.1 Applications

The novel communication principle opens up a wide range of possible applications. While Zimmerman [Zim95; Zim96] mentioned more conservative scenarios in which portable devices are connected in a PAN through IBC, the ongoing miniaturization encouraged following work to investigate more creative ways of interacting with environment, objects, and other people. Shortly thereafter, Post and Orth [PO97] presented BodyNet, a system worth mentioning not for the 9600 bps data rate, but for its capability to transmit up to 56 mW power, which was still considered safe. One of the first and since then regularly mentioned applications of IBC is a wearable key, presented as TouchNet [Mat+00], to identify users and personalize their nearby environment "by simply touching them". Dietz and Leigh [DL01] presented DiamondTouch, a desk-like multi-user touch display for collaborative work environments, which instrumented chairs with built-in receivers allow to determine the touch locations independently for each user. "Earthlings Attack!" by Takahashi et al. [Tak+11] was probably the first presented interactive IBC-based game, in which body-worn receivers detect the users' contact to an active ball with built-in transmitter. Fukumoto and Shinagawa [FS05] presented a smart floor system that uses the user's body to connect devices to the Ethernet and enables positioning in large areas. Große-Puppendahl et al. [Gro+14] investigated different ways of interacting with ubiquitous smart objects in a short-range spatial context, distances of up to 15 cm. The well-known team around Sen presented diverse approaches for secure ultra-low power (ULP) WBAN, secure authentication, and social networking, enabling the exchange of business cards or Facebook / LinkedIn requests by shaking hands [Sen16; Mai+17]. Varga et al. [Var+18a] introduced TouchCom that enables interactive infrastructure for ambient intelligence and presented a portable sphere device, a wristband, and stationary wall or floor tiles to connect through the body. For the first time, they also "present guidelines for future wearable BCC systems and their applications", considering "the whole body as user interface" [Var+18b]. In earlier work, Suzuki et al. [SHI16] presented EnhancedTouch, a smart bracelet to "measure human-human touch events and provide visual feedback to augment touch interaction". In their recent paper, Hachisu and Suzuki [HS21] demonstrate that these devices can connect to other "interpersonal hand area network module[s]" by shaking hands or touching in the style of Michelangelo's fresco 'The Creation of Adam'.

3.1.2 Capacitive Coupling

Capacitances are established between any conductive surfaces and their different charging results in an electric field [Mor16]. This physical phenomenon is leveraged in IBC to transmit signals throughout the human body by modulating its electric field.

The capacitance C of an ideal parallel plate capacitor is given in **Equation 3.1** through two facing electrodes with an area A and a distance d, separated by a dielectric with the absolute permittivity ε_0 of free space in vacuum ($8.854 \times 10^{-12}\,\mathrm{F\,m^{-1}}$) and a relative permittivity ε_r. While air has $\varepsilon_r \approx 1$, any different material has $\varepsilon_r > 1$.

$$C \;=\; \varepsilon_0\,\varepsilon_r\,\frac{A}{d} \tag{3.1}$$

All objects couple to the environment, basically to the mass of earth and its earth ground potential. Likewise the human body forms natural capacitances in the order of several hundred pF [Smi+98; Gro+13; Gro+17]. Due to the insulating dielectric between the electrodes, no DC can flow from one side to the other. The application of a changing potential difference, and hence a time-varying electric field, induces, however, an AC,

denoted as displacement current $\vec{i_d}$. For such an alternating signal at frequency f, the ideal capacitance C results in the complex impedance $Z_C = \frac{1}{j\omega C}$ with the angular frequency $\omega = 2\pi f$. For an increasing f the impedance Z_C hence decreases and with $\lim_{f\to\infty} Z_C = 0$ it virtually resembles a short circuit.

The original approach of Zimmerman [Zim95] is based on two stacked electrodes that form a parallel plate capacitor. While one faces the skin and couples to the body, the other one provides a delicate return path through the environment and earth ground [Gro+17]. To emit a signal, the transmitter changes the potential difference among the electrodes and hence modulates the electric field of the user's body. This variation induces a tiny current flow, spreading in the tissue, and in turn causes a small potential difference among the electrodes of the receiver, which can be detected using a sensitive circuit. The electrical properties of the tissues, conductivity and dielectric permittivity respectively, exhibit a considerable frequency dependency which results in the human body showing a transmission behavior similar to the one of a HP filter. The effect of different tissue compositions on the transmission characteristics have been investigated, modeled, and simulated in diverse studies, surveyed in [Nar+18].

Recent research in IBC continued to investigate capacitive coupling, where signals are transmitted and received using a pair of vertically configured electrodes: A signal electrode close to the skin that couples to the body, and a feedback electrode that provides a return path through the wearer's environment. By varying the potential of the signal electrode, the transmitter modulates the weak electric field of the body and induces a slight displacement current. Resulting variations of the electric field can then be detected at the receiver's side by measuring the tiny current flowing between the electrodes. This closing of the channel circuit through the environment's common ground has on several occasions been identified as an issue: While the transmission behavior of human tissue is adequate and predictable, the feedback path through the environment provides a stronger and highly varying attenuation.

Grounding

While the signal's forward path is formed through the human body [MMS18], the capacitive coupling principle requires the channel circuit to be closed through the environmental ground potential [NMS20]. Therefore, the channel loss as well as the signal quality are considerably affected by any environmental changes. In general, the grounding issues limit the reliability of such approaches outside the laboratory environment, as discussed in [Gro+17].

In recent years, different approaches neglected even the reference electrodes, necessary to close the transmission circuit. Therefore, the established capacities, spanned between local ground potential and environment, get even more tiny. The already delicate return path, the bottle neck of the whole channel, is more affected and the desired signal tends to be much weaker. Consequently, a much higher effort of the signal's modulation, boosting, filtering, amplification, and demodulation is necessary to, nevertheless, enable the achieved data rate.

Systems such as the ones implemented in [Pop11; Gro+14; MAK15] solved the issue of the delicate feedback path by providing a large ground plane in the vicinity. Due to the improved direct coupling, the prototypes can be kept simple and there is no need of complex circuits. The signals are directly generated by a microcontroller pin and the signal detection, amplification, and demodulation is either done by a simple transimpedance amplifier and the microcontroller in [Gro+14; MAK15] or an off-the-shelf receiver chip in [Pop11]. However, the large ground planes, needed for these solutions, make them

challenging to adopt for more generic IBC.

In general, shorting the feedback path and bypassing the environment can hence significantly improve the channel loss **[C17]**. An interesting effect of improved grounding has already been mentioned by [Zim95]: the "feet are the best location for [IBC] devices" since the coupling to both the body and the environment is the strongest.

Channel Models

As already mentioned by [Zim95] and elaborated in [Gro+17], capacitive coupling suffers primarily from the delicate return path through earth ground, the environment which is susceptible to changes and provides a highly variable loss. If both devices are floating, the transmitter as well as the receiver, and do not share a common potential, the SNR, associated with signal amplitude and quality, decreases significantly. However, a stationary transmitter with a link to earth ground consequently results in a significantly higher SNR and less complex circuits that, as stated in [Don09], "can be done by graduate students with limited budgets" as presented in [MAK15].

Particularly at low frequencies, the body can be considered as a conductor to form the signal's forward path with a marginal loss of about 0.5 dB [MMS18]. The return path, however, is established via the environment, and the earth ground respectively, which has been identified to be the bottleneck of the channel circuit, resulting in a total channel loss of typically 45 – 55 dB [Gro+17; NMS20].

The characterization and modeling of the body channel turned out to be difficult and findings vary widely depending on the setup and equipment used [Mai+18]. Primarily the measurement devices' (unintended) grounding but also the port termination, typically to 50 Ω, have a large impact on the determined channel loss. The transmission behavior resembles a high-pass filter whose corner frequency lowers with increasing input impedance [Mai+18; Mai+21].

The effect of different tissue compositions on the transmission characteristics have been investigated, modeled, and simulated in diverse studies, surveyed in [Nar+18].

Frequency Ranges

The electrical properties of the tissues, conductivity and dielectric permittivity respectively, exhibit a considerable frequency dependency which results in the human body showing a transmission behavior similar to the one of a HP filter. In contrast to the busy air channel, the body is still free and its limited distribution volume significantly improves the energy efficiency [Don09; KTL14]. At higher frequencies, however, the human body or parts of it act as a radiating antenna, hence narrowing the suitable frequency band to 100 kHz – 50 MHz [Maz08; Bae+12; Cho+09; KTL14]. Thus, it demands only for baseband processing and no HF front-end is needed, which usually requires most power budget of radio communication [Bal+09; KTL14]. At these relatively low frequencies, the near field outside the confined body decays abruptly which makes IBC insusceptible to eavesdropping and physically secure [Mai+20a].

As illustrated in **Figure 3.1**, Bae et al. [Bae+12] explain the three frequency-dependent transmission mechanisms: quasi-static near-field coupling (predominating below 40 MHz), reactive induction-field radiation (maximal at 40 MHz), and surface wave far-field propagation (predominating beyond 40 MHz). A particularly important aspect is stated by [HKW12]: "Low frequencies in the range of few Hz are susceptible to electromagnetic interferrence and demand very high input impedance amplifiers".

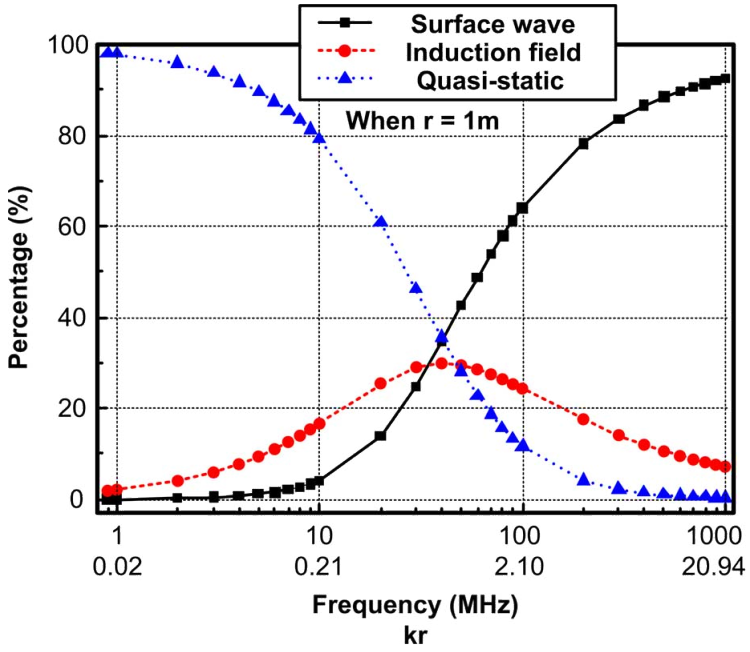

Figure 3.1: The signal transmission mechanism on the surface of the human body and the ratio of their contribution in terms of frequency. Figure from [Bae+12] (© 2012 IEEE)

Electrode Design

As stated by [Maz08], also the electrode size and distance play an important role while "using an electrode with a larger area specifically at TX will result in less propagation loss". The 'sandwich' electrode setup, used in most case studies, has been adapted from previous research [WMa16] and is made from standard FR4 PCB substrate (1.55 mm) with laminated copper foil (35 µm). Both electrodes measure an area A of $3 \times 3\,\mathrm{cm}^2$ and are stacked with an air gap d of 1 cm. This forms a parallel plate capacitor which ideal intrinsic capacitance C_{ec} is 0.797 pF.

To achieve the intended poor coupling of the electrodes, neither the circuitry nor any filling ought to be placed between the electrodes. Any material other than air ($\varepsilon_r \approx 1$) would result in a larger $\varepsilon_r > 1$, improve coupling, and hence increase C_{ec}. The electrodes' substrate as well as the four spacers at the corners are, however, required to keep the plates in place, and inevitably increase the capacitance slightly. A larger d would reduce coupling, but the dimensions are limited through the device's obtrusiveness. A solder mask is applied to prevent direct skin contact.

Figure 3.2: The first case study proposes a novel IBC approach that also uses the human body as a transmission medium for the signal path, but additionally a nearby conductive fabric to provide a robust feedback path. This way, it simplifies the channel, significantly reduces the channel loss, and resembles a Faraday cage which improves SNR. **[C17]**

3.2 Case Study 1: Conductive Clothes

Early portable computer systems mostly relied on fixed cable joints to enable the communication between their distributed units, attached to different parts of the body. Today, wearable devices primarily apply traditional radio transmission which tends to reach even beyond the individual's body surface. For more than two decades, conductive clothes with wires woven into textile are developed to distribute data between body-worn units, and even the supply from a central power source is possible. Especially the latter one is a unique selling point for conductive fabrics enabling the transfer of energy, which is not as simple with radio frequency (RF). The compromise suffers, however, from inflexible traces and rigid electronic modules that are connected to predetermined positions via bulky mechanical connectors. The concept of IBC would allow for more flexibility as modules could be placed anywhere on the wearer's skin. However, as previously discussed in **Section 3.1.2**, capacitive coupling suffers significantly from grounding issues. The devices' individual ground electrodes require a reliable return path through the environment and thus have a large impact on the received signal amplitude and quality.

In this case study **[C17]**, the combination of capacitive coupling and conductive textiles is investigated to simplify the delicate physical layer of IBC. The presence of conductive clothing are assumed nearby the wearable units to reduce the channel loss and to improve the SNR. The additional layer is intended to provide a stable reference potential for the feedback path in proximity to the attached devices on the skin. Therefore, it would cancel the erratic dependency on the environmental ground [Gro+17] and increase the system's reliability. In addition, inspired by the approach of [MAK15], an efficient modulation scheme is presented which is based on pulse-width modulation (PWM) and represents symbols by means of different pulse duty cycles.

3.2.1 System Design

The system consists of multiple wearable devices that are attached to the user's body. A layer of conductive clothing is added to provide a stable reference potential in proximity of the transceiver units. The typical capacitive coupling channel setup is thus simplified by replacing the environment and its delicate earth ground with conductive fabric and an adjacent ground potential. Therefore, the distance between the electrode and the reference potential is significantly reduced, the return path is hence strengthened through close coupling (**Section 3.1.2**), the total channel loss is significantly reduced, and, as a

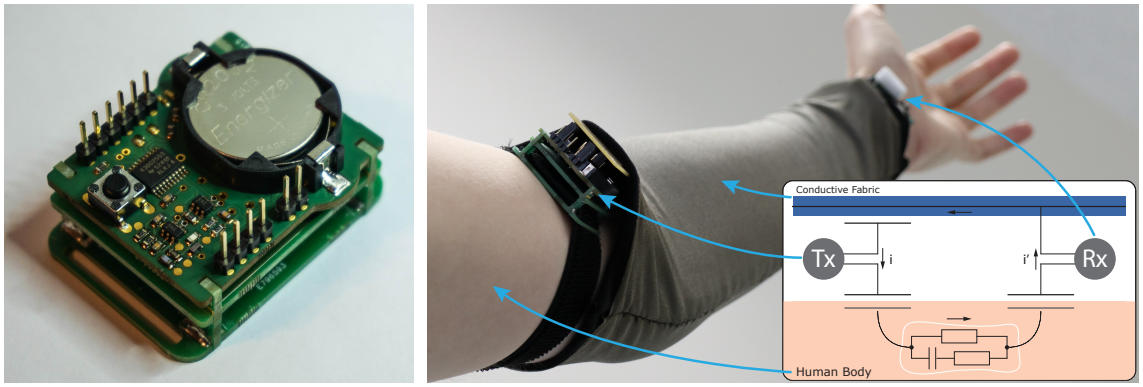

Figure 3.3: The prototypes (close-up: left) communicate through capacitive coupling: The signal's forward path goes via the wearer's body and the feedback return path via nearby conductive textile layer (right). The induced displacement current i at the transmitter (Tx) and the much weaker counterpart i' at the receiver (Rx). **[C17]**

result, the SNR is significantly increased. Consequently, the corresponding analog circuits can be simplified while the coupler dimensions can be scaled down. **Figure 3.3** shows the experimental setup at the arm, with two modules communicating via the tissue between wrist and upper arm, utilizing an insulated conductive textile sleeve as the return path. Since the approach uses capacitive coupling for the signal induction, the modules can be placed on any part of the body surface that is, as well, covered by the fabric. By providing a local common ground, the sleeve establishes an independent volume inside, resembling a Faraday cage that floats in the natural surrounding electric field. It shields the entire channel, lowers the noise level inside, improves the coupling, and decreases the channel loss with a return path in significantly lower distance than the environment.

Conductive textiles can be incorporated in regular clothing, conductive fabrics come with additional properties such as elasticity and they are washable as well as antibacterial due to the used metal coating of the threads. The stable reference potential is provided by a single module, for example the hub or gateway module which could forward data, such as sensor readings, to an external device like a computer or smartphone. The conductive connection can be realized through a conductive hook-and-loop fastener, a snap fastener, or just a simple contact area. A small but ohmic connection is sufficient due to the tiny displacement currents flowing, whose voltage drop at the contact point, according to Ohm's law $V = R \times I$, would be negligible. However, the additional wearable units do not require a conductive connection, as these couple capacitively to both the human tissues and the conductive reference layer. Due to the use of this principle, the presence of additional insulators between the electrodes and the corresponding medium is possible. Although an additional textile layer impedes the direct contact of metal and skin, additional coatings could also prevent from any allergy and dermatitis. Furthermore, the manufacturing of clothes with an overall conductive layer might be easier to produce than the stitching of a particular signal bus or supply lines. The fabric behaves similar to non-conductive ones and is also easier to repair or recycle since it is available as a single, separate layer.

Transceiver Circuit

The significantly reduced channel loss allows for a reduced complexity of the analog front-end of the receiver part, but also allows to remove the LC tank circuit that has originally been used to boost the signal amplitude at the transmitter [Zim95; Zim96]. This way, the transceiver mainly consists of a microcontroller as the central unit that directly modulates

and demodulates the signals in software. The prototypes, shown in **Figure 3.3**, are based on the low-power microcontroller MSP430G2553 [MSPa] and the operational amplifier OPA320S [OPA3] for the analog receiver front end. The power is supplied by a compact 3 V lithium CR2032 coin cell. To link conductively or to couple capacitively to the fabric, a header including either a short pin or an electrode is attached on top of the basic module that itself is a spatial assembly of PCB pieces [WMa16].

In transmitter mode, the microcontroller modulates the electric field by switching the signal electrode's potential directly with a single GPIO. As **Figure 3.4** illustrates, the resulting signal contour is a rectangular wave. The individual periods' duty cycles are set according to the modulation scheme introduced below. The internal pin driver enables abrupt edges that are essential for the proposed transmission principle and result in distinct peaks of displacement current. Due to the negligible load of the intrinsic electrode capacitance (**Sections 3.1.2** and **3.4**), no external driver stage is necessary.

In receiver mode, the transmit pin is configured as input, resulting in a high-Z input impedance ($Z_{\text{gpio}} \geq 60\,\text{M}\Omega$, $I_{\text{leak}} \leq 50\,\text{nA}$ [MSPa]) that does not noticeably impede with the delicate signal. The displacement current that arises between the electrodes, induced through the varying electric field of the body, is then transformed into a voltage signal using a transimpedance amplifier (TIA) with low input impedance. The applied measurement principle results in an output signal representing the charging and discharging current peaks of the electrodes at the rising and falling edges of the rectangular waveform. To enable the detection of both positive and negative amplitudes, the input is biased and set to half the supply voltage through a buffered voltage divider, thus shifting the operating point to half of the amplitude swing. The amplification factor is simply given through $\frac{V_{\text{out}}}{I_{\text{in}}} = -R_{\text{f}}$ and corresponds to the value of the resistor R_{f} in the feedback network. The frequency response is adjusted with an additional capacitor in the input line to suppress low frequencies in the order of the mains supply. The circuit therefore resembles an active, 1^{st}-order inverting BP filter (**Figure A.5**). The transformed and amplified voltage signal V_{out} is more robust and hence easier to process than the delicate displacement current at the input I_{in}. It is forwarded to a Schmitt trigger circuit (**Figure A.6**) that recovers the original rectangular pulse wave by detecting the positive and negative peaks associated with the rising and falling edges.

The components have been chosen to achieve a high energy efficiency. To transmit signals, the microcontroller selects a medium clock frequency f_{c} of 8 MHz, whereas the whole receiver block, including the operational amplifiers, is turned off. In receiver mode, it is turned on, and during the reception of data the microcontroller activates the maximum f_{c} of 16 MHz. This performance is required to provide a sufficiently high timer resolution for the capturing of precise timestamps and to demodulate the incoming signals by executing the sophisticated state machine, detailed in the following Section. In contrast to most radio communication modules, the circuit is thus dissipating less energy in transmit than in receiver mode, due to the higher consumption of the analog circuits, also the quiescent currents I_{q} in idle, and the microcontroller's high-performance mode.

Modulation Scheme

In IBC usually standard modulation schemes from radio communication or RFID / NFC are applied. However, these are not directly applicable to capacitive coupling and do not take into account the different channel properties, such as a lower frequency domain and a broad bandwidth available. While most ambient noise is excluded, shielded through the conductive textile, resembling a Faraday cage, conventional modulation schemes tend to use large symbols and extensive techniques to provide a certain level of robustness against such interference from the surroundings.

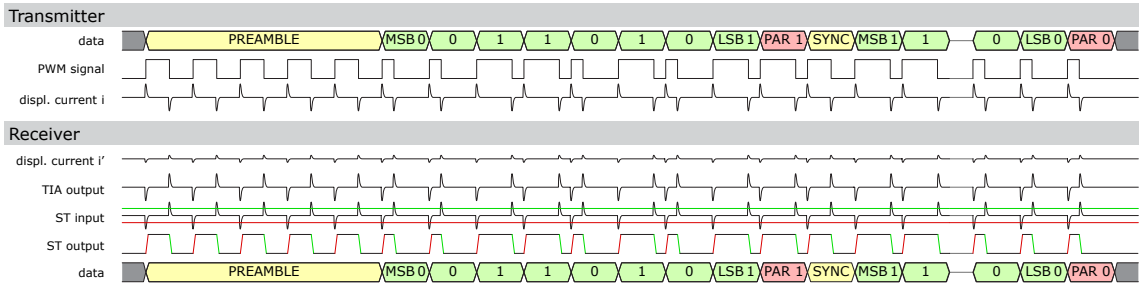

Figure 3.4: Communication with the stepwise transfer of information from the transmitter to the receiver. Top: Signal modulation at the transmitter and the resulting displacement current i in the tissues. Bottom: The weak displacement current i' among the receiver electrodes, detection, amplification, and filtering at the transimpedance amplifier (TIA), reconstruction at the Schmitt trigger (ST), with hysteresis of a threshold for rising and falling edges. **[C17]**

The proposed modulation scheme is inspired by and based on [MAK15] which introduced a PWM scheme representing the binary values with the two duty cycles 25 % and 75 %. Due to the IBC channel's HP characteristic (**Section 3.1.2**), the signal's DC part gets lost. The desired information is, however, still present in the zero-crossings. The proposed method LP filters the recovered pulse wave to extract the information by sampling the analog mean. Due to the analog filter's slow step response, several pulses of the same duty cycle are representing each symbol and binary value.

The adopted scheme improves this inefficiency by applying a digital demodulation technique that directly takes the information from the duty cycles. The microcontroller's internal timer captures the time elapsed to calculate the pulse width and stores these values in a ring buffer. Afterwards, the pulse widths are converted into the corresponding binary values within the main routine. In addition, a third duty cycle of 50 % is introduced to enable the continuous calibration and byte synchronization. As illustrated in **Figure 3.4**, the preamble consists of multiple pulses to define a reference value. Each data bit is then represented by a singular pulse of either 25 % or 75 % duty cycle, while every byte, followed by a parity bit, is again separated by a 50 % pulse. This one, as well as the preamble of several 50 % pulses, is used to synchronize the bit stream and to recalibrate the bit interpretation threshold of the demodulation. As presented in a later case study (**Section 3.5**), the preamble can also be leveraged to wake up a receiver circuit from a low-power sleep mode.

3.2.2 Evaluation

The advantages and performance of the proposed concept have been evaluated in multiple experiments. While the transmitter part is not crucial, the receiver block consists of two critical parts which decide on and limit the maximum performance: **a)** the analog input stage with its certain transmission behavior and **b)** the microcontroller that is hosting the demodulation routine.

Analog Input Stage

The circuit shows sufficient performance to process fundamental frequencies f_0 up to 1 MHz while suppressing noise and DC disturbances. However, the small slew rate of the low-power operational amplifier (10 V/µs) chamfers the abrupt slopes and narrows the

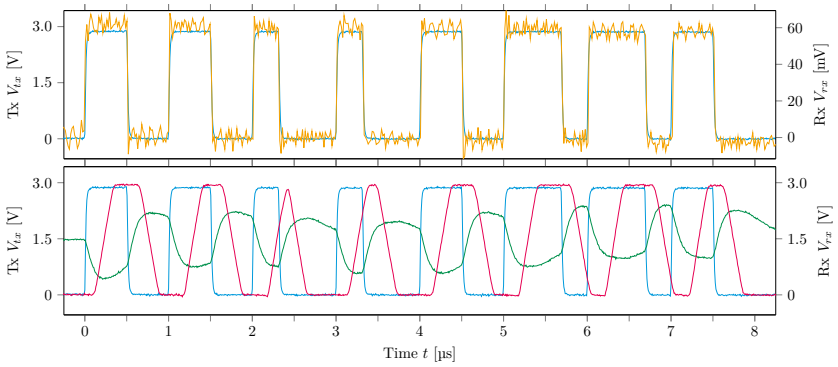

(a) Direct coupling.

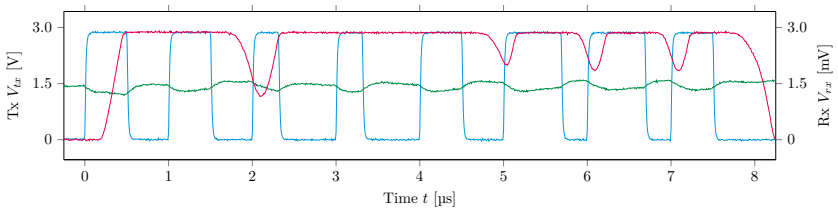

(b) Weak coupling.

Figure 3.5: (a) Direct coupling signal electrodes without air gap, battery-powered transmitter and receiver, notebook-battery-powered oscilloscope for data logging, separated potentials. Original transmitter signal with f_0 of 1 MHz and 3 V (blue), received 60 mV signal (yellow), transimpedance amplifier (TIA) output (green), Schmitt trigger output (red). **(b)** Weak coupling, air gap of about 3 cm, insufficient signal amplitude after TIA (green). Thresholds reached too late to raise or sink output punctually with available slew rate of operational amplifier. Only insufficient notches or entirely ignored pulses. **[C17]**

rectangular pulses considerably (**Figure 3.5a**), which no longer shape a trapezoid but a wedge with lowered amplitude. Therefore, the output of the Schmitt trigger is not ideal but the threshold of the microcontroller input is low enough to cope with that. The widths of the recovered pulses are discriminable and the actual 50 % reference value is recalibrated continuously. In case of weak coupling (**Figure 3.5b**), the current peaks become too flat, too close to the thresholds, and pulse recovery is not successful.

Digital Demodulation

The maximum f_c of 16 MHz determines the resolution of the pulse width capturing. Therefore, the captured values are relatively small compared to the counter register size. The ratio of deviation to pulse width is gaining, thus jitter and interference have an increasing impact. Consequently, the demodulation performance is limited (**Figure 3.6**). Beyond a f_0 of 250 kHz, the Nyquist-Shannon sampling theorem [Sha49] is violated and the readings tend to be imprecise, inaccurate, or even incorrect. Moreover, the capture interrupt on the falling edge of the pulse needs a certain number of cycles to execute the interrupt service routine (ISR) and to store the difference of the two captured values, of rising and falling edge, into the ring buffer. The demodulating state machine is tweaked to a maximum performance but is, nevertheless, limiting the maximum pulse frequency possible. The incoming readings need to be processed and converted into binary data before the ring buffer is full or even overwriting earlier, unprocessed positions. Due to the shielding of ambient noise sources, the unsuccessful capturing of higher pulse frequencies is, therefore, likely caused by the too slow ISR.

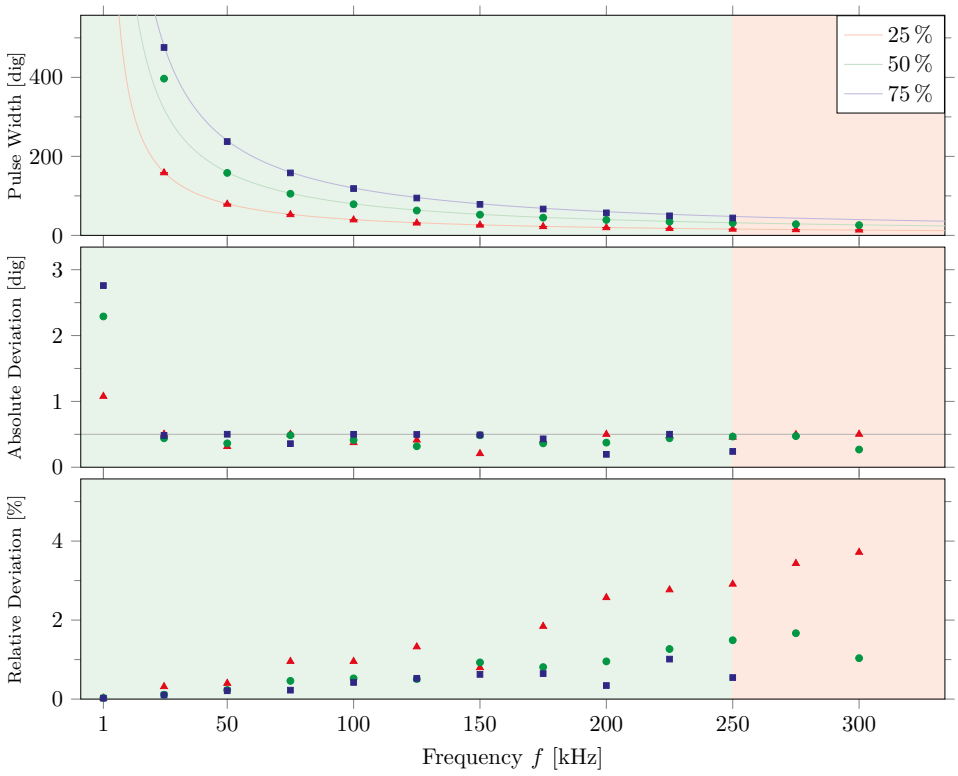

Figure 3.6: Captured pulse widths and deviation of duty cycles 25 %, 50 %, 75 % (red, green, blue), and modulation frequency f_0 of 1 to 300 kHz. Green area: Successful and reliable pulse width measurement. Red area: Eratic pulse width measurement. Top: Timer values of the captured pulse widths (blurred: ideal course). Middle: Absolute standard deviation, quickly converging to 0.5 of quantization noise. Bottom: Relative standard deviation of the pulse width error in % (desired vs. actual pulse width). **[C17]**

Transmission Range

Because the prototype is based on a simple, unsophisticated front-end circuit, it enables only naive close coupling [WMa16]. Placing two modules close to each other at a distance of about 0.5 cm, a wireless link can be established via near-field coupling through air. With a shared potential, e.g. by means of connecting the modules' local ground potentials, even a wider range of 10 cm is possible. Attaching the modules' signal electrodes additionally to the human body enables to easily detect an output signals with an amplitude of about 1.85 V throughout the entire body. However, without the common potential, and hence establishing the return path through direct coupling, the range drops to about 3 cm. Adding the conductive fabric, the signal amplitude of about 190 mV remains significantly smaller, but sufficient to extend the range and to enable a distance-independent signal transmission over at least 30 cm, solely limited by the sleeve's length.

Power Consumption

The power consumption is measured for a reference signal of 250 kHz with 50 % duty cycle, either being generated or demodulated. In transmitter mode, with the f_c of 8 MHz selected, this resulted in an average power consumption of 7.6 mW (2.5 mA) and in receiver mode, with a f_c of 16 MHz and an enabled analog front-end, in 18.9 mW (6.3 mA).

3.2.3 Results

The presented approach enables to reliably transmit data across the user's body using capacitive coupling. An additional layer of conductive clothing is used to extend the range of near-field coupling by providing a stable reference potential and reliable, nearby feedback path that results in a significantly lower channel loss and a negligible interference level. The implementation effort of the transceiver modules is considerably lowered, since neither LC tank circuits, to boost the transmitter's amplitude, nor complex filters, to extract data from a noisy signal, are needed. The prototype demonstrates the successful signal transmission and allows for the evaluation of communication between wrist and upper arm. The applied PWM scheme is based on three duty cycles to not only represent and encode the binary values, but also to continuously recalibrate the symbols, and to synchronize the bit stream of up to 200 kbps, applying a f_0 of 250 kHz. The evaluation proved that the approach is feasible and especially suited for applications in which sensor nodes are placed on the body surface. The reception (18.9 mW) demands for more power than the transmission (7.6 mW) because of the higher clock frequency of the microcontroller and the I_q of the dissipative AFE. Due to the obligatory conductive fabric layer, the design suits especially applications which utilize any kind of functional clothing, vest, or all-in-one suit. The star topology is applicable and would allow sensor nodes to forward their measurements to a hub or gateway module in the center, which then would also provide the common reference potential.

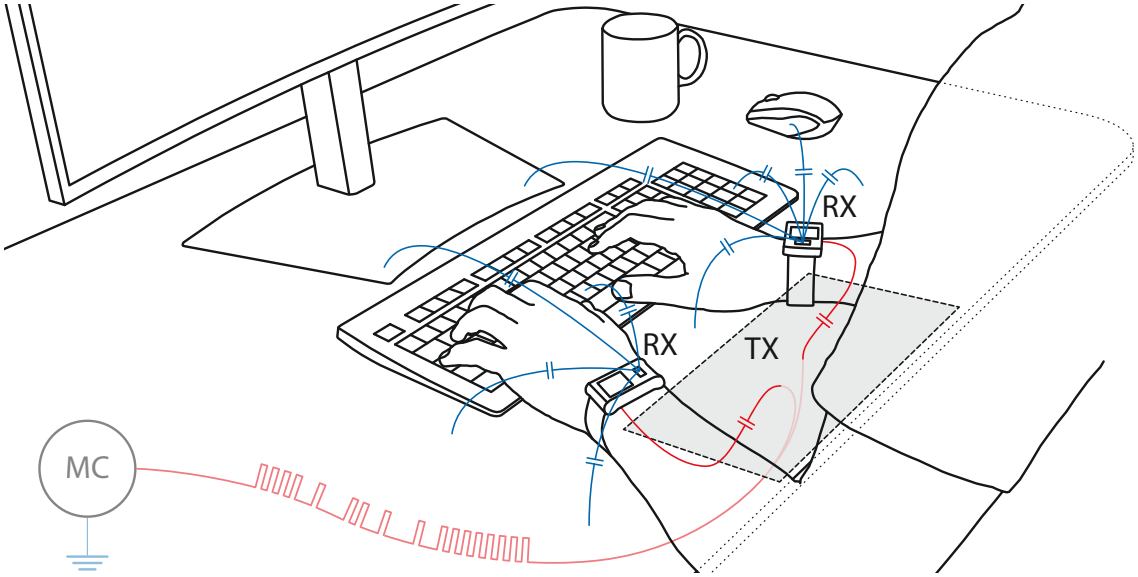

Figure 3.7: Exemplary scenario for the contextualization of wearable devices: microcontroller (MC) with transmitter electrode (TX) embedded into a desktop; information implicitly and incidentally provided to two sensing devices (RX) worn at the wrists; artificial landmark signal (red), capacitively induced into the human body; detection by means of repurposed analog ECG sensor front-ends; weak return paths (blue) to close the circuit; MC is grounded via environment, the earth ground. **[C21b; J22b]**

3.3 Case Study 2: ECG Sensor Front-Ends

One main feature of modern wearables is the monitoring of vital signs. To provide medical-grade HR readings, commercial devices provide an ECG sensor that is not only very sensitive but also optimized for ULP applications. This case study **[C21b; J22b]** follows the idea of "Your noise is my signal" [Abo12] and repurposes the single-lead ECG sensor, integrated in recent off-the-shelf wearables, to detect artificial landmark signals. Those are either consciously or implicitly and incidentally induced into the user's skin by touching, approaching, or passing certain areas, surfaces, or objects with embedded beacons. In close proximity, the signals are capacitively induced into the skin and propagate in the tissue as harmless displacement currents. This way, landmarks are made available throughout the entire body surface, which serves as a confined transmission medium that turned out to be more efficient than air. Considering the limitations of the ECG AFE, a suitable modulation scheme is presented and a signal processing pipeline for the landmark detection and demodulation is evaluated. To substantiate the method's general feasibility, a possible application is demonstrated that enriches the landmark signal with the situational context (**Section 3.3.2**) of the measurements taken, thus providing information about the readings through the ECG sensor channel. In a similar way, the landmark signals are leveraged to implement the second implicit synchronization method IBSync in **Section 4.4**.

It is important to consider that the presented technique is not intended to compete with cutting-edge research in IBC, especially not in terms of data throughput and efficiency. Instead, the use of accessible, commercially available devices is intended to pave the way for applications that, when finally made available, can directly be translated to future single-chip solutions, specifically designed for IBC.

3.3.1 Situational Context

In the late 20$^{\text{th}}$ century, research in human-computer interaction (HCI) aimed at "seamlessly bridging the gulf between physical and virtual worlds" [Wan+99]. First commercial approaches used wireless technology such as Bluetooth for the privacy-preserving distribution of electronic coupons [Zha+11]. Running as smartphone applications, commercial platforms such as LinkedIn and Facebook leverage the "mutual discovery and information exchange" to suggest people for networking or to make friends on weekends [LS14].

Also the interest of psychologists in experience sampling motivated computer-assisted methods to replace the traditional pen-and-paper procedures and to get a "window into [a user's] daily experience and behavior" [BB01]. Such approaches require, however, the reliable classification of activities of daily living (ADL) and the unobtrusive detection of interactions with objects [Phi+04]. With the emergence of micro electro-mechanical systems (MEMS), accelerometers and inertial measurement units (IMUs) became not only affordable but also very popular instruments. Since then, wearable sensing devices are commonly applied for the classification of signal patterns in HAR, the recognition of activities from limited sets, but the obtained information is often not rich enough to distinguish similar activities that show ambiguous, confusable signal patterns [Ber+10].

The knowledge of the object grasped [Ber+10] can, however, help to classify activities, to interpret interactions, and to "reason on the intention of the user" [Sch00]. This knowledge allows the interpretation of the way objects are used, and can, moreover, help to minimize the labeling efforts [Wan+07]. In course of this development, Schmidt et al. [SGM00] introduced in 2000 the term implicit HCI which describes "a shift [...] from explicit interaction [...] towards a more implicit interaction based on situational context". Accordingly, not only the location but especially the awareness of the situational context brings advantages in the interpretation of observations and the inference of sensor signals.

Toward this concept, different projects aimed to identify the objects grasped to support the more reliable and precise classification of activities. First approaches used barcodes to tag objects [SDH03]. Following research used radio-frequency identification (radio-frequency identification (RFID)) tags instead, attached to certain objects, tools, or even the environment, e.g. at a doorknob [Ber+10]. Different wearable setups then combined inertial sensors for activity recognition and RFID readers to simultaneously detect the objects' tags. The yet wired and bulky prototype of [Sch00] allowed to trigger different applications by handling tagged objects, read through a coil sewn into a work glove. The lighter iGlove in [Phi+04] used a reader coil in the palm while the iBracelet in [FPR05] as well as the prototype of [Ber+10] applied a PCB coil worn around the wrist instead. Most RFID tags are passive and receive the energy, required for data transmission, from the reader coil through electromagnetic induction, so no battery is needed. The reader requires, however, a coil with a certain quality for a long range, which normally is not available in commercial wearables. As presented in the remainder of this Section, the use of ECG sensors for the detection of unique object identifiers, continuously provided by long-lasting active beacons, might hence be a promising alternative.

3.3.2 System Design

The exemplary scenario, tested in scope of this case study, is illustrated in **Figure 3.7**. It consists of a transmitter beacon, embedded into a desktop, and two off-the-shelf wearable devices with integrated ECG sensor front-end, repurposed as the receiver for the artificial landmark signals. In the following Sections, the used hardware, modulation scheme, signal processing pipeline, and proposed applications are described.

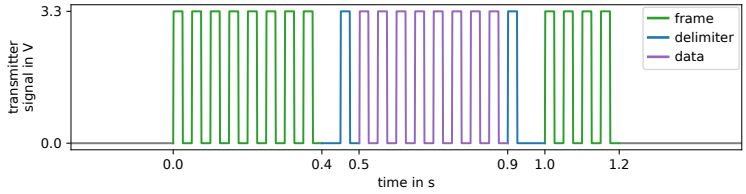

Figure 3.8: Simulated, synthetic illustration of a single landmark packet at the transmitter: 8 pulses preamble (green), gap and pulse as delimiter (blue), 8 pulses or gaps to encode the data in OOK scheme (violet) with the MSB first, pulse and gap as delimiter (blue), and 4 pulses terminator (green). Modulation frequency f_0 of 20 Hz. **[J22b]**

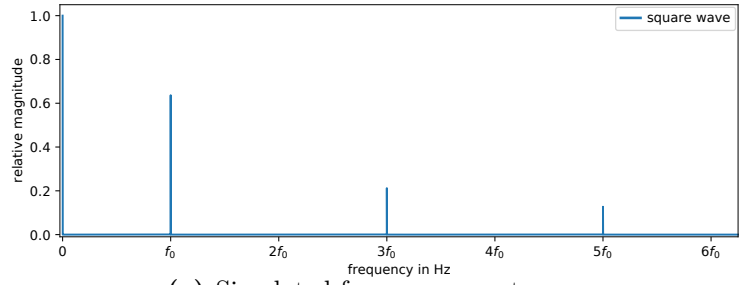

(a) Simulated frequency spectrum.

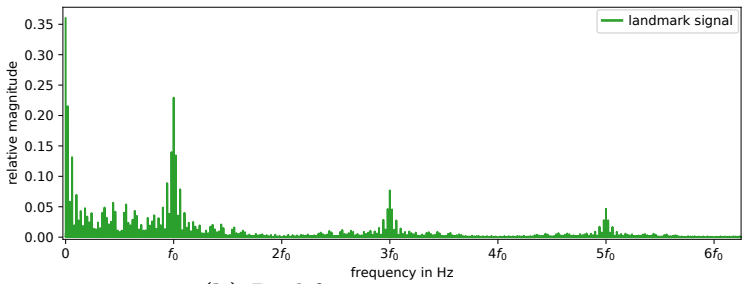

(b) Real frequency spectrum.

Figure 3.9: (a) Simulated, synthetic frequency spectra of an ideal, continuous square wave with f_0 of 20 Hz and 50 % duty cycle (blue) and **(b)** a landmark signal with 2.5 s intervals, 1.2 s active period, and an incrementing 8 bit data segment (green). In both cases, the even harmonics of f_0 are zero. For the discontinuous landmark signal, the spectrum spreads around the odd multiples of f_0. The energy contained in the DC component at 0 as well as in f_0 and its harmonics decreases considerably (note the y axes). **[J22b]**

Stationary Transmitter Beacon

In order to easily assemble and deploy beacons at a larger scale, the transmitter circuit is kept simple. The GPIO pin of a conventional MSP430FR5969 [MSPb] microcontroller directly drives the signal electrode and hence modulates its surrounding quasi-static electric field. Unlike for antennas in RF, there are no special requirements on the electrode since low frequencies are applied [Fin10; Gro+14]. It is made from metal foil and has a relatively large size of $16 \times 32\,\mathrm{cm}^2$ to provide a sufficiently wide contact face. The scenario in **Figure 3.7** shows the electrode fixed under the front edge of a conventional desktop. It is intended to couple to the user's arms through a 1.5 cm plate of wood and plastic.

A second ground electrode, to close the channel circuit, is not required since the beacon is supplied by and hence grounded through a USB link to a computer, in turn connected to mains. This way, the environment serves as a large, virtual ground electrode and only a single excitation electrode is required at the transmitter. As previously mentioned

in **Section 3.1.2**, cutting the beacon's link to earth ground would largely affect the simplified setting, considerably attenuate the signal amplitude, and hence degrade the SNR at the receiver. In case of both devices floating, the transmitter as well as the receiver, the received signal amplitude would considerably be attenuated by typically 45 – 55 dB [Gro+17; NMS20]. Keeping the transmitter grounded, therefore, has the advantage that no additional power amplification stage is required, to boost the transmitter's output amplitude to tens of V as done in the original approach [Zim95].

To ensure a precise timing, the computer is also employed to regularly, every 2.5 s, instruct the microcontroller to send a landmark signal through the electrode. In future scenarios, however, this task could independently be performed by the microcontroller itself. Precise timing could then be obtained from a high-quality real-time clock (**Section 4.1**) or, even absolute time, from the internet.

Signal Modulation

To generate the landmark signal, a pulse train of a certain pattern is generated by toggling the GPIO pin between 0 and 3.3 V. As reasoned below in **Section 3.3.3.1**, the applied modulation frequency f_0 is tuned to 20 Hz. **Figure 3.8** illustrates the applied scheme for a single landmark packet. Each packet consists of eight pulses as a preamble, one gap and one pulse as delimiter, eight pulses or gaps as symbols to represent the 8 bit of data, again one pulse and one gap as delimiter, and finally four pulses as a terminator. The preamble, terminator, and two delimiters form a constant packet frame which embraces the variable data segment. As usual, the data byte is transferred with the MSB first.

Figure 3.13 illustrates that the generation and transmission of rectangular waves is not ideal in terms of bandwidth and efficiency since the energy spreads in a wide frequency band and the effective signal magnitude within the desired band decreases considerably. Nevertheless, the on-off-keying (OOK) modulation scheme is reasonable since it is simple and easy to implement with a conventional, cheap, and low-power microcontroller.

When coupling to the user's body, the beacon capacitively modulates the quasi-electrostatic field (**Section 3.1.2**) and induces a harmless displacement current in the order of pA [Tom+19]. Due to the body's transmission characteristics and the applied preprocessing at the receivers (**Section 3.3.2**), the rectangular wave is detrended and smoothed. This way, it shows a rounded, quasi-sinusoidal wave, centered at the baseline (**Figure 3.15**).

Wearable Receiver

There exist no commercial IBC transceiver modules yet. Therefore, the study is based on the AFE of the single-lead ECG sensors available in recent wearable devices such as smartwatches or fitness trackers. These AFEs offer themselves to be repurposed for the detection of artificial landmark signals since they are carefully designed with regard to both energy efficiency and the sensitive detection of tiny potential differences.

Two off-the-shelf MAXREFDES101# [MAX1b] devices have been employed to conduct the experiments. The reference designs have the shape of a wristwatch and, besides IMU, PPG, and body temperature sensors, they include an AFE for bio-impedance and biopotential measurements, thus enabling ECG monitoring as well as the proposed approach. The devices grant access to the sensor configuration, the source code of their firmware, and the raw measurements. The on-board MAX30001 [MAX3] AFE draws only 95 µA at 1.8 V while providing both, a very high $Z_{\text{in}} > 1\,\text{G}\Omega$ and a CMRR > 100 dB. This way, it enables the unloaded detection of the tiny voltage drop that is caused by the displacement current between the electrodes. Sampled at a rate f_s of 128 Hz, the raw measurements can directly be recorded to the 32 MB flash memory.

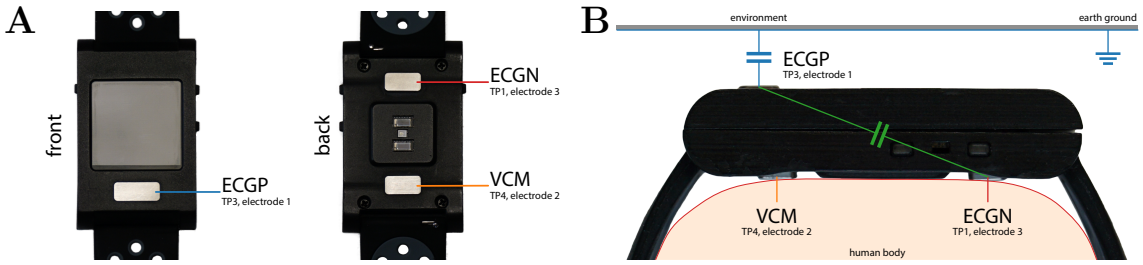

Figure 3.10: (**A**) The ECG sensing device MAXREFDES101# [MAX1b] has three electrodes on its casing: a positive input (ECGP) at the front, a negative input (ECGN) and a body bias (VCM) at the back; (**B**) The detection of the artificial landmark signals according to the capacitive coupling principle for IBC: ECGP and ECGN resemble a parallel plate capacitor (green); ECGN directly couples to the human body (red); ECGP is floating, weakly coupling to the environment to close the circuit (blue). VCM is applied to establish a DRL circuit and improve the CMRR (orange). **[J22b]**

As illustrated in **Figure 3.10**, the devices' casing shows three electrodes of which two virtually form the parallel plate capacitor required for capacitive coupling in the proposed application. The positive input of an ECG sensor AFE (ECGP) at the front is kept floating and is intended to couple to the environment. The negative input of an ECG sensor AFE (ECGN) at the back directly couples to the body and enables the measurement of the potential difference in reference to ECGP at the front. Labeled in the datasheet as body bias, the third electrode VCM serves as a driven-right-leg (DRL) circuit (**Section 2.1.1**) to improve the CMRR. Its activation connects the body through a 499 kΩ resistor [1] to the device's internal common-mode voltage V_{CM} of 0.650 V.

Signal Demodulation

To detect the landmarks, to determine their position in the devices' local time t', and to decode the contained data d, the signal processing pipeline illustrated in **Figure 3.11** is applied. It starts with three 2^{nd}-order ($2 \times 1^{\mathrm{st}}$) IIR filter stages to extract the weak, desired signal. The use of zero-phase forward-backward filters is expedient to preserve the signal's phase, the temporal information of the signal, which is particularly important for the synchronization method IBSync, proposed in **Section 4.4**. First, an anti-aliasing LP filter with a cutoff frequency f_c of 63 Hz $< f_s/2$ below the Nyquist frequency is applied. Then, the power line's humming noise at 50 / 60 Hz is suppressed using a band-stop / notch (BS) filter, to provide an interference-reduced signal (IRS). Centered at the carrier's fundamental frequency f_0 of 20 Hz, the desired frequency band is finally extracted using a BP filter. As evaluated in **Section 3.3.3.2**, the wide bandwidth $B = f_{\mathrm{c,\,high}} - f_{\mathrm{c,\,low}}$ of 20 Hz, i.e. from 10 to 30 Hz, is required to cover the sidebands of the OOK modulation.

After preprocessing, the short-time Fourier transform (STFT) is applied to the IRS, yet before BP filtering, using a von Hann window with a size of 4 s (512 samples) and 75 % overlap (384 samples respectively). Then, analog to the determination of the SNR, the RSSI of each window interval S is derived from the STFT. It is computed according to **Equation (3.2)** by averaging the bins associated with the signal core $A_{\mathrm{signal}} = \overline{b_s}$ with $b_s \in \langle 17.5, \ldots, f_0, \ldots, 22.5\,\mathrm{Hz} \rangle$ and the adjacent bins of in-band noise $A_{\mathrm{noise}} = \overline{b_{\mathrm{n}}}$ with

[1] The datasheet of the MAX30001 [MAX3, p. 31] mentions a 200 kΩ resistor while the schematic files of the MAXREFDES101# [MAX1b] specify a value for R7 of 499 kΩ.

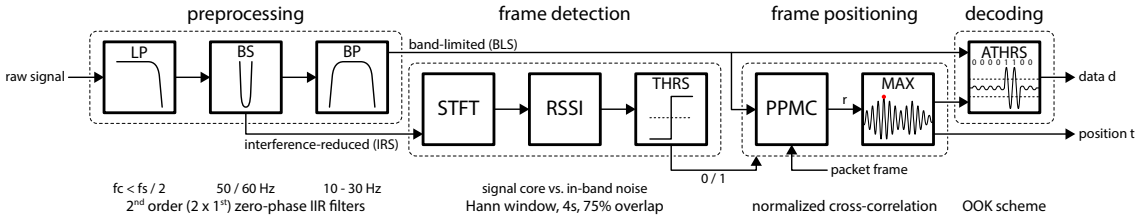

Figure 3.11: The processing pipeline consists of four blocks: signal preprocessing, frame detection, frame positioning, and data decoding. First, the raw, noisy signal is filtered. While the band-limited signal (BLS) is forwarded to the frame positioning, the less preprocessed, interference-reduced signal (IRS) is provided to the frame detection block. It inspects the frequency components using a STFT and assesses the signal quality applying the received signal strength indicator (RSSI). If the RSSI heuristic exceeds a certain threshold (THRS), the landmarks' temporal position t is determined within the relevant interval using a PPMC. The data d is decoded according to an OOK modulation scheme applying an adaptive threshold (ATHRS) mechanism. **[J22b]**

$b_\mathrm{n} \in \langle 10, \ldots, 17.5\,\mathrm{Hz} \langle \cap \rangle 22.5, \ldots, 30\,\mathrm{Hz} \rangle$:

$$\mathrm{RSSI}_\mathrm{dB} \;=\; 20\, log_{10} \left(\frac{A_\mathrm{signal}}{A_\mathrm{noise}} \right) \tag{3.2}$$

The RSSI is a measure of the desired signal's predominance over the noise floor. It is applied as a heuristic to identify the characteristic frequency components around f_0, which are associated with the presence of a landmark frame (**Figure 3.8** and **3.13B**). The subsequent steps are only continued if the RSSI exceeds a significance threshold (THRS), i.e. at least the minimum of 0 dB. Next, a universal frame template F with empty data segment $d = 0$ is shifted along the relevant window interval S and inspected using the Pearson product-moment correlation (PPMC) coefficient $r(S, F)$ [Pea95]:

$$r(S,F) \;:=\; \frac{\sum_i (s_i - \overline{S})(f_i - \overline{F})}{\sqrt{\sum_i (s_i - \overline{S})^2 \sum_i (f_i - \overline{F})^2}} \tag{3.3}$$

The significant and maximum correlation (MAX) between the template F and S unveils the frame's temporal position t'. The data d are finally extracted by decoding the interval according to the OOK scheme using an adaptive threshold (ATHRS). Its level orientates on the amplitude of the frame's preamble and terminator, to distinguish the pulses from the gaps and, therefore, to assign the symbols to the binary values 0 and 1. Depending on the target application, the frame position t' and the contained data d are then used to either contextualize the measurements or to synchronize devices as proposed in **Section 4.4**.

Contextualization

This case study makes use of the human body as a unidirectional communication channel between stationary transmitters and body-attached devices. This way, the body tissues enable the wearables to receive artificial signals by simply touching, approaching, or passing beacons, embedded into certain areas, surfaces, or objects. These landmarks can be enriched with temporal information to enable the alignment and synchronization of recordings (**Section 4.4**) or can be enriched with information about the situational context (**Section 3.3.2**), such as the type of object touched. The fundamental principle of capacitive coupling for IBC hence enables either the intentional and continuous, or the

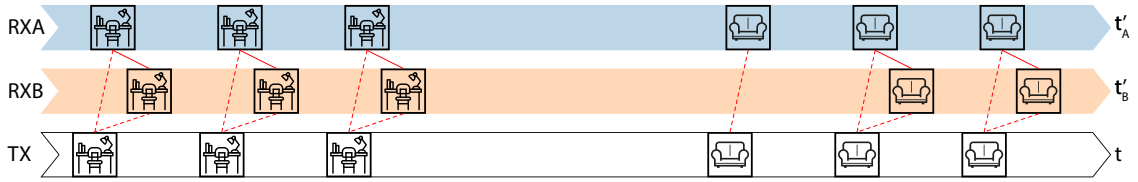

Figure 3.12: Illustration of the proposed application that enriches the landmark signal with unique location or object identifier (icons), transported in the data segment (8 bit), to provide the situational context to wearables. The landmarks are transmitted by beacons (TX), enabling the receiving devices (RX) to contextualize their recordings. **[J22b]**

implicit and incidental reception of contextual information by means of the detected landmarks. Motivated through **Figure 3.7**, the scenario to be evaluated and discussed uses a transmitter beacon, embedded into a desktop, and two wrist-worn receivers.

To provide context information, the landmarks' 8 bit of data serve as a context identifier and can be associated with up to 256 areas, surfaces, or objects, illustrated in **Figure 3.12**. The exemplary scenario in **Figure 3.7** shows the transmitter beacon embedded into a desktop. Consequently, the receiving wearable devices would get aware of the user being close to and probably sitting at the desktop, likely to work on the computer. The motion and the user's vital signs, and hence e.g. inferable arousal and stress, could now be interpreted in the context of work. In contrast, e.g. sitting on the couch would indicate the user's leisure and intention to relax.

3.3.3 Evaluation

Three experiments have been conducted to first optimize the filter parameters, and then evaluate the performance and demonstrate the approach's applicability. The first experiment (**Section 3.3.3.1**) aims to determine the characteristic noise floor, caught from a typical environment, to dimension carrier frequency f_0, and to identify the applicable frequency band. The second experiment (**Section 3.3.3.2**) concentrates on the technical aspects of optimal bandwidth B, the heuristic RSSI, the metric PPMC r, and the resulting packet error rate (PER). Finally, the third experiment (**Section 3.3.3.3**) demonstrates the applicability in an everyday life usage scenario. Due to the COVID-19 pandemic, the evaluation is based only on a single subject (male, 33 yr., 198 cm, 102 kg), however with 215 min recordings from two wearable devices, attached to the left and right wrist, in a typical scenario with a desk in an ordinary living space.

3.3.3.1 Noise Floor Characterization

The normal use of the wearables' AFE according to their original purpose, the measurement of the natural ECG signal (**Section 2.1.1**), requires a finger from the opposite arm to form the traditional lead I (**Figure 3.13A**). Without closing this circuit, the floating sensor predominantly catches noise from the environment and the ECG signal vanishes in the noise floor (**Figure 3.13B**).

For the new purpose of detecting the artificial landmark signals, the most suitable modulation frequency f_0 and possible bandwidth B needs to be determined first. To estimate the present noise floor, measurements in an ordinary living space have been recorded, performing seven different activities such as sitting, working on a computer, walking, and doing different gymnastics for 60 s each. **Figure 3.14A** shows the respective Welch periodograms [Wel67] for power spectral density (PSD) estimation (**Section 2.4.2**). The spectra indicate that the frequency band from about 10 to 45 Hz would be applicable.

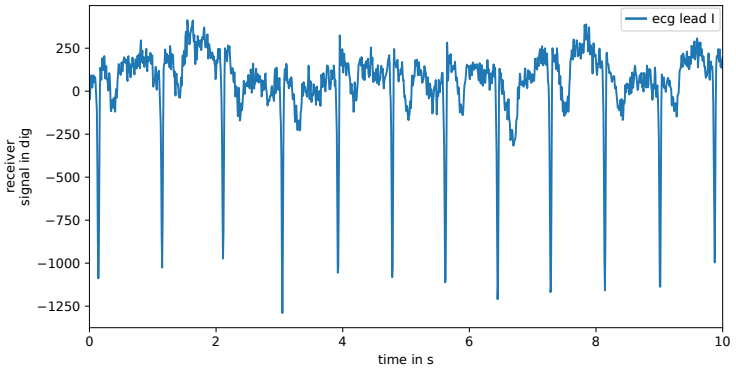

(a) Detected ECG signal through closed lead I.

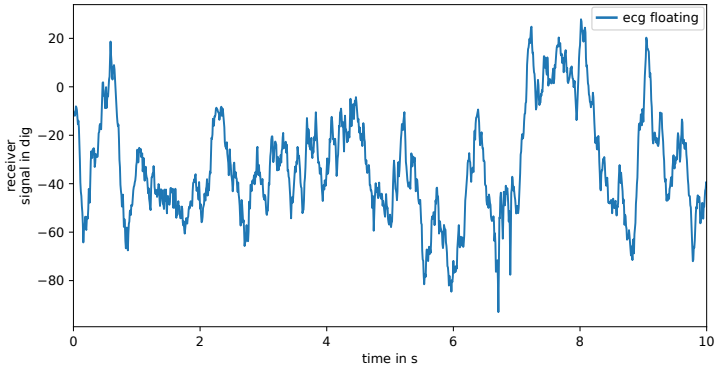

(b) Floating electrode.

Figure 3.13: Excerpts from raw measurements of the MAXREFDES101# [MAX1b] ECG sensing device: **(a)** Touching the ECGP electrode at the front closes the traditional lead I and results in visible, distinct yet possibly inverted R peaks; **(b)** For a floating electrode, the pulses vanish into the noise floor and the heart beat can only be guessed. **[J22b]**

Unfortunately, the possible band is sporadically interfered by oscillations at about 15 Hz, accompanied by harmonics at 30 and 45 Hz. The origin of this interference is not evident but might either be induced from the environment or the device itself. Because it is very specific to the device worn on the right wrist, it could come from resonance due to filter instability and the absence of the ECG signal sought, or a defect of the circuits.

While the HP characteristic of the body channel favors a higher f_0 in the order of a few MHz, the sensor's sampling rate f_s of 128 Hz, and hence a Nyquist frequency of 64 Hz, demands for a lower f_0 to increase the sample coverage $N_s = f_s/f_0$ of a unit pulse period $T_0 = 1/f_0$. Therefore, as shown in **Figure 3.14B**, a trade-off is made on an f_0 of 20 Hz, resulting in 6.4 samples scanning a 50 ms pulse period. The determination of the optimal B is detailed below in **Section 3.3.3.2**.

3.3.3.2 Controlled Setting

To evaluate the approach from a technical perspective, three specific ways of coupling between the user and the transmitter have been investigated: **a)** directly touching the transmitter electrode, **b)** touching the desktop surface above the electrode with both hands, and **c)** sitting at the desktop without touching the electrode and leaning back in the office chair. The actions have been recorded consecutively, with each interval spanning at least 15 min. The interval of **a)** covers 379 landmarks (15.8 min) with 6585 pulses and 2511 gaps, **b)** covers 377 landmarks (15.7 min) with 6619 pulses and 2429 gaps, and **c)**

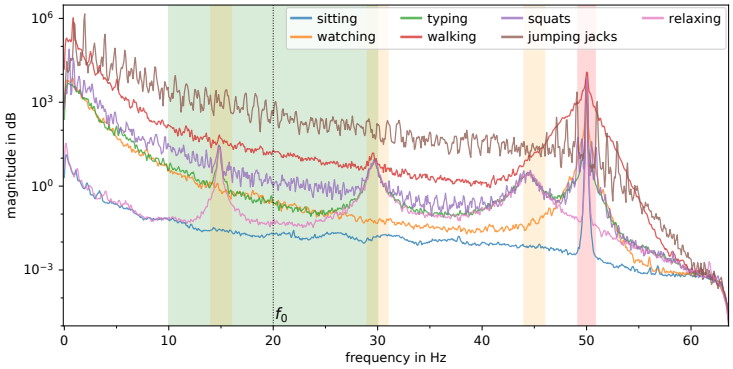

(a) Noise floor.

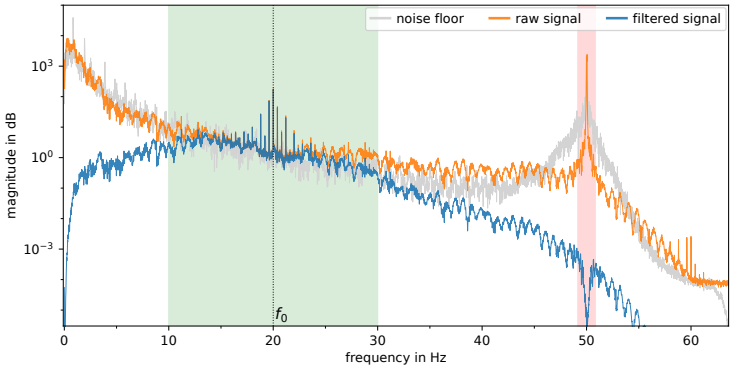

(b) Desired signal.

Figure 3.14: (a) Analysis of the frequency spectra (PSD) of the noise floor: interference generated by seven activities; 50 Hz power line noise (red); unknown interference source, oscillation at 15 Hz with its first and second harmonics (orange); **(b)** Analysis of the frequency spectra (PSD) of the desired signal extracted from the raw measurements: Noise floor, overall average of the activities (grey); raw signal (orange); filtered signal (blue); selected bandwidth B of 20 Hz, pass-band from 10 to 30 Hz (green). **[C21b; J22b]**

covers 389 landmarks (16.2 min) with 6811 pulses and 2525 gaps. For each interval, the pulses and gaps have semi-automatically been annotated in the IRS and manually been revised and validated. The results from this setting are summarized in **Table A.1**.

Optimal Filter Bandwidth

To be able to adequately reconstruct the discontinuous pulse wave, the filter pass-band is required to cover the sidebands of the modulation, adjacent to the carrier f_0. These frequency components allow for a fast transient response, the change between the two symbols pulse and gap representing the binary values 1 and 0. As shown in **Figure 3.15**, the filter bandwidth B considerably affects not only the shape of the particular pulses but also the signal's envelope contour and the remaining ripple within the gaps. Therefore, the optimal B has been discovered through 399 filter configurations, by applying the bandwidths $\{0.1\,\text{Hz}, \ldots, 39.9\,\text{Hz}\}$ at steps of 0.1 Hz, centered at the previously specified f_0 of 20 Hz. Since the right wrist's recordings are considerably interfered from an unknown noise source (**Section 3.3.3.1**), only the results from the left wrist are further evaluated here. For each way of coupling and each configuration, the pulse heights p and the gap ripple $|g|$, the absolute distance to the baseline, have been determined for the labeled positions. After calculating their mean and standard deviation, the ratio $\overline{p}\,/\,\overline{|g|}$ of mean pulse amplitude $\overline{p}$ and mean gap ripple magnitude $\overline{|g|}$ is computed. As illustrated

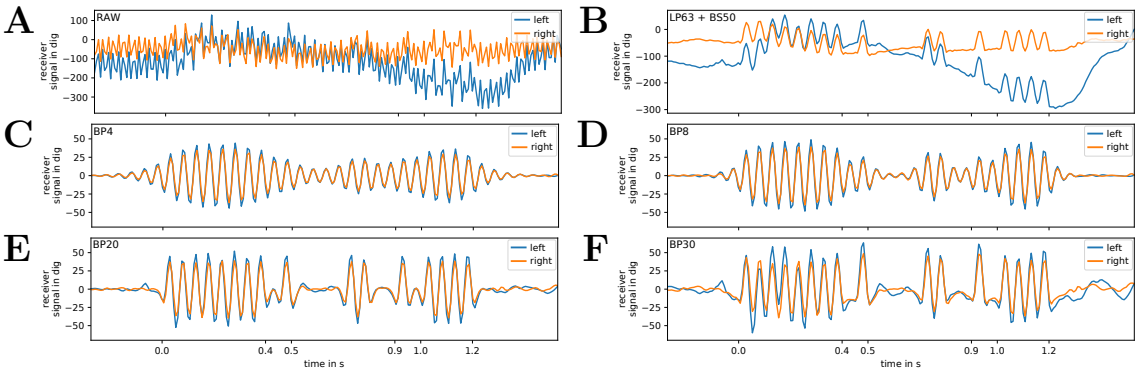

Figure 3.15: Matched landmark packets of two receivers worn at the left (blue) and right wrist (orange). Raw, unfiltered measurements (**A**). IRS after anti-alias filtering (LP) and power line noise rejection (BS) with contained data 00001100_2 (MSB first) visible (**B**). Applied filter bandwidths B of 4 Hz (**C**), 8 Hz (**D**), 20 Hz (**E**), 30 Hz (**F**). Best result regarding fast transient response, pulse-to-gap ratio $\overline{p}\,/\,\overline{|g|}$, as well as minimal interference and baseline wander for a B of 20 Hz (**E**). **[J22b]**

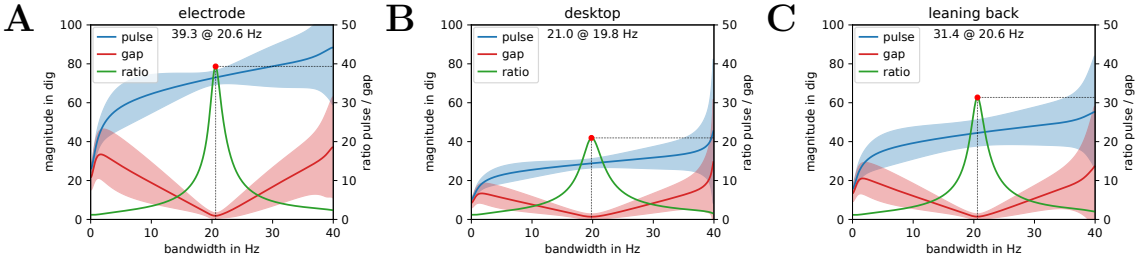

Figure 3.16: Determination of the optimal filter bandwidth B, centered at f_0, for the scenario's three ways of coupling. From 0.1 – 39.9 Hz in steps of 0.1 Hz, 399 iterations each, considering the mean $\overline{p}$ and standard deviation of the pulse amplitudes p (blue), the mean $\overline{|g|}$ and standard deviation of the absolute gap magnitudes $|g|$ (red), the remaining ripple respectively, and the ratio of the means $\overline{p}\,/\,\overline{|g|}$ (green) with the maximum marked (red dot). Best ratio 39.3 dig for 20.6 Hz by directly touching the electrode (**A**), second best 31.4 dig for 20.6 Hz by leaning back (**C**), and lowest 21.0 dig for 19.8 Hz by touching the desktop (**B**). The filter bandwidth B of 20 Hz is, therefore, selected as optimal. Note that, due to considerable interference, the results are based on signals from the left wrist only. **[J22b]**

in **Figure 3.16**, along with a minimal standard deviation among the pulses and gaps, the pulse-to-gap ratio unveils the optimal filter bandwidth B by reaching its maximum at about 20 Hz, which corresponds to f_0 itself, for all three couplings. In the optimal configuration, **a)** showed the best coupling with a pulse-to-gap ratio of 39.3, **b)** showed the weakest coupling with a ratio of 21.0, and **c)** is in between with a ratio of 31.4.

Processing Pipeline

The processing pipeline and its discrete metrics are evaluated applying the determined optimal bandwidth B of 20 Hz. **Figure 3.17** visualizes the output of the consecutive stages. It shows the generated STFT, the derived RSSI, the PPMC coefficient r, and the decoded data d along the entire recording of both devices with the relevant intervals **a)**, **b)**, and **c)**. While the STFT of the device at the left wrist shows a clearly distinguishable signal core, the right sensor again caught the aforementioned oscillation at 15 Hz. Starting at about

900 s it unintentionally demonstrates the effect of in-band noise on the metrics. While the average RSSI at the left wrist is **a)** 23.504 dB, **b)** 21.558 dB, and **c)** 22.945 dB, the signal strength at the right wrist significantly decreases on occurrence of the interference to values of **a)** 21.078 dB (semi-affected), **b)** −4.581 dB, and **c)** 10.841 dB. Nevertheless, r significantly indicates the presence of the landmark signal with an average $\overline{r}$ of 0.835 at the left and a marginally lower value of 0.764 at the right wrist. Despite the presence of noise, the data is successfully decoded for most landmark packets, even though the RSSI is below 0 dB for a certain period. The detection of erroneous landmarks and the relation to the proposed RSSI heuristic is evaluated in the following.

Packet Error Rate

The PER is a measure of the number of landmark packets that have not successfully been detected due to at least one symbol being interfered and hence erroneously detected or missed. It is the quotient $N_{\text{error}} \,/\, N_{\text{total}}$ of erroneous packets N_{error} per total packets sent N_{total}. For the device at the left wrist, the PER of **a)** is virtually 0 since all packets have been decoded correctly. Interval **b)** shows the largest PER of 26.525×10^{-3} with ten errors occurred: five erroneously detected pulses and one missed pulse in the data segment, two times a excessive fifth pulse and once a missed pulse in the terminator, and once an undetected pulse in the preamble. The PER of **c)** is 2.571×10^{-3}, only one packet was erroneous due to a glitch in the data segment. The noise present at the right wrist largely interferes with the landmark signals and hence results not only in considerably decreased RSSI and r, but also in a significantly higher PER of **a)** 23.747×10^{-3} and **b)** 281.167×10^{-3}. However, the coupling of interval **c)** showed with a PER of 0 to be more robust against the noise. In general, there is a manifest link between the RSSI and the PER. However, a low RSSI, even below 0 dB, does not inevitably result in a large PER. The RSSI is, nevertheless, a suitable heuristic, helpful to indicate whether a signal interval likely contains the desired landmark signal and should be further analyzed, or not.

3.3.3.3 Application In-the-Wild

To finally demonstrate the concept's feasibility and its applicability in the wild, the two devices were worn for about 23 min while performing activities of daily living which includes partly working at the desk, equipped with a transmitter beacon (**Figure 3.7**). This way, the recording does neither contain exclusively the desired landmark signal nor the ambient noise, but both varying in an uncontrolled setting.

As in the previous experiment (**Section 3.3.3.2**), the landmarks transport a continuously incrementing 8 bit packet counter which overruns every 640 s. This way, discontinuities in the decoded values indicate packet errors. **Figure 3.18** visualizes the output of the processing pipeline. Again, as in the previous experiment, the oscillation at 15 Hz is visible and starts at about 900 s, immediately decreasing both RSSI and PPMC r. Nevertheless, the landmarks can successfully be decoded when the subject is at the desk and either the arms or the thighs are in proximity to the desktop and couple sufficiently to the beacon's electrode. There are periods in which the landmark signal is present at both wrists, as intended. Interestingly, in other periods it is only present at a single wrist. Therefore, we have to conclude that the IBC signal does not always propagate well throughout the entire body surface under all conditions. The observations showed that the signal propagates better, and is hence available at both wrists, when induced through the thighs. When induced at one hand, the signal might, however, not be detectable at the other one. One reason might be the larger distance between the wrists, compared to the shorter one from the thighs to both wrists. However, the presumably major reason has already been mentioned by [Zim95]: the "feet are the best location for [IBC] devices" since the coupling to both the body and the environment is the strongest.

3.3.4 Results

In three experiments, the detection of artificial landmarks has successfully been demonstrated using ECG AFEs available in virtually every modern commercial wearable device. Furthermore, the general feasibility of the implicit contextualization of measurements taken with wearable devices have been showcased. The evaluation is based on data from an exemplary scenario in which a transmitter beacon is embedded into a desktop and two sensing devices record the ECG signal captured at the user's left and right wrist. In a controlled setting, the coupling between the user's body and the transmitter has been evaluated in three different ways: **a)** directly touching the electrode, **b)** touching the desktop, and **c)** leaning back in the office chair and primarily coupling through the thighs. The results are summarized in **Table A.1**. Unfortunately, the recordings at the right wrist are considerably affected by oscillations at about 15 Hz, unintentionally demonstrating the effect of in-band noise on the proposed metrics. The proposed RSSI heuristic successfully indicates the presence of a landmark signal with values ranging from 21.6 to 23.5 dB. The maxima of the PPMC r, ranging from 0.845 to 0.863, then enable to locate the landmark packets in time and thus the decoding of the data segments. In all three coupling cases, the reception of landmarks was successful and resulted in a low PER of 0 to 26.5×10^{-3}. Due to the interference, all measurements at the right wrist are weaker and show a lower RSSI and r as well as higher PER. In general, the coupling **a)** apparently showed the best results, but **c)** was somewhat unexpectedly good and even better than **b)** which constantly showed the lowest yet sufficient performance.

The ECG's low sampling rate f_s of 128 Hz inherently limits the realizable carrier frequency f_0 to 20 Hz which is multiple orders below the optimal frequency band of capacitive coupling IBC (**Section 3.1.2**). In combination with the discovered optimal B of 20 Hz, the filtered signal shows, however, a good ratio between the pulse amplitude and the remaining gap ripple, in the range of 21.0 and 39.3. The relatively wide B is required to cover the modulated sidebands and to adequately reconstruct the discontinuous pulse wave, allowing for a fast transient response between the symbols, representing the binary values 0 and 1. However, the comparably slow f_0 results in a slow symbol rate, and a landmark packet with in total 24 pulse periods takes 1.2 s. Therefore, the achievable data throughput is apparently not sufficient for the transmission of larger data, but the 8 bit of data can already transport a unique object identifier for the proposed contextualization. To improve the noise immunity, future implementations should consider the implementation of error-checking and -correction techniques since redundancy can significantly improve the PER. The strength of the coupling to the environment, but also the devices themselves and the tightness of their attachment have large influence on the signal quality. Also the user's tissue composition has an influence on the signal amplitude, however the propagation velocity is probably less affected. Consequently, the distance-related delay can be neglected and landmarks are assumed to be immediately and without any delay present throughout the entire body surface. This assumption is particularly valid, considering that the ECG's low f_s limits the achievable accuracy to a quantization error of ± 3.9 ms.

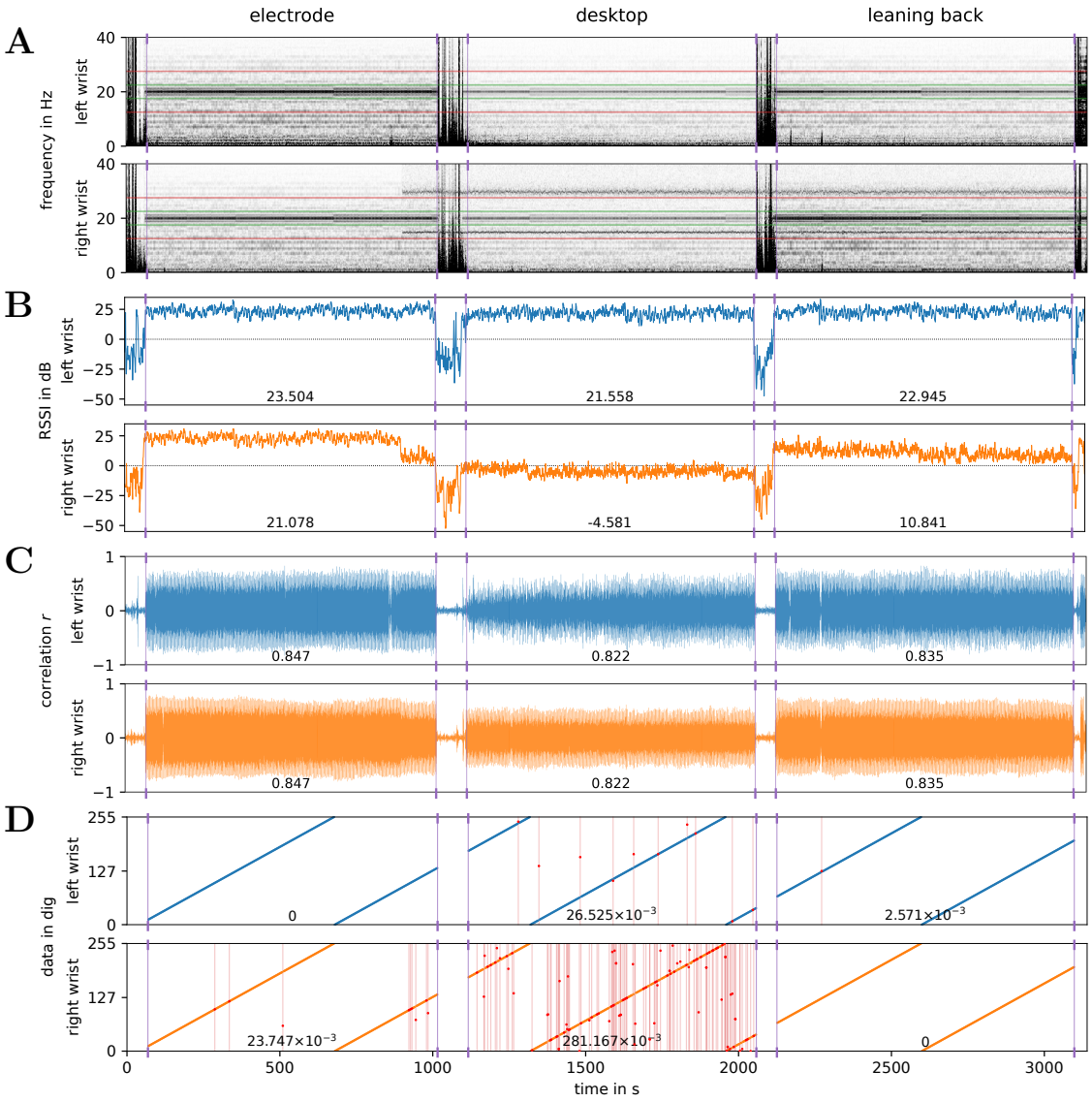

Figure 3.17: Output of the processing pipeline for the desktop experiment: (**A**) STFT with a window length of 4 s (512 samples) and 75 % overlap, presence of the signal core in 17.5 – 22.5 Hz (green lines) and in-band noise in 12.5 – 17.5 Hz and 22.5 – 27.5 Hz (red lines); (**B**) RSSI heuristic derived from the signal core and the adjacent in-band noise, resulting in an average RSSI of the segments; (**C**) PPMC r maxima of the detected landmarks resulting in mean $\bar{r}$ of the segments; (**D**) decoded data d and damaged information (red) due to erroneously detected pulses, resulting in PER of the segments. **[C21b; J22b]**

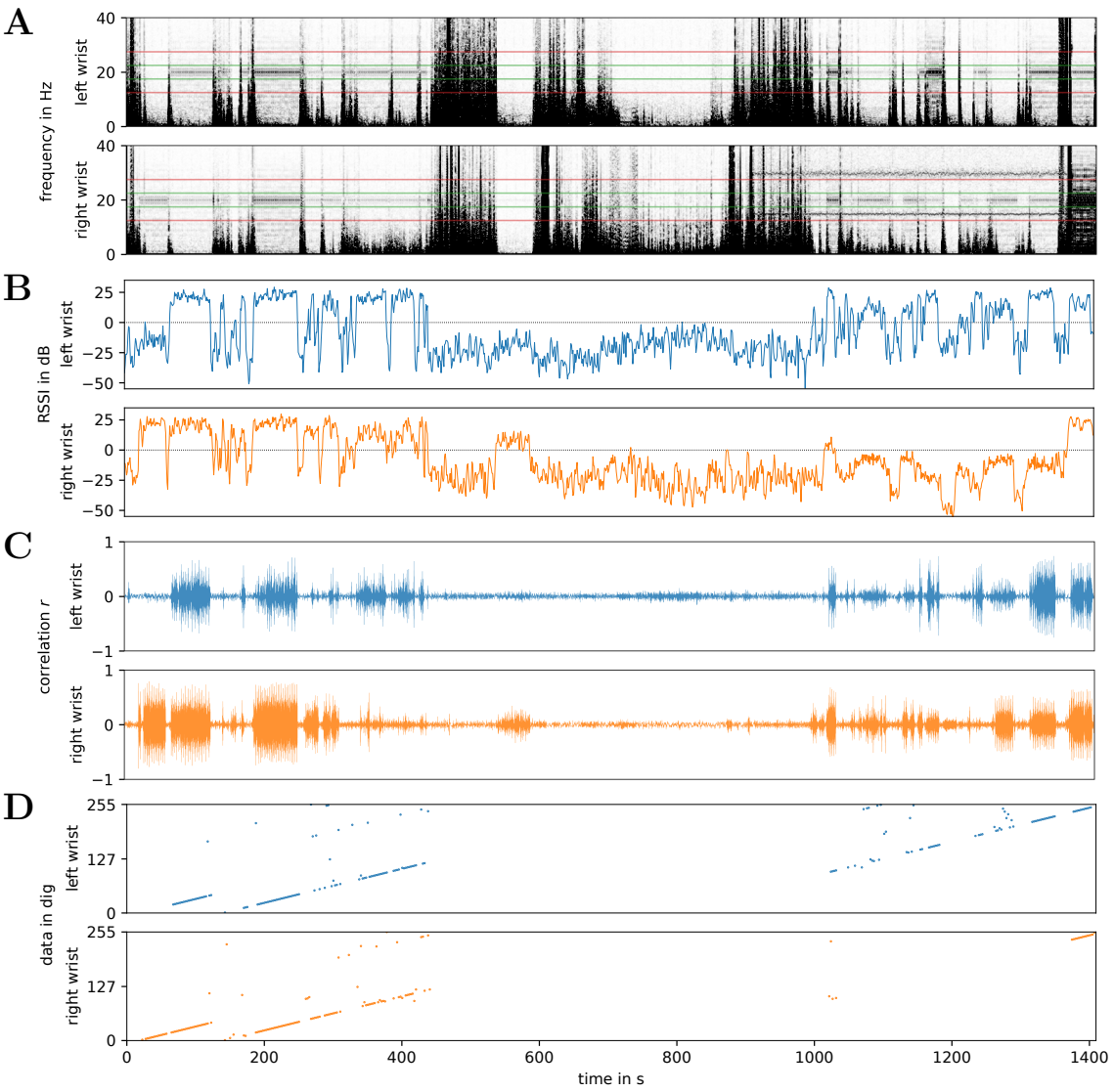

Figure 3.18: Output of the processing pipeline for the in-the-wild experiment: (**A**) STFT with a window length of 4 s (512 samples) and 75 % overlap, presence of the signal core in 17.5 – 22.5 Hz (green lines) and in-band noise in 12.5 – 17.5 Hz and 22.5 – 27.5 Hz (red lines); (**B**) RSSI derived from the signal core and the adjacent in-band noise; (**C**) PPMC r maxima of the detected landmarks; (**D**) decoded data d, considerable disrupted through motion, partly damaged information, erroneously detected pulses within the data segment at position x result in jumps that change the value by $\pm 2^x$. Correlation executed if RSSI > 0 dB, data decoded if $r \geq 0.65$ and preamble amplitude ≥ 5. **[J22b]**

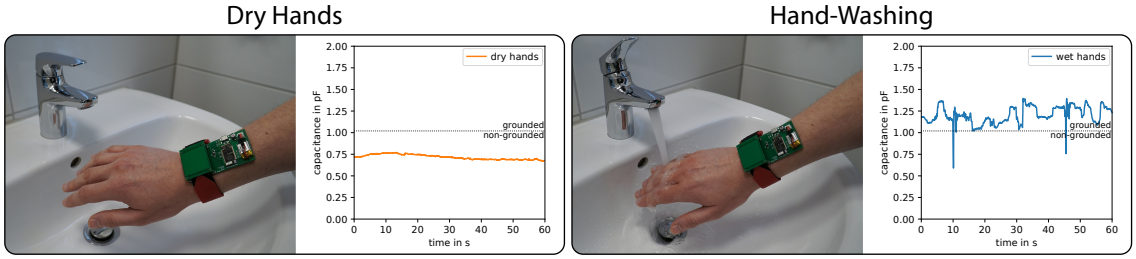

Figure 3.19: The effect of environmental changes on the inter-electrode capacitance measured with the wearable WetTouch prototype at the user's wrist. Illustrative time series of the measured capacitance: When performing washing gestures, yet solely air-coupled to the environment (left), and when washing hands, touching running water from the tap, and hence water-coupled to the virtually infinite area of earth ground (right). **[W22a]**

3.4 Case Study 3: Electrode Characterization

The third case study **[W22a]** presents a wearable prototype that allows to characterize the inter-electrode capacitance in everyday situations and to continuously monitor its fluctuations due to environmental changes on the go. In addition, it turned out that it can also enable the detection of hand-washing, as illustrated in **Figure 3.19**.

Hand-washing detection is not only of interest since the emergence of the COVID-19 pandemic. Obsessive-compulsive disorder (OCD) often manifests itself in terms of hand-washing compulsions. Detecting these compulsions can potentially improve the effectiveness of treatments. Therapists could offer additional just-in-time mobile interventions, improved momentary assessment, and interactive exposure and reaction prevention (ERP) training. This requires, however, the reliable detection of obsessive hand-washing.

The presented approach relies on the effect that touching running tap water yields a strong change in the capacitance between the wearer and the environment. The prototype exploits this effect and paves the path towards reliable and unobtrusive hand-washing detection in ambulatory applications with capacitive sensing. This case study contributes, therefore, substantially to a better understanding of capacitance fluctuations due to environmental changes, such as touching the water jet in particular.

Tap Water

Water is regularly expected to conduct electric current perfectly, but pure water (H_2O) is actually an excellent insulator ($\rho \approx 18.2\,\mathrm{M\Omega\,cm}$ at $25\,^\circ\mathrm{C}$). However, dissolved substances and salts, such as sodium chloride (NaCl), bring in ionic compounds which free ions increase electric conductivity. Nevertheless, the specific electrical resistance ρ of tap water is still high, in the order of 0.2 to $20\,\mathrm{k\Omega\,cm}$. In contrast to air ($\varepsilon_r \approx 1$), water shows, however, a comparatively large relative permittivity ε_r of about 80. The preferred quality of water to wash the hands is drinking water. According to the WHO, about 87 % of the global population have access to drinking water from "improved sources" while 54 % have a piped supply [WHO]. Early pipelines were made from cast iron or even toxic lead, and hence conductive (ρ in the order of $\mu\Omega\,\mathrm{cm}$). They have often been utilized to ensure the potential equalization throughout a building, since they were leading into the mass of earth and hence connected to ground. Today, besides the remaining old facilities, new pipelines are now and then made from costly yet durable copper, but more often made from cheap insulating plastics. Hence, potential equalization cannot be implemented and guaranteed through the supply pipes anymore. Nevertheless, all conductive connections leading into buildings (service entrance), as well as all metallic facilities inside, must be bonded to ground to avoid electric shocks [Mor16].

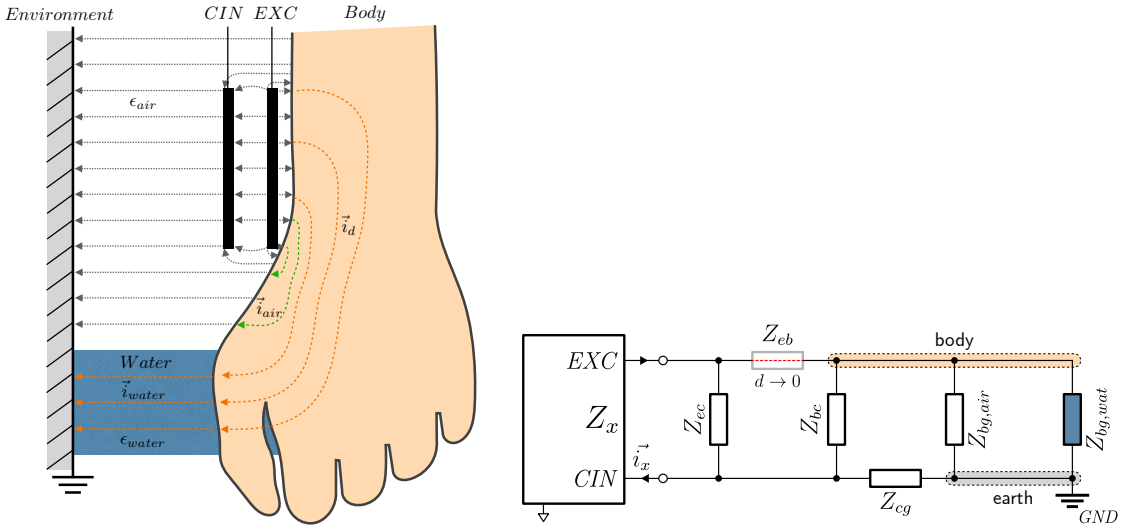

(a) The proposed sensing principle. **(b)** The equivalent circuit.

Figure 3.20: (a) Illustration of the proposed sensing principle. It is hypothesized that by touching the water jet, the coupling to earth ground is improved through its virtually infinite area, which in turn can be measured with the wrist-worn WetTouch prototype. **(b)** Derived from the physical model, the sensing impedance Z_x is formed between the excitation (EXC) and the sensing electrode (CIN) at the AD7151 [AD71]. The equivalent circuit is a two-port from the perspective of the floating wearable device. Due to $d \to 0$, the contact impedance Z_{eb} disappears and virtually enlarges the EXC electrode to the entire body surface (transmit mode, according to [Smi+98; Gro+17]). **[W22a]**

Physical Model

The physical model, illustrated in **Figure 3.20a**, has been developed to comprehend and understand the effect of environmental changes, such as touching tap water, on the measurable capacitance. The model is based on the fundamentals of capacitive coupling and grounding provided in **Section 3.1.2**. It posits that the excitation electrode at EXC strongly couples to the adjacent skin. In the resulting transmit mode [Smi+98; Gro+17], it virtually enlarges to the entire body surface and hence modulates the electric field of the human body. Meanwhile, the floating sensing electrode at CIN couples to diverse surfaces: Directly to the counterpart electrode at EXC, but also to the body surface modulated through EXC and the environment, earth ground with its virtually infinite area. Once the water jet is touched, a new branch bypasses the path through air with a larger permittivity and hence a stronger electric field. The respective change of the capacitance C_x is measured by means of the wearable hardware unit. The equivalent circuit from its two-port perspective is provided in **Figure 3.20b**. Every facing conductive surfaces establish a capacitance C, represented by a complex impedance Z. Following the high potential from EXC via the floating CIN to earth ground GND, those are exemplified as follows: The impedance Z_x, the equivalent circuit of the sensing two-port respectively, is illustrated in **Figure 3.20b** and given by **Equation 3.4**. The water $Z_{bg,wat}$ hence bypasses the air path $Z_{bg,air}$ and increases the measurable total displacement current $\vec{i_x}$.

$$Z_x = (Z_{ec} \parallel Z_{bc}) \parallel (Z_{cg} + (Z_{bg,air} \parallel Z_{bg,wat})) \tag{3.4}$$

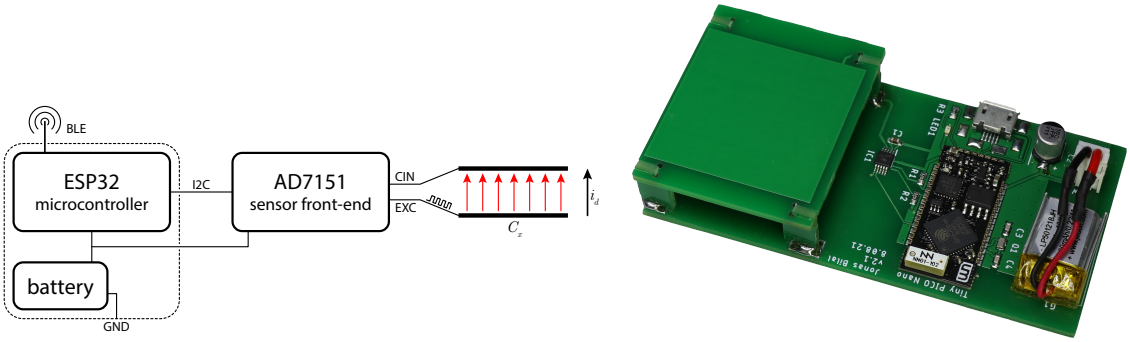

(a) Schematic of the wearable prototype.

(b) Photo of the wearable prototype.

Figure 3.21: (a) Block diagram of the prototype's circuit: The ESP32 fetching measurements from the AD7151 [AD71] capacitance-to-digital converter (CDC) via an I2C interface. The battery supplying both ESP32 and CDC, while the antenna and CDC are excluded from the ground plane (GND, dotted line). The floating sensing electrodes have no relation to ground (GND). The excitation EXC electrode and sensing CIN electrode measure the inter-electrode sensing capacitance C_x by means of the transferred charges, the displacement current i_d respectively. **(b)** The assembled prototype: The two $3 \times 3\,\mathrm{cm}^2$ electrodes, stacked with 1 cm air gap, the AD7151 CDC, the ESP32 microcontroller with wireless Bluetooth LE / Wi-Fi connectivity, and a small rechargeable battery. **[W22a]**

3.4.1 System Design

To confirm the physical model, the wearable WetTouch prototype has been developed to perform basic experiments. It enables to sensitively measure the capacitance between the two electrodes: An excitation electrode (EXC) to couple to the wearer's body and a floating sensing electrode (CIN) to couple to the earth.

Wearable Sensing Device

As presented in **Figure 3.21**, the wearable WetTouch prototype has two electrodes, arranged one above the other with an air gap. Capacitance changes are measured by an AD7151 [AD71] CDC and then provided to an ESP32 [ESP] microcontroller that either forwards the recordings via Bluetooth / Wi-Fi or stores them locally. The battery-powered device can be attached to limbs through a hook-and-loop tape and is designed to be comfortably worn at the lower arm, almost like a traditional wristwatch. The 'sandwich' electrode setup has been adapted from previous research, as elaborated in **Section 3.1.2**, and forms a parallel plate capacitor which ideal intrinsic capacitance C_{ec} is 0.797 pF.

Capacitance-to-Digital Converter

There exist diverse techniques to measure the tiny capacitance between conductive structures, reviewed by Ramanathan et al. [Ram+13]. Because the effect of hand-washing on the inter-electrode capacitance is expected to be rather weak, a sensitive front-end is required. The AD7151 [AD71] is an ultra-low power (70 µA at 3.3 V) CDC that enables to directly obtain a digitized value. It is designed for the single-channel measurement of floating capacities at the ranges 0 to 0.5, 1.0, 2.0, or 4.0 pF with 12 bit resolution, at a maximum sensitivity of 1 fF respectively. The range of 2 pF has been applied, resulting in a sensitivity of 1.6 fF. To capture the sensor's C_x, the integrated circuit measures the charge transfer between its two pins EXC and CIN. It applies a square wave to EXC, with limited slew rate and an excitation frequency of 16 kHz, while the opposite CIN meters

the charge using a Σ-Δ modulator. A subsequent digital filter averages the measurements while the conversion time is 10 ms. The microcontroller is employed to read and trigger the measurement every 50 ms, resulting in a sampling rate of 20 Hz.

3.4.2 Evaluation

Two experiments are conducted to characterize the inter-electrode capacitance in everyday situations and to test whether it is possible to distinguish hand-washing from other activities with the change of capacitance through touching the jet from the water tap. It is hypothesized that the capacitance of the wrist-worn electrode pair changes due to the adjacent body coupling through the water jet and via the supply pipes to earth ground. If this effect causes a significantly measurable difference in the capacitive reading, hand-washing should be distinguishable from other activities.

Experiment 1

To show whether such an effect exists, measurements with different conditions and activities were taken. A single subject (S1: male, 25 yr., 177 cm, 70 kg) wore the device performing the following: ⟨1⟩ grounding himself through the mains' neutral wire, ⟨2⟩ washing gestures with dry hands, ⟨3⟩ hand-washing with water running from a tap, ⟨4⟩ washing gestures with wet hands in a wash pan, ⟨5⟩ arbitrary gestures, ⟨6⟩ contacting one foot with running tap water, and ⟨7⟩ brushing teeth with a traditional toothbrush. The histograms of the CDC readings are shown together with the respective activity in the **Figures 3.22** and **3.23**. The overlapping conditions ⟨1, 3, 6⟩ confirm the aforementioned hypothesis. The body is coupled to earth ground in those *grounded* conditions, either through direct skin contact or the water jet. In contrast, the *non-grounded* conditions ⟨2, 4, 5, 7⟩ do not overlap with the *grounded* ones, even for ⟨5⟩. The close proximity of the wearable sensor to the subject's head in ⟨7⟩ might cause the relatively large capacitance while the other activities are performed with stretched arms and hence the sensor farther away from the body. Instead of the contacted water, the body then acts as a large, proximate ground plane. Although the hands get in contact with water, activity ⟨4⟩ lies in the *non-grounded* part of the measurements, confirming that the connection to earth ground is required to achieve the desired capacitance measure. Therefore, hand-washing activities can only be detected when the water is running through a ground-bonded tap or a pipeline originated in the mass of earth. For S1, hand-washing and simultaneously touching the water running from a tap ⟨3⟩ yields an average capacitance of 1.205 ± 0.099 pF and forms a distinct cluster that may allow to distinguish hand-washing from other activities such as arbitrary motion ⟨5⟩ with an average capacitance of 0.793 ± 0.325 pF. To enable the detection of grounding in a first approach, a simple threshold is set to the midpoint between the means of *non-grounded* and *grounded* classes at 1.011 pF. Further distinction of hand-washing from other activities with a grounded body is probably possible since additional motion leads to a wider spread of the measurements, as apparent from the clusters ⟨1⟩ versus ⟨3⟩.

Experiment 2

In order to proof the reproducibility of the observed effect, the conditions ⟨2⟩ washing gestures with dry hands and ⟨3⟩ hand-washing with water running from a tap have been repeated with two subjects, five times and for 30 s each. S1 is male, 25 years, 177 cm, 70 kg and S2 is male, 61 years, 170 cm, 90 kg. The histogram in **Figure 3.24** shows a similar distribution as **Figure 3.22** from the first experiment. The clusters of ⟨2⟩ and ⟨3⟩ are clearly separated. However, ⟨2⟩ is rather scattered while ⟨3⟩ appears evenly spread.

In conclusion, hand-washing is indeed detectable and distinguishable from other activities, but the system has not yet been applied to a larger variety of users and sinks in different environments. When considering the results, it is visible that the effect of grounding the body has the largest influence, which means that different body types, composition, and height will only have a limited influence. Furthermore, the sensing mechanism is based on the change in capacitance, caused by the water jet which bypasses the air path and hence improves the coupling between the human body and earth ground. On the one hand, this feature limits the possible applications of the sensing principle to water taps which supply pipes are originated in the mass of earth or even directly bonded to earth ground, commonly found in building installations. On the other hand, the body is required to be properly insulated from ground. For the application that motivated this work, i.e. detecting obsessive hand-washing, this situation can be safely assumed. Hand-washing is not the only activity where the body comes into contact with water and some confounding activities, e.g. dish-washing with a running tap, will probably show quite similar measurements. These could be distinguishable by more sophisticated analyses, for example by considering the overall water contact time or other time-dependent characteristics. The swept-frequency capacitive sensing method, presented in Touché [SPH12], might also be an option to improve the classification by analyzing the frequency-dependent coupling instead of measuring at a constant excitation frequency of 16 kHz. IMU sensors can also be used in conjunction with the presented approach to remove possible confounding situations.

3.4.3 Results

Along with the characterization of the inter-electrode capacitance for IBC purposes, a novel technique for the detection of hand-washing has been presented. It is based on capacitive sensing and uses the effect of grounding through touching water from a running tap to distinguish *non-grounded* and *grounded* activities. The developed physical model has been substantiated in two initial experiments with recordings from two subjects. The results are promising and show that the proposed method allows to distinguish hand-washing from other activities. The measured capacitance during hand-washing is distributed around 1.152 ± 0.106 pF and hence separates clearly from washing gestures with dry hands around 0.671 ± 0.065 pF. A simple threshold on a running average might, therefore, be sufficient to detect if the body is grounded through water while an additional analysis of the standard deviation allows to identify hand-washing. Obsessive hand-washing could then be detected by the duration and frequency of the hand-washing sessions.

The measurements taken during the performance of other, *non-grounded* activities, such as arbitrary gestures, have shown a characteristic capacitance of 0.793 ± 0.325 pF (S1), which is surprisingly close to the calculated ideal value of 0.797 pF. This confirms the validity of using this value in the simulations conducted in the following case study of **Section 3.5**. However, the observed variations have shown to be comparatively large and, therefore, can result in a relative impact of about ± 40.7 %, which is not negligible.

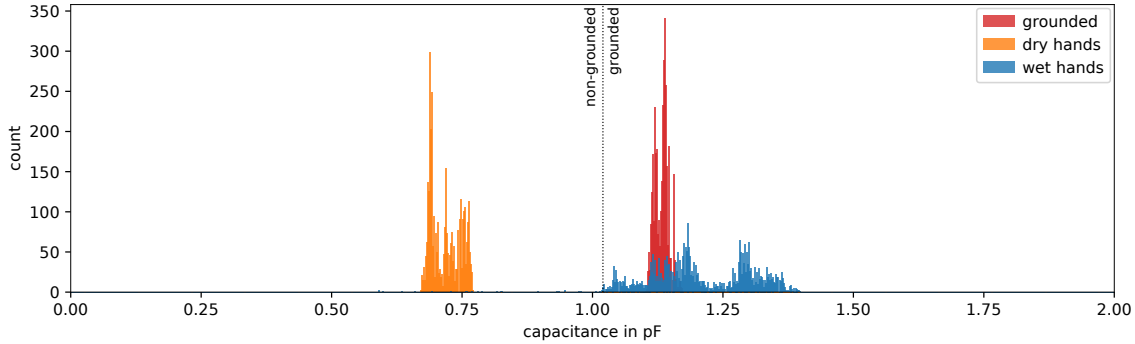

Figure 3.22: Distribution of measurements from a single subject (S1): ⟨1⟩ intentionally grounded body (red, 1.133 ± 0.013 pF), ⟨2⟩ performing washing gestures with dry hands (orange, 0.718 ± 0.028 pF), and ⟨3⟩ hand-washing with water running from a tap (blue, 1.205 ± 0.099 pF). Separation line and simple threshold between the classes *non-grounded* and *grounded* at 1.011 pF (dotted line). **[W22a]**

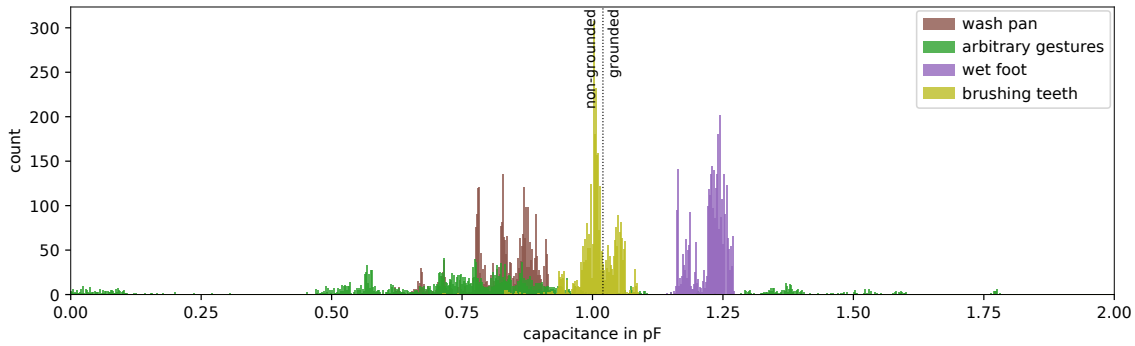

Figure 3.23: Distribution of measurements from a single subject (S1): ⟨4⟩ performing washing gestures with wet hands in a wash pan (brown, 0.823 ± 0.065 pF), ⟨5⟩ performing arbitrary gestures (green, 0.793 ± 0.325 pF), ⟨6⟩ contacting one foot with running tap water (violet, 1.225 ± 0.031 pF), ⟨7⟩ and brushing teeth with a traditional toothbrush (light green, 1.007 ± 0.047 pF). Separation line at 1.011 pF (dotted line). **[W22a]**

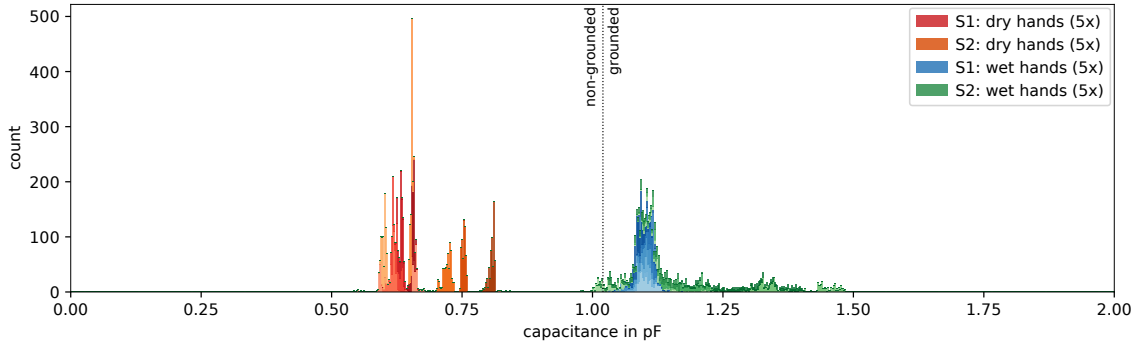

Figure 3.24: Accumulated distribution of additional measurements from two subjects: S1 (male, 25 yr., 177 cm, 70 kg) and S2 (male, 61 yr., 170 cm, 90 kg). Dry hands ⟨2⟩: S1 (5×30 s, red, 0.635 ± 0.026 pF) and S2 (5×30 s, orange, 0.707 ± 0.073 pF). Wet hands ⟨3⟩: S1 (5×30 s, blue, 1.099 ± 0.018 pF) and S2 (5×30 s, green, 1.205 ± 0.128 pF). Five 30 s measurements per subject and class, 10 min recordings in total. In-class averages for ⟨2⟩ dry hands of 0.671 ± 0.065 pF and for ⟨3⟩ wet hands of 1.152 ± 0.106 pF. Separation line at 1.011 pF (dotted line). **[W22a]**

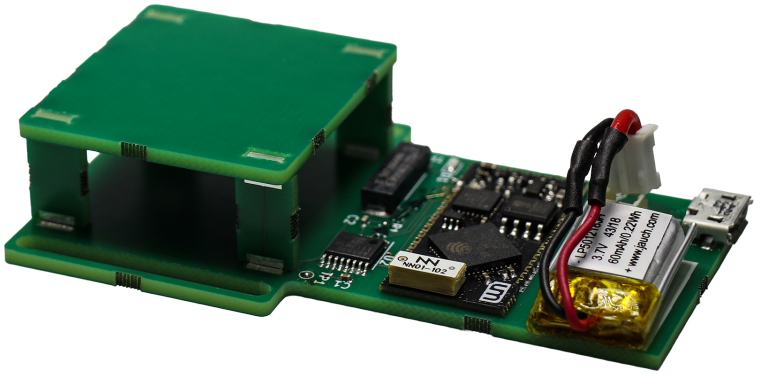

Figure 3.25: The OpenIBC prototype with the proposed open-source IBC receiver, assembled from (left to right): $30 \times 30\,\mathrm{mm}^2$ electrodes with 1 cm air gap **[C17]**, LF OOK wake-up receiver AS3930 [SAS], 125 kHz LC BP filter with 7.2 mH inductance, TinyPICO NANO stamp module with ESP32 microcontroller, 3.7 V / 60 mA h LiPo battery, and USB connector. Size of the assembled prototype: $40 \times 67 \times 10\,\mathrm{mm}^3$. **[W22a]**

3.5 Case Study 4: RFID / NFC Front-Ends

Due to the absence of commercially available IBC transceiver modules, research on possible applications benefiting from the promising communication principle, is lagging behind. Especially concepts for more intuitive human-computer interaction (HCI) and the impact on the user experience (UX) cannot be explored yet. In contrast, integrated transceiver circuits for radio-frequency identification (RFID) and near-field communication (NFC) are fully developed and ubiquitous. In this case study, off-the-shelf AFEs for RFID / NFC systems are repurposed to implement open-source IBC interfaces which thus enable the faster prototyping. The OpenIBC prototype **[C22c]**, presented in **Figure 3.25**, is not intended to compete with cutting-edge research, especially not in terms of data rate and efficiency. Instead, standard components are used to pave the way for applications that can directly be translated to future fully-integrated solutions, when finally made available.

RFID and NFC

The fundamental principle of radio-frequency identification (RFID) was developed in the 1970 / 80s and targets since then commercial low-cost applications which require the identification and tracking of tagged objects. It allows a reader device to contactless obtain simple but unique information from a transponder tag in range, such as an identification number associated with the object. While active tags have to come along with their own energy source, which however enables the response over larger distances in the far field, passive transponders take the required energy from the reader's induction field and apply load modulation to provide a response in the near field.

Most passive RFID transponders operate in the low frequency (LF, 125.0 – 134.2 kHz) and high frequency (HF, 13.56 MHz) bands which tend to be robust against interference. There are also passive tags that use the ultra-high frequency (UHF, 433 MHz and 858 – 930 MHz) band, but UHF and super-high frequency (SHF, 2.4 or 5.8 GHz) microwaves are more common for active tags, enabling faster data transmission. [Fin10; PENa]

Wrapped around the popular RFID standards, in 2002 the companies Sony and Philips initiated the development of near-field communication (NFC) for contactless, wireless communication between devices in close proximity (ISO/IEC 18092). Based on the 13.56 MHz HF band, it enables a bidirectional, peer-to-peer data transmission at high data rates of

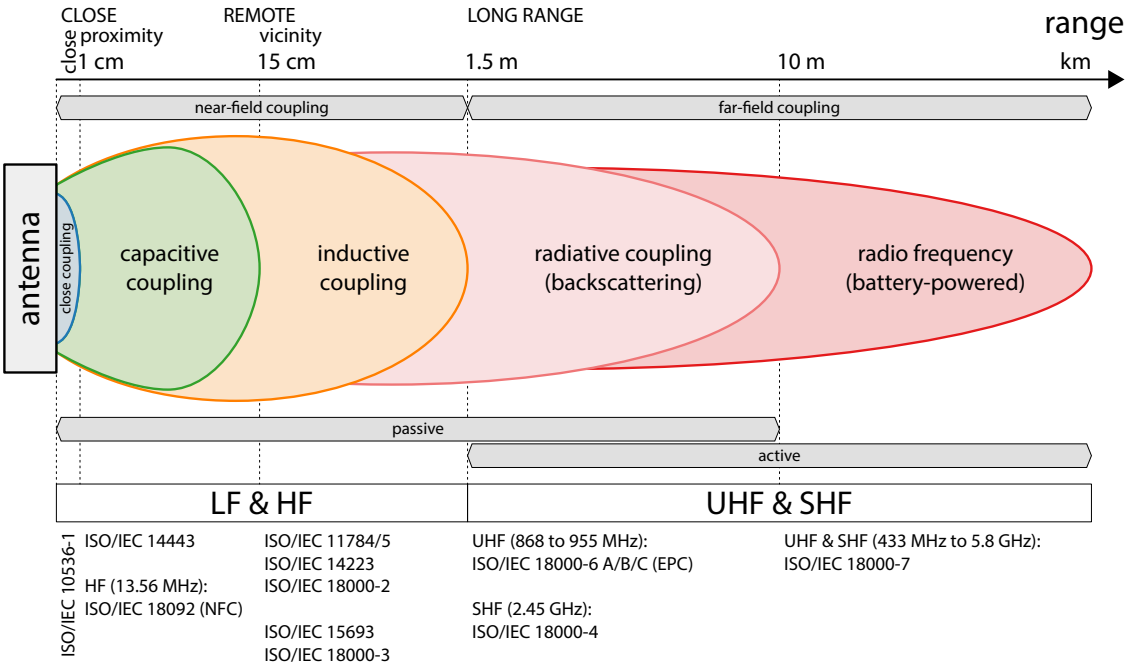

Figure 3.26: Summary of the different coupling principles, possible ranges, and numerous ISO / IEC standards of RFID / NFC that are commonly applied. **[C22c]** cf. [SD14]

up to 424 kbit/s, but it is still downward compatible to passive targets. The different coupling principles, their possible ranges, and the numerous, commonly applied standards are summarized in **Figure 3.26**. [Fin10; PENb]

Wake-up Receivers

The aforementioned active readers as well as radio receivers in general suffer from front-ends that often dissipate most of the energy for idle listening. Systems with rare or only sporadic, event-based communication, therefore, usually minimize their active time through a low duty cycle, at cost of higher latency, however. They regularly switch between an energy-saving sleep mode and a dissipative receive mode, to listen to the channel and preferably not miss a message. Although the typical power consumption of IBC transceivers is multiple orders lower than of conventional RF modules [Mai+21; Pet+16], their dissipation is nevertheless predominant. So-called wake-up receiver (WuRx) are specifically designed for the continuous, always-on channel listening at low power. Usually, a long but LF carrier burst is used to trigger a wake-up process that releases an interrupt request (IRQ) to activate the primary receiver circuit, allowing for the reception of data using a HF carrier and higher data rates [CAM20], and using a microcontroller with more performance to eventually process the incoming data. For IBC, such WuRx systems have already been presented in [CBY13; BY15; Pet+16; YH17; Mai+19].

3.5.1 System Design

In recent years, RFID and near-field communication (NFC) turned into ubiquitous alternatives to traditional radio transmission for short- and medium-range communication. Instead of a dipole antenna for far-field radio propagation, usually a loop antenna is used for both data transmission and energy transfer via electromagnetic near-field coupling. Although capacitive coupling is being mentioned in the standard ISO/IEC 10536 for close

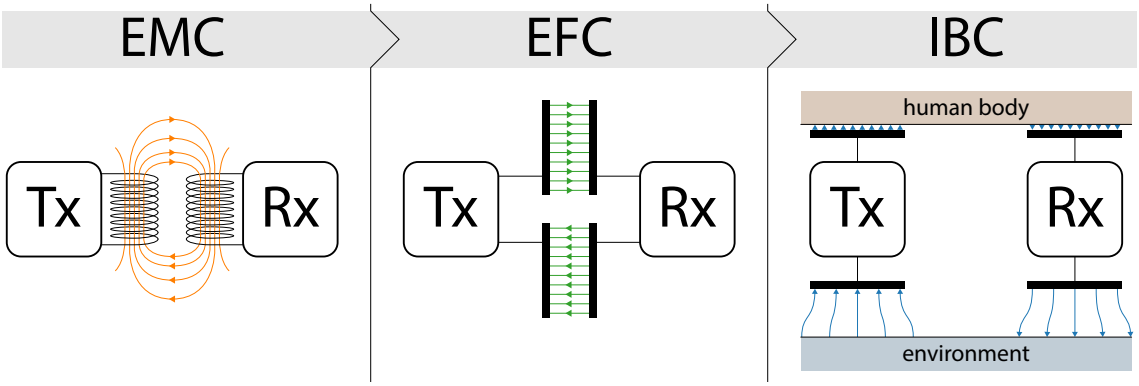

Figure 3.27: Illustration of the evolution from the conventional electromagnetic, inductive near-field coupling (EMC) via uncommon electric field, capacitive coupling (EFC) toward intra-body coupling or communication (IBC) which uses the human body to extend the capacitive close-coupling range. **[C22c]**

coupling, "it is not used by very many RFID systems on the market today" because it "is only effective at such a small proximity" [Smi16]. The standard specifies a maximum range of 1 cm through air, which is not sufficient for typical WBANs. Moreover, the implementation based on available front-ends is not easily done by just replacing the coil with electrodes. To overcome this hurdle, the proposed approach uses the human body as an intermediate transmission medium. The desired evolution from conventional electromagnetic coupling via capacitive, electric field coupling toward capacitive intra-body coupling is illustrated in **Figure 3.27**. According to this concept, the transmitter induces signals via close coupling into the body and modulates its surrounding electric field. The receiver again couples to the body, detects the induced fluctuations in the electric field, and demodulates the desired signal. While the forward path is established via the human tissue, which at the targeted frequencies virtually acts like a conductor [MMS18], the return path, to close the channel circuit, is formed through the environment, the earth ground respectively [Gro+17; NMS20]. Therefore, in principle, it should be possible to repurpose RFID / NFC transceiver circuits for IBC.

Unfortunately, the use of these AFEs comes along with multiple obstacles due to fundamental differences of RFID / NFC compared to the IBC principle. Several integrated circuits are available which enable the implementation of tags or wireless sensors. The majority acts, however, as a passive transponder / target, supplied by an active reader / initiator via electromagnetic induction, and the requested information are returned by means of load modulation – the active generation of signals is hence not provided.

The current density of the signal, induced by an IBC transmitter's excitation electrode to the skin, has to conform with safety regulations such as the standard of the international commission on non-ionizing radiation protection (ICNIRP) [Lin+10]. Therefore, the maximum amount of energy that can be transferred through the human tissue is limited. The typical displacement current induced is, however, multiple orders smaller than the allowed maximum [Mai+20b; Tom+19]. Although demonstrated in [PO97], the remote supply of devices and the use of backscattering or even load modulation are, therefore, at least difficult. Instead, the active signal generation and a more advanced peer-to-peer connection are required, similar to NFC. The popular, fully integrated multi-protocol RFID / NFC transceiver TRF7970A [TRF] supports all desirable standards. It is, nevertheless, optimized for inductive coupling and hence shows not only a low output impedance Z_{out} of 4 or 8 Ω, but also a relatively low input impedance Z_{in} of typically 10 kΩ. In preliminary

experiments, impedance matching to this circuit, from a sensor's high impedance Z_{out} to a low Z_{in}, turned out to be cumbersome – as discussed in [Bri06].

Continued research revealed the AS3930 [SAS], which shows promising characteristics such as a high Z_{in}. Based on this low-power wake-up receiver front-end, a receiver circuit was developed as a first step toward an open-source IBC transceiver. The AFE is originally designed for reading active RFID tags in applications such as operator identification, access control, object localization, or wireless sensing. The developed system consists of the wake-up receiver IC itself, two coupling electrodes, an adjoined LC filter circuit, and an ESP32 [ESP] microcontroller to be woken up on data reception. Embedded into a suitable channel model (**Section 3.1.2**), the circuit is simulated to estimate its feasibility and achievable performance. The considerations made are detailed in the following.

Frequency Band

Essential requirement is the use of a free and unlicensed frequency spectrum. The LF and HF bands, typically applied in RFID and NFC systems, are located in the ISM band, internationally reserved for industrial, scientific, and medical purposes. Given by the selected IC, the 125 kHz LF band is applied. It shows good resistance to interference, but the low f_0 results in a long wavelength that requires for larger components compared to those typically applied in systems using the 13.56 MHz HF band.

Receiver

The AS3930 [SAS] is a low-power OOK wake-up receiver for LF signals. With a bandwidth B of 110 – 150 kHz, its input is optimized for a carrier f_0 of 125 kHz, at which it shows a comparatively high input Z_{in} of 2 MΩ. It is designed to continuously run as an always-on WuRx that allows to activate a connected system on detection of a carrier burst with a sensitivity of 100 μV_{RMS}. After the successful correlation of a custom signal pattern, the following data is demodulated and streamed to the microcontroller which puts the front-end back to listening mode after the reception is complete. The chip can be supplied with 2.4 – 3.6 V and draws, according to the datasheet, 2.7 µA in continuous listening mode and 5.3 µA when correlating wake-up patterns or receiving data.

Microcontroller

The receiver IC does not provide computing power for applications itself. It is only intended to wake up a connected circuit via IRQ and to then forward the demodulated, received data. The selection of a suitable microcontroller depends on the target application. To allow for an easy setup and to provide sufficient performance for evaluation purposes, the popular ESP32 [ESP] in form of a small TinyPICO NANO [TPN] stamp module. The powerful SoC provides diverse operation modes, in particular a deep sleep mode at less than 20 µA, which enables battery-powered applications.

Transmitter

Since this case study concentrates on the receiver front-end, the transmitter is again kept simple and is based on the same stacked electrode setup as the receiver previously presented in **Section 3.1.2** and characterized in the study of **Section 3.4**. Instead of using a power amplifier to boost the amplitude [Zim96], the signal is directly modulated with an ESP32 microcontroller which regularly (e.g. every 10 ms) generates a wake-up signal with a 3.3 V_{pp} amplitude, 1.17 V_{RMS} respectively. As discussed below, the transmitter is still grounded through the mains' neutral wire, which considerably reduces the channel loss.

Protocol

The AS3930 supports two different wake-up protocols. While the first one consists of a burst directly followed by the data, the second one adds a preamble for clock recovery and a programmable 16 bit wake-up pattern for a more reliable detection of the desired signal through correlation. The data is preferably Manchester encoded, resulting in eight applicable symbol rates ranging from 512 – 4096 S/s with a period time per symbol and bit t_{bit} of 1.953 – 0.244 ms. The application of the advanced protocol requires first a comparatively long carrier burst of 0.360 ms $< t_{\text{burst}} < 16\times\ t_{\text{bit}}$ (e.g. 1 ms), followed by a preamble of $t_{\text{pre}} > 4\times\ t_{\text{bit}}$, and a wake-up pattern of t_{pat}, considering that $t_{\text{pre}} + t_{\text{pat}} < 40\times\ t_{\text{bit}}$, before the desired data (e.g. 2 byte, $16\times\ t_{\text{bit}}$ respectively) are sent. While lower data rates are more immune to ambient noise, higher rates require a wider B to also pass sidebands through for a faster transient response. As demonstrated in **Section 3.3.3.2**, this results in a more accentuated envelope but also injects a larger portion of the noise.

Electrode Setup

The previously presented setup (**Section 3.2**) of two $30 \times 30\,\text{mm}^2$ electrodes with an air gap of 1 cm is used again **[C17; W22a]**. The design reduces the dielectric material between the electrodes, minimizes the intrinsic capacitance C_{int}, and hence maximizes the coupling through the tissue. The use of the LF band, and hence the modulation of the quasi-electrostatic field, is "eliminating the necessity for high-frequency design and complex hardware components" [Gro+14]. The ideal C_{int} of the formed parallel plate capacitor is calculated as 0.797 pF (**Section 3.1.2**). However, as demonstrated and characterized in the previous case study of **Section 3.4**, the capacitance at the receiver C_{rx}, including parasitic effects, typically fluctuates around 0.987 ± 0.234 pF **[W22a]**.

LC Band-Pass Filter

The AS3930 requires an external BP filter to extract the desired signal at f_0 of about 125 kHz. Implemented as a rejector in parallel to the input circuit, with a high but finite Z_{in} of 2 MΩ, it drains undesired components outside the intended frequency band, such as ambient noise. In-band components are, therefore, forwarded and turn the BS quasi into a BP filter. The filter is implemented as a parallel LC resonant circuit whose resonant frequency f_{r} with $\omega = 2\pi f$ is given as:

$$\omega_r = \frac{1}{\sqrt{LC}} \tag{3.5}$$

The complex impedances of L and C are given as $Z_L = j\omega L$ and $Z_C = \frac{1}{j\omega C}$. In case of ideal and loss-free resonance, their reactances X in $Z = R + jX$ become equal $X_L = X_C$, resulting in the balanced yet counter-acting condition $Z_L = -Z_C$ for $\omega \to \omega_r$:

$$\lim_{\omega \to \omega_r} Z_{LC}(\omega) = \lim_{\omega \to \omega_r} \frac{1}{\underbrace{\frac{1}{Z_L(\omega)}}_{-Z_C} + \frac{1}{Z_C(\omega)}} = \frac{1}{-\frac{1}{Z_C} + \frac{1}{Z_C}} = \frac{1}{0} = \infty \tag{3.6}$$

In RFID / NFC applications, the filter normally consists of the coupling coil with a specific inductance and a countering capacitor to form the resonant tank circuit. In the intended IBC receiver, however, only the inductance L is fixed while the capacitance C is given through the inter-electrode capacitance C_{rx} and hence fluctuating as mentioned before. It is composed of the intrinsic C_{int}, which needs to be minimized, and the parasitic C_{par}

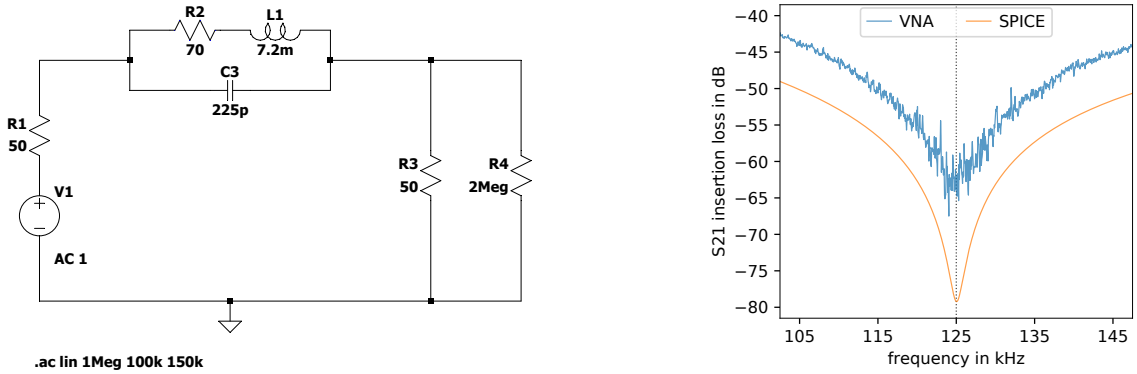

(a) SPICE model. **(b)** SPICE simulation.

Figure 3.28: (a) SPICE model of the LC resonant circuit between port 1 and port 2 of the vector network analyzer (VNA). **(b)** Simulation and measurement of the insertion loss $\text{loss}_{\text{dB}}(S_{21})$ in dB, derived from the S_{21} parameter, for f_0 of 125 kHz. **[C22c]**

coupling through body and environment, which is crucial as it finally makes IBC possible:

$$C_{\text{rx}} = C_{\text{int}} + C_{\text{par}} \tag{3.7}$$

Consequently, f_{r} deviates from f_0 and shifts slightly according to the affected C_{rx}.

Furthermore, the selection of real, discrete components appears to be difficult. The C_{rx} with around 1 pF is too small and, in combination with the low f_{r}, it would require a huge L of 1.6 H, meaning many windings and thus large dimensions. With the transponder coil B82450A7204A [TDK] we found a suitable component that is available at a maximum of 7.2 mH, and its size of $11.4 \times 3.5 \times 2.4\,\text{mm}^3$ also meets the spatial requirements. To nevertheless reach the resonant state, according to **Equation 3.5**, C_{rx} is enhanced with C_{add} of 224 pF to reach the required 225.16 pF. **Figure 3.28** shows the circuit's SPICE simulation, the characterized S_{21} parameter and the derived insertion loss $\text{loss}_{\text{dB}}(S_{21})$:

$$\text{loss}_{\text{dB}}(S_{21}) = -20 \log_{10} |S_{21}| \tag{3.8}$$

Channel Model

For LF IBC systems ($f_0 < 1$ MHz, Section 3.1.2) in the quasi-electrostatic domain, and with a capacitive high impedance (high-Z) termination at the receiver, the channel model of [Mai+21] is valid. The applied lumped SPICE model is illustrated in **Figure 3.29**. Accordingly, the channel loss largely depends on the capacitances that form between the environment and the transmitter $C_{\text{ret, tx}}$, the receiver $C_{\text{ret, rx}}$, the body C_{body}, and the load at the receiver side C_{load}, approximated by [Mai+21]:

$$\text{loss}_{\text{dB}} \approx -20 \log_{10} \left(\frac{C_{\text{ret, tx}} \cdot C_{\text{ret, rx}}}{C_{\text{body}} \cdot C_{\text{load}}} \right) \tag{3.9}$$

While larger $C_{\text{ret, tx}}$ and $C_{\text{ret, rx}}$ in the return path reduce the channel loss, larger C_{body} and C_{load} increase its value. Due to the imbalance 1:224 of C_{rx} and C_{add}, fluctuations of C_{rx} do not considerably affect f_{r}. The extended $C_{\text{load}} = C_{\text{rx}} + C_{\text{add}}$ is, however, not ideal as it considerably limits the receiver's efficiency and sensitivity. To compensate for this effect, the transmitter is connected to ground. The simulation, presented in **Figure 3.29**, allows to estimate whether the signal would probably reach the required sensitivity threshold of

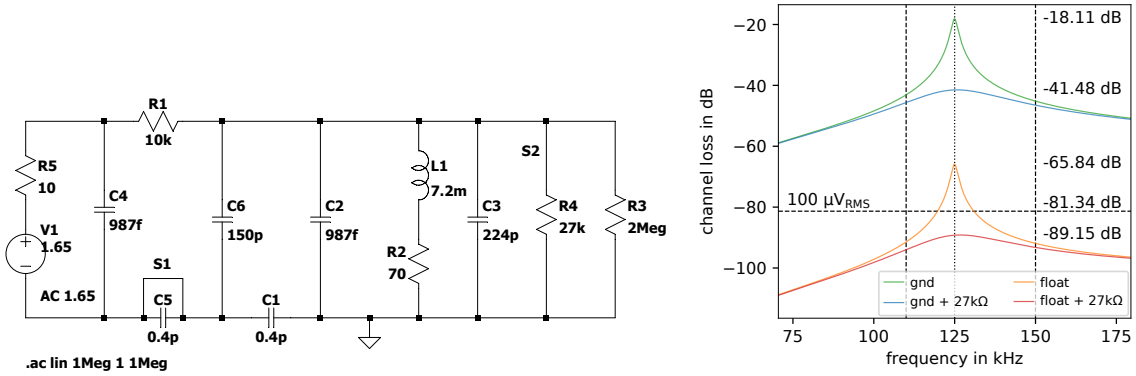

(a) SPICE model. **(b)** SPICE simulation.

Figure 3.29: (a) Lumped circuit, SPICE model for the simulation of the LF, high-Z IBC receiver front-end, according to [Mai+21]. Switch S1: floating (open) or grounded (closed) transmitter; Switch S2: disabled (open) or enabled (closed) shunt resistor of 27 kΩ for a wider filter bandwidth B but lower sensitivity. **(b)** Simulation: the front-end's bandwidth B (verticals), sensitivity threshold at 100 μV_{RMS} (horizontal), grounded (gnd) and floating (float) transmitter, disabled or enabled shunt resistor (27 kΩ). **[C22c]**

100 μV_{RMS} or −81.339 dB, respectively. In line with the conducted experiments, the use of a grounded transmitter is still required to enable the successful signal transmission to a floating receiver device.

3.5.2 Evaluation

The OpenIBC prototype is subsequently evaluated regarding its power consumption, wake-up latency, achievable data rate, and packet error rate.

Power Consumption

The Power Profiler Kit II [NPP] is used to precisely monitor the consumed power. Excerpts are provided in **Figure 3.30**. The ESP32 microcontroller is not considered part of the receiver and does not count toward the determined values. The used front-end allows for a very low average power of 7.4 µW (2.24 µA at 3.3 V) in listening mode and of 8.4 µW (2.56 µA at 3.3 V) during the reception of a wake-up signal and the data.

Wake-Up Latency

The wake-up latency describes the delay between the initiation of the wake-up signal at the transmitter and its successful detection at the receiver, excluding the data transmission itself. As an example, it sums up from a burst of 1000 µs, a preamble of 1220 µs ($5 \times t_{bit}$), and the pattern of 1952 µs ($8 \times t_{bit}$) to a total of 4172 µs. To measure the latency, an output pin of the transmitter is directly wired to an input pin of the receiver, enabling the notification of an initiated transmission. The receiver then determines the time passed between the detection of the flag and the interrupt request from the receiver circuit. For 100 000 packets, the latency showed to be stable with 4215 ± 3.6 µs. The slight error of about 43 µs between the calculated and the measured latency is probably originated in the devices' internal processing.

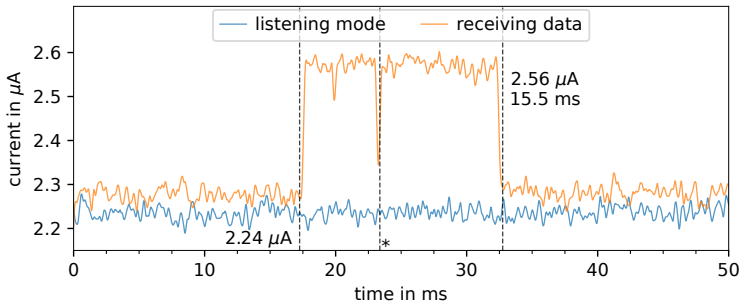

Figure 3.30: Excerpts from current measurements with the Power Profiler Kit II [NPP]. Average current consumption of the OpenIBC receiver in listening mode of 2.24 µA (blue) and during data reception of 2.56 µA (orange), after a successful pattern correlation (*). Sampled at 100 kHz and carefully denoised using a $2 \times 2^{\text{nd}}$-order zero-phase 2.5 kHz LP Butterworth IIR filter. **[C22c]**

Data and Error Rate

The achievable data rate primarily depends on the packet error rate (PER) which is the ratio of erroneous packets and number of packets sent. High data rates require shorter symbols and hence a wider filter bandwidth for a faster transient response of the signal envelope. This way, more ambient noise is injected which results in more symbol errors. Lower data rates are, therefore, more robust because larger symbols are transmitted which are less affected by less noise. A single subject (male, 29) wore the prototype at one wrist while touching the transmitter's electrode with the palm of the other hand. The arms were kept wide apart and away from objects which would improve the direct coupling between the electrodes. On three days with different weather conditions, the transmitter sent 100 000 wake-up sequences at a rate of 100 Hz, each time taking 16.7 min. At the maximum data rate of 4096 bit/s, with a wide passband but lower sensitivity (27 kΩ shunt resistor enabled), the achieved average PER is 320.0×10^{-6}.

Limitations

Although the AFE AS3930 is quite sensitive (100 μV_{RMS}), the presented prototype does not enable fully wearable systems yet. While the receiver can be worn floating, at least the transmitter is still required to be grounded, to reduce the channel loss by about 40 – 45 dB. Moreover, the applied 125 kHz LF band is located at the lower bound of the frequency spectrum applicable in IBC [Bae+12; Cho+09; KTL14] (**Section 3.1.2**). The use of the 13.56 MHz HF band instead would not only reduce the component sizes, but also increase the potentially achievable data rate to NFC levels, toward a maximum of 424 kbit/s. It might also eliminate the need to expand C_{rx} by C_{add} for resonance, diminish C_{load}, and hence reduce the channel loss loss_{dB}, as described in **Equation 3.9**.

3.5.3 Results

This last case study has presented the open-source IBC receiver OpenIBC that is based on the commercially available AS3930 wake-up receiver front-end, originally designed for reading active RFID tags. Its high input impedance enables the capacitive signal reception in the 125 kHz LF band with up to 4096 bit/s and a PER of 320.0×10^{-6}. The designed, simulated, and evaluated prototype draws a low power of 7.4 µW when listening to the channel and 8.4 µW during correlation and data reception. The sensitivity of 100 μV_{RMS} is not sufficient for the intended use in fully wearable applications yet. Therefore, adding a pre-amplifying circuit might allow to further improve the front-end's input impedance Z_{in}, lower the load capacitance C_{load}, and in turn improve the sensitivity.

3.6 Summary and Discussion

Since its invention in 1995, research in IBC continuously pushes the boundaries of what is possible. The results and prototypes have, however, never reached the market and remained closed-source. Without the required resources, manpower, and the background in chip design, catching up recent IBC research seems impossible. Therefore, potential applications as well as concepts for more intuitive human-computer interaction and their impact on the user experience have not been explored yet. This Chapter presented four case studies that made certain trade-offs to approach the target of an open-source solution for IBC communication step by step. It is, however, important to consider that the presented techniques are not intended to compete with cutting-edge research in IBC, especially not in terms of data throughput and efficiency. Instead, the use of accessible, commercially available devices and components was intended to pave the way for applications that, when finally made available, can directly be translated to future single-chip solutions, specifically designed for IBC.

The first case study addressed this issue by replacing the unsteady environmental ground through an additional layer of conductive clothing with a local reference potential. It extends the range of near-field coupling and thus enables data to be sent reliably across the user's body using capacitive coupling. This way, the channel's bottle neck is removed by significantly improving the devices' coupling to a nearby potential that results in a significantly lower channel attenuation. In addition, the conductive fabric forms a Faraday cage that shields ambient noise sources and considerably improves the SNR. Also the implementation effort of the tranceiver modules is lowered significantly, since neither LC resonator circuits to boost the transmitter's amplitude, nor complex filters to extract data from a noisy signal are needed. The presented prototype for such data transmissions has been evaluated for the communication between wrist and upper arm. The utilized PWM scheme is based on three duty cycles to not only represent the binary values, but also to continuously recalibrate the symbols, and to synchronize the bit stream of up to 200 kbps at 250 kHz. The reception consumes with 18.9 mW more energy than the transmission with 7.6 mW, caused by the higher clock frequency of the microcontroller and the dissipative analog front end. Due to obligatory conductive fabric layer, the design suits especially applications that utilize any kind of functional clothing, vest, or all-in-one suit.

The second case study tried a different way by using the analog ECG front-ends of commercial wearable devices. Those are carefully designed regarding their energy efficiency and the sensitive detection of tiny signals on the human skin. The demonstrated scenario shows a desktop, with an embedded transmitter beacon that capacitively induces artificial landmark signals into the user's body. The presented methods allows for the intentional or incidental and implicit contextualization of wearable devices by touching, approaching, or passing certain areas, surfaces, or objects equipped with transmitter beacons. The evaluation is based on three experiments. First, the ambient noise captured by the ECG AFE has been characterized. Second, the optimal parameters and the system's performance have been evaluated in a controlled setting, investigating the coupling between the user's body and the transmitter beacon in three different ways: a) directly touching the electrode, b) touching the desktop, and c) leaning back in the office chair and primarily coupling with the thighs. Third, the concept has been tested in an everyday life setting, demonstrating its feasibility and applicability in-the-wild. The signal quality primarily depends on the coupling strength between the transmitter's electrode and the user's body. Of course, also the attachment of the devices has a large influence on the captured signal. The deployment in-the-wild discovered that, moreover, the induced signal does not always

propagate throughout the entire body surface. When picking up the signal through one hand, it tends to be available only at the respective wrist. However, leaning back and coupling through the thighs showed somewhat unexpectedly good signal quality at both wrists. One reason might be that the distance between the wrists is larger than the ones from the thighs to the wrists. Another reason might be the extremely low carrier frequency that is several orders below the optimal frequency range of IBC (**Section 3.1.2**). Moreover, as already mentioned by Zimmerman [Zim95], the presumably main reason is that the "feet are the best location for [IBC] devices" since the coupling to both the body and the environment is the strongest. The proposed method uses the on-board ECG sensor of wearable devices to enable the implicit contextualization as well as the synchronization, as detailed in **Section 4.4**. Moreover, the research of [HIG16] demonstrated the use of commodity devices and their fingerprint or touch sensors to transmit signals confined to the human body. With the presented approach, now also the receiver side is provided. The concepts' combination would therefore enable wearable devices, such as wristwatches, to transmit signals via a fingerprint sensor or touchscreen, and to receive these signals using their embedded analog ECG front-end.

The third case study does not present an IBC device itself but supports the development by characterizing the typical electrode setup used in prototypes such as the one simulated and evaluated in the subsequent, fourth case study. Based on capacitive sensing, furthermore a novel technique for the detection of hand-washing is presented that uses the effect of grounding through touching water from a running tap. A physical model was developed and substantiated in two initial experiments with recordings from two subjects. The results show that the proposed method allows to distinguish hand-washing from other activities. In the experiments, the measured capacitance during hand-washing is distributed around $1.152 \pm 0.106\,\mathrm{pF}$ and hence separates clearly from washing gestures with dry hands around $0.671 \pm 0.065\,\mathrm{pF}$ and other activities such as arbitrary gestures around $0.793 \pm 0.325\,\mathrm{pF}$. A simple threshold on a running average is therefore sufficient to detect if the user's body is grounded through water while an additional analysis of the standard deviation allows to identify hand-washing.

Finally, the fourth case study presented a first open-source IBC receiver based on a commercially available WuRx front-end, originally designed for reading active RFID tags. Its high input impedance enables the capacitive signal reception in the 125 kHz LF band with up to 4096 bit/s and a PER of 320.0×10^{-6}. The designed, simulated, and evaluated prototype draws a low power of 7.4 µW when listening to the channel and 8.4 µW during data reception. However, the sensitivity of $100\,\mu\mathrm{V_{RMS}}$ is not sufficient for the intended use in fully wearable applications yet. Therefore, the next step is to develop a pre-amplifying circuit which would further improve the front-end's input impedance, lower the load capacitance, and in turn improve the sensitivity.

This Chapter has presented multi-varied case studies that target the common goal of implementing IBC. Case study 1 demonstrated simple way to simplify the channel circuit. This way, the approach achieves a low SNR and comparatively large signal amplitudes that do not require for sophisticated amplifier stages. The compromise of an additional conductive textile layer results, however, in a significantly higher possible data rate of 200 kbps than would be achievable with the prototypes presented in the other case studies. Case study 2 repurposed commercial ECG sensor front-ends with a high input impedance of $Z_{\mathrm{in}} > 1\,\mathrm{G\Omega}$ and a CMRR $> 100\,\mathrm{dB}$ to detect artificial landmarks induced through capacitive coupling. This way, the approach gets close to the electrical properties of IBC front-ends presented in research, but unfortunately not in terms of data rate as the sensor's sampling rate f_s of 128 Hz limits the applicable modulation frequency to 20 Hz.

Nevertheless, the study demonstrates the possibility of using very low frequencies for IBC and repurposing commercial ECG sensor front-ends for simple applications such as the contextualization of measurements. Case study 3 then paved the way toward the goal by characterizing the electrode setup used in the subsequent open-source prototype. Case study 4 finally presented a first iteration of the desired OpenIBC prototype. It repurposes RFID / NFC front-ends with a relatively high input impedance of 2 MΩ to detect capactively induced signals at a comparatively high carrier frequency of 125 kHz. Originated in the original RFID applications, the OOK or amplitude-shift keying (ASK) modulation schemes show relatively large symbols that are clearly less efficient as the PWM modulation of case study 1, but show a better tolerance against typical noise present in non-shielded system. Unfortunately, the LC filter at the input does not go along well with the small input capacitance of the electrodes. The added capacitance to achieve the resonance at the modulation frequency thus lowers the sensitivity of the circuit from $100\,\mu V_{RMS}$ down to a fraction of probably about 1:224. When this undesirably large capacitance can be avoided through a higher input impedance with less capacitance, the WuRx circuit should be sufficiently sensitive and hence enable even the reception of signals from floating transmitters.

In scope of this dissertation, the goal of developing a fully wearable open-source IBC transceiver module for research purposes has not yet been achieved. Nevertheless, the case studies pave the way toward this intent and contribute with diverse findings and insights into the requirements especially in the LF band and when using high-impedance front-ends. In addition, the two applications of implict and incidental measurement contextualization and synchronization, as presented in the remainder of this work, are feasible and already beneficial for wearable systems.

Data Availability

Researchers are encouraged to replicate and improve on this work, to develop open-source IBC transceivers and to explore potential applications. The design files and software of the OpenIBC prototype are made available for download from this public GitHub repository: https://github.com/fwolling/OpenIBC/

4 Implicit Synchronization

While single all-round devices, worn at familiar and convenient locations such as the wrist, have been standard for many years, wearables are recently evolving rather into a conglomerate of simultaneously deployed hardware units. This way, the specialized sensor nodes enable to capture complementary perspectives that allow inferring a more complete bigger picture of the user. The applied cutting-edge sensor fusion and machine learning techniques allow, for instance, the recognition of human activities or the detection of the wearer's emotional state and stress level. Based on multi-modal recordings from distributed devices, the accuracy of these systems has shown to be superior to that from a single device. However, the applied techniques substantially suffer from the inaccuracy of the devices' internal clocks, the manual temporal alignment of the sensor channels, and the recordings' unmatched time bases. Available online synchronization methods to continuously update and adjust the devices' local time are usually based on radio communication. However, the required built-in hardware interfaces are not standard, and if provided, they considerably affect the devices' battery life. In addition, these methods require the explicit interaction of the user to actively set up the network or pair the devices. Originated in human activity recognition, offline synchronization methods defer the temporal alignment of recordings to a data-driven post-processing step. They align the local time bases by matching coincident external events, such as significant motion patterns, that are simultaneously detected by the different sensor nodes. However, the achieved accuracy of these approaches is usually relatively low and depends on the quality of the obtained signals. Therefore, synchronization actions are usually performed explicitly, typically at the beginning and the end of recordings.

In this Chapter, the potential of the human body to enable the implicit synchronization of multiple distributed wearable devices is investigated. First, **Section 4.1** describes the origin of asynchronicity and then reviews the available online (**Section 4.1.1**) and offline (**Section 4.1.2**) synchronization methods. Subsequently, **Section 4.2** introduces and explains the concept of implicit synchronization. The following two Sections then present two methods that implement this concept, leveraging either the fingerprint-like signal patterns in the naturally available heart rate variability interval function (**Section 4.3**) or artificial landmark signals provided through intra-body communication (**Section 4.4**). In the end, **Section 4.5** summarizes and discusses the findings by comparing these with the research intent and other available methods.

Contributions by the Author

[W21a] **Florian Wolling**, Kristof Van Laerhoven, Pekka Siirtola, and Juha Röning. "PulSync: The Heart Rate Variability as a Unique Fingerprint for the Alignment of Sensor Data Across Multiple Wearable Devices". In: *Proceedings of the 2021 IEEE International Conference on Pervasive Computing and Communications Workshops, PerHealth Workshop*. Virtual, Germany: IEEE, 2021, pp. 188–193. ISBN: 978-1-6654-0424-2. DOI: 10.1109/PerComWorkshops51409.2021.9431015.

[C21b] **Florian Wolling**, Cong Dat Huynh, and Kristof Van Laerhoven. "IBSync: Intra-body Synchronization of Wearable Devices Using Artificial ECG Landmarks". In: *Proceedings of the 2021 ACM International Symposium on Wearable Computers*. ISWC '21. Virtual, USA: ACM, 2021, pp. 102–107. ISBN: 9781450384629. DOI: 10.1145/3460421.3478815.

[J22b] **Florian Wolling** and Kristof Van Laerhoven. "IBSync: Intra-body synchronization and implicit contextualization of wearable devices using artificial ECG landmarks". In: *Frontiers in Computer Science* 4 (2022). DOI: 10.3389/fcomp.2022.915448.

4.1 Synchronization Methods

Modern wearables successively develop from single all-round devices toward a collection of simultaneously deployed hardware units [Ome+21] that allow to cover multiple, complementary perspectives [LL22]. The application of cutting-edge signal fusion, data analysis, and model training on the collected multi-modal and multi-device data, thus, allows to infer the user's bigger picture, resulting in more distinct and successful interpretations and classifications [Wes+09; SS16; Lu+20]. As previously discussed in **Section 2.3.2**, datasets obtained from such conglomerates often substantially suffer from the inaccuracy of the devices' internal clocks, the manual alignment of the sensor channels, and, therefore, the recordings' unmatched time [Ohm+06; Xu+17; Wan+19; Goo+22]. In the order of seconds, the improper alignment of interpretable observations may result in "wrong conclusions about the analyzed situation" [BDB21]. Especially for the application of modern machine learning techniques on IMU motion data and more definite modalities of physiological signals, such as ECG and PPG, already slight inaccuracies and jitters in the order of milliseconds can disassociate coincidences [Ohm+06]. In this way, the learned blurry models inevitably result in a poor classification [Wan+19] and the valuable information contained in the data, for example the "correlation and possible causation between multiple measurements", can be lost [BGJ17].

The influence of time discrepancy on the accuracy of data analysis and fusion in multi-wearable systems has been investigated and modeled by Xu et al. [Xu+17]. Accordingly, time discrepancy is originated in different levels of factors such as clock drift, processing delay, and network latency, which result in timestamps with scale and frequency inconsistency, drift, or even absence. In addition to the inherent inaccuracy due to production, oscillators are also affected by aging in the long term and even largely affected by environmental conditions such as temperature, barometric pressure, acceleration, magnetic fields, and electromagnetic noise in the short term [Vig92]. Because ones with a higher accuracy come along with increased costs and energy demands [BDE13], developers of commercial devices are often forced to compromise [TA19] and hence do not use the most accurate clock technology available, which amplifies the effect of drift and the need for adjustments [BGJ17]. Typical accuracies range from $\pm\,500$ ppm of CMOS MEMS oscillators over $\pm\,20$ ppm of conventional crystal oscillators (XO) to $\pm\,5$ ppm of temperature-compensated crystal oscillators (TCXO) [TA19]. However, even with highly accurate clock sources, a drift over time will sooner or later be perceptible [TA19].

Experiments with smartphones have revealed an accumulated clock drift of more than 150 ms per day in the worst case [LKK+17]. While mobile phones nowadays usually have access to the internet, can hence continuously update their local time and calibrate their real-time clocks (RTCs), most off-the-shelf wearable sensing devices do not support the synchronization during operation [BAL09]. They would require specific built-in hardware, an interface such as a bidirectional radio link, and the protocol overhead [LYK06; vR03; Wan+19] would presumably exceed the devices' small energy budget [BGJ15a].

The synchronization of distributed, multi-device systems is a "longstanding challenge in HCI, neuroscience, [and] psychology" [LL22] as well as in digital health, with different devices collecting multi-modal physiological signals [XDH22], and in HAR with multiple body-worn sensing devices [BAL09; Wan+19]. Diverse synchronization approaches have been proposed "using (1) dedicated hardware; (2) dedicated software; or (3) alignment algorithms", but tend to be "vendor-locked, non-generalizable, or difficult to adopt in practice" [LL22]. In general, the methods are typically divided into the two classes online and offline synchronization. While online approaches rely on network technology to up-

date, negotiate, and adjust the time base at runtime, offline approaches detect and exploit external events but defer synchronization to a data-driven post-processing step.

Since the number and status of wearables devices can change dynamically in these systems, they require a synchronization technique that achieves the "necessary degree of precision" [Xu+17]. The obtained time can either be the relative local network time or an absolute time such as the coordinated universal time (UTC). Attached to Greenwich mean time (GMT), it is "the basis for the world's civil time", intended to be independent from the location on earth and its 24 time zones, "and it is kept using a precise atomic clock and the Earth's rotation". [Wor]

In contrast to large computer networks, body-attached distributed systems often require only local synchronization, relative between the nodes. As stated by Elson et al. [EGE02], referring to the first formalization of Lamport [Lam78], in most applications the "causality is more important than absolute time".

In general, online and offline methods have in common that the synchronization is done consciously. The user has either to network the devices for their coordination or to perform specific actions to delimit and align the recordings. In contrast, the concept of implicit synchronization might use both online and offline methods but is intended to take a back seat and not to require any intentional interaction of the user. The two subsequently proposed methods are either entirely passive, based on the naturally available heartbeat (**PulSync**: **4.3**), or semi-passively using artificial landmarks to unidirectionally obtain information from deployed beacons to align the time series (**IBSync**: **4.4**).

4.1.1 Online Synchronization

A long history of research has lead to a large variety of available methods for the continuous coordination and tuning of devices' local clocks and the synchronization of time in distributed systems at runtime. While online methods are generally based on communication and networks, their requirements on temporal precision and accuracy as well as the limits in costs and complexity are very different and application-specific. Time obtained from a network can either be the relative local network time or an absolute time such as UTC. Thereby, a unidirectional link tends to be less accurate, since network latency cannot be measured, while the negotiation of a common network time via bidirectional communication typically achieves a higher accuracy [Fai+20].

The network time protocol (NTP) of Mills [Mil91] has established as the most popular method to obtain absolute time in LAN as well as wide area networks, e.g. the internet (WAN) such as the internet. The applied master-slave scheme is, however, the simplest way to synchronize both wired and wireless networks. The theoretical error of NTP ranges from several milliseconds to 100 ms [Mil11]. Luo et al. [LKK+17] investigated the temporal drift of smartphone clocks and developed a rapid clock synchronization method that uses publicly available NTP servers. The experiments revealed an accumulated clock drift of more than 150 ms per day in the worst case and also NTP showed to be noisy with errors up to 1800 ms in one request. The presented synchronization method reduced the error to 27 ms on average and to a maximum error of 411 ms.

More advanced protocols such as the precision time protocol (PTP) of Lee and Eldson [LE04], the simple network time protocol (SNTP) of Mills [Mil06], the reference broadcast synchronization (RBS) of [LYK06] [LYK06], and the lightweight time synchronization (LTS) of van Greunen and Rabaey [vR03] have also their rationale for existence in cases in which the precision of NTP is insufficient or its implementation is too complex. These protocols as well as their modified, often application-specific derivatives can achieve sub-millisecond performance under ideal conditions, but they "suffer considerably in the

case of a lack in stable latency and asymmetric connections" [Fai+20].

Although unidirectionally provided, global navigation satellite systems (GNSS) allow to obtain time with very high accuracy: the popular global positioning system (GPS) < 25 ns, GLONASS < 1 µs, BeiDou < 100 ns, and the European Galileo < 50 ns [ESA20]. However, time from GNSS suffers considerably if a clear line of sight and good signal quality cannot be guaranteed, e.g. in indoor applications. Although primarily relying on GPS, "system faults common to environmental sensing systems" can result in "large time offsets" which were repaired using one of the first offline synchronization approaches [Luk+09]. Moreover, the receiver circuits tend not only to be too complex, large, and costly for most wearable applications, but are also inapplicable when energy efficiency and resulting battery life are the critical parameters as in long-term deployment of wearable devices [PLP20].

In wireless sensor networkss (WSNs), especially energy efficiency is a critical parameter that decides about battery life and, therefore, about the systems' required maintenance, which is desirably low for deployed systems [Cho+19]. The surveys of Sundararaman et al. [SBK05] and Lasassmeh and Conrad [LC10] provide a detailed overview of common online synchronization techniques applied in WSNs.

In body area network (BAN), the human body is the habitat for multiple nodes attached to it and relatively close to each other. Although superior in terms of energy efficiency and accuracy, wired links for a shared master clock are commonly perceived as less flexible, obtrusive, and even uncomfortable. Advances in conductive textiles, such as in [Pou+16], would, of course, easily enable to share a master clock, and even to supply the modules with power at once. For wired low-power wearable sensor networks with the requirement of high precision, an average clock skew of about 4.6 ns has been achieved, which is said to even outperform PTP [DFT16]. Nevertheless, wireless radio communication still remains the preferred technology in wearable applications. Not only the methods applied in WSN but in particular those running on wearable devices, as discussed in [Zhe+14], primarily focus on energy efficiency. As discussed in [Bar+08; MK10; Nag+15; Toc+22], radio transmission suffers largely not only from the general inefficiency of radio transmission due to a lossy air channel, but in particular from shadowing effects due to the vicinity to the water-rich tissue, which causes a variable path loss [Hal+07]. Based on the short-range wireless standard Bluetooth, approaches for synchronized measurements in body sensor networks (BSNs) achieved accuracies ranging from 3.5 ms [RR07] over 100 µs using the sniff mode [Pfl+14] to even 17.4 µs utilizing the spark state mechanism which, however, is not supported by all devices [Rob05].

4.1.2 Offline Synchronization

Instead of regularly obtaining temporal information from a network and repeatedly negotiating a general time base with the other nodes at runtime, offline synchronization techniques exploit external detectable events to align the recordings from distributed sensing systems in a post-processing step. Therefore, these techniques are still only relevant if online synchronization cannot be applied, either due to a lack of built-in hardware support, such as a missing radio module, or due to resource-constraints and a limited battery. The synchronization process is data-driven, solely based on the information available in the measurements. A central hub, usually a computer, collects the irregularly transmitted measurements and performs the synchronization, as it usually provides more computing power and is less constrained regarding energy demands than the sensor nodes.

In 1976, Knapp and Carter [KC76] described the fundamental concept of determining the "time delay between signals" from multiple sensor nodes. Two time series with "uncorrelated noise" are compared using a cross-correlation function and the "time argument

at which the correlator achieves a maximum is the delay estimate". Based on this concept, the data driven time synchronization (DDTS) of Lukac et al. [Luk+09] was one of the first applications of this offline concept and aimed at repairing the timestamps of measurements from 100 distributed seismic sensors. Primarily synchronized online through GPS, the system suffered, however, from large time offsets due to "system faults common to environmental sensing systems". To correct the received temporal information, the approach leverages microseisms, regularly occurring yet irrelevant seismic waves in the ground. By applying a model of the microseisms' propagation, the error has been reduced to an offset of 0.05 to 0.2 s. The model requires, however, information on the sensor deployment, the sensor locations and their distances respectively.

4.1.2.1 Stationary Settings

As recently stated by [XDH22], "it remains challenging to obtain precise time synchronization of multimodal physiological signals collected through different devices". Therefore, diverse approaches targeted the synchronization of different sensing devices and modalities, to conduct studies on their performance and comparability, or signal fusion. With the Observer XT, Zimmerman et al. [Zim+09] continued the development of a successful tool for the collection, integration, and synchronization of multi-modal signals. It enables the automatic synchronization of diverse sources such as video cameras. Proprietary sensors, e.g. for physiological signals, are connected through an external DAQ which requires a trigger pulse from the computer to align the time series with system time. Alternatively, visual and auditory events can be used to manually synchronize sources that are not connected to the computer. With OpBox, Kimchi et al. [Kim+20] provide an open-source hardware and a MATLAB toolbox for the simultaneous multi-subject recording of EEG, EMG, event triggers, and rotary encoders. The sensor channels as well as supplementary video streams from standard webcams are synchronized in software. The evaluation with an IR LED showed an accuracy of 66.1 ± 13.2 ms. The system of Notaro and Diamond [ND18] also allows the ms-accurate simultaneous recording of electroencephalography (EEG), gaze (eye tracking), event triggers, and a screen-capture. Xue et al. [Xue+17] evaluated different co-registration methods and the use of a trigger signal to determine the sampling onset for the alignment of EEG and gaze recordings from two computers. Shah et al. [SCL20] synchronized an eye tracker and supplementary videos by means of a blinking IR LED which light is visible in both recordings. In order to investigate the feasibility of emotion recognition outside the lab, Ragot et al. [Rag+18] developed a software to synchronize the HR and EDA signals from one laboratory (Biopac MP150) and one wearable (Empatica E4 [EmE4]) sensing device. And recently, Latifzadeh and Leiva [LL22] presented the tool Gustav that enables to "orchestrate the recording of sensory signals across devices and computers". It consists of two components, "an event logger and a file post-processor".

4.1.2.2 Motion Signals

In HAR the sensor channels from distributed sensing devices are often aligned manually. Therefore, also research aiming at the automatic offline synchronization can mostly be found in context of resource-constrained, battery-powered devices of this domain. Bannach et al. [BAL09] established the concept of aligning time series from multi-modal wearable and ambient sensors through the correlation of predefined signal patterns. The approach is not intended to compete with network-based online methods and rather aims at the synchronization of systems of stand-alone devices without the capability of synchronization via wireless communication. Synchronization actions of the wearer, significant motion

patterns such as "clapping, jumping, and hitting a surface", are detected and used as "characteristic signature" to automatically align signal segments from different sensors capturing e.g. motion, sound, or force. The content-based approach achieved a synchronization error of about 0.3 s for more than 80 % of the data. It therefore enables to reduce communication to a unidirectional channel or even an offline alignment of the recorded data. In this way, not only the design of devices without wireless connection becomes easier, but also the use of sensors from different manufacturers and with insufficient built-in synchronization support is hence possible. The authors mention, however, that "in realistic scenarios achieving high synchronization performance is not trivial". Especially the quality of event spotting is essential for the accuracy, and for different sensing modalities specific spotting algorithms are required. The required synchronization performance, however, would also largely depend on the target application. An accuracy below 1 s is said to be sufficient for the recognition of "motion-related activities in daily life" while a performance better than 0.1 s is considered as "typically not needed".

Based on this fundamental concept, more sophisticated approaches for the data-driven offline synchronization have been proposed. Bennett et al. [BGJ15b] developed two methods for the selection of "alignment points". The first one is based on signal templates that are aligned using dynamic time warping (DTW) [BC94] and a technique from image registration [PMV03]. The second one is based on entropy, the statistical measure of randomness in a signal [CT01]. While the template-based approach results in an average error of 49 ms, the entropy-based approach achieved a considerably lower average error of 8.6 ms, less than two samples at a clock frequency of 200 Hz respectively. The subsequent work [BGJ15a] introduces the detection of so-called "physical and cyber couplings" between the interacting signals of multiple wearable sensors. Couplings are defined as events that occur at sensors at the same global time, regardless of the devices' local time. Dijkstra's algorithm [Dij59] is then applied to find the shortest path and, therefore, to determine those signal couplings that minimize the overall clock drift in the system, resulting in a decrease in average drift of about 60 %. An additional outlier detection further reduced the median drift error from 66 to 98 % [BGJ17].

Wang et al. [Wan+19] presented an advanced method which combines the single-time use of the energy-demanding NTP with the continuous identification and alignment of "context markers". Similar to the previous signal couplings, these are physical actions which are known to have been detected simultaneously by multiple sensors. In contrast to predefined synchronization actions, context markers are incidentally performed throughout the entire recording and do not interrupt the experiment. The approach has been tested with multiple Myo armbands that, before being attached to the user, have been initialized by hitting the table they are placed on. This seismic event creates a sequence of simultaneous pulses in the time series that allow to eliminate missing inserted events as well as temporal jitters. The method reduced the synchronization error to 20 ms in comparison to the exclusive use of NTP with 250 ms or of context markers with 1312 ms.

Instead of explicit synchronization actions, signal couplings, or context markers, yet similar to the entropy approach [BGJ15a], Hölzemann et al. [HOV19] utilize the uniqueness of variations present in accelerometer signals from IMUs to align independently recorded time series. For a successful alignment, with an accuracy in the order of few seconds, sufficient periods of resting with low variations as well as sufficient similarities and accordance in the signals from different locations, such as head and wrist, are required.

In general, the consciously performed synchronization actions have to be performed "at least once at the start of a data collection" [BAL09]. Since longer recordings are increasingly affected by drift [BGJ15b; Fai+20], at least one alignment point at the beginning

and one at the end are advisable to adjust the sampling periods and, therefore, to compensate the difference in pace. Irregularly repeating events throughout the recording can improve the achieved accuracy by reducing ambiguity [BGJ15a; BGJ17] but, in this way, the performed actions also become less incidental yet more cumbersome and obtrusive.

Also the recent online synchronization approach of Faizullin et al. [Fai+20] exploits motion to improve the accuracy of SNTP to several microseconds. For applications such as "multi-camera bundle-adjustment or [...] geo-localization for mapping", it assumes gyroscope sensors to be attached to a rigid body and therefore to be exposed to "equal angular velocity". This assumption is, however, not valid for the complex human body with "hundreds of degrees of freedom" [Ron22] and the sensors being attached to soft tissue. Placed at diverse locations, the captured signal patterns of performed actions can show up different in shape and at different time of arrival to the sensors due to delays in performed motion sequences and the inertia of the body parts [Lop+15]. The signals from accelerometers can for example show significant offsets: the "squat jump with arm swing" for instance would show partly independent signal patterns at the arms first, followed by a delayed pattern at the torso and the legs [Har+08]. Like HAR also motion-based synchronization methods suffer from inaccuracies due to loose device attachment [Bañ+12; Zha+18] and soft tissue deformation [TB90; Kim+93; Lop+15; Wu+16; Ron22; UA22].

4.1.2.3 Other Signal Sources

Ahmed et al. [Ahm+20] presented a novel approach that does not rely on motion patterns but specifically aims at the multi-modal detection and analysis of cough events across multiple devices. Coughs are high energy events with a concise length of 0.3 to 0.7 s and simultaneously perceptible in audio and acceleration measurements. The alignment of these sporadic events, by means of a normalized cross-correlation, resulted in an average synchronization error of 46 ms.

Spilz and Munz [SM21] developed a technique for the synchronization of wearable magnetic, angular rate, and gravity (MARG) sensors, IMUs enhanced by integrated magnetometers. Before and after the actual use of the sensors, those are put into a docking station that is equipped with an array of inductors, one underneath each device. Switching the coils for eight seconds at a frequency of 6 Hz is sufficient to enable the synchronization of the devices' recordings by means of the magnetometer channels. Sampled at 100 Hz, the accuracy of the method would naturally be limited to 10 ms. By leveraging the coils' transient response as a characteristic, a ploynomial fitting allows for the alignment even at a sub-sample accuracy of less than 2.6 ms.

Based on the noise-induced phase synchronization phenomenon [TT04; NAK07], Harashima et al. [HYH12] exploited the noise present in the measurements from the natural environment, i.e. temperature and humidity, to synchronize WSNs. It is assumed that all sensors observe the same environmental conditions and are, therefore, exposed to the same noise. If aligned, the cross-correlation of the time series from neighboring sensor nodes reached a coefficient of 0.8 or higher. Similarly, Vaz et al. [Vaz+15] proposed the correlation and alignment of physiological signal channels by means of the inherently present white noise. The achieved sub-ms accuracy is, however, bought dearly through high sampling rates of 2 and 20 kHz.

The entirely different approach of Li and Tan [LT10] presents a time division multiple access (TDMA) protocol for medium-access control (MAC) which utilizes the rhythm of the human heartbeat, instead of periodically broadcasted radio beacons, to schedule the time slots in star-topology wireless BSNs. Based on the assumption that body-worn devices have access to the wearer's vital signs, the "naturally synchronized" information

are used to allocate time slots and, thus, achieve a coarse synchronization without the need to enable the energy-consuming radio to receive periodic timing information. However, the changing IBIs and, hence, the changing duration of the time slots according to a varying HR are not considered.

Published after **[W21a]**, the method proposed by Xiao et al. [XDH22] follows a similar approach, aiming at the synchronization of cross-device multi-modal data with a common sensor modality such as ECG. The cross-correlation function is directly applied to signal amplitudes "without the need for identifying signal landmarks". Two channels of a 12-lead ECG are used to simulate inherently synchronous data from locations associated with smartwatches (lead I) and ECG patches (lead V2). A 30 s sample window, chosen as a trade-off between performance and efficiency, resulted in a remaining inaccuracy of 0.29 s. The authors state that the method "can be readily applied to other common physiological signals [...] such as PPG, electrodermal activity signal, etc.", which is, however, questionable as discussed into detail in **Section 4.5**.

To be able to analyze the level of agreement between HR estimates, Alfonso et al. [Alf+22] proposed a method to align the time series from commercial wearable PPG sensors with the instantaneous HR derived from ECG as the gold standard. The approach is based on an optimization which minimizes the total error between the irregularly sampled ground truth values and their closest HR estimates, averaged and with a low but regular update rate. This way, the method avoids the application of linear interpolation. The method compares to the implicit synchronization approach published in **[W21a]** and is, therefore, also discussed in detail in **Section 4.5**.

4.2 Concept

The concept of implicit synchronization is based on the idea of "implicit human-computer interaction" of Schmidt et al. [SGM00] that describes "a shift [...] from explicit interaction [...] towards a more implicit interaction based on situational context" (**Section 3.3.2**). Therefore, it follows the vision of "Augmented Interaction" by Rekimoto and Nagao [RN93] which "aims to reduce computer manipulations by using environmental information as implicit input". This trend is visible, for example, in previous research on offline synchronization methods (**Section 4.1.2**). As an alternative to conventional online synchronization techniques, these started with explicit synchronization actions such as specific motion patterns [BAL09] and continued with unspecified, less obtrusive, and more incidental actions as reference points for the alignment of sensor channels and time series [BGJ15b; Wan+19]. The process finalized in the most general notion of information possible, the use of variance [HOV19] or noise naturally being present in signals [HYH12; Vaz+15].

Diverse prototypes [Sch00; Phi+04; FPR05; Wan+07; Ber+10] have been presented to obtain "knowledge" [Ber+10], or more generally information, by grasping "augmented objects" [Fel+05]. However, "Mobile and wearable interfaces [...] usually require more attention than is appropriate and often fail to do so in a natural and socially acceptable way". In this dissertation, the human body is interpreted as a kind of augmented object which devices could discretely and unobtrusively be attached to and which they can obtain valuable information from. These information can either naturally and inherently be available, i.e. the primary vital signs (**Chapter 2**), or artificially provided for this purpose, i.e. induced by means of IBC (**Chapter 3**). Furthermore, Wellner et al. [WMG93] describe "Computer-augmented environments [that] merge electronic systems into the physical world instead of attempting to replace them". However, these systems "require a complex, distributed infrastructure, precise alignment between the real

and electronic worlds". In context of this research, the "alignment" is interpreted as temporal alignment, and hence as the synchronization of multiple devices among themselves as well as with a common real time.

In the understanding of this work (**Figure 1.2**), explicit synchronization requires conscious interaction with and manipulation by the user, such as the active pairing of wireless devices or the performance of specific synchronization actions. Moreover, explicit methods may use both online and offline techniques, and are not tied to either one. In contrast, implicit synchronization is considered as the necessary step toward ubiquitous computing by "seamlessly bridging the gulf between physical and virtual worlds" [Wan+99]. Implicit methods do not require the user's conscious interaction and manipulation, and deployed devices do not demand for attention, which makes such systems more unobtrusive.

With the advances in energy efficiency and ultra-low power computing, concepts for "intermittent computing" become necessary [HS17; Luc+17; MA17; Win+20]. These allow devices equipped with energy harvesters and very limited energy storage to nevertheless effectively and reliably process data whenever there is just enough energy available. Analog, implicit synchronization is intended to enable also the intermittent synchronization of devices whenever a synchronization signal is available, simultaneously observable by all relevant devices. This implies, however, situations in which a device does not have the necessary energy to receive the synchronization signal. Whenever a stable and reliable synchronization signal is available, even if only for a fraction of time, the devices can fetch the required information to either adjust and calibrate the local time in case of the online method, or align and adjust the time series in case of the offline method. According to Lucia et al. [Luc+17], "Distributed collections of intermittently operating devices must interact with one another via radio" which is an essential issue because "The cost of communicating is high". They conclude that "Synchronizing a collection of intermittently operating devices is an unsolved problem and a communication between unsynchronized, intermittent end-points is only successful if both are coincidentally operating for a long enough time, at the same time". The proposed concept also addresses this problem, even though it will not be able to solve it completely, since at least a part of the devices must continuously be active and listen to the signals provided by or through the human body. The combination of energy harvesting and energy-saving sensor or receiver front-ends might, however, one day make it possible to solve the issue entirely.

From the perspective of the user, by using implicit methods, the synchronization of devices turns from an active decision, such as pairing devices or performing certain gestures, to a more incidental resource. This way, a better signal quality, due to the improved timing and a more accurate alignment of coincident events, will achieve more accurate inferences. Furthermore, it can also help to minimize labeling efforts and overhead [Wan+07]. Consequently, systems do not necessarily require radio modules and bidirectional communication interfaces, which always come at cost of a considerable protocol overhead [LYK06; vR03; Wan+19]. Therefore, implicit synchronization techniques would help to minimize power consumption and might eventually support the implementation of devices running from harvested energy only.

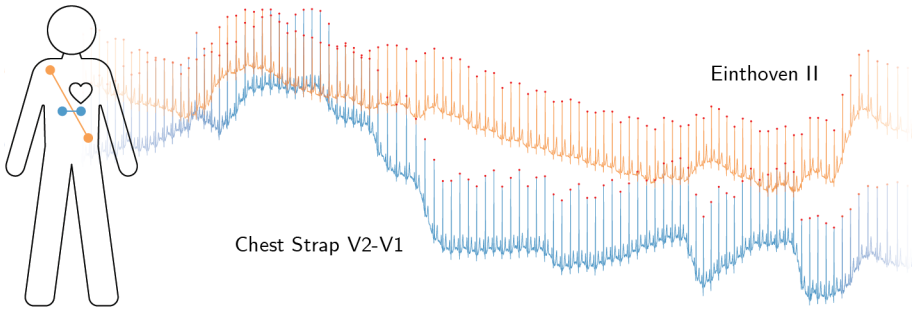

Figure 4.1: The measurement setup (left) uses an exercise chest strap at the torso, resembling a V2 – V1 ECG lead (blue), and the traditional Einthoven II ECG lead (orange). At the right, an excerpt from the "sitting" recordings of subject 23 [HP18] shows non-stationary physiological signals, superimposed by baseline wander; V2 – V1 lead (blue), II lead (orange); identified R peaks (red); matched by the PulSync method. **[W21a]**

4.3 Method 1: PulSync

The first synchronization method, named as PulSync **[W21a]**, enables to align the recordings from multiple wearable devices solely based on the readings of the wearer's HR. The previous **Chapter 2** has introduced different measurement principles that allow to detect the human heartbeat throughout the entire body surface. Accordingly, signal source can potentially be any modality and kind of sensor that allows to detect significant pulse features and to derive the IBIs. While the R peak in ECG measurements can serve as a significant fiducial point, PPG signals are less pointed but available throughout the entire body surface and even at a single site. The data-driven method enables to reduce the communication to an unidirectional streaming channel or even an offline synchronization as no bidirectional exchange of beacon signals or the negotiation of a time base is required. The human heartbeat is a ubiquitous vital sign that is continuously available. The frequent landmarks of the pulse wave are conserved and the IBI stays the same throughout the entire body surface. As described in **Section 2.1.3**, the raw measurements as well as the IBIs are superimposed by diverse physiological processes, such as respiration and activity of the ANS, and show a degree of chaos. Consequently, the derived HRV patterns exhibit a certain uniqueness and thus enable the absolute alignment of datasets, even in absence of global timestamps, through the matching and assignment of coincident pulse patterns. Moreover, the comparison of the aligned IBIs enables to determine and compensate the relative clock drift between devices with autonomous clock sources.

The presented method is set up in two stages. The first one applies a PPMC normalized cross-correlation once for initialization to match the individual HRV signals. In this way, it cancels the offset of the devices' starting times and the difference in PAT to coarsely align the local time bases. Afterwards, the second stage enables to refine the pulse peak adjustment and to determine the relative drift using a linear regression through the trend in the distances between the devices' assigned peak pairs. It can either be applied on the entire time series at once, if the external conditions and the drift are assumed to be constant, or on shorter window intervals to successively update the relative drift, if, for example, temperature changes affect the devices' drift rate.

Instead of using the raw sensor measurements, as proposed in [XDH22], the approach utilizes the IBIs as they contain aggregated information about the pulse peaks' temporal positions which are conserved throughout the entire body and independent from the measurement site. Furthermore, they contain less noise as well as no varying baseline.

4.3.1 Implementation

PulSync leverages the natural, irregular rhythm of the heartbeat that is ubiquitously and simultaneously available throughout the entire body surface of every living human being. The ECG signal's prominent R peaks are significant fiducial points and serve as coincident landmarks for the alignment. In contrast to the commonly used motion signals (**Section 4.1.2**) the pulsatile vital sign is continuously available. Even at rest, the HR results in an update rate of about 0.8 Hz (48 bpm), but it can vary within the extreme boundaries ranging from 0.5 Hz in case of bradycardia up to 3.0 Hz in case of tachycardia or heavy physical activity (30 – 180 bpm) [Deh+18; Fle+11] (**Section 2.4**). Because the HR is modulated by diverse physiological processes (**Section 2.1.3.2**), the HRV interval function [Bas+87] is highly varying and unique like a fingerprint, but also location-independent and hence identical throughout the entire body surface. This singularity enables to unambiguously align the independent recordings with their local time bases by matching the patterns of these HRV fingerprints.

The processing pipeline is illustrated in **Figure 4.2**. The heartbeat's fiducial R points in real, absolute time t^* define a unique sequence of timestamps $t_i^* \in T^*$, allocated by:

$$T^* := \langle t_0^*, \ldots, t_i^*, \ldots, t_\infty^* \rangle_{i \in \mathbb{N}} \tag{4.1}$$

These heartbeat events t_i^* are then captured by two devices, denoted as A and B, which sample the individual subsets $T_A^* \subset T^*$ and $T_B^* \subset T^*$, and hence translate t_i^* into their local times $t_A(t_i^*)$ and $t_B(t_i^*)$. These images $T_A^* \to T_A$ and $T_B^* \to T_B$ are specified by:

$$T_A(T_A^*) := \langle t_0^A, \ldots, t_j^A, \ldots \mid t_j^A = t_A(t_i^*) \rangle_{j \in \mathbb{N}} \tag{4.2}$$

$$T_B(T_B^*) := \langle t_0^B, \ldots, t_k^B, \ldots \mid t_k^B = t_B(t_i^*) \rangle_{k \in \mathbb{N}} \tag{4.3}$$

Because the devices were supposedly not started at the exact same moment, $\forall x \in \mathbb{N}$: $t_x^A \neq t_x^B$ applies. Furthermore, as the individual t_i^* are not retrievable, the relative but unique IBIs $t_i^* - t_{i-1}^*$ are used as a fingerprint pattern. The window $T_W^* = \langle t_x^*, \ldots, t_{x+w-1}^* \rangle$, with begin x and length w. Because T_W^* is contained in both overlapping sequences $T_W^* \subset (T_A^* \cap T_B^*)$, the sequence $T_W^* \subset T_A^*$ is translated to t_A and used as a search window $T_W \subset T_A$ in its counterpart T_B.

As introduced in **Section 2.1.3.2**, the sequences are first transformed into HRV interval functions to enable the matching by means of the PPMC normalized cross-correlation:

$$HRV(T_X) := \langle \{t_x, t_x - t_{x-1}\}, \ldots \rangle_{x=1}^{\|T_X\|-1} \tag{4.4}$$

As these functions are sampled by means of the irregular heartbeat, the sequences have to be linearly interpolated and resampled at the sampling rate f_{hrv} [Bas+87], resulting in $\alpha = intp(HRV(T_A))$ and $\beta = intp(HRV(T_B))$, for the devices A and B respectively.

To finally align $\alpha = \langle a_i \rangle_{i=1}^{\|T_A\|-1}$ and $\beta = \langle b_i \rangle_{i=1}^{\|T_B\|-1}$, just like the associated T_A and T_B, a windowed segment $\alpha_p \subseteq \alpha$ with position p is sliding along $\beta_q \subset \beta$ at position q. In doing so, a normalized cross-correlation with PPMC coefficient r[Pea95] is applied, as defined in equation (4.5), to determine the position $\hat{q}$ of maximum accordance $argmax_q(r(\alpha_p, \beta_q))$ between the segments.

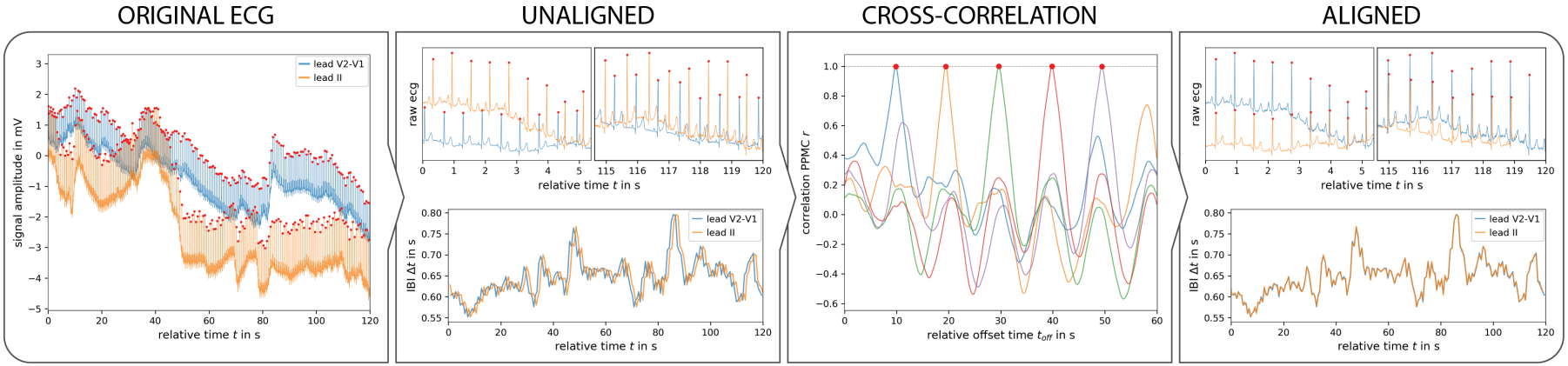

Figure 4.2: PulSync processing pipeline for the alignment of independent wearables' time bases, applied on ECG measurements. Example from dataset 716 [HP18]: subject 23, Einthoven's II (orange) and resembled V2 – V1 (blue) leads. From left to right: 1) original ECG signals, labeled with precise fiducial points at the prominent R peaks (red); 2) derived HRV interval functions (bottom) from the original, unaligned time series (top); 3) identification of the positions with maximum accordance (red) and determination of the time series' relative alignment offset Δ using normalized cross-correlation; exemplary correlation of five 60 s segments α_p with their associated reference β_q; 4) aligned interval functions (bottom) and ECG time series (top). **[W21a]**

$$r(\alpha_p, \beta_q) := \frac{Cov(\alpha_p, \beta_q)}{\sigma_{\alpha_p}\sigma_{\beta_q}} = \frac{\sum_{i=1}^{w}(a_i - \bar{a})(b_i - \bar{b})}{\sqrt{\sum_{i=1}^{w}(a_i - \bar{a})^2 \sum_{i=1}^{w}(b_i - \bar{b})^2}} \tag{4.5}$$

The resulting difference $p - \hat{q}$, based on f_{hrv}, is then multiplied by the factor f_s/f_{hrv} to translate it back into the original time base of f_s. The original time series can finally be aligned according to the determined relative offset $\Delta = \frac{f_s}{f_{hrv}}(p - \hat{q})$, by adjusting their time bases towards each other.

4.3.2 Evaluation

The performance of PulSync is evaluated using a publicly available dataset from 25 subjects, monitored with two independent ECG devices attached to the chest. The evaluation primarily aims at the demonstration of the general feasibility of the data-driven alignment, solely utilizing the HRV interval function as a unique fingerprint. Furthermore, the accuracy of the time series' alignment is determined by means of a metric based on the distance between the IBIs' proximate peaks.

Dataset

The evaluation of PulSync requires recordings from different measurement sites with the largest possible diversity. The final decision was made on the research dataset 716 of Howell and Porr from the University of Glasgow that is accessible through the university's research data portal [HP18]. The dataset contains a large collection of two-minute ECG recordings from 25 subjects. Those performed 5 different tasks of which the "sitting" subtask has been chosen due to the availability of precise R peak labels. In addition, the absence of motion artifacts in these recordings supports the evidence of the general feasibility independently from specific circumstances. As illustrated in **Figure 4.1**, two independent devices recorded the ECG signals at a sampling rate f_s of 250 Hz, pretended synchronously, with one device measuring the traditional Einthoven II lead while the second one, an exercise chest strap ECG, resembled approximately a V2 – V1 lead. The dataset provides validated R peak annotations with a very high accuracy of ± 1 sample. As no R peaks have to be identified before the derivation of the HRV interval functions, the evaluation is independent from the selection of any preprocessing and QRS detection algorithm which, in turn, ensures reproducibility of the presented results.

To enable the application of the PPMC normalized cross-correlation on the irregular sample sequences, the derived HRV interval functions are linearly interpolated and regularly resampled at f_{hrv} of 25 Hz. The evaluation is conducted with a window length w of 60 s and an overlap of 1 %, resulting in 101 segments of the V2 – V1 lead's HRV. Those are shifted along and correlated with the reference HRV interval function from the Einthoven II lead. Due to boundary effects of datasets with large displacement, the first or last few segments' r values are rejected to prevent a falsification of the results.

Ground Truth

There exist no publicly available datasets of two or more independent and at the same time hardware-synchronized ECG devices. Hence, a metric has been developed according to the fundamental assumption that ECG signals are immediately and simultaneously

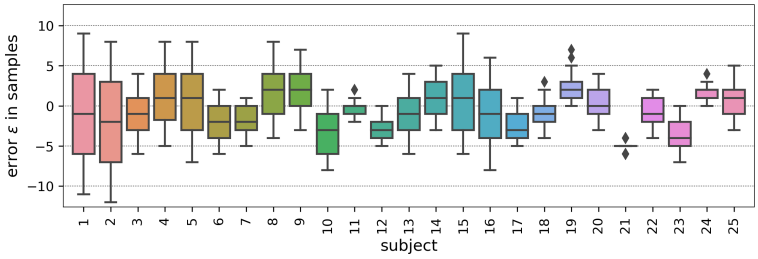

Figure 4.3: Illustration of the remaining alignment error ε for the recordings of all individual 25 subjects, which is determined through the differences between proximate peaks after the alignment and given in samples at 250 Hz. **[W21a]**

detectable throughout the entire body surface, and delays of the signal can be neglected (**Section 2.1.3.1**). In accordance with the previous assumption, **Equation 4.6** introduces the alignment error $\varepsilon(j,k)$. Applied to all proximate peaks with a minimum temporal distance, it serves as a metric of synchronicity.

$$\varepsilon(j,k) \;:=\; t_j^A - t_k^B \tag{4.6}$$

Further, it is assumed that any displacement of the time series results in an asynchronous interference pattern that generates an $\varepsilon \neq 0$, with a large standard deviation in presence of drift. In contrast, ideally aligned time series result in a minimum $\varepsilon \to 0$, and a minimum deviation as the peaks are simultaneously following the same IBI pattern, respectively heartbeat rhythm.

Limitations

Because no QRS detection has to be applied before deriving the HRV interval functions, the evaluation is independent from the selection of any algorithm and thus ensures the ideal reproducibility of the approach.

The previously made assumption, that the fiducial R points are immediately and simultaneously detectable at every arbitrary location, is exclusively valid for ECG-related measurements and the targeted accuracy in the order of a few ms. Since electrical fields propagate in tissue with a mean velocity of $1500\,\mathrm{m\,s^{-1}}$ [Buc+22], there are, of course, measurable delays in the order of $666.67\,\mu\mathrm{s\,m^{-1}}$. However, assuming a maximum distance of 1.5 m between the measurement site on the body surface and the heart, the origin of the electrical action potentials, would consequently result in a worst-case delay of 1 ms. This systematic error adds to the determined accuracy, but still results in a considerably better performance than the dataset's original, manual alignment by the authors. Furthermore, it still fulfills the requirements of the targeted applications such as HAR, which need an accuracy of at least 100 ms [BAL09].

4.3.3 Results

Figure 4.3 details the achieved accuracies for all 25 individual recordings while the overall results are summarized in **Figure 4.4**. Since the original recordings have been aligned manually [HP18], the time bases are not ideally synchronized. This is reflected by the original dataset's large initial error $\overline{\varepsilon}$ of -28.921 ± 89.015 samples (-115.684 ± 356.060 ms) for the proximate peaks with a minimum distance (middle, orange). Accordingly, the misalignment (left, red), determined by means of the presented method, range from 0.035 s (subject 5) to even 4.961 s (subject 19) with an overall average $\overline{\varepsilon}$ of 15.328 ± 428.023

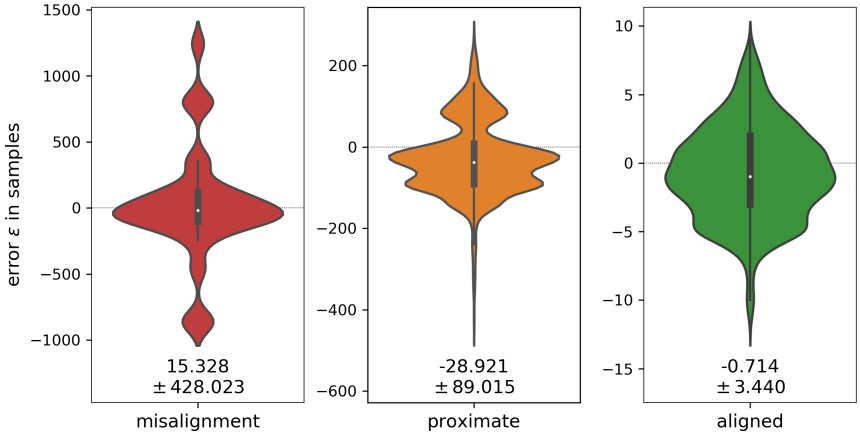

Figure 4.4: Summary of the overall evaluation results with the error ε distribution on the y-axes, given in samples at 250 Hz. Left (red): ε of assigned peaks shows initial misalignment of the original data. Middle (orange): ε of interference between proximate peaks in original, unaligned data. Right (green): ε of proximate peaks after the alignment. Note the significantly different scaling of the y-axes. **[W21a]**

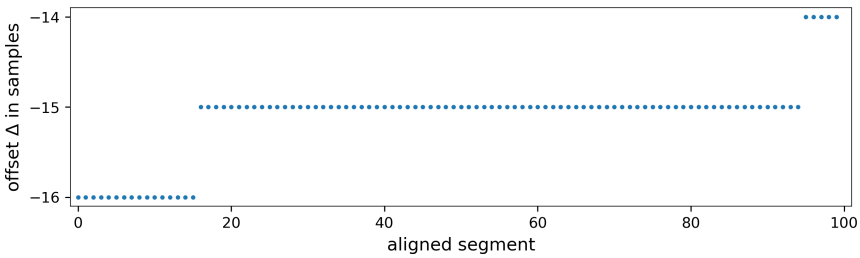

Figure 4.5: Illustration of the determined offset Δ for subject 1 with 100 matched segments, 1 of 101 rejected. Visible quantization steps demonstrate the approach's sensitivity and hence the potential to detect even small drift across individual devices' times. Significant PPMC $\overline{r}$ of $0.999\,428 \pm 0.000\,159$ with low deviation, Δ in samples at 250 Hz. **[W21a]**

samples (0.061 ± 1.712 s). In contrast, the proposed alignment approach resulted in a remaining average error $\overline{\varepsilon}$ of -0.714 ± 3.440 samples (-2.856 ± 11.427 ms). Besides small drift, another reason for the large standard deviation might be the HRV interval functions' rather coarse temporal resolution, due to a resampling rate f_{hrv} of 25 Hz, intended to limit the computational efforts, which is, however, already higher than the typically applied 4–10 Hz for HRV analysis [Gil92; Cha+18; Mor+19] (**Section 2.1.3.1**).

Without exception, for all recordings and valid segments, the PPMC r is virtually 1 and the deviation negligible as the two devices' HRV interval functions are almost identical. For signals interfered by motion artifacts, this ideal value will likely decrease according to the ratio of the affected heartbeats.

Figure 4.5 shows a typical trace of the determined offsets Δ for 100 matched segments α_p along the reference β_q. Only 1 of 101 determined r values is rejected due to boundary effects. The clearly visible quantization steps, intersecting the straight horizontal line, indicate a small drift of about 2 samples over the entire 120 s length.

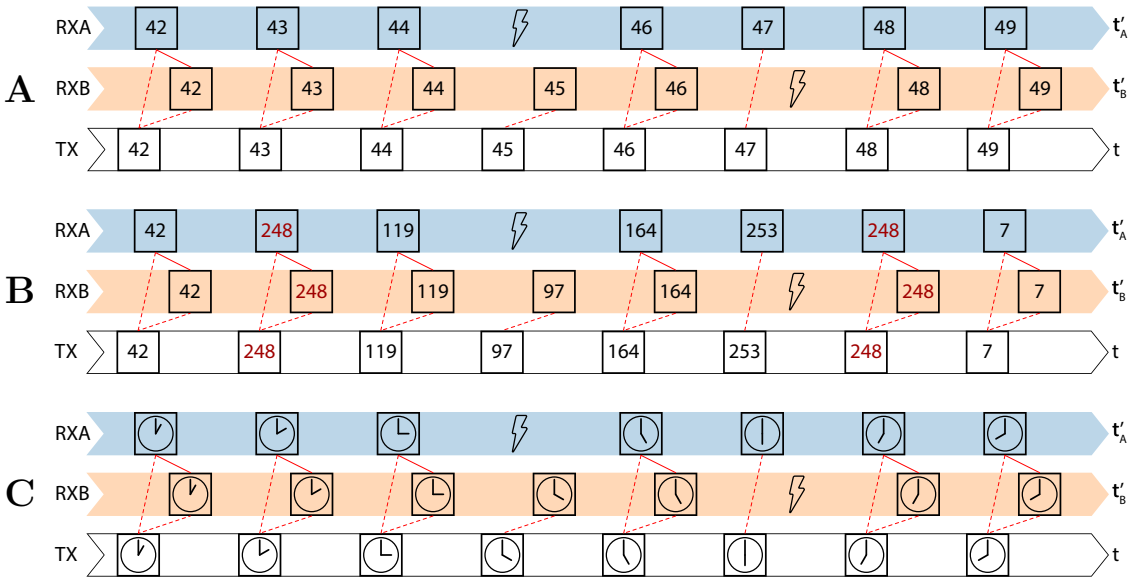

Figure 4.6: Proposed synchronization schemes using the data of the landmark packets: (**A**) incrementing packet counter as identifier for a limited recurrence interval of $2^8 \times 2.5\,\mathrm{s} = 640\,\mathrm{s}$, 10 min 40 s respectively; (**B**) sequences of random numbers as unique identifier patterns for a quasi-infinite recurrence interval of ideally $2^8!$ landmarks, lasting for 6.8×10^{499} years; (**C**) allocation of landmarks with respect to absolute time, preferentially with larger data segments of four bytes, *unsigned long* for ms-accurate timestamps. **[J22b]**

4.4 Method 2: IBSync

The second synchronization method, named as IBSync, is based on the IBC technique previously presented in **Section 3.3**. It repurposes the single-lead ECG sensors, integrated in recent off-the-shelf wearables, to detect artificial landmarks. A landmark signal is either consciously or implicitly and incidentally induced into the user's skin by touching, approaching, or passing certain areas, surfaces, or objects with embedded beacons. In close proximity, the signal is capacitively induced into the skin and propagates in tissue as a harmless displacement current. In this way, the landmarks are assumed to be made available throughout the entire body surface. The demonstrated scenario (**Figure 3.7**) shows a desktop, equipped with an embedded transmitter beacon that capacitively induces artificial landmark signals into the user's body. IBSync leverages these landmarks to synchronize wearable devices. Because the regularly transmitted landmark frames would be ambiguous and confusable, the contained data is used to discriminate them and hence enables the unique alignment of time series across different devices.

4.4.1 Implementation

The changes in the quasi-electrostatic field are virtually instantaneously detectable throughout the entire body surface (**Section 2.1.3.1**), which enables the use of IBC for synchronization purposes. The simultaneous reception of significant landmark signals by multiple devices allows the precise offline alignment of recordings at the devices' local times. Moreover, even the exact temporal allocation of landmarks and, therefore, the online synchronization of a single or multiple devices in respect to absolute time is hence possible.

4.4.1.1 Relative Alignment

A landmark L_i is defined as the i^{th} packet frame at position t_i^* in absolute time t^* and enriched with the data d_i:

$$L_i \;=\; L(t_i^*, d_i) \tag{4.7}$$

Generated by the transmitter at t_i^*, a landmark event L_i' is captured by the receiver at the local time t_i. Its deviation from t^* is given through the initial offset t_0, interpreted as the start time of the device, and the drift rate δ.

$$t'(t) \;=\; (1+\delta)\, t \;+\; t_0' \tag{4.8}$$

If not disturbed by noise and interference, which is not assumed here, the data $d_i' = d_i$ naturally remains the same and the detected landmark event is given as:

$$L_i' = L(t'(t_i), d_i) \tag{4.9}$$

After the detection of landmarks at different devices, those could be assigned to each other by aligning their closest temporal occurrence. The devices' start times t_0' and drift rate δ are, however, unknown. Furthermore, due to a continuous repetition every 2.5 s, the pure packet frames would be interchangeable and thus confusable. For any arbitrary but constant data x, all landmarks at two devices A and B are therefore prone to temporal displacement, ambiguous, and cannot uniquely be assigned to each other. Consequently, the following condition of any arbitrary assignment has to be avoided:

$$\forall a, \forall b :\; d_a = d_b = x \;\longrightarrow\; L(t_a', x) = L(t_b', x) \;\longrightarrow\; L_a' \sim L_b' \tag{4.10}$$

As illustrated in **Figure 4.6**, to actually match the coincident landmarks, the information contained in the data segment d_i between the delimiters is used. The data can transport a landmark identifier such as an incrementing packet counter (**Figure 4.6A**). To minimize the probability of a disrupted data packet, e.g. through motion during a transmission at the relatively slow symbol rate of 20 Hz, the amount of carried data per packet is limited to 8 bit. The identifier would, therefore, be unique as long as the measurement time of $2^8 \times 2.5\,\text{s} = 640\,\text{s}$ (10 min 40 s) is not exceeded. If two landmarks, detected at the devices A and B, then contain the identical data $d_a = d_b$, these must be originated in the same moment $t_a = t_b$, generated by the transmitter at the same absolute time t. In this way, the data enables the landmarks to be uniquely assigned $L_a' \sim L_b'$ and aligned despite their different local times $t_a' \neq t_b'$:

$$\forall a, \exists! b :\; d_a = d_b \;\longrightarrow\; L\,(t_a, d_a) = L\,(t_b, d_b) \;\longrightarrow\; t_a = t_b \;\longrightarrow\; L_a' \sim L_b' \tag{4.11}$$

To enhance the uniqueness beyond the aforementioned time limit, and to furthermore improve the Hamming distance between subsequent packets according to [Ham50], the data can also contain a random number as a unique landmark identifier (**Figure 4.6B**). Consequently, the probability of two random numbers following each other in subsequent landmark packets is very small, and of three or more ones in a row even infinitesimal. Theoretically, the landmarks and their order would, in this way, remain unique for $2^8!$ repetition-free permutations, resulting in a recurrence interval of 6.8×10^{499} years.

4.4.1.2 Absolute Time

The data could also be related to the absolute time, which, however, is again constrained to the 8 bit of the proposed packet scheme (**Figure 4.6C**). A longer data segment of two, three, or even four bytes for an `unsigned long` ms-accurate timestamp would significantly upgrade this concept, however at cost of robustness against disruption through motion.

4.4.2 Evaluation

The evaluation continues the technical evaluation of the case study in **Section 3.3** and relies on the measurements presented in **Figure 3.17**. To evaluate the synchronization performance achievable with IBSync, the deviation of the landmark positions from ground truth has been evaluated for both devices. The ground truth positions are given through the labels, set in context of the bandwidth determination (**Section 3.3.3.2**).

Synchronization Error

To evaluate the synchronization accuracy achievable by means of IBSync, the deviation of the landmark positions from ground truth has been evaluated for both devices. The ground truth positions are given through the labels that were set in context of the bandwidth determination before. Despite of the interference at the right wrist, the mean synchronization error ϵ of 0.761 ± 1.521 samples at the left and of 0.838 ± 2.027 samples at the right wrist are close. Consequently, the overall mean ϵ is 0.800 ± 1.792 samples or 6.249 ± 14.004 ms. Most determined landmark positions distribute evenly with an error ϵ of either 0 or 1 sample, which is originated in the quantization. In a few cases, for 161 landmarks or 7.03 %, the PPMC r did not maximize at the position of the first pulse of the preamble but matched the position of the second one instead. This effect is caused by ripple artifacts, remaining from filtering, and the correlation template being non-ideal and edgy due to its sampling with a low sample coverage $N_s = f_s/f_0$ of 6.4. Consequently, the determined landmark position skips one unit pulse period T_0 or its respective sample count N_s, resulting in a deviation of 7 samples. This alignment error can be detected, aligned, and thus corrected by validating the number of detected preamble and terminator pulses with a simple algorithm. This way, the synchronization error further decreases to even 0.360 ± 0.482 samples or 2.811 ± 3.765 ms, which now is in the order of the inevitable quantization error of ± 3.9 ms.

4.4.3 Results

IBSync enables the synchronization without communication between the sensing devices and, therefore, causes no overhead at the sensors. Based on the manually revised and validated ground truth labels, the achieved synchronization is promising with a mean error ϵ of 0.800 ± 1.792 samples (6.249 ± 14.004 ms). In 92.97 % of the landmarks, the position error was just in the order of a single sample, resulting in an ϵ of 0.360 ± 0.482 samples or 2.811 ± 3.765 ms, which is in the order of the quantization error of ± 3.9 ms. The larger deviations of 7 samples are caused by erroneous matching, due to filter ripple and a non-ideal, edgy correlation template, but are easily solvable by validating the number of detected preamble and terminator pulses. Due to the interference, all measurements at the right wrist are weaker and show a lower RSSI and rPPMC r as well as higher PER and ϵ (**Table A.1**). Considering the scenario of the controlled setting in **Section 3.3.3.2**, the coupling **a)** apparently showed the best results, but **c)** was somewhat unexpectedly good and even better than **b)** which constantly showed the lowest yet sufficient performance.

Nevertheless, the PPMC r, typically ranging from 0.845 to 0.863, enables to successfully locate the landmark packets in time and thus to decode the data segments.

The comparably slow f_0 results in a slow symbol rate, and a landmark packet with in total 24 pulse periods takes 1.2 s. Therefore, the achievable data throughput is apparently not sufficient for extensive data, not even of four bytes for an `unsigned long` ms-accurate timestamp. However, the 8 bit of data are, nevertheless, sufficient for the proposed application, to serve as a unique landmark for the temporal alignment in relative time.

4.5 Comparison and Discussion

This Chapter combined the findings from the previous ones to implement two methods for the implicit synchronization of wearable devices. The first method, PulSync, is a data-driven method for the alignment of independent time bases across multiple wearable devices and leverages the local HR measurements of the user. The derived HRV interval functions serve as a unique and location-independent temporal fingerprint that enables the distinct and accurate matching of sensor data from distributed, body-worn devices. The results demonstrate not only the approach's general feasibility, but also show a promising accuracy of -0.714 ± 3.440 samples and accordingly -2.856 ± 11.427 ms at 250 Hz sampling rate. In addition, the analysis demonstrates that allegedly synchronized research datasets can still exhibit a considerable inaccuracy, which can lead to difficulties when applying machine learning techniques on them. The evaluation also revealed the approach's potential to sensitively track the relative drift between devices' local time bases. The method is particularly promising as an accurate and energy-efficient method for wearables that provide a built-in ECG sensor, as it can be applied exclusively on recorded data and then neither requires an extra channel nor imposes an overhead on radio communication. Especially scenarios in which body-worn devices are deployed over long term, and which avoid online synchronization methods due to energy requirements, will benefit from it.

However, besides small drift, also the HRV interval functions' rather coarse temporal resolution, resampled at a rate f_{hrv} of 25 Hz to limit the computational efforts, might be a reason for the relatively weak precision, apparent from the large standard deviation. The use of wearable ECG devices at different sites is possible but requires the accurate placement of the electrodes, preferably resembling conventional leads. If a wearable is placed in line with the electric field's summation vector, then no potential difference and hence no R wave can be detected. Also the use of PPG sensors should be possible when considering the PAT, which adds to the achievable accuracy as a more or less constant bias. The key challenge of the evaluation was the missing ground truth as it was impossible to find any publicly available dataset using two independent but hardware-synchronized ECG devices. However, recent research of Xiao et al. [XDH22] presents an approach that took two independent channels from a 12-lead ECG that are already synchronized by nature. Their cross-device multi-modal synchronization method also uses ECG as the common sensor modality but directly applies the cross-correlation function to the raw signals. The achieved accuracy of 0.29 s for a 30 s sample window demonstrates and confirms PulSync being superior by deriving the more robust and location-independent HRV interval functions first. Moreover, the authors state that their method "can be readily applied to other common physiological signals [...] such as PPG, electrodermal activity signal, etc.". This statement is, however, questionable as the raw measurements of physiological signals usually exhibit tremendous differences in their DC components and trends, as is visible in **Figure 4.1**. Even the preprocessing and filtering, to remove the baseline wander and detrend the signal, cannot entirely remove these components. Beyond that, the application of the cross-correlation function on raw measurements, especially when recorded at high

sampling rates, considerably increases the processing efforts. Consequently, the analysis of the HRV interval function, interpolated at only 25 Hz, is much more efficient and also more accurate. The method proposed by Vaz et al. [Vaz+15] exploits the noise-induced phase synchronization phenomenon [TT04; NAK07] and achieves sub-ms by correlating the white noise present in physiological signals. The accuracy is, however, bought dearly through a high sampling rate of 2 or 20 kHz. Increasing the ECG sampling rate would probably also increase the accuracy of PulSync to some degree. However, the achievable performance largely depends on the quality of the fiducial point detection. The method presented by [SM21] [SM21] achieves a sub-sample accuracy of 2.6 ms for magnetometer measurements sampled at 100 Hz. The application of polynomial fitting or similar methods might also be interesting to improve on PulSync.

The second method, IBSync, uses the artificial signals induced through IBC and enables the synchronization of wearable devices through their on-board ECG sensor. Evaluated on a total of 215 min of recordings from two devices, the methods's general feasibility is demonstrated and achieved a promising synchronization error of 0.800 ± 1.792 samples, or 6.249 ± 14.004 ms at a device's sampling rate of 128 Hz respectively. Three different approaches for the synchronization of wearable devices, both offline and online, have been proposed. While a simple, incrementing packet counter guarantees only a low uniqueness for a relatively short time of 10 min 40 s, a random pattern of random numbers in consecutive landmarks can extend the recurrence interval, and thus the uniqueness, to quasi infinity (6.8×10^{499} years). The transmitted data can, however, also contain timestamps or values that are associated with absolute time. However, the 8 bit of data currently hamper the real utility of this concept, since four bytes are needed for useful ms-accurate timestamps. The achievable synchronization accuracy naturally depends on the coupling strength and the signal quality respectively. The RSSI has proven to be a suitable heuristic to identify intervals which likely contain a stable landmark signal.

The research of Hessar et al. [HIG16] demonstrated the use of commodity devices and their fingerprint or touch sensors to induce and transmit signals confined to the human body. With IBSync, the receiver side is now provided. The concepts' combination would enable wearable devices, such as wristwatches, to transmit signals via a fingerprint sensor or touchscreen, and to receive these signals using their analog ECG front-end. However, the use of devices intended for the transmission and reception of IBC signals would be preferable here. Until these are commercially available, the presented OpenIBC prototype (**Section 3.5**) might be an option for continued research. The synchronization of prototypes based on it would immediately be possible.

The achieved accuracy of both methods is clearly superior to a manual alignment of recordings and the motion-based offline methods with accuracies in the order of tens to hundreds of ms or even seconds [BAL09; BGJ15b; BGJ15a; Wan+19; HOV19; Ahm+20; XDH22]. They can even keep up with conventional online methods such as NTP with a typical accuracy ranging from several milliseconds to 100 ms [Mil11] and come close to the performance of wireless synchronization techniques with accuracies in the order of µs to few ms [RR07; Pfl+14; Rob05]. Therefore, the achieved synchronization performance is clearly sufficient for the targeted applications such as HAR with a requirement of at least 100 ms accuracy [BAL09]. However, also more demanding and ambitious applications with higher requirements on accuracy would become possible in this way.

Data Availability

PulSync is implemented as a Python toolbox for the offline alignment of ECG recordings and is made available for download from the following public GitHub repository: https://github.com/fwolling/PulSync

5 | Conclusions

This dissertation hypothesizes that the attachment of devices to the human body can enable technologies and methods that would not be possible without its presence. In three research questions, the human body is considered as a source of natural signals (**RQ 1**), as a transmission medium to provide artifical signals throughout the body surface (**RQ 2**), and as an augmented object from which information and data can be obtained to enable the implicit synchronization of distributed wearable systems (**RQ 3**):

RQ 1 In the early 2000s, a new generation of commercial wearable devices entered the market, which experienced an impressive evolution since then. Boosted by the still ongoing miniaturization, the mostly wrist-worn devices turned from a niche, applied only by members of the quantified-self movement, into lifestyle products, everyday companions for the entire society, designed to support and motivate the users to be more physically active and promising a healthier, happier, and more productive life. Research in wearable computing has recently demonstrated the advantage of using multiple distributed instead of one single all-round device, contributing with multiple complementary perspectives to infer on the user's bigger picture. Today, diverse sensing modalities allow to obtain multifaceted information from the body surface. The transfer of the medical standard modalities ECG and PPG from the hospital to the user's wrist poses, however, diverse challenges that are still not entirely solved and hence subject to research.

The wearable ECG sensing principle is kept relatively close to the original, clinical standard and is, due to passive sensing, also very energy efficient. The recording at the wrist resembles the standard lead I and, in this way, enables to obtain medical-grade measurements. Consequently, proven standard algorithms can be applied to these readings. However, the measurement is only possible at specific sites, and the line of zero potential across the chest needs to be considered when placing the electrodes. Because the formed lead needs to span a larger potential difference, capturing the signal at a single and arbitrary body location is not yet possible. At the wrist, for example, the signal is weak, and its SNR quickly drops to 0 dB, thus immediately impeding the detection of the pulsatile signal. Also, the standard DRL circuit, to suppress common-mode interference such as 50 or 60 Hz humming noise from the power line, can improve the signal quality only up to a certain degree. However, the recent development of high-Z front-ends, with input impedances beyond several GΩ and very high CMRR beyond 80 dB, is attempting to solve this problem. Therefore, the reliable and continuous ECG measurement at a comfortable location, such as the wrist, will probably be possible one day.

In the meantime, PPG already enables the continuous HR measurement at any sufficiently perfused body position. In contrast to ECG, the principle required a larger adaption from the clinical pulse oximetry in transmission mode to the reflective mode applied in modern fitness trackers at the wrist. The active sensing principle requires to illuminate the skin with high-intensity LEDs to capture the pulse from the skin layers with different modulation depth and motion-robustness. Consequently, there is a large interest in efficient sampling schemes and strategies that allow the reading of reliable and accurate measurements, but do not affect the battery life of resource-constrained wearables.

Diverse approaches for sparse sampling and compressed sensing have been presented. Nevertheless, as surveyed in this dissertation, most commercial devices still rely on standard regular sampling and dim down the rate to the minimum possible to save energy.

For the smallest examples of such devices, it can be beneficial to aggregate long recordings over minutes rather than seconds to then analyze the data in the frequency domain. In this dissertation, the application of FFT and PSD on one-minute measurements has been evaluated, presenting the successful determination of HR and RR from the spectra with a relatively stable accuracy. Applied to a common benchmark dataset that contains considerably preprocessed signals from transmission mode PPG, it correctly identified 90 % of the HR and 80 % of the RR dominant components down to a sampling rate of 9 Hz. Applied on actual raw measurements from a wearable prototype, an accuracy of around 80 % for HR and 70 % for RR is achieved even down to a sampling rate of 4 Hz. However, it is important to consider that the dominant frequency components F0 do not directly represent the average rates, but their predominant component present in the analyzed signal interval. Therefore, especially for longer window intervals, additional features, such as the central frequency F50 and the frequency dispersion SF50, can serve as supplementary heuristics to support the estimation of the actual mean from the spectra. Overall, the evaluation of the required minimum sampling rate showed that 10 Hz is sufficient to determine the HR and RR with adequate accuracy in the frequency domain.

Most modern wearable devices are interested in more sophisticated secondary information such as features derived from the HRV. Therefore, the individual pulses need to be identified in the time domain, to enable the derivation of the IBIs. The development and benchmark of efficient algorithms for this purpose require suitable and raw data from compatible sensors. Most publicly available datasets, however, are originated in clinical studies that applied conventional transmission mode PPG and, beyond that, are considerably filtered. As a result, performing benchmarks on such data suffers evidence, and the developed algorithms might not show the expected performance on real data from wearable devices that usually apply reflective mode PPG.

In this dissertation, 10 datasets have been reviewed by applying 7 multi-varied metrics. Of these datasets, only one contained the advertised raw measurements, and from the desired reflective mode PPG on top of that. Although results from research based on considerably preprocessed data, such as from the popular and convenient Empatica E4, do probably not need to be questioned in general, at least caution is advisable when transferring the approaches and findings to data from other devices with different filters and sensors, e.g. applying green light PPG instead of using IR light. Especially flipping the pulse amplitude by default, to be consistent with ABP, has caused additional uncertainty and confusion among researchers for a long time, since also certain measurement setups can cause a natural inversion of the signal, e.g. by turning the wrist.

Although preprocessing has previously been shown to considerably affect the performance of algorithms, and even the quality of the derived features, there exist no standards yet. In this dissertation, the impact of preprocessing on the pulse peak positions and the performance of two popular algorithms has been demonstrated and evaluated. A filter passband from the theoretical minimum HR of 0.5 Hz to appropriate 15.0 Hz, to cover multiple harmonics of the varying fundamental frequency, has shown to be most universal and effectual. The two benchmarked algorithms from 2012 and 2019 are based on two fundamentally different principles to identify the pulse peaks in the time domain. Nevertheless, both have demonstrated very good performance with an F1-score of 0.958 and a peak position error of 3.037 samples for the first, and an F1-score of 0.970 and an impressively small peak position error of 0.051 samples for the second one.

RQ 2 Energy efficiency and privacy are probably the most relevant requirements for wearable computing. Today, wearable devices considerably suffer from the high power dissipation of radio modules. In addition, the wireless transmission of health-related data poses privacy concerns since radio reaches even beyond the body surface and thus facilitates eavesdropping. For almost three decades, the novel communication principle of IBC has received enduring attention as it promises to solve, or at least significantly improve, both issues at once. It is somewhat located between the traditional wired and wireless techniques while showing advantages over both. Diverse transmission principles have been proposed and evaluated, all with their respective pros and cons, but the original capacitive coupling technique is still considered to be the most relevant. Diverse channel models have been developed and validated, turning the confined human body into an efficient transmission medium. While the signal's forward path is formed through the tissues of the human body, the return path, to close the channel circuit, is formed through the environmental ground and, thus, significantly suffers from grounding issues.

Case study 1 of this dissertation addresses this problem and considerably simplifies the transmission channel by combining capacitive coupling with conductive clothes. The conductive fabric establishes a local ground potential that resembles a Faraday cage, shields ambient noise, and hence significantly improves the SNR. This way, even the application of a simple modulation scheme based on PWM, modulating the symbols at 250 kHz, can already achieve a very good performance of 200 kbps. While the prototype consumes 7.6 mW in transmission mode, the reception mode demands for 18.9 mW because of a higher clock frequency for the microcontroller, necessary to process the demodulating state machine, and the quiescent current of the dissipative AFE in stand-by.

Also, the characterization of the IBC body channel is susceptible to and has largely been affected by measurement equipment that is either grounded or has at least a large surface, which in turn unintentionally improves coupling to the environmental ground potential. Therefore, most of the proposed channel models have recently turned out to be affected and hence inapplicable, especially for the LF range. The human body channel provides a comparatively wide, applicable frequency band from 100 kHz – 50 MHz. In all models the lower frequencies below 1 MHz showed a significantly increasing channel loss. Therefore, most research concentrated on higher frequencies of multiple MHz up to even GHz. However, at frequencies beyond 50 Hz, the human body turns into an antenna and the transmission principle resembles normal radio propagation with all its characteristics and disadvantages. While most measurement equipment applies 50 Ω termination, standard in RF circuit and antenna design, the use of high-Z input impedances has recently been demonstrated to considerably improve the performance of capacitive coupling IBC in the LF band. The finding that the input impedance of the receiver front-end considerably affects the channel circuit, and therefore the transfer function of the body channel, has broken a lance. Since then, well-known research teams have demonstrated the data transmission at high rates and impressively low power, presented fully integrated ASICs, and thus continue to push the boundaries of what is possible.

In case study 2, the ECG front-ends of commercial wearable devices have been repurposed to detect signals in the LF band. The front-ends are carefully designed for ULP applications, and the very sensitive high-Z input allows to successfully detect also the induced artificial signals. These signals can be enriched with unique object identifiers and data for synchronization purposes, and are either consciously or implicitly and incidentally induced to the user's skin by touching, approaching, or passing certain areas, surfaces, or objects with embedded beacons. The evaluation is based on a scenario with a transmitter beacon embedded into a desktop that provides artificial landmark signals to two sensing

devices at the user's wrists. Filters are applied and have been optimized to extract and demodulate the desired signals, which typically vanish in the ambient noise floor. In this way, it is possible to provide situational context to devices through their ECG sensor and to automatically annotate the recordings through the ECG channel. However, the sensors' low sampling rate of 128 Hz limits the possible modulation frequency to 20 Hz, and a landmark packet with in total 24 pulse periods but only 8 bit of data takes 1.2 s. Consequently, the achievable data throughput is apparently not sufficient for the transmission of more extensive data, which limits the imaginable applications. While the wearable receivers are battery-powered and floating, the transmitter beacons still need to be grounded, e.g. through a power socket, to achieve a sufficient SNR at the receiver.

Due to the possible use of LF signals, the design of coupling electrodes and front-ends is relatively simple as no RF design rules need to be considered. As a part of the channel circuit, the inter-electrode capacitance of IBC transceivers has an effect on the achievable sensitivity and performance. Therefore, the awareness of the characteristic capacitance is required for the modeling and simulation of the transmission channel. To investigate the effect of environmental changes on the applied IBC coupling electrodes, in case study 3, a wearable prototype has been developed to enable the continuous measurement of the intrinsic capacitance in the wild. The common $3 \times 3\,\mathrm{cm}^2$ electrodes are stacked with an air gap of 1 cm, thus forming a parallel plate capacitor with a calculated, ideal capacitance of 0.797 pF. The performance of non-grounded activities, such as arbitrary gestures, has shown a characteristic capacitance of $0.793 \pm 0.325\,\mathrm{pF}$, which is surprisingly close to the calculated value and, thus, validates its application in simulation models. However, the observed variations are comparatively large and can result in a relative impact of about $\pm 40.7\,\%$, which is far from negligible. In addition to these findings, it was also possible to detect hand-washing through a distinct effect on the measured capacitance that separated grounded hand-washing at $1.152 \pm 0.106\,\mathrm{pF}$ clearly from non-grounded washing gestures with dry hands at $0.671 \pm 0.065\,\mathrm{pF}$. Therefore, a physical model has been developed that attempts to explain and substantiate the observed effect.

Based on the insights on the coupling electrodes' typical capacitance, an open-source IBC wake-up receiver has been developed. The OpenIBC prototype repurposes the AFE for active RFID / NFC transponders. In contrast to most RFID / NFC modules, the utilized IC provides a high input impedance that allows the use of capacitive coupling instead of the standard inductive coupling. Based on the recently published findings regarding the modeling of the human body in the LF band, the channel circuit established by this prototype has been modeled and simulated to validate the general feasibility of the approach. The results have then been confirmed by implementing the prototype, with a carrier frequency of 125 kHz in the LF band, showing a good performance of 4096 bit/s and a PER of 320.0×10^{-6}. The used front-end is relatively sensitive with $100\,\mu\mathrm{V}_{\mathrm{RMS}}$ or $-81.339\,\mathrm{dB}$, respectively. However, the added capacitive load, necessary to extend the intrinsic inter-electrode capacitance and allow for the resonance at the specified carrier frequency, significantly degrades the circuit's sensitivity by factor 1:224. Therefore, only the reception of data from a grounded transmitter is possible, again.

RQ 3 In recent years, the interest of research in wearable devices seems to successively turn from single all-round devices into a collection of simultaneously deployed units, covering different, complementary perspectives of the user. This trend makes the synchronization of the resource-constrained devices increasingly crucial as the cutting-edge signal fusion and machine learning techniques, applied to the collected data, suffer considerably from the inaccuracy of the devices' internal clocks, the manual temporal alignment of the time series, and the recordings' unmatched time bases.

In this dissertation, the human body is not only considered as a physical carrier of devices and a valuable source of the user's health-related information. It is, beyond that, considered as the central element of a wearable system that is augmented with information, whether it is naturally available or artificially induced, that can be obtained from its surface through various sensors. This way, the human body enables technologies and methods, demonstrated on the example of implicit synchronization. Based on the previously elaborated wearable sensing and IBC communication techniques, two methods are presented that enable the implicit synchronization of distributed wearable devices attached to the same body. Therefore, neither the explicit configuration of a network and pairing of devices, nor the conscious performance of synchronization actions are required.

The first method, termed as PulSync, leverages the natural, irregular rhythm of the heartbeat that is ubiquitously and simultaneously available throughout the entire body surface of every living human being. It can be detected through different sensing modalities, of which ECG and PPG are still the most relevant. In contrast to other physiological signals, which tend to be too insignificant and are not as simple to detect, the heartbeat's nature makes it perfectly suitable for synchronization purposes by providing a continuous master clock. Even at rest, the HR results in an update rate of typically 0.8 Hz but can vary between 0.5 Hz and 3.0 Hz depending on the user's health and performed physical activity. The HR is modulated through diverse physiological processes, making the HRV interval function highly varying and unique like a fingerprint, but also location-independent and hence identical throughout the entire body surface. In addition, it is less and, in case of artifacts, only locally disturbed through erroneous samples. This singularity enables to unambiguously align the independent recordings and their local time bases by matching these HRV fingerprints. The unique patterns are aligned using the PPMC normalized cross-correlation. This way, the method is superior to other approaches that directly correlate the raw physiological signals, which usually exhibits immense differences in their baseline and appearance. PulSync has been evaluated on a public ECG dataset with a sliding window of 60 s. It shows a promising performance with a remaining alignment error of -0.714 ± 3.440 samples or -2.856 ± 11.427 ms. For all subjects and window segments, the PPMC r virtually reaches 1 and the achieved deviation is negligible as the two HRV interval functions are almost identical, although obtained from two different devices at different sites. Since the HRV interval function is irregularly sampled, the sequence is resampled and linearly interpolated at 25 Hz to limit the computational efforts. Although this rate is already higher than the typically applied $4-10$ Hz for HRV analysis, it nevertheless limits the achievable alignment accuracy.

The second method, termed as IBSync, applies the previously implemented IBC technique and repurposes the single-lead ECG sensors integrated into recent off-the-shelf wearables. Analog to the previous case study 2, artificial landmarks are either consciously or implicitly and incidentally induced into the user's skin by touching, approaching, or passing certain areas, surfaces, or objects equipped with transmitter beacons. Because the regular pattern of the landmark signal, even if transporting the unique object identifiers, would be ambiguous and confusable, the landmark packets are enriched with varying data. This allows either to uniquely align multiple devices' recordings offline, in a post-processing step, or to allocate the temporal position of landmarks, detected at a single or multiple devices online, with respect to absolute time. However, the low data throughput, with 8 bit of data taking 1.2 s, is not sufficient to reliably transmit larger data, required for the online synchronization based on 32 bit ms-accurate timestamps. However, utilizing random values as data, the offline synchronization theoretically guarantees landmark packets and their order to remain unique for $2^8!$ repetition-free permutations. For the presented system

with one landmark every 2.5 s, this hence results in a recurrence interval of 6.8×10^{499} years, which can apparently be considered sufficient. IBSync has been evaluated on a total of 215 min of recordings from two devices, demonstrating the general feasibility and achieving a promising synchronization error of 0.800 ± 1.792 samples or 6.249 ± 14.004 ms at a sampling rate of 128 Hz. For 92.97 % of the landmarks, the position error was just in the order of the quantization error. Larger deviations in the order of 7 samples are caused by the erroneous matching of the packet frame, which can easily be solved by validating the number of detected preamble and terminator pulses. The achievable accuracy naturally depends on the coupling strength and the resulting signal quality. For successfully detected and decoded landmark packets, the applied PPMC r typically ranges from 0.845 to 0.863. The experiment in the wild shows periods in which the landmark signal is present at both wrists, as intended, while in other periods, it is only detectable at a single wrist. It seems like the IBC signal does not always propagate well throughout the entire body surface under all conditions. While it is available at both wrists when induced through the thighs, the induction at one hand might not be detectable at the other one. It is assumed that the larger distance between the wrists, compared to the shorter path from the thighs to both wrists, mainly causes this effect. Moreover, having the legs closer to the floor, and thus better grounded, further amplifies this effect.

The achieved alignment accuracies of PulSync with -0.714 ± 3.440 samples at 250 Hz and of IBSync with 0.800 ± 1.792 samples at 128 Hz are of comparable quality. However, while PulSync enables only the offline synchronization of recordings, IBSync could also provide absolute time to a single or multiple devices. Using the naturally available HRV interval function promises to be more convenient as no additional transmitter beacons are required to induce the artificial landmarks to the skin. Especially in research experiments, IBSync could, however, also provide additional situational context information and hence enable not only the automatic alignment but also the annotation of the recordings. In comparison to other existing synchronization methods, both presented methods can clearly keep up with the performance of typical online methods such as NTP with a theoretical accuracy ranging from several milliseconds to 100 ms [Mil11]. In addition, they are distinctly more accurate than most offline methods, particularly those originated in HAR, which accuracy is typically in the order of several milliseconds: 8.6 ms [BGJ15b] (template-based), 20 ms [Wan+19], 49 ms [BGJ15b] (entropy-based), 0.29 s [XDH22], 0.3 s [BAL09], up to few seconds [HOV19]. In this way, the proposed methods PulSync and IBSync clearly justify their existence. They can be beneficial in applications that require the recordings to be aligned more accurately than possible with motion-based offline synchronization methods, but at the same time cannot apply radio-based online synchronization techniques, e.g. due to energy constraints.

5.1 Future Work

The application of machine learning techniques will lead to a plethora of emerging products and research projects in the next few years. Their success will, however, depend on the reliability of the used data, thus demanding for accurate timing. The foundations explored in this dissertation open up several interesting questions that point in this direction:

RQ 1 In a couple of years, ECG sensors that can detect the heartbeat at a single site will likely become standard in wearable devices. Whether they are less affected by motion remains an open question, but at least they have the potential to be significantly more energy efficient as they do not need to actively sample and illuminate the skin with

intensive light sources, as in the case of PPG. For PPG, the findings from recent years need to trickle through, settle in the research community, and require validation to show evidence until they become common sense. For this purpose, more large datasets from suitable sensors, compatible with the intended target system, with good signal quality and detailed documentation are required to benchmark the developed algorithms. There is a need to raise awareness that preprocessing has a significant impact on the evidence of research, and, therefore, the applied filters need to be specified in publications. In both research areas, the number of developed conventional algorithms seems to stagnate while the majority of recent publications apply machine learning techniques, which require even larger and more diverse datasets. This further increases the need for well-documented, thoroughly recorded, and publicly available benchmark datasets.

RQ 2 A few years ago, research into smart clothes and conductive textiles flourished, but currently, interest seems to focus on other topics. Nevertheless, the combination of conductive textile layers and capacitive coupling is an effective way to enable the communication between body-worn devices without the need for fixed cable joints. However, when finally made available, fully integrated IBC transceivers would, of course, be even more convenient as they would not require the additional and relatively costly layer of conductive material. Until then, using and repurposing commercially available off-the-shelf hardware is an interesting aspect as it immediately allows other researchers to adapt the solution and improve on it. The presented case study using ECG front-ends would benefit from more sophisticated preamble patterns, which would probably improve the correlation and, therefore, the detection of the signal even from battery-powered, floating transmitters. Moreover, the data throughput can easily be improved by setting the ECG's sampling rate to the devices' maximum of 512 Hz, which would presumably allow for a modulation frequency of 80 Hz. However, the mains' humming noise, with harmonics at multiples of 50 / 60 Hz, should be avoided. Nevertheless, this way, even four bytes of data could be transmitted within the current packet duration of 1.2 s and, therefore, enable the online synchronization of devices with ms-accurate timestamps. Capacitive sensing is an interesting yet adjacent research area. The wearable characterization of the inter-electrode capacitance discovered an interesting approach to detect hand-washing. The preliminary study shows a surprisingly clear discrimination of grounded and non-grounded activities. However, a larger study is required to consolidate the first observations with more subjects and buildings, and, therefore, a larger diversity of water taps and supply pipes. Nevertheless, the determined capacitance can still support the simulation of the open-source OpenIBC prototype. The first iteration will be followed by gradually improved ones, aiming for a more sensitive front-end that will hopefully allow fully-wearable applications. A first trial might use a pre-amplifier with high input impedance to reduce the circuit's input capacitance. This way, the project presented will hopefully find favor in the research community, compensate for the lack of commercially available IBC transceiver modules, and foster the research on concepts for more intuitive HCI and their impact on UX. It might accelerate the research and development of potential applications which can directly be implemented when commercial front-ends are finally made available. Actually, just a few weeks before the submission of this dissertation, a new commercial product [1] has been released by a spinout of the Purdue University and was presented at the trade fair CES in 2023, which might finally trigger the breakthrough of IBC.

[1] IEEE Spectrum: "Ixana's through-the-body low-power communications technology", https://spectrum.ieee.org/future-tech-ces-2023 and "Turning the Body Into a Wire", https://spectrum.ieee.org/turning-the-body-into-a-wire, accessed on 2023-01-23.

RQ 3 The presented concept of implicit synchronization has the potential to cover an essential niche of scenarios in which distributed wearable devices are attached to the same body and require the temporal synchronization at a certain accuracy. It comes into play when a better accuracy is required than is achievable with conventional offline methods, but, at the same time, the use of hardware interfaces and radio-based online synchronization is not possible or intended. So far, PulSync is only evaluated for ECG signals. The adaption to PPG signals is assumed not to be difficult as HRV and PRV are proven to be very similar, but the PAT of the measurement location needs to be considered. It will add up as a constant bias to the achievable accuracy and typically is in the order of 0.133 s at the ears, 0.199 s at the thumbs, and 0.301 s at the toes. For signals interfered with motion artifacts, this achievable accuracy will likely decrease according to the amount of affected samples. In addition, other sensing modalities could be used to detect the electric field or mechanical pulse, if clearly related to the heartbeat. While the performance of IBSync is primarily limited due to the slow ECG sensor front-end, the OpenIBC prototype could also be used to obtain both situational context as well as temporal information for either offline or online synchronization. Its higher throughput would immediately allow for the transmission of more extensive data and the landmark packets being less affected and disturbed through motion. In general, a review of the available offline synchronization methods and their typical accuracy is not available but it would be helpful to select the technique that fulfills the requirements for the intended application most. Moreover, the effect of temporal inaccuracies on standard machine learning tasks has not yet been quantified sufficiently.

Overall, this dissertation contributes versatile methods, evaluated in various case studies, that support the research on human body-enabled technologies and methods. Accordingly, from a very technical perspective, the human body is considered as an essential part of a distributed wearable system. The presented methods aim at the implicit synchronization of independent devices while keeping an eye on the resource constraints and the requirements on power consumption typical for wearable devices.

A Appendix

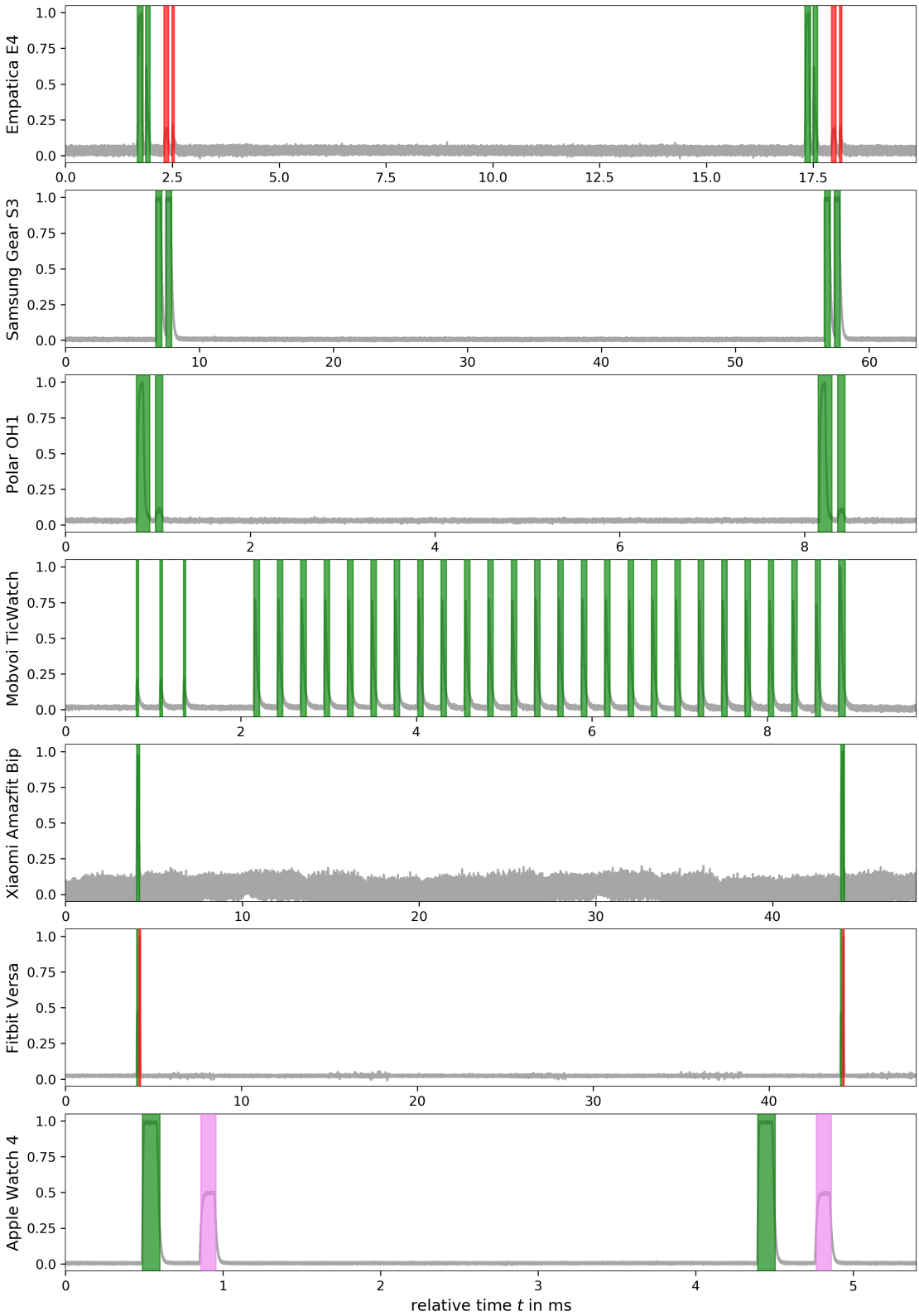

Figure A.1: Recorded sampling schemes of seven commercial wearable devices as time series plots with highlighted pulses corresponding to the applied light wavelengths (green, red, and IR). All devices were put in a mode that enables continuous measurement, for instance for physical activity monitoring. **[A19]**

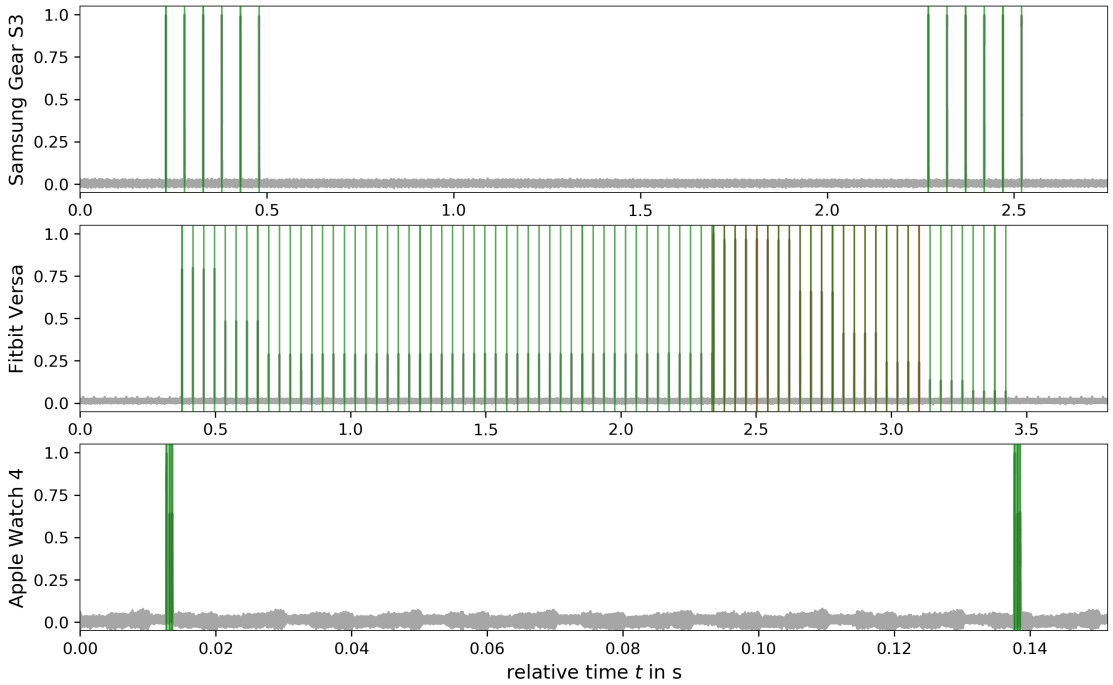

Figure A.2: Recorded sampling strategies of three commercial wearable devices, with sampling highlighted according to the applied light wavelengths (green, red, and IR). The wearables were put in a sporadic sampling mode, which is usually enabled in casual wearing. [**A19**]

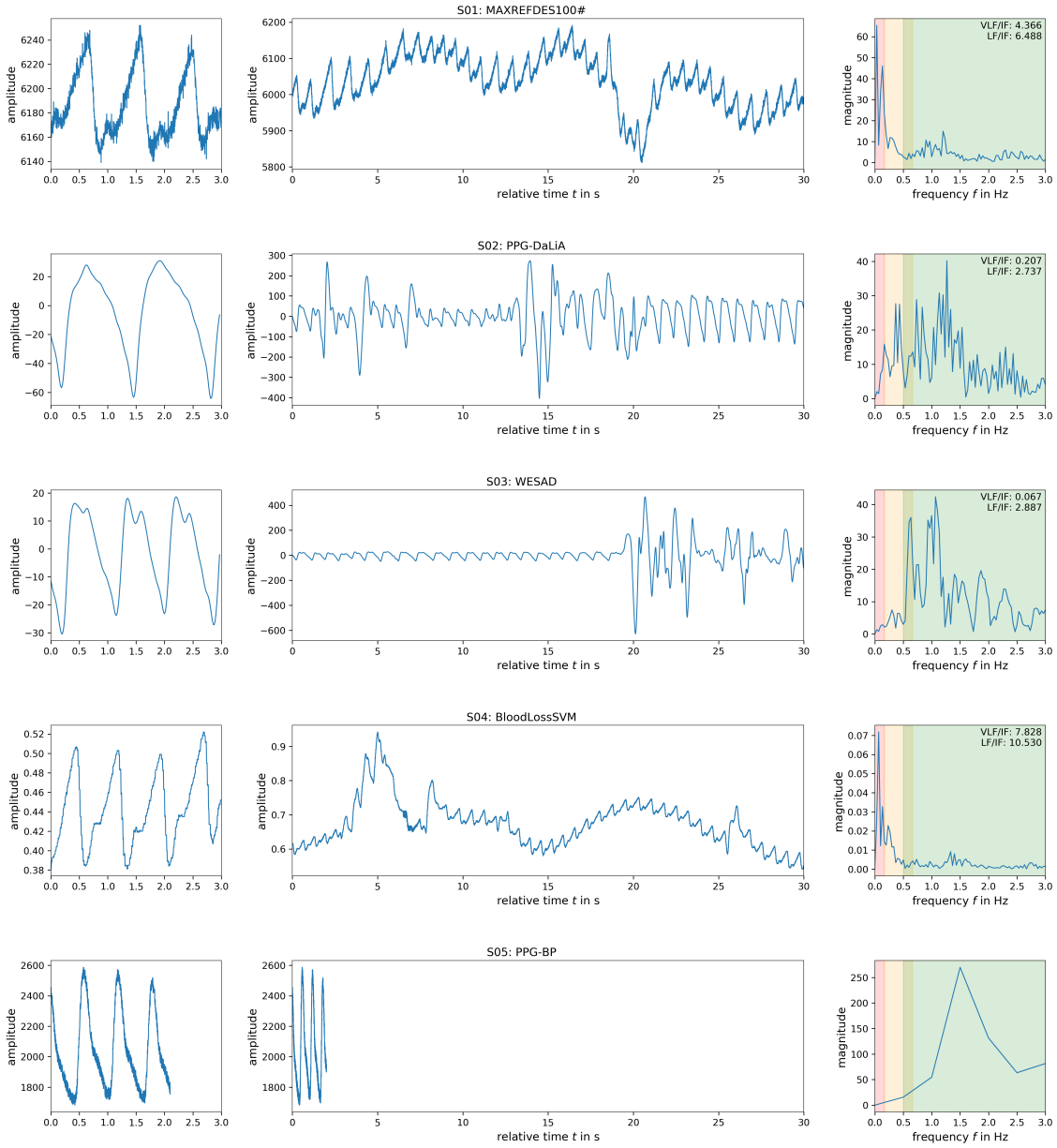

Figure A.3: Excerpts from the first five reviewed datasets: Short close-up of few pulses on the left, a 30-second window in the middle, and its respective frequency spectrum (FFT) on the right. Note that the PPG-BP dataset (bottom) contains only snippets of 2.1 s length. Frequency bands: very low frequency (VLF, < 0.167 Hz, red), low frequency (LF, 0.167 to 0.667 Hz, orange), and intermediate frequency (IF, 0.5 to 3.0 Hz , green) while the high frequency (HF, > 3.0 Hz) noise and harmonics are clipped. **[W20a]**

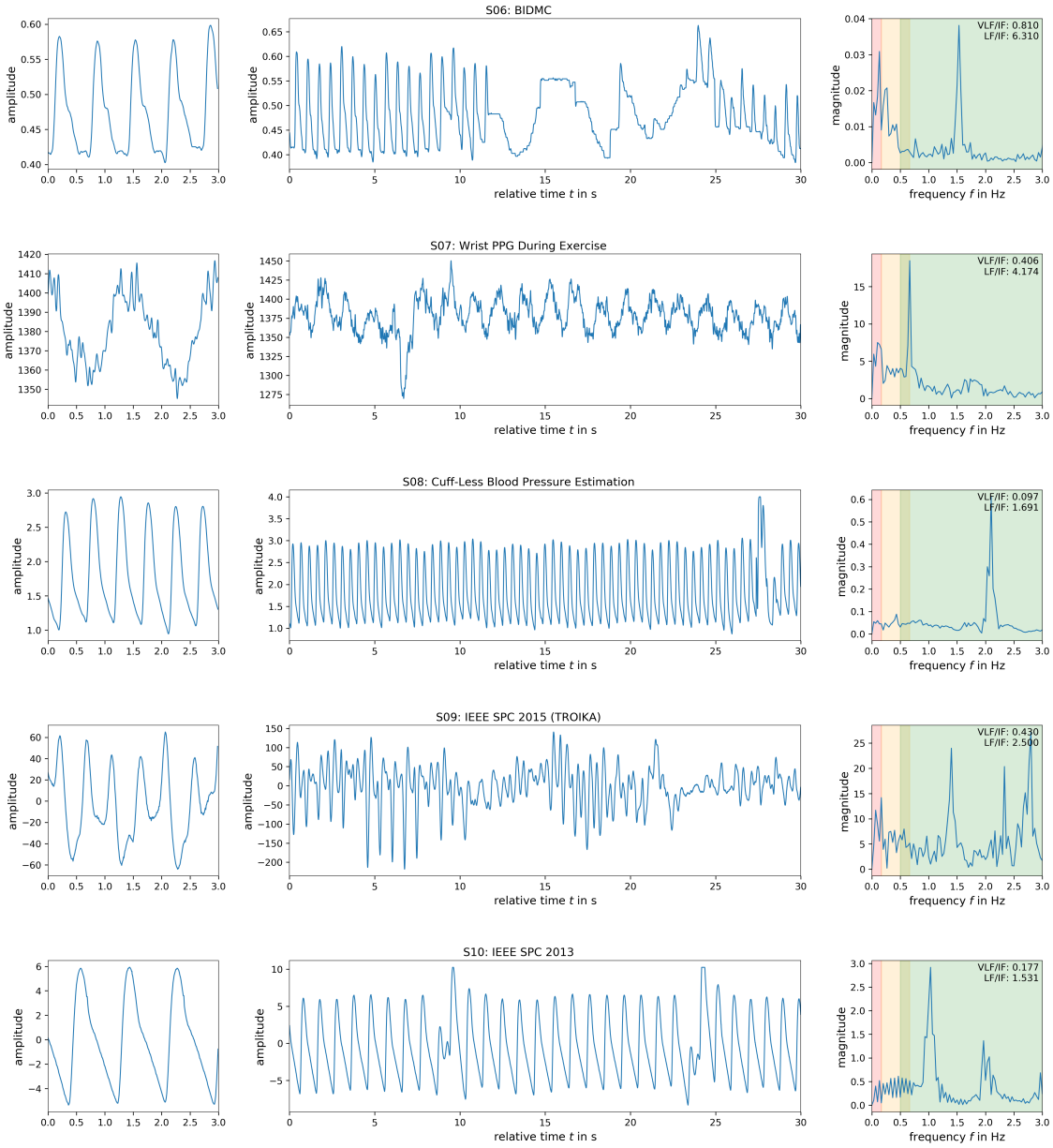

Figure A.4: Excerpts from the last five reviewed datasets: Short close-up of few pulses on the left, a 30-second window in the middle, and its respective frequency spectrum (FFT) on the right and cannot be analyzed in the frequency domain. Frequency bands: very low frequency (VLF, < 0.167 Hz, red), low frequency (LF, 0.167 to 0.667 Hz, orange), and intermediate frequency (IF, 0.5 to 3.0 Hz , green) while the high frequency (HF, > 3.0 Hz) noise and harmonics are clipped. **[W20a]**

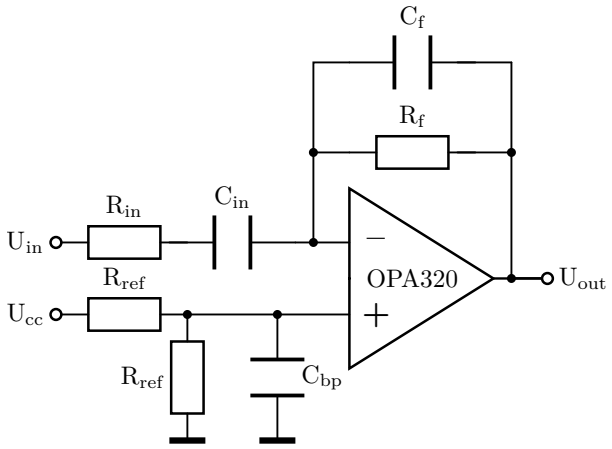

Figure A.5: Schematic of of the transimpedance amplifier (TIA) circuit which resembles rather a differentiator due to the capacitive impedance of the signal electrode. Figure from [WMa16]

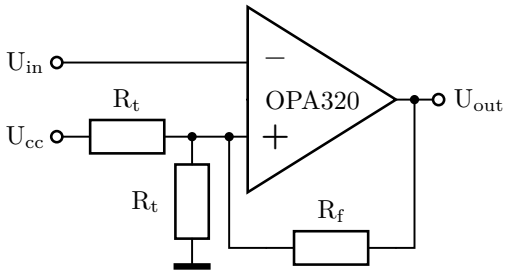

Figure A.6: Schematic of the Schmitt trigger circuit for pulse recovery. Figure from [WMa16]

Table A.1: IBSync: Overview of the results from the technical evaluation. [**J22b**]

	coupling	device	$\overline{p}$ in dig	$\overline{\lvert g \rvert}$ in dig	$\overline{p}$ / $\overline{\lvert g \rvert}$	B in Hz	RSSI in dB	PPMC r	PER $\times 10^{-3}$	ϵ in dig	ϵ in ms
a)	electrode	left	73.0 ± 3.6	1.9 ± 1.5	39.3	20.6	23.504	0.847 ± 0.045	0.000	0.802 ± 1.543	6.262 ± 12.056
		right	53.8 ± 6.7	4.1 ± 3.3	13.3	21.9	21.078	0.810 ± 0.041	23.747	0.654 ± 1.855	5.112 ± 14.490
b)	desktop	left	28.8 ± 2.4	1.4 ± 1.4	21.0	20.6	21.558	0.822 ± 0.040	26.525	0.780 ± 1.514	6.093 ± 11.832
		right	32.9 ± 6.9	5.5 ± 4.3	5.9	22.1	-4.581	0.684 ± 0.037	281.167	0.997 ± 2.483	7.792 ± 19.401
c)	leaning back	left	44.5 ± 6.7	1.4 ± 1.4	31.4	19.8	22.945	0.835 ± 0.038	2.571	0.704 ± 1.503	5.503 ± 11.744
		right	70.1 ± 11.3	6.6 ± 4.8	10.7	22.2	10.841	0.798 ± 0.040	0.000	0.864 ± 1.646	6.748 ± 12.858

right device: results affected by in-band noise at about 15 Hz.

List of Figures

List of Tables

Abbreviations

Symbols

|F50−F0|	distance between central frequency F50 and fundamental frequency F0

A

ABP	arterial blood pressure
AC	alternating current
ADC	analog-to-digital converter
ADL	activities of daily living
AFE	analog front-end
ANS	autonomic nervous system
ASIC	application-specific integrated circuit
ASK	amplitude-shift keying
ATHRS	adaptive threshold
AUC	area under the curve

B

BAN	body area network
BCC	body-coupled communication / body channel communication
BCG	ballistocardiography
BFV	blood flow velocity
BLS	band-limited signal
BP	band-pass
BS	band-stop / notch
BSN	body sensor network
BSPM	body surface potential mapping

C

CDC	capacitance-to-digital converter
CES	consumer electronics show, annual trade show in Las Vegas, USA
CIN	sensing electrode of the AD7151
CMOS	complementary metal–oxide–semiconductor
CMRR	common-mode rejection ratio

D

DAC	digital-to-analog converter
DAQ	data acquisition system
DC	direct current
DDTS	data driven time synchronization
DRL	driven-right-leg

DTW dynamic time warping
DUS doppler ultrasonography

E

ECG electrocardiography
ECGN negative input of an ECG sensor AFE
ECGP positive input of an ECG sensor AFE
EDA electrodermal activity
EEG electroencephalography
EMG electromyography
EMI electromagnetic interference
ERP exposure and reaction prevention
EXC excitation electrode of the AD7151

F

F0 fundamental frequency
F50 central frequency
FFT fast Fourier transformation
FIR finite impulse response
FN false negative
FP false positive
FR4 glass-reinforced epoxy laminate material

G

GF group frequency
GMT Greenwich mean time
GND ground potential, either local or provided by the earth
GNSS global navigation satellite systems
GPIO general-purpose input / output
GPS global positioning system

H

H_2O water
HAR human activity recognition
HBC human body communication
HCI human-computer interaction
HF high frequency
HHb deoxyhaemoglobin
high-Z high impedance
HP high-pass
HR heart rate
HRV heart rate variability

I

IBC intra-body communication
IBI inter-beat interval

IBSync method 2, using the human body as a transmission medium to provide artificial information
IC integrated circuit
ICG impedance cardiography
ICNIRP international commission on non-ionizing radiation protection
IF intermediate frequency
IIR infinite impulse response
IMS incremental-merge segmentation
IMU inertial measurement unit
IoWT internet of wearable things
IR infrared
IRQ interrupt request
IRS interference-reduced signal
ISM radio frequency spectrum reserved internationally for industrial, scientific, and medical purposes
ISR interrupt service routine

L

LAN local area network
LDV laser Doppler velocimetry
LED light-emitting diode
LF low frequency
LP low-pass
LR-WPAN low-rate wireless personal area network
LTS lightweight time synchronization

M

MAC medium-access control
MARG magnetic, angular rate, and gravity
MAX maximum correlation
MCG magneto-cardiography
MEMS micro electro-mechanical systems
MODWT maximal overlap discrete wavelet transform
MRI magnetic resonance imaging
MSB most significant bit

N

NaCl sodium chloride
NFC near-field communication
NTP network time protocol

O

O_2Hb oxyhaemoglobin
OCD obsessive-compulsive disorder
OOK on-off-keying
OpenIBC open-source intra-body communication receiver

P

PAN	personal area network
PAT	pulse arrival time
PCB	printed circuit board
PCG	phonocardiography
PD	photodiode
PEP	pre-ejection period
PER	packet error rate
PPG	photoplethysmography
PPMC	Pearson product-moment correlation
PPV	positive predictive value (precision)
PRF	pulse repetition frequency
PRV	pulse rate variability
PSD	power spectral density
PTP	precision time protocol
PTT	pulse transit time
PulSync	method 1, using the human body as a source of natural information
PV	peak value
PwC	PricewaterhouseCoopers
PWM	pulse-width modulation
PWV	pulse wave velocity

R

RBS	reference broadcast synchronization
RF	radio frequency
RFID	radio-frequency identification
RIAV	respiratory-induced amplitude variations
RIFV	respiratory-induced frequency variations
RIIV	respiratory-induced intensity variations
ROI	region of interest
RR	respiratory rate
RSA	respiratory sinus arrhythmia
RSSI	received signal strength indicator
RTC	real-time clock

S

S_{21}	S_{21} represents the power transmission from port 1 to port 2, it is one of the four common S-parameters applied to characterize two-port networks
SCG	seismocardiography
SDSD	standard deviation of successive differences
SF50	frequency dispersion
SHA	sample and hold amplifier
SHF	super-high frequency
SNA	sympathetic nervous activity
SNR	signal-to-noise ratio
SNTP	simple network time protocol
SoC	system on a chip
SPICE	acronym of an open-source analog circuit simulator, simulation program with integrated circuit emphasis
SpO_2	peripheral oxygen saturation

SQI signal quality index
STFT short-time Fourier transform

T

TCXO temperature-compensated crystal oscillator with ± 5 ppm
TDMA time division multiple access
THRS threshold
TIA transimpedance amplifier
ToF time-of-flight
TP true positive
TPR true positive rate (sensitivity or recall)

U

UHF ultra-high frequency
ULP ultra-low power
UTC coordinated universal time
UX user experience

V

VCM common mode voltage, reference electrode of an ECG sensor AFE, DRL or body bias circuit
VLF very low frequency
VNA vector network analyzer
VTT vessel transit time

W

WAN wide area networks, e.g. the internet
WBAN wireless body area network
WetTouch wearable prototype to measure the fluctuations of the inter-electrode capacitance due to environmental changes, e.g. grounding due to hand-washing
Wi-Fi Wireless Fidelity, IEEE 802.11
WSN wireless sensor networks
WuRx wake-up receiver

X

XO conventional crystal oscillator with ± 20 ppm

Nomenclature

Symbols

B	bandwidth
$C_{\mathbf{add}}$	added capacitance to achieve resonance
$C_{\mathbf{body}}$	capacitance formed between the environment and the human body
$C_{\mathbf{int}}$	intrinsic capacitance of the electrode setup
$C_{\mathbf{load}}$	load capacitance at the receiver
$C_{\mathbf{par}}$	parasitic capacitance
$C_{\mathbf{ret,\,rx}}$	capacitance formed between the environment and the receiver
$C_{\mathbf{ret,\,tx}}$	capacitance formed between the environment and the transmitter
$C_{\mathbf{rx}}$	capacitance at the receiver input
$I_{\mathbf{in}}$	input current
$I_{\mathbf{leak}}$	leakage current
$I_{\mathbf{q}}$	quiescent current
$N_{\mathbf{error}}$	number of erroneous packets
$N_{\mathbf{total}}$	total number of packets sent
$R_{\mathbf{f}}$	resistor in the feedback network
$V_{\mathbf{CM}}$	common-mode voltage
$V_{\mathbf{out}}$	output voltage
$Z_{\mathbf{gpio}}$	impedance of the GPIO
$Z_{\mathbf{in}}$	input impedance of a circuit
$Z_{\mathbf{out}}$	output impedance of a circuit
$\mathrm{loss}_{\mathbf{dB}}(S_{\mathbf{21}})$	insertion loss derived from the S_{21} parameter
$f_{\mathbf{0}}$	fundamental frequency
$f_{\mathbf{c}}$	clock frequency
$f_{\mathbf{r}}$	resonance frequency
f_0	carrier frequency of the modulated signal
f_c	cutoff / corner frequency of a filter
f_{hrv}	frequency at which the HRV interval function is resampled
f_s	sampling rate / frequency
r	Pearson product-moment correlation coefficient r
$t_{\mathbf{bit}}$	time period per bit
$t_{\mathbf{burst}}$	time period of the burst
$t_{\mathbf{pat}}$	time period of the correlation pattern
$t_{\mathbf{pre}}$	time period of the preamble

Contributions

Journal Articles

[J20b] Elina Kuosmanen, **Florian Wolling**, Julio Vega, et al. "Smartphone-Based Monitoring of Parkinson Disease: Quasi-Experimental Study to Quantify Hand Tremor Severity and Medication Effectiveness". In: *Journal of Medical Internet Research (JMIR), mHealth & uHealth* 8.11 (2020), e21543. ISSN: 2291-5222. DOI: 10.2196/21543.

[J22b] **Florian Wolling** and Kristof Van Laerhoven. "IBSync: Intra-body synchronization and implicit contextualization of wearable devices using artificial ECG landmarks". In: *Frontiers in Computer Science* 4 (2022). DOI: 10.3389/fcomp.2022.915448.

Conference Papers

[C21c] **Florian Wolling**, Sudam Maduranga Wasala, and Kristof Van Laerhoven. "Optimal Preprocessing of Raw Signals from Reflective Mode Photoplethysmography in Wearable Devices". In: *Proceedings of the 43rd Annual International Conference of the IEEE Engineering in Medicine & Biology Society*. EMBC '21. Virtual, Mexico: IEEE, 2021, pp. 1157–1163. ISBN: 978-1-7281-1179-7. DOI: 10.1109/EMBC46164.2021.9630955.

[C17] **Florian Wolling**, Philipp M. Scholl, Leonhard M. Reindl, and Kristof Van Laerhoven. "Combining Capacitive Coupling with Conductive Clothes: Towards Resource-Efficient Wearable Communication". In: *Proceedings of the 2017 ACM International Symposium on Wearable Computers*. ISWC '17. Maui, Hawaii, USA: ACM, 2017, pp. 146–149. ISBN: 978-1-4503-5188-1. DOI: 10.1145/3123021.3123059.

[C21b] **Florian Wolling**, Cong Dat Huynh, and Kristof Van Laerhoven. "IBSync: Intra-body Synchronization of Wearable Devices Using Artificial ECG Landmarks". In: *Proceedings of the 2021 ACM International Symposium on Wearable Computers*. ISWC '21. Virtual, USA: ACM, 2021, pp. 102–107. ISBN: 9781450384629. DOI: 10.1145/3460421.3478815.

[C22c] **Florian Wolling**, Florian Hauck, Günter Schröder, and Kristof Van Laerhoven. "OpenIBC: Open-Source Wake-Up Receiver for Capacitive Intra-Body Communication". In: *Proceedings of the 2022 International Conference on Embedded Wireless Systems and Networks*. EWSN '22. Linz, Austria: ACM, 2022, pp. 186–191.

Workshop Papers

[W20a] **Florian Wolling** and Kristof Van Laerhoven. "The Quest for Raw Signals: A Quality Review of Publicly Available Photoplethysmography Datasets". In: *Proceedings of the 3rd Workshop on Data: Acquisition To Analysis*. DATA '20. Virtual, Japan: ACM, 2020, pp. 14–19. ISBN: 9781450381369. DOI: 10.1145/3419016.3431485.

[W18] **Florian Wolling** and Kristof Van Laerhoven. "Fewer Samples for a Longer Life Span: Towards Long-Term Wearable PPG Analysis". In: *Proceedings of the 5th International Workshop on Sensor-based Activity Recognition and Interaction*. iWOAR '18. Berlin, Germany: ACM, 2018, 5:1–5:10. ISBN: 978-1-4503-6487-4. DOI: 10.1145/3266157.3266209.

[W22a] **Florian Wolling**, Kristof Van Laerhoven, Jonas Bilal, Philipp M. Scholl, and Benjamin Völker. "WetTouch: Touching Ground in the Wearable Detection of Hand-Washing Using Capacitive Sensing". In: *2022 IEEE International Conference on Pervasive Computing and Communications Workshops, WristSense Workshop*. Virtual, Italy: IEEE, 2022, pp. 769–774. ISBN: 978-1-6654-1647-4. DOI: 10.1109/PerComWorkshops53856.2022.9767345.

[W21a] **Florian Wolling**, Kristof Van Laerhoven, Pekka Siirtola, and Juha Röning. "PulSync: The Heart Rate Variability as a Unique Fingerprint for the Alignment of Sensor Data Across Multiple Wearable Devices". In: *Proceedings of the 2021 IEEE International Conference on Pervasive Computing and Communications Workshops, PerHealth Workshop*. Virtual, Germany: IEEE, 2021, pp. 188–193. ISBN: 978-1-6654-0424-2. DOI: 10.1109/PerComWorkshops51409.2021.9431015.

Magazine Articles

[A19] **Florian Wolling**, Simon Heimes, and Kristof Van Laerhoven. "Unity in Diversity: Sampling Strategies in Wearable Photoplethysmography". In: *IEEE Pervasive Computing* 18.3 (2019). Ed. by Oliver Amft, pp. 63–69. ISSN: 1536-1268. DOI: 10.1109/MPRV.2019.2926613.

References

[Aba16] Tomas Ysehak Abay. "Reflectance Photoplethysmography for Non-invasive Monitoring of Tissue Perfusion". Doctoral Thesis. London, UK: University of London, 2016.

[Abo12] Gregory D. Abowd. "What next, Ubicomp? Celebrating an intellectual disappearing act". In: *Proceedings of the 2012 ACM Conference on Ubiquitous Computing*. Ed. by Anind K. Dey. New York, NY: ACM, 2012, pp. 31–40. ISBN: 9781450312240. DOI: 10.1145/2370216.2370222.

[Agu+19] Antonio A. Aguileta, Ramon F. Brena, Oscar Mayora, Erik Molino-Minero-Re, and Luis A. Trejo. "Multi-Sensor Fusion for Activity Recognition-A Survey". In: *Sensors (Basel, Switzerland)* 19.17 (2019). DOI: 10.3390/s19173808.

[AMK20] Ammar Ahmad Tarar, Umair Mohammad, and Soumya K Srivastava. "Wearable Skin Sensors and Their Challenges: A Review of Transdermal, Optical, and Mechanical Sensors". In: *Biosensors* 10.6 (2020). DOI: 10.3390/bios10060056.

[Ahm+20] Tousif Ahmed, Mohsin Y. Ahmed, Md Mahbubur Rahman, et al. "Automated Time Synchronization of Cough Events from Multimodal Sensors in Mobile Devices". In: *International Conference on Multimodal Interaction*. ACM, 2020, pp. 614–619. ISBN: 9781450375818. DOI: 10.1145/3382507.3418855.

[Ahm+19] Parvez Ahmmed, James Dieffenderfer, Jose Manuel Valero-Sarmiento, et al. "A Wearable Wrist-Band with Compressive Sensing based Ultra-Low Power Photoplethysmography Readout Circuit". In: *BSN*. Piscataway, New Jersey: Institute of Electrical and Electronics Engineers, 2019, pp. 1–4. ISBN: 978-1-5386-7477-2. DOI: 10.1109/BSN.2019.8771074.

[Akd+13] Saime Akdemir Akar, Sadık Kara, Fatma Latifoğlu, and Vedat Bilgiç. "Spectral analysis of photoplethysmographic signals: The importance of preprocessing". In: *Biomedical Signal Processing and Control* 8.1 (2013), pp. 16–22. ISSN: 17468094. DOI: 10.1016/j.bspc.2012.04.002. URL: https://www.sciencedirect.com/science/article/pii/S1746809412000468.

[Akh+15] Nazneen Akhter, Sumegh Tharewal, Vijay Kale, Ashish Bhalerao, and K. V. Kale. "Heart-Based Biometrics and Possible Use of Heart Rate Variability in Biometric Recognition Systems". In: *Advanced computing and systems for security. Volume 1*. Ed. by Rituparna Chaki, Agostino Cortesi, Khalid Saeed, and Nabendu Chaki. Advances in intelligent systems and computing. New Delhi: Springer, 2015, pp. 15–29. ISBN: 978-81-322-2650-5.

[Ad24] alfa md, Adobe Stock. *Einthoven's Triangle*. Images: #579187406, #590287684, and #629716468. URL: https://stock.adobe.com/de/contributor/208709583/alfa-md (visited on 02/10/2024).

[Alf+22] Carla Alfonso, Miguel A. Garcia-Gonzalez, Eva Parrado, et al. "Agreement between two photoplethysmography-based wearable devices for monitoring heart rate during different physical activity situations: a new analysis methodology". In: *Scientific Reports* 12.1 (2022), pp. 1–11. ISSN: 2045-2322. DOI: 10.1038/s41598-022-18356-9. URL: https://www.nature.com/articles/s41598-022-18356-9.

[AL12] Majd AlGhatrif and Joseph Lindsay. "A brief review: history to understand fundamentals of electrocardiography". In: *Journal of community hospital internal medicine perspectives* 2.1 (2012). ISSN: 2000-9666. DOI: 10.3402/jchimp.v2i1.14383.

[Alh+19] Samah Alharbi, Sijung Hu, David Mulvaney, et al. "Oxygen Saturation Measurements from Green and Orange Illuminations of Multi-Wavelength Optoelectronic Patch Sensors". In: *Sensors* 19.1 (2019), p. 118. DOI: 10.3390/s19010118. URL: https://www.mdpi.com/1424-8220/19/1/118/pdf.

[AM00] J. Allen and A. Murray. "Variability of photoplethysmography peripheral pulse measurements at the ears, thumbs and toes". In: *IEE Proceedings - Science, Measurement and Technology* 147.6 (2000), pp. 403–407. ISSN: 1350-2344. DOI: 10.1049/ip-smt:20000846.

[All07] John Allen. "Photoplethysmography and its application in clinical physiological measurement". In: *Physiological measurement* 28.3 (2007), R1–39. ISSN: 0967-3334. DOI: 10.1088/0967-3334/28/3/R01.

[ADD21] Marco Altini, Lucy E. Dunne, and Lucy Dunne. "What's Next For Wearable Sensing?" In: *IEEE Pervasive Computing* 20.4 (2021), pp. 87–92. ISSN: 1536-1268. DOI: 10.1109/MPRV.2021.3108377.

[AL09] Oliver Amft and Paul Lukowicz. "From Backpacks to Smartphones: Past, Present, and Future of Wearable Computers". In: *IEEE Pervasive Computing* 8.3 (2009), pp. 8–13. ISSN: 1536-1268. DOI: 10.1109/MPRV.2009.44.

[AV17] Oliver Amft and Kristof Van Laerhoven. "What Will We Wear After Smartphones?" In: *IEEE Pervasive Computing* 16.4 (2017), pp. 80–85. ISSN: 1536-1268. DOI: 10.1109/MPRV.2017.3971124.

[AOD20] Vicente J. P. Amorim, Ricardo A. O. Oliveira, and Mauricio Jose Da Silva. *Recent Trends in Wearable Computing Research: A Systematic Review*. 2020. URL: https://arxiv.org/pdf/2011.13801.

[AD71] Analog Devices, Inc. *Power Profiler Kit II, commercial product*. 2007. URL: https://www.analog.com/en/products/ad7151.html (visited on 11/09/2021).

[MAX3] Analog Devices, Inc. *MAX30001, commercial product*. URL: https://www.analog.com/en/products/max30001.html (visited on 02/13/2023).

[MAX8] Analog Devices, Inc. *MAX86140, commercial product*. URL: https://www.analog.com/en/products/max86140.html (visited on 02/13/2023).

[MAX1a] Analog Devices, Inc. *MAXREFDES100#, commercial product*. URL: https://www.analog.com/en/design-center/reference-designs/maxrefdes101.html (visited on 02/13/2023).

[MAX1b] Analog Devices, Inc. *MAXREFDES101#, commercial product*. URL: https://www.analog.com/en/design-center/reference-designs/maxrefdes101.html (visited on 02/13/2023).

[AP81] R. Rox Anderson and John A. Parrish. "The Optics of Human Skin". In: *Journal of Investigative Dermatology* 77.1 (1981), pp. 13–19. ISSN: 0022202X. DOI: 10.1111/1523-1747.ep12479191.

[AB13] Bogdan Antonescu and Stefano Basagni. "Wireless Body Area Networks: Challenges, Trends and Emerging Technologies". In: *BodyNets '13*. ICST. 2013, pp. 1–7. DOI: 10.4108/icst.bodynets.2013.253722.

[AMH19] Gobinath Aroganam, Nadarajah Manivannan, and David Harrison. "Review on Wearable Technology Sensors Used in Consumer Sport Applications". In: *Sensors* 19.9 (2019), p. 1983. DOI: 10.3390/s19091983. URL: https://www.mdpi.com/1424-8220/19/9/1983/pdf.

[Ate+22] H. Ceren Ates, Peter Q. Nguyen, Laura Gonzalez-Macia, et al. "End-to-end design of wearable sensors". In: *Nature Reviews Materials* 7.11 (2022), pp. 887–907. ISSN: 2058-8437. DOI: 10.1038/s41578-022-00460-x. URL: https://www.nature.com/articles/s41578-022-00460-x.

[Avi19] Cesar O. Avila. "Novel Use of Apple Watch 4 to Obtain 3-Lead Electrocardiogram and Detect Cardiac Ischemia". In: *The Permanente Journal* 23 (2019). ISSN: 1552-5767. DOI: 10.7812/TPP/19-025.

[AA06] Benhur Aysin and Elif Aysin. "Effect of Respiration in Heart Rate Variability (HRV) Analysis". In: *Conference proceedings : ... Annual International Conference of the IEEE Engineering in Medicine and Biology Society. IEEE Engineering in Medicine and Biology Society. Annual Conference* 1 (2006), pp. 1776–1779. ISSN: 1557-170X. DOI: 10.1109/IEMBS.2006.260773.

[Bae+12] Joonsung Bae, Hyunwoo Cho, Kiseok Song, Hyungwoo Lee, and Hoi-Jun Yoo. "The Signal Transmission Mechanism on the Surface of Human Body for Body Channel Communication". In: *IEEE TMTT* 60.3 (2012), pp. 582–593. ISSN: 0018-9480. DOI: 10.1109/TMTT.2011.2178857.

[BY15] Joonsung Bae and Hoi-Jun Yoo. "A 45 µW Injection-Locked FSK Wake-Up Receiver With Frequency-to-Envelope Conversion for Crystal-Less Wireless Body Area Network". In: *IEEE JSSC* 50.6 (2015), pp. 1351–1360. ISSN: 1558-173X. DOI: 10.1109/JSSC.2015.2420311.

[BG09] Pawan K. Baheti and Harinath Garudadri. *Heart rate and blood pressure estimation from compressively sensed photoplethysmograph*. 2009. DOI: 10.4108/ICST.BODYNETS2009.6023. URL: http://dl.acm.org/ft_gateway.cfm?id=1658517&type=pdf.

[Bal+09] Heribert Baldus, Steven Corroy, Alberto Fazzi, Karin Klabunde, and Tim Schenk. "Human-centric connectivity enabled by body-coupled communications". In: *IEEE Communications Magazine* 47.6 (2009), pp. 172–178. ISSN: 0163-6804. DOI: 10.1109/MCOM.2009.5116816.

[BAL09] David Bannach, Oliver Amft, and Paul Lukowicz. "Automatic Event-based Synchronization of Multimodal Data Streams from Wearable and Ambient Sensors". In: *Smart Sensing and Context*. EuroSSC'09. Springer, 2009, pp. 135–148. ISBN: 978-3-642-04470-0.

[Bañ+12] Oresti Baños, Miguel Damas, Héctor Pomares, et al. "A benchmark dataset to evaluate sensor displacement in activity recognition". In: *Proceedings of the 2012 ACM Conference on Ubiquitous Computing*. Ed. by Anind K. Dey. New York, NY: ACM, 2012, p. 1026. ISBN: 9781450312240. DOI: 10.1145/2370216.2370437.

[Bar+18] Kim E. Barrett, Susan M. Barman, Scott Boitano, and Jane F. Reckelhoff. *Ganong's medical physiology examination & board review*. 1st ed. McGraw-Hill's AccessMedicine. New York: McGraw-Hill, 2018. ISBN: 9780071832328. URL: https://accessmedicine.mhmedical.com/book.aspx?bookid=2139.

[BB01] Lisa Feldman Barrett and Daniel J. Barrett. "An Introduction to Computerized Experience Sampling in Psychology". In: *Social Science Computer Review* 19.2 (2001), pp. 175–185. DOI: 10.1177/089443930101900204.

[Bar+08] Adam T. Barth, Mark A. Hanson, Harry C. Powell Jr., et al. "Body-Coupled Communication for Body Sensor Networks". In: *Proceedings of the 3rd International ICST Conference on Body Area Networks*. Ed. by Sethuraman Panchanathan. ICST, 2008. ISBN: 978-963-9799-17-2. DOI: 10.4108/ICST.BODYNETS2008.2964.

[Bas+87] G. Baselli, S. Cerutti, S. Civardi, et al. "Heart rate variability signal processing: A quantitative approach as an aid to diagnosis in cardiovascular pathologies". In: *International Journal of Bio-Medical Computing* 20.1 (1987), pp. 51–70. ISSN: 0020-7101. DOI: 10.1016/0020-7101(87)90014-6.

[Bas+19a] Shikder Shafiul Bashar, Md. Sazal Miah, A.H.M. Zadidul Karim, and Md. Abdullah Al Mahmud. "Extraction of Heart Rate from PPG Signal: A Machine Learning Approach using Decision Tree Regression Algorithm". In: *2019 4th International Conference on Electrical Information and Communication Technology (EICT)*. IEEE, Dec. 2019, pp. 1–6. ISBN: 978-1-7281-6040-5. DOI: 10.1109/EICT48899.2019.9068845.

[Bas+19b] L. Bastos, D. Rosario, E. Cerqueira, A. Santos, and M. Nogueira. "Filtering Parameters Selection Method and Peaks Extraction for ECG and PPG Signals". In: *IEEE LATINCOM*. 2019, pp. 1–6. ISBN: 978-1-7281-3955-5. DOI: 10.1109/LATINCOM48065.2019.8937861.

[Bea+18] Christopher Beach, Sammy Krachunov, James Pope, et al. "An Ultra Low Power Personalizable Wrist Worn ECG Monitor Integrated With IoT Infrastructure". In: *IEEE Access* 6 (2018), pp. 44010–44021. ISSN: 2169-3536. DOI: 10.1109/ACCESS.2018.2864675.

[BGJ15a] Terrell R. Bennett, Nicholas Gans, and Roozbeh Jafari. "A Data-driven Synchronization Technique for Cyber-Physical Systems". In: *Proceedings of the Second International Workshop on the Swarm at the Edge of the Cloud*. ACM, 2015, pp. 49–54. DOI: 10.1145/2756755.2756763.

[BGJ15b] Terrell R. Bennett, Nicholas Gans, and Roozbeh Jafari. "Multi-Sensor Data-Driven Synchronization Using Wearable Sensors". In: (2015). DOI: 10.1145/2802083.2808393.

[BGJ17] Terrell R. Bennett, Nicholas Gans, and Roozbeh Jafari. "Data-Driven Synchronization for Internet-of-Things Systems". In: *ACM Transactions on Embedded Computing Systems* 16.3 (2017), pp. 1–24. ISSN: 1539-9087. DOI: 10.1145/2983627.

[Ben+20] Brinnae Bent, Benjamin A. Goldstein, Warren A. Kibbe, and Jessilyn P. Dunn. "Investigating sources of inaccuracy in wearable optical heart rate sensors". In: *NPJ digital medicine* 3 (2020), p. 18. DOI: 10.1038/s41746-020-0226-6.

[BDD16] Mary Ellen Berglund, Julia Duvall, and Lucy E. Dunne. "A survey of the historical scope and current trends of wearable technology applications". In: *Proceedings of the 2016 ACM International Symposium on Wearable Computers*. Ed. by Michael Beigl. New York, NY: ACM, 2016, pp. 40–43. ISBN: 9781450344609. DOI: 10.1145/2971763.2971796.

[Ber+21] Jake Bergquist, Lindsay Rupp, Brian Zenger, et al. "Body Surface Potential Mapping: Contemporary Applications and Future Perspectives". In: *Hearts* 2.4 (2021), pp. 514–542. ISSN: 2673-3846. DOI: 10.3390/hearts2040040. URL: https://www.mdpi.com/2673-3846/2/4/40.

[Ber+10] Eugen Berlin, Jun Liu, Kristof Van Laerhoven, and Bernt Schiele. "Coming to grips with the objects we grasp". In: *Proceedings of the fourth international conference on Tangible, embedded, and embodied interaction - TEI '10*. Ed. by Hiroshi Ishii, Robert J.K. Jacob, Pattie Maes, et al. New York, New York, USA: ACM Press, 2010, p. 57. ISBN: 9781605588414. DOI: 10.1145/1709886.1709898.

[BC94] Donald J. Berndt and James Clifford. "Using Dynamic Time Warping to Find Patterns in Time Series". In: *Proceedings of the 3rd International Conference on Knowledge Discovery and Data Mining*. AAAIWS'94. Seattle, WA: AAAI Press, 1994, pp. 359–370.

[Bia+20] Giorgio Biagetti, Paolo Crippa, Laura Falaschetti, et al. "Dataset from PPG wireless sensor for activity monitoring". In: *Data in brief* 29 (2020), p. 105044. DOI: 10.1016/j.dib.2019.105044.

[BFS05] Philip E. Bickler, John R. Feiner, and John W. Severinghaus. "Effects of Skin Pigmentation on Pulse Oximeter Accuracy at Low Saturation". In: *Anesthesiology* 102.4 (2005), pp. 715–719. DOI: 10.1097/00000542-200504000-00004.

[Bil11] George E. Billman. "Heart rate variability - a historical perspective". In: *Frontiers in Physiology* 2 (2011), p. 86. ISSN: 1664-042X. DOI: 10.3389/fphys.2011.00086.

[BL22] Zhao Bin and Guo Lili. "Trend and Strategy of Wearable Devices Design". In: *Journal of Design Thinking* (2022). ISSN: 2645-3304. DOI: 10.22059/jdt.2022.343562.1075. URL: https://jdt.ut.ac.ir/article_89804.html.

[Bis+19] Dwaipayan Biswas, Neide Simoes-Capela, Chris van Hoof, and Nick van Helleputte. "Heart Rate Estimation From Wrist-Worn Photoplethysmography: A Review". In: *IEEE Sensors Journal* 19.16 (2019), pp. 6560–6570. ISSN: 1530-437X. DOI: 10.1109/JSEN.2019.2914166.

[Boc+20] Giuseppe Boccignone, Donatello Conte, Vittorio Cuculo, et al. "An Open Framework for Remote-PPG Methods and Their Assessment". In: *IEEE Access* 8 (2020), pp. 216083–216103. ISSN: 2169-3536. DOI: 10.1109/ACCESS.2020.3040936. URL: https://hal.science/hal-03046044/.

[BDB21] Anna Borawska, Jarosław Duda, and Konrad Biercewicz. "Best practices of neurophysiological data collection for media message evaluation in social campaigns". In: *Procedia Computer Science* 192 (2021), pp. 4017–4026. ISSN: 18770509. DOI: 10.1016/j.procs.2021.09.176. URL: https://www.sciencedirect.com/science/article/pii/S1877050921019153.

[BL16] Deborah Bothun and Matthew Lieberman. *The Wearable Life 2.0: Connected living in a wearable world*. 2016.

[Böt+22] Sebastian Böttcher, Solveig Vieluf, Elisa Bruno, et al. "Data quality evaluation in wearable monitoring". In: *Scientific Reports* 12.1 (2022), p. 21412. ISSN: 2045-2322. DOI: 10.1038/s41598-022-25949-x. URL: https://www.nature.com/articles/s41598-022-25949-x.

[Bra+20] Fabian Braun, Patrick Theurillat, Martin Proenca, et al. "Pulse Oximetry at the Wrist During Sleep: Performance, Challenges and Perspectives". In: *Annual International Conference of the IEEE Engineering in Medicine and Biology Society. IEEE Engineering in Medicine and Biology Society. Annual International Conference* 2020 (2020), pp. 5115–5118. DOI: 10.1109/EMBC44109.2020.9176081.

[Bri06] Glen Brisebois. "Signal conditioning for high-impedance sensors". In: *EDN* (2006). URL: https://www.edn.com/signal-conditioning-for-high-impedance-sensors/ (visited on 05/12/2022).

[BDE13] David Broman, Patricia Derler, and John Eidson. "Temporal Issues in Cyber-Physical Systems". In: *Journal of the Indian Institute of Science* 93.3 (2013), pp. 389–402. ISSN: 0970-4140. URL: http://journal.library.iisc.ernet.in/index.php/iisc/article/view/1686.

[BG15] Teodor Buchner and Jan Gierałtowski. "How fast does the ECG signal propagate within the body". In: *Working Group for Cardiovascular Physics. Faculty of Physics, Warsaw University of Technology. Sixth Cardiology Meets Physics & Mathematics.* 6 (2015).

[Buc+22] Teodor Buchner, Maryla Zajdel, Kazimierz Pęczalski, and Paweł Nowak. *How fast is ECG signal? Propagation of the endogenous electromagnetic wave of cardiac origin*. 2022. DOI: 10.21203/rs.3.rs-1916139/v1.

[BK14] K. Budidha and P. A. Kyriacou. "The human ear canal: investigation of its suitability for monitoring photoplethysmographs and arterial oxygen saturation". In: *Physiological Measurement* 35.2 (2014), p. 111. ISSN: 0967-3334. DOI: 10.1088/0967-3334/35/2/111. URL: http://iopscience.iop.org/article/10.1088/0967-3334/35/2/111/pdf.

[BBS14] Andreas Bulling, Ulf Blanke, and Bernt Schiele. "A tutorial on human activity recognition using body-worn inertial sensors". In: *ACM Computing Surveys* 46.3 (2014), pp. 1–33. ISSN: 0360-0300. DOI: 10.1145/2499621.

[CAM20] Felix Cabarcas, Juan Aranda, and Diego Mendez. "OpenWuR - An Open WSN Platform for WuR-Based Application Prototyping". In: *EWSN '20* (2020), pp. 212–217.

[CTF20] Raymundo Cassani, Abhishek Tiwari, and Tiago H. Falk. "Optimal filter characterization for photoplethysmography-based pulse rate and pulse power spectrum estimation". In: *IEEE EMBC* 2020 (2020), pp. 914–917. DOI: 10.1109/EMBC44109.2020.9175396.

[Cas+08] M. Cassim Munshi, Xiaoyuan Xu, Xiaodan Zou, et al. "Wireless ECG plaster for body sensor network". In: *5th International Summer School and Symposium on Medical Devices and Biosensors, 2008*. Piscataway, NJ: IEEE, 2008, pp. 310–313. ISBN: 978-1-4244-2252-4. DOI: 10.1109/ISSMDBS.2008.4575081.

[Cas14] Alexander J. Casson. "Performance of wrist based electrocardiography with conventional ECG analysis algorithms". In: *2014 8th Conference of the European Study Group on Cardiovascoular Oscillations (ESGCO 2014)*. Piscataway, NJ: IEEE, 2014, pp. 11–12. ISBN: 978-1-4799-3969-5. DOI: 10.1109/ESGCO.2014.6847494.

[Cas+18] Denisse Castaneda, A. Esparza, Mohammad Ghamari, Cinna Soltanpur, and Homer Nazeran. "A review on wearable photoplethysmography sensors and their potential future applications in health care". In: 2018. URL: https://pdfs.semanticscholar.org/3457/4e47059cfe7a49fbd5f9d7ef704ad68b97be.pdf.

[CBR91] Denis Chabot, Max Bayer, and André de Roos. "Instantaneous heart rates and other techniques introducing errors in the calculation of heart rate". In: *Canadian Journal of Zoology* 69.4 (1991), pp. 1117–1120. ISSN: 0008-4301. DOI: 10.1139/z91-156.

[Cha+19a] Gabriel Chan, Rachel Cooper, Manish Hosanee, et al. "Multi-Site Photoplethysmography Technology for Blood Pressure Assessment: Challenges and Recommendations". In: *Journal of clinical medicine* 8.11 (2019). ISSN: 2077-0383. DOI: 10.3390/jcm8111827.

[Cha+19b] Cheng-Chun Chang, Chien-Ta Wu, Byung Il Choi, and Tong-Jing Fang. "MW-PPG Sensor: An on-Chip Spectrometer Approach". In: *Sensors (Basel, Switzerland)* 19.17 (2019). DOI: 10.3390/s19173698.

[Cha+18] Peter H. Charlton, Drew A. Birrenkott, Timothy Bonnici, et al. "Breathing Rate Estimation from the Electrocardiogram and Photoplethysmogram: A Review". In: *IEEE Reviews in Biomedical Engineering* 11 (2018), pp. 2–20. DOI: 10.1109/RBME.2017.2763681.

[Cha+16] Peter H. Charlton, Timothy Bonnici, Lionel Tarassenko, et al. "An assessment of algorithms to estimate respiratory rate from the electrocardiogram and photoplethysmogram". In: *Physiological Measurement* 37.4 (2016), pp. 610–626. ISSN: 0967-3334. DOI: 10.1088/0967-3334/37/4/610.

[Cha+22a] Peter H. Charlton, Panicos A. Kyriaco, Jonathan Mant, et al. "Wearable Photoplethysmography for Cardiovascular Monitoring". In: *Proceedings of the IEEE* 110.3 (2022), pp. 355–381. ISSN: 0018-9219. DOI: 10.1109/JPROC.2022.3149785.

[CM+19] Peter H. Charlton, Jorge Mariscal Harana, et al. "Modeling arterial pulse waves in healthy aging: a database for in silico evaluation of hemodynamics and pulse wave indexes". In: *American journal of physiology. Heart and circulatory physiology* 317.5 (2019), H1062–H1085. ISSN: 0363-6135. DOI: 10.1152/ajpheart.00218.2019.

[CPK22] Peter H. Charlton, Kristjan Pilt, and Panicos A. Kyriacou. "Establishing best practices in photoplethysmography signal acquisition and processing". In: *Physiological measurement* 43.5 (2022), p. 050301. ISSN: 0967-3334. DOI: 10.1088/1361-6579/ac6cc4. URL: https://iopscience.iop.org/article/10.1088/1361-6579/ac6cc4.

[CVS16] Peter H. Charlton, Mauricio Villarroel, and Francisco Salguiero. "Waveform Analysis to Estimate Respiratory Rate". In: *Secondary Analysis of Electronic Health Records*. Springer International Publishing, 2016, pp. 377–390. ISBN: 978-3-319-43742-2. DOI: 10.1007/978-3-319-43742-2_26.

[CR18] Ayan Chatterjee and Uttam Kumar Roy. "PPG Based Heart Rate Algorithm Improvement with Butterworth IIR Filter and Savitzky-Golay FIR Filter". In: *2018 2nd International Conference on Electronics, Materials Engineering & Nano-Technology (IEMENTech)*. Ed. by Satyajit Chakrabarti. [Piscataway, New Jersey]: IEEE, 2018, pp. 1–6. ISBN: 978-1-5386-5550-4. DOI: 10.1109/IEMENTECH.2018.8465225.

[Cha+22b] Baibhab Chatterjee, Arunashish Datta, Mayukh Nath, et al. "A 65nm 63.3µW 15Mbps Transceiver with Switched-Capacitor Adiabatic Signaling and Combinatorial-Pulse-Position Modulation for Body-Worn Video-Sensing AR Nodes". In: *IEEE ISSCC*. IEEE, 2022, pp. 276–278. ISBN: 978-1-6654-2800-2. DOI: 10.1109/ISSCC42614.2022.9731793.

[CBK20] Subhasri Chatterjee, Karthik Budidha, and Panayiotis A. Kyriacou. "Investigating the origin of photoplethysmography using a multiwavelength Monte Carlo model". In: *Physiological measurement* 41.8 (2020), p. 084001. ISSN: 0967-3334. DOI: 10.1088/1361-6579/aba008.

[Che+00] W. Chen, T. Kobayashi, S. Ichikawa, Y. Takeuchi, and T. Togawa. "Continuous estimation of systolic blood pressure using the pulse arrival time and intermittent calibration". In: *Medical & biological engineering & computing* 38.5 (2000), pp. 569–574. DOI: 10.1007/BF02345755. URL: https://link.springer.com/article/10.1007/BF02345755.

[CMC11] Yu M. Chi, Christoph Maier, and Gert Cauwenberghs. "Ultra-High Input Impedance, Low Noise Integrated Amplifier for Noncontact Biopotential Sensing". In: *IEEE Journal on Emerging and Selected Topics in Circuits and Systems* 1.4 (2011), pp. 526–535. ISSN: 2156-3357. DOI: 10.1109/JETCAS.2011.2179419.

[CJC10] Yu Mike Chi, Tzyy-Ping Jung, and Gert Cauwenberghs. "Dry-contact and noncontact biopotential electrodes: methodological review". In: *IEEE reviews in biomedical engineering* 3 (2010), pp. 106–119. DOI: 10.1109/RBME.2010.2084078.

[Chi+91] Y. C. Chiu, P. W. Arand, S. G. Shroff, T. Feldman, and J. D. Carroll. "Determination of pulse wave velocities with computerized algorithms". In: *American Heart Journal* 121.5 (1991), pp. 1460–1470. ISSN: 0002-8703. DOI: 10.1016/0002-8703(91)90153-9. URL: https://www.sciencedirect.com/science/article/pii/0002870391901539.

[CBY13] Hyunwoo Cho, Joonsung Bae, and Hoi-Jun Yoo. "A 37.5 µW Body Channel Communication Wake-Up Receiver With Injection-Locking Ring Oscillator for Wireless Body Area Network". In: *IEEE TCSI* 60.5 (2013), pp. 1200–1208. ISSN: 1549-8328. DOI: 10.1109/TCSI.2013.2249173.

[Cho+16] Hyunwoo Cho, Hyunki Kim, Minseo Kim, et al. "A 79 pJ/b 80 Mb/s Full-Duplex Transceiver and a 100 kb/s Super-Regenerative Transceiver for Body Channel Communication". In: *IEEE JSSC* 51.1 (2016), pp. 310–317. ISSN: 0018-9200. DOI: 10.1109/JSSC.2015.2498761.

[Cho+09] Namjun Cho, Long Yan, Joonsung Bae, and Hoi-Jun Yoo. "A 60 kb/s–10 Mb/s Adaptive Frequency Hopping Transceiver for Interference-Resilient Body Channel Communication". In: *IEEE JSSC* 44.3 (2009), pp. 708–717. ISSN: 0018-9200. DOI: 10.1109/JSSC.2008.2012328.

[CS17] A. Choi and H. Shin. "Photoplethysmography sampling frequency: pilot assessment of how low can we go to analyze pulse rate variability with reliability?" In: *Physiological Measurement* 38.3 (2017), pp. 586–600. ISSN: 0967-3334. DOI: 10.1088/1361-6579/aa5efa.

[Cho+17] Changmok Choi, Byung-Hoon Ko, Jongwook Lee, et al. "PPG pulse direction determination algorithm for PPG waveform inversion by wrist rotation". In: *Conference proceedings : ... Annual International Conference of the IEEE Engineering in Medicine and Biology Society. IEEE Engineering in Medicine and Biology Society. Annual Conference* 2017 (2017), pp. 4090–4093. ISSN: 1557-170X. DOI: 10.1109/EMBC.2017.8037755.

[Cho+19] Yung-Wey Chong, Widad Ismail, Kwangman Ko, and Chen-Yi Lee. "Energy Harvesting For Wearable Devices: A Review". In: *IEEE Sensors Journal* 19.20 (2019), pp. 9047–9062. ISSN: 1530-437X. DOI: 10.1109/JSEN.2019.2925638.

[Cho+22] Anirban Dutta Choudhury, Rohan Banerjee, Sanjay Kimbahune, and Arpan Pal. "Proliferation of a new generation of sensors: Smartphones and wearables". In: *NEW FRONTIERS OF CARDIOVASCULAR SCREENING USING UNOBTRUSIVE SENSORS*. [S.l.]: ELSEVIER ACADEMIC PRESS, 2022, pp. 31–59. ISBN: 9780128244999. DOI: 10.1016/B978-0-12-824499-9.00002-7.

[CCL15] Ching-Che Chung, Chi-Tung Chang, and Chih-Yu Lin. "A 1 Mb/s–40 Mb/s human body channel communication transceiver". In: *VLSI-DAT*. IEEE, 2015, pp. 1–4. ISBN: 978-1-4799-6275-4. DOI: 10.1109/VLSI-DAT.2015.7114536.

[CLL19] Heewon Chung, Hooseok Lee, and Jinseok Lee. "Finite State Machine Framework for Instantaneous Heart Rate Validation Using Wearable Photoplethysmography During Intensive Exercise". In: *IEEE J-BHI* 23.4 (2019), pp. 1595–1606. DOI: 10.1109/JBHI.2018.2871177.

[Cle21] Cleveland Clinic. *Blood Vessels*. https://my.clevelandclinic.org/health/body/21640-blood-vessels. Accessed: 2023-02-09. 2021.

[CT65] James W. Cooley and John W. Tukey. "An Algorithm for the Machine Calculation of Complex Fourier Series". In: *Mathematics of Computation* 19.90 (1965), pp. 297–301. ISSN: 1088-6842. DOI: 10.1090/S0025-5718-1965-0178586-1. URL: https://www.ams.org/journals/mcom/1965-19-090/S0025-5718-1965-0178586-1/.

[Cou11] Robert Couronné. *Erfassung der Pulswelle am Unterarm mittels optisch-transmissiver Plethysmographie*. Universität Erlangen-Nürnberg, 2011.

[CT01] Thomas M. Cover and Joy A. Thomas. "Entropy, Relative Entropy and Mutual Information". In: *Elements of Information Theory*. John Wiley & Sons, Ltd, 2001, pp. 12–49. DOI: 10.1002/0471200611.ch2. URL: https://onlinelibrary.wiley.com/doi/10.1002/0471200611.ch2.

[COL90] W. J. Cui, L. E. Ostrander, and B. Y. Lee. "In Vivo Reflectance of Blood and Tissue as a Function of Light Wavelength". In: *IEEE Transactions on Bio-Medical Engineering* 37.6 (1990), pp. 632–639. ISSN: 0018-9294. DOI: 10.1109/10.55667.

[Dao+17] Duy Dao, S. M. A. Salehizadeh, Yeonsik Noh, et al. "A Robust Motion Artifact Detection Algorithm for Accurate Detection of Heart Rates From Photoplethysmographic Signals Using Time-Frequency Spectral Features". In: *IEEE J-BHI* 21.5 (2017), pp. 1242–1253. DOI: 10.1109/JBHI.2016.2612059.

[Deh+18] Parastoo Dehkordi, Ainara Garde, Behnam Molavi, J. Mark Ansermino, and Guy A. Dumont. "Extracting Instantaneous Respiratory Rate From Multiple Photoplethysmogram Respiratory-Induced Variations". In: *Frontiers in physiology* 9 (2018), p. 948. ISSN: 1664-042X. DOI: 10.3389/fphys.2018.00948.

[DFT16] Fardin Derogarian, Joao Canas Ferreira, and Vitor M. Grade Tavares. "A Precise and Hardware-Efficient Time Synchronization Method for Wearable Wired Networks". In: *IEEE Sensors Journal* 16.5 (2016), pp. 1460–1470. ISSN: 1530-437X. DOI: 10.1109/JSEN.2015.2501645.

[DL01] Paul Dietz and Darren Leigh. "DiamondTouch: A Multi-User Touch Technology". In: *UIST '01*. Ed. by Joe Marks and Elizabeth Mynatt. New York, New York, USA: ACM Press, 2001, p. 219. ISBN: 158113438X. DOI: 10.1145/502348.502389.

[Dij59] E. W. Dijkstra. "A note on two problems in connexion with graphs". In: *Numerische Mathematik* 1.1 (1959), pp. 269–271. ISSN: 0029-599X. DOI: 10.1007/BF01386390.

[DH41] John B. Dillon and Alrick B. Hertzman. "The form of the volume pulse in the finger pad in health, arteriosclerosis, and hypertension". In: *American Heart Journal* 21.2 (1941), pp. 172–190. ISSN: 0002-8703. DOI: 10.1016/S0002-8703(41)90966-3. URL: https://www.sciencedirect.com/science/article/pii/S0002870341909663.

[Don09] João Henrique Donker. "The body as a communication medium". In: *Department of EMCS, 11th Conference on IT, University of Twente*. 2009.

[DV90] P. Duhamel and M. Vetterli. "Fast fourier transforms: A tutorial review and a state of the art". In: *Signal Processing* 19.4 (1990), pp. 259–299. ISSN: 0165-1684. DOI: 10.1016/0165-1684(90)90158-U. URL: https://www.sciencedirect.com/science/article/pii/016516849090158U.

[EFW50] W. Einthoven, G. Fahr, and A. de Waart. "On the direction and manifest size of the variations of potential in the human heart and on the influence of the position of the heart on the form of the electrocardiogram". In: *American Heart Journal* 40.2 (1950), pp. 163–211. ISSN: 0002-8703. DOI: 10.1016/0002-8703(50)90165-7. URL: https://www.sciencedirect.com/science/article/pii/0002870350901657.

[Elg12] Mohamed Elgendi. "On the Analysis of Fingertip Photoplethysmogram Signals". In: *Current Cardiology Reviews* 8.1 (2012), pp. 14–25. ISSN: 1573403X. DOI: 10.2174/157340312801215782.

[EGE02] Jeremy Elson, Lewis Girod, and Deborah Estrin. "Fine-grained network time synchronization using reference broadcasts". In: *ACM SIGOPS Operating Systems Review* 36.SI (2002), p. 147. ISSN: 01635980. DOI: 10.1145/844128.844143.

[EmE4] Empatica, Inc. *Empatica E4 Wristband, commercial product.* URL: https://www.empatica.com/research/e4/ (visited on 09/15/2020).

[Ern17] Gernot Ernst. "Hidden Signals-The History and Methods of Heart Rate Variability". In: *Frontiers in public health* 5 (2017), p. 265. ISSN: 2296-2565. DOI: 10.3389/fpubh.2017.00265.

[ESP] Espressif Systems. *ESP32, commercial product.* URL: https://www.espressif.com/en/products/socs/esp32 (visited on 05/12/2022).

[FAG+10] F.U.S. Mattace-Raso, A. Hofman, G.C. Verwoert, et al. "Determinants of pulse wave velocity in healthy people and in the presence of cardiovascular risk factors: 'establishing normal and reference values'". In: *European Heart Journal* 31.19 (2010), pp. 2338–2350. ISSN: 0195-668X. DOI: 10.1093/eurheartj/ehq165.

[Fai+20] Marsel Faizullin, Anastasiia Kornilova, Azat Akhmetyanov, and Gonzalo Ferrer. "Twist-n-Sync: Software Clock Synchronization with Microseconds Accuracy Using MEMS-Gyroscopes". In: *Sensors (Basel, Switzerland)* 21.1 (2020). DOI: 10.3390/s21010068.

[Fel+05] A. Feldman, E. M. Tapia, S. Sadi, P. Maes, and C. Schmandt. "ReachMedia: on-the-move interaction with everyday objects". In: *Ninth IEEE International Symposium on Wearable Computers (ISWC'05)*. 2005, pp. 52–59. DOI: 10.1109/ISWC.2005.44.

[Fer+22] Andrea Ferlini, Alessandro Montanari, Chulhong Min, et al. "In-Ear PPG for Vital Signs". In: *IEEE Pervasive Computing* 21.1 (2022), pp. 65–74. ISSN: 1536-1268. DOI: 10.1109/MPRV.2021.3121171.

[FGM20] Nicolas De Pinho Ferreira, Claudine Gehin, and Bertrand Massot. "Optical flow sensor as a reference for reduction of motion artefacts in photoplethysmographic measurements". In: *IEEE EMBC* 2020 (2020), pp. 4421–4424. DOI: 10.1109/EMBC44109.2020.9175787.

[Fin10] Klaus Finkenzeller. *RFID Handbook: Fundamentals and Applications in Contactless Smart Cards, Radio Frequency Identification and Near-Field Communication*. 3rd. Wiley and IEEE Press, 2010. ISBN: 0470665122. DOI: 10.1002/9780470665121. URL: https://onlinelibrary.wiley.com/doi/book/10.1002/9780470665121.

[Fio+21] Laura Fiorini, Filippo Cavallo, Mihail Martinelli, and Erika Rovini. "Characterization of a PPG Wearable Sensor to Be Embedded into an Innovative Ring-Shaped Device for Healthcare Monitoring". In: Springer, Cham, 2021, pp. 49–63. DOI: 10.1007/978-3-030-63107-9_5. URL: https://link.springer.com/chapter/10.1007/978-3-030-63107-9_5.

[Fis+17] Christoph Fischer, Benno Domer, Thomas Wibmer, and Thomas Penzel. "An Algorithm for Real-Time Pulse Waveform Segmentation and Artifact Detection in Photoplethysmograms". In: *IEEE J-BHI* 21.2 (2017), pp. 372–381. DOI: 10.1109/JBHI.2016.2518202.

[FPR05] K. P. Fishkin, M. Philipose, and A. Rea. "Hands-On RFID: Wireless Wearables for Detecting Use of Objects". In: *ISWC 2005*. IEEE, 2005, pp. 38–43. ISBN: 0-7695-2419-2. DOI: 10.1109/ISWC.2005.25.

[Fle+11] Susannah Fleming, Matthew Thompson, Richard Stevens, et al. "Normal ranges of heart rate and respiratory rate in children from birth to 18 years of age: a systematic review of observational studies". In: *The Lancet* 377.9770 (2011), pp. 1011–1018. ISSN: 01406736. DOI: 10.1016/S0140-6736(10)62226-X.

[FS05] Masaaki Fukumoto and Mitsuru Shinagawa. "CarpetLAN: A Novel Indoor Wireless(-like) Networking and Positioning System". In: *UbiComp 2005*. 2005, pp. 1–18. DOI: 10.1007/11551201_1. URL: https://link.springer.com/chapter/10.1007/11551201_1.

[GLG96] S. Gabriel, R. W. Lau, and C. Gabriel. "The dielectric properties of biological tissues: II. Measurements in the frequency range 10 Hz to 20 GHz". In: *Physics in Medicine & Biology* 41.11 (1996), pp. 2251–2269. ISSN: 0031-9155. DOI: 10.1088/0031-9155/41/11/002. URL: https://iopscience.iop.org/article/10.1088/0031-9155/41/11/002/meta.

[Gal+12] Laura Galluccio, Tommaso Melodia, Sergio Palazzo, and Giuseppe Enrico Santagati. "Challenges and implications of using ultrasonic communications in intra-body area networks". In: *2012 9th Annual Conference on Wireless On-Demand Network Systems and Services (WONS)*. IEEE, 2012, pp. 182–189. ISBN: 978-1-4577-1722-2. DOI: 10.1109/WONS.2012.6152227.

[Gar+18] Laura García, Lorena Parra, Jose M. Jimenez, and Jaime Lloret. "Physical Wellbeing Monitoring Employing Non-Invasive Low-Cost and Low-Energy Sensor Socks". In: *Sensors (Basel, Switzerland)* 18.9 (2018). DOI: 10.3390/s18092822.

[Gar+13] Gaetano D. Gargiulo, Alistair L. McEwan, Paolo Bifulco, et al. "Towards true unipolar bio-potential recording: a preliminary result for ECG". In: *Physiological measurement* 34.1 (2013), N1–7. ISSN: 0967-3334. DOI: 10.1088/0967-3334/34/1/N1.

[Gem+98] F. Gemperle, C. Kasabach, J. Stivoric, M. Bauer, and R. Martin. "Design for wearability". In: *Second international symposium on wearable computers*. IEEE Comput. Soc, 1998, pp. 116–122. ISBN: 0-8186-9074-7. DOI: 10.1109/ISWC.1998.729537.

[Ges89] D. B. Geselowitz. "On the theory of the electrocardiogram". In: *Proceedings of the IEEE* 77.6 (1989), pp. 857–876. ISSN: 0018-9219. DOI: 10.1109/5.29327.

[Gil+10] E. Gil, M. Orini, R. Bailón, et al. "Photoplethysmography pulse rate variability as a surrogate measurement of heart rate variability during non-stationary conditions". In: *Physiological measurement* 31.9 (2010), pp. 1271–1290. ISSN: 0967-3334. DOI: 10.1088/0967-3334/31/9/015. URL: https://iopscience.iop.org/article/10.1088/0967-3334/31/9/015/meta.

[Gil92] Jeff Gilham. "Details of a real world implementation of Fourier techniques for power spectral analysis of heart rate variability". In: *Journal of Electrocardiology* 25 (1992), pp. 221–223. ISSN: 00220736. DOI: 10.1016/0022-0736(92)90107-B.

[Gio+16] Elisabetta De Giovanni, Srinivasan Murali, Francisco Rincon, and David Atienza. "Ultra-Low Power Estimation of Heart Rate Under Physical Activity Using a Wearable Photoplethysmographic System". In: *DSD 2016*. Ed. by Paris Kitsos and EUROMICRO Conference on Digital System Design. Piscataway, NJ: IEEE, 2016, pp. 553–560. ISBN: 978-1-5090-2817-7. DOI: 10.1109/DSD.2016.101.

[Git13] Lisa Gitelman. *Raw data is an oxymoron*. Infrastructures series. Cambridge, Massachusetts: The MIT Press, 2013. ISBN: 9780262518284. URL: https://cds.cern.ch/record/1530979.

[Gol+00] A. L. Goldberger, L. A. Amaral, L. Glass, et al. "PhysioBank, PhysioToolkit, and PhysioNet: components of a new research resource for complex physiologic signals". In: *Circulation* 101.23 (2000), E215–20. DOI: 10.1161/01.cir.101.23.e215.

[Goo+22] Andrew J. Goodwin, Danny Eytan, William Dixon, et al. "Timing errors and temporal uncertainty in clinical databases—A narrative review". In: *Frontiers in Digital Health* 4 (2022). DOI: 10.3389/fdgth.2022.932599.

[Got+22] Eric Raphael Gottlieb, Jennifer Ziegler, Katharine Morley, Barret Rush, and Leo Anthony Celi. "Assessment of Racial and Ethnic Differences in Oxygen Supplementation Among Patients in the Intensive Care Unit". In: *JAMA internal medicine* 182.8 (2022), pp. 849–858. DOI: 10.1001/jamainternmed.2022.2587.

[Gro+13] Tobias Große-Puppendahl, Yannick Berghoefer, Andreas Braun, Raphael Wimmer, and Arjan Kuijper. "OpenCapSense: A rapid prototyping toolkit for pervasive interaction using capacitive sensing". In: *2013 IEEE International Conference on Pervasive Computing and Communications (PerCom 2013)*. Piscataway NJ: IEEE, 2013. ISBN: 978-1-4673-4573-6. DOI: 10.1109/PerCom.2013.6526726.

[Gro+14] Tobias Große-Puppendahl, Sebastian Herber, Raphael Wimmer, et al. "Capacitive Near-Field Communication for Ubiquitous Interaction and Perception". In: *UbiComp '14*. ACM, 2014, pp. 231–242. DOI: 10.1145/2632048.2632053.

[Gro+17] Tobias Große-Puppendahl, Christian Holz, Gabe Cohn, et al. "Finding Common Ground: A Survey of Capacitive Sensing in Human-Computer Interaction". In: *Proceedings of the 2017 CHI Conference on Human Factors in Computing Systems*. CHI '17. ACM, 2017, pp. 3293–3315. ISBN: 9781450346559.

[Gud+19] Amogh Gudi, Marian Bittner, Roelof Lochmans, and Jan van Gemert. "Efficient Real-Time Camera Based Estimation of Heart Rate and Its Variability". In: 2019. URL: https://openaccess.thecvf.com/content_ICCVW_2019/html/CVPM/Gudi_Efficient_Real-Time_Camera_Based_Estimation_of_Heart_Rate_and_Its_ICCVW_2019_paper.html.

[Ha+14] Sohmyung Ha, Chul Kim, Yu M. Chi, and Gert Cauwenberghs. "Low-Power Integrated Circuit Design for Wearable Biopotential Sensing". In: *Wearable sensors*. Ed. by Edward Sazonov and Michael R. Neuman. Amsterdam: AP Academic Press is an imprint of Elsevier, 2014, pp. 323–352. ISBN: 9780124186620. DOI: 10.1016/B978-0-12-418662-0.00018-0.

[HJ13] Gerard de Haan and Vincent Jeanne. "Robust pulse rate from chrominance-based rPPG". In: *IEEE Transactions on Biomedical Engineering* 60.10 (2013), pp. 2878–2886. ISSN: 1558-2531. DOI: 10.1109/TBME.2013.2266196.

[Hv14] Gerard de Haan and Arno van Leest. "Improved motion robustness of remote-PPG by using the blood volume pulse signature". In: *Physiological Measurement* 35.9 (2014), p. 1913. ISSN: 0967-3334. DOI: 10.1088/0967-3334/35/9/1913. URL: http://iopscience.iop.org/article/10.1088/0967-3334/35/9/1913/pdf.

[HS21] Taku Hachisu and Kenji Suzuki. "Interpersonal Touch Sensing Devices Using Inter-Body Area Network". In: *IEEE Sensors Journal* 21.24 (2021), pp. 28001–28008. ISSN: 1530-437X. DOI: 10.1109/JSEN.2021.3126866.

[Hae+15] Marian Haescher, Denys J. C. Matthies, John Trimpop, and Bodo Urban. "A study on measuring heart- and respiration-rate via wrist-worn accelerometer-based seismocardiography (SCG) in comparison to commonly applied technologies". In: *Proceedings of the 2nd international Workshop on Sensor-based Activity Recognition and Interaction*. Ed. by Bodo Urban. New York, NY: ACM, 2015, pp. 1–6. ISBN: 9781450334549. DOI: 10.1145/2790044.2790054.

[Hai19] Ruth Hailu. *Fitbits and other wearables may not accurately track heart rates in people of color*. https://www.statnews.com/2019/07/24/fitbit-accuracy-dark-skin/. Accessed: 2023-01-20. 2019.

[ACK22] Raghda Al-Halawani, Subhasri Chatterjee, and Panayiotis A. Kyriacou. "Monte Carlo Simulation of the Effect of Human Skin Melanin in Light-Tissue Interactions". In: *Annual International Conference of the IEEE Engineering in Medicine and Biology Society. IEEE Engineering in Medicine and Biology Society. Annual International Conference* 2022 (2022), pp. 1598–1601. DOI: 10.1109/EMBC48229.2022.9871350.

[Hal+07] P. S. Hall, Yang Hao, Y. I. Nechayev, et al. "Antennas and propagation for on-body communication systems". In: *IEEE Antennas and Propagation Magazine* 49.3 (2007), pp. 41–58. ISSN: 1045-9243. DOI: 10.1109/MAP.2007.4293935.

[Ham50] R. W. Hamming. "Error Detecting and Error Correcting Codes". In: *Bell System Technical Journal* 29.2 (1950), pp. 147–160. ISSN: 00058580. DOI: 10.1002/j.1538-7305.1950.tb00463.x.

[Han+97] T. Handa, S. Shoji, S. Ike, S. Takeda, and T. Sekiguchi. "A Very Low-Power Consumption Wireless ECG Monitoring System Using Body as a Signal Transmission Medium". In: *Transducers 97*. IEEE, 1997, pp. 1003–1006. ISBN: 0-7803-3829-4. DOI: 10.1109/SENSOR.1997.635344.

[Har+08] Mikiko Hara, Akira Shibayama, Daisuke Takeshita, Dean C. Hay, and Senshi Fukashiro. "A comparison of the mechanical effect of arm swing and countermovement on the lower extremities in vertical jumping". In: *Human movement science* 27.4 (2008), pp. 636–648. ISSN: 0167-9457. DOI: 10.1016/j.humov.2008.04.001.

[HYH12] Makoto Harashima, Hiroyuki Yasuda, and Mikio Hasegawa. "Synchronization of Wireless Sensor Networks Using Natural Environmental Signals Based on Noise-Induced Phase Synchronization Phenomenon". In: *IEEE 75th Vehicular Technology Conference (VTC Spring), 2012*. Piscataway, NJ: IEEE, 2012, pp. 1–5. ISBN: 978-1-4673-0990-5. DOI: 10.1109/VETECS.2012.6240066.

[HKW12] Prakash Harikumar, Muhammad Irfan Kazim, and J Jacob Wikner. "An Analog Receiver Front-End for Capacitive Body-Coupled Communication". In: *NORCHIP, 2012*. IEEE. 2012, pp. 1–4.

[HCP02] C. J. Harland, T. D. Clark, and R. J. Prance. "Electric potential probes - new directions in the remote sensing of the human body". In: *Measurement Science and Technology* 13.2 (2002), pp. 163–169. ISSN: 0957-0233. DOI: 10.1088/0957-0233/13/2/304.

[Har+19] Vera Hartmann, Haipeng Liu, Fei Chen, et al. "Quantitative Comparison of Photoplethysmographic Waveform Characteristics: Effect of Measurement Site". In: *Frontiers in physiology* 10 (2019), p. 198. ISSN: 1664-042X. DOI: 10.3389/fphys.2019.00198.

[HS01] M. J. Hayes and P. R. Smith. "A new method for pulse oximetry possessing inherent insensitivity to artifact". In: *IEEE transactions on bio-medical engineering* 48.4 (2001), pp. 452–461. ISSN: 0018-9294. DOI: 10.1109/10.915711.

[He+16] Jianman He, Mengjun Wang, Xiaoxia Li, Gang Li, and Ling Lin. "Pulse wave detection method based on the bio-impedance of the wrist". In: *Review of Scientific Instruments* 87.5 (2016), p. 055001. ISSN: 0034-6748. DOI: 10.1063/1.4947514. URL: https://aip.scitation.org/doi/10.1063/1.4947514.

[HP16] Mathilde C. Hemon and Justin P. Phillips. "Comparison of foot finding methods for deriving instantaneous pulse rates from photoplethysmographic signals". In: *Journal of Clinical Monitoring and Computing* 30.2 (2016), pp. 157–168. ISSN: 1573-2614. DOI: 10.1007/s10877-015-9695-6. URL: https://link.springer.com/article/10.1007/s10877-015-9695-6.

[Her37] Alrick B. Hertzman. "Photoelectric Plethysmography of the Fingers and Toes in Man". In: *Experimental Biology and Medicine* 37.3 (1937), pp. 529–534. ISSN: 1535-3702. DOI: 10.3181/00379727-37-9630.

[HIG16] Mehrdad Hessar, Vikram Iyer, and Shyamnath Gollakota. "Enabling On-Body Transmissions with Commodity Devices". In: *Proceedings of the 2016 ACM International Joint Conference on Pervasive and Ubiquitous Computing*. Heidelberg, Germany: ACM, 2016, pp. 1100–1111. ISBN: 9781450344616. DOI: 10.1145/2971648.2971682.

[HS17] Josiah Hester and Jacob Sorber. "The Future of Sensing is Batteryless, Intermittent, and Awesome". In: *Proceedings of the 15th ACM Conference on Embedded Network Sensor Systems*. Ed. by Rasit Eskicioglu. [Place of publication not identified]: ACM, 2017, pp. 1–6. ISBN: 9781450354592. DOI: 10.1145/3131672.3131699.

[Hol61] Norman J. Holter. "New Method for Heart Studies". In: *Science (New York, N.Y.)* 134.3486 (1961), pp. 1214–1220. ISSN: 0036-8075. DOI: 10.1126/science.134.3486.1214.

[HK15] Christian Holz and Marius Knaust. "Biometric Touch Sensing: Seamlessly Augmenting Each Touch with Continuous Authentication". In: *UIST'15*. Ed. by Celine Latulipe, Bjoern Hartmann, and Tovi Grossman. New York: ACM, 2015, pp. 303–312. ISBN: 9781450337793. DOI: 10.1145/2807442.2807458.

[HOV19] Alexander Hölzemann, Henry Odoemelem, and Kristof Van Laerhoven. "Using an in-ear wearable to annotate activity data across multiple inertial sensors". In: *Proceedings of the 1st International Workshop on Earable Computing*. EarComp'19. ACM, 2019. DOI: 10.1145/3345615.3361136.

[HL04] Jason I. Hong and James A. Landay. "An Architecture for Privacy-Sensitive Ubiquitous Computing". In: *MobiSys 2004*. Ed. by Guruduth S. Banavar, Willy Zwaenepoel, Doug Terry, and Roy Want. New York, NY, USA: ACM, 2004, pp. 177–189. ISBN: 1581137931. DOI: 10.1145/990064.990087.

[HP18] Luis Howell and Bernd Porr. *High precision ECG Database with annotated R peaks, recorded and filmed under realistic conditions*. 2018. DOI: 10.5525/GLA.RESEARCHDATA.716.

[Hu+09] Sijung Hu, Vicente Azorin Peris, Angelos Echiadis, Jia Zheng, and Ping Shi. "Development of effective photoplethysmographic measurement techniques: from contact to non-contact and from point to imaging". In: *Conference proceedings : ... Annual International Conference of the IEEE Engineering in Medicine and Biology Society. IEEE Engineering in Medicine and Biology Society. Annual Conference* 2009 (2009), pp. 6550–6553. ISSN: 1557-170X. DOI: 10.1109/IEMBS.2009.5334505.

[HS20] Nicholas Huang and Nandakumar Selvaraj. "Robust PPG-based Ambulatory Heart Rate Tracking Algorithm". In: *IEEE EMBC* 2020 (2020), pp. 5929–5934. DOI: 10.1109/EMBC44109.2020.9175346.

[HMR20] Matti Huotari, Kari Määttä, and Juha Röning. "Photoplethysmographic waves and their detailed pulse interval distribution analysis on Poincare plots before and after the sauna exposures". In: *Biophotonics–Riga 2020*. Ed. by Janis Spigulis. SPIE, 2020, p. 18. ISBN: 9781510639997. DOI: 10.1117/12.2582204.

[INJ17] Bassem Ibrahim, Viswam Nathan, and Roozbeh Jafari. "Exploration and Validation of Alternate Sensing Methods for Wearable Continuous Pulse Transit Time Measurement Using Optical and Bioimpedance Modalities". In: *IEEE Engineering in Medicine and Biology Society.* 2017 (2017), pp. 2051–2055. ISSN: 1557-170X. DOI: 10.1109/EMBC.2017.8037256.

[IEE12] IEEE Standards Association. *IEEE 802.15.6-2012 - Wireless Body Area Networks*. 2012. URL: https://standards.ieee.org/standard/802_15_6-2012.html (visited on 06/16/2021).

[IM20] Nino Isakadze and Seth S. Martin. "How useful is the smartwatch ECG?" In: *Trends in Cardiovascular Medicine* 30.7 (2020), pp. 442–448. ISSN: 1050-1738. DOI: 10.1016/j.tcm.2019.10.010. URL: https://www.sciencedirect.com/science/article/pii/S1050173819301495.

[IH20] Kohei Ishii and Nobuaki Hiraoka. "Nail tip sensor: Toward reliable daylong monitoring of heart rate". In: *IEEJ Transactions on Electrical and Electronic Engineering* (2020). ISSN: 19314973. DOI: 10.1002/tee.23132.

[IAS21] Shahid Ismail, Usman Akram, and Imran Siddiqi. "Heart rate tracking in photoplethysmography signals affected by motion artifacts: a review". In: *EURASIP* 2021.1 (2021), pp. 1–27. DOI: 10.1186/s13634-020-00714-2.

[Isr+05] Steven A. Israel, John M. Irvine, Andrew Cheng, Mark D. Wiederhold, and Brenda K. Wiederhold. "ECG to identify individuals". In: *Pattern Recognition* 38.1 (2005), pp. 133–142. ISSN: 00313203. DOI: 10.1016/j.patcog.2004.05.014.

[JC17] Delaram Jarchi and Alexander Casson. "Description of a Database Containing Wrist PPG Signals Recorded during Physical Exercise with Both Accelerometer and Gyroscope Measures of Motion". In: *Data* 2.1 (2017), p. 1. DOI: 10.3390/data2010001.

[Jar+18] Delaram Jarchi, Dario Salvi, Lionel Tarassenko, and David A. Clifton. "Validation of Instantaneous Respiratory Rate Using Reflectance PPG from Different Body Positions". In: *Sensors* 18.11 (2018), p. 3705. DOI: 10.3390/s18113705.

[Jey+15] Vala Jeyhani, Shadi Mahdiani, Mikko Peltokangas, and Antti Vehkaoja. "Comparison of HRV parameters derived from photoplethysmography and electrocardiography signals". In: *Conference proceedings : ... Annual International Conference of the IEEE Engineering in Medicine and Biology Society. IEEE Engineering in Medicine and Biology Society. Annual Conference* 2015 (2015), pp. 5952–5955. ISSN: 1557-170X. DOI: 10.1109/EMBC.2015.7319747.

[Jin+16] Liu Jing, Zhang Yuan-Ting, Ding Xiao-Rong, Dai Wen-Xuan, and Zhao Ni. "A Preliminary Study on Multi-Wavelength PPG Based Pulse Transit Time Detection for Cuffless Blood Pressure Measurement". In: *Conference proceedings : ... Annual International Conference of the IEEE Engineering in Medicine and Biology Society.* 2016 (2016), pp. 615–618. ISSN: 1557-170X. DOI: 10.1109/EMBC.2016.7590777.

[Joh+06] A. Johansson, C. Ahlstrom, T. Lanne, and P. Ask. "Pulse wave transit time for monitoring respiration rate". In: *Medical & biological engineering & computing* 44.6 (2006), pp. 471–478. DOI: 10.1007/s11517-006-0064-y.

[JVR20] F. John Dian, Reza Vahidnia, and Alireza Rahmati. "Wearables and the Internet of Things (IoT), Applications, Opportunities, and Challenges: A Survey". In: *IEEE Access* 8 (2020), pp. 69200–69211. ISSN: 2169-3536. DOI: 10.1109/ACCESS.2020.2986329.

[Joh+16] Alistair E. W. Johnson, Tom J. Pollard, Lu Shen, et al. "MIMIC-III, a freely accessible critical care database". In: *Scientific Data* 3 (2016), p. 160035. DOI: 10.1038/sdata.2016.35.

[Jul06] Claude Julien. "The enigma of Mayer waves: Facts and models". In: *Cardiovascular research* 70.1 (2006), pp. 12–21. ISSN: 0008-6363. DOI: 10.1016/j.cardiores.2005.11.008.

[Kac+15] Mohamad Kachuee, Mohammad Mahdi Kiani, Hoda Mohammadzade, and Mahdi Shabany. "Cuff-less high-accuracy calibration-free blood pressure estimation using pulse transit time". In: (2015), pp. 1006–1009. DOI: 10.1109/ISCAS.2015.7168806.

[Kam+89] A.A.R. Kamal, J. B. Harness, G. Irving, and A. J. Mearns. "Skin photoplethysmography — a review". In: *Comp. Meth. Prog. Biomed.* 28 (1989), pp. 257–269. ISSN: 01692607. DOI: 10.1016/0169-2607(89)90159-4.

[Kam+05] Atsunori Kamiya, Junichiro Hayano, Toru Kawada, et al. "Low-frequency oscillation of sympathetic nerve activity decreases during development of tilt-induced syncope preceding sympathetic withdrawal and bradycardia". In: *American journal of physiology. Heart and circulatory physiology* 289.4 (2005), H1758–69. ISSN: 0363-6135. DOI: 10.1152/ajpheart.01027.2004..

[KM17] Alexei A. Kamshilin and Nikita B. Margaryants. "Origin of Photoplethysmographic Waveform at Green Light". In: *Physics Procedia* 86 (2017), pp. 72–80. ISSN: 18753892. DOI: 10.1016/j.phpro.2017.01.024.

[Kam+16] Alexei A. Kamshilin, Igor S. Sidorov, Laura Babayan, et al. "Accurate measurement of the pulse wave delay with imaging photoplethysmography". In: *Biomedical optics express* 7.12 (2016), pp. 5138–5147. ISSN: 2156-7085. DOI: 10.1364/BOE.7.005138.

[Kan+12] Masahide Kano, Masatoshi Ishii, Kensuke Kanda, et al. "Reflective photoplethysmography sensor with ring-shaped photodiode". In: *2012 IEEE International Conference on Systems, Man, and Cybernetics*. Ed. by IEEE Staff. [Place of publication not identified]: IEEE, 2012, pp. 2058–2061. ISBN: 978-1-4673-1714-6. DOI: 10.1109/ICSMC.2012.6378042.

[KCW19] Yung-Hua Kao, Paul C.-P. Chao, and Chin-Long Wey. "Design and Validation of a New PPG Module to Acquire High-Quality Physiological Signals for High-Accuracy Biomedical Sensing". In: *IEEE Journal of Selected Topics in Quantum Electronics* 25.1 (2019), pp. 1–10. ISSN: 1077-260X. DOI: 10.1109/JSTQE.2018.2871604.

[Kar+12] Walter Karlen, J. Mark Ansermino, and Guy Dumont. "Adaptive Pulse Segmentation and Artifact Detection in Photoplethysmography for Mobile Applications". In: *IEEE EMBS* 2012 (2012), pp. 3131–3134. ISSN: 1557-170X. DOI: 10.1109/EMBC.2012.6346628.

[Kar+13] Walter Karlen, Srinivas Raman, J. Mark Ansermino, and Guy A. Dumont. "Multiparameter Respiratory Rate Estimation from the Photoplethysmogram". In: *IEEE TBME* 60.7 (2013), pp. 1946–1953. ISSN: 0018-9294. DOI: 10.1109/TBME.2013.2246160.

[Kar+10] Walter Karlen, M. Turner, Erin Cooke, Guy Dumont, and J. Mark Ansermino. "CapnoBase: Signal database and tools to collect, share and annotate respiratory signals". In: *2010 Annual Meeting of the Society for Technology in Anesthesia*. Society for Technology in Anesthesia, 2010, p. 25.

[KCS84] Juha Karvonen, Jolanta Chwalbinska-Moneta, and Seppo Saynajakangas. "Comparison of Heart Rates Measured by ECG and Microcomputer". In: *The Physician and Sportsmedicine* 12.6 (1984), pp. 65–69. ISSN: 0091-3847. DOI: 10.1080/00913847.1984.11701872.

[Kaw+18] Fahim Kawsar, Chulhong Min, Akhil Mathur, and Allesandro Montanari. "Earables for Personal-Scale Behavior Analytics". In: *IEEE Pervasive Computing* 17.3 (2018), pp. 83–89. ISSN: 1536-1268. DOI: 10.1109/MPRV.2018.03367740.

[Kel+10] David U. J. Keller, Frank M. Weber, Gunnar Seemann, and Olaf Dössel. "Ranking the influence of tissue conductivities on forward-calculated ECGs". In: *IEEE Transactions on Biomedical Engineering* 57.7 (2010), pp. 1568–1576. ISSN: 1558-2531. DOI: 10.1109/TBME.2010.2046485.

[Kv18] Jochen Kempfle and Kristof van Laerhoven. "Respiration Rate Estimation with Depth Cameras". In: *iWOAR 2018*. Ed. by Denys J. C. Matthies, Marian Haescher, Kristina Yordanova, et al. ACM Digital Library. New York, NY: ACM, 2018, pp. 1–10. ISBN: 9781450364874. DOI: 10.1145/3266157.3266208.

[KTL14] Behailu Kibret, Assefa K. Teshome, and Daniel T. H. Lai. "Human Body as Antenna and Its Effect on Human Body Communications". In: *Progress In Electromagnetics Research (PIER)* 148 (2014), pp. 193–207. DOI: 10.2528/PIER14061207.

[Kim+07] E. J. Kim, C. G. Park, J. S. Park, S. Y. Suh, et al. "Relationship between blood pressure parameters and pulse wave velocity in normotensive and hypertensive subjects: invasive study". In: *Journal of Human Hypertension* 21.2 (2007), pp. 141–148. ISSN: 1476-5527. DOI: 10.1038/sj.jhh.1002120.

[Kim+93] W. Kim, A. S. Voloshin, S. H. Johnson, and A. Simkin. "Measurement of the impulsive bone motion by skin-mounted accelerometers". In: *Journal of Biomechanical Engineering* 115.1 (1993), pp. 47–52. ISSN: 0148-0731. DOI: 10.1115/1.2895470.

[Kim+20] Eyal Y. Kimchi, Brian F. Coughlin, Benjamin E. Shanahan, et al. "OpBox: Open Source Tools for Simultaneous EEG and EMG Acquisition from Multiple Subjects". In: *eNeuro* 7.5 (2020). DOI: 10.1523/ENEURO.0212-20.2020. URL: https://www.ncbi.nlm.nih.gov/pmc/articles/PMC7598913/.

[Kin+20] Hannu Olavi Kinnunen, Aleksi Rantanen, Tuomas Viljami Kenttä, and Heli Koskimäki. "Feasible assessment of recovery and cardiovascular health: accuracy of nocturnal HR and HRV assessed via ring PPG in comparison to medical grade ECG". In: *Physiological measurement* (2020). ISSN: 0967-3334. DOI: 10.1088/1361-6579/ab840a. URL: https://iopscience.iop.org/article/10.1088/1361-6579/ab840a/pdf.

[Klu+19] Michael Klum, Fabian Leib, Casper Oberschelp, et al. "Wearable Multimodal Stethoscope Patch for Wireless Biosignal Acquisition and Long-Term Auscultation". In: *Annual International Conference of the IEEE Engineering in Medicine and Biology Society. IEEE Engineering in Medicine and Biology Society. Annual International Conference* 2019 (2019), pp. 5781–5785. DOI: 10.1109/EMBC.2019.8857210.

[KC76] C. Knapp and G. Carter. "The generalized correlation method for estimation of time delay". In: *IEEE Transactions on Acoustics, Speech, and Signal Processing* 24.4 (1976), pp. 320–327. ISSN: 0096-3518. DOI: 10.1109/TASSP.1976.1162830.

[KM82] M. Kobayashi and T. Musha. "1/f fluctuation of heartbeat period". In: *IEEE TBME* 29.6 (1982), pp. 456–457. ISSN: 0018-9294. DOI: 10.1109/TBME.1982.324972.

[KHO02] Bert-Uwe Köhler, Carsten Hennig, and Reinhold Orglmeister. "The Principles of Software QRS Detection". In: *IEEE Engineering in Medicine and Biology Magazine* 21.1 (2002), pp. 42–57. ISSN: 0739-5175. DOI: 10.1109/51.993193.

[KYK12] Fukuro Koshiji, Nanako Yuyama, and Kohji Koshiji. "Wireless body area communication using electromagnetic resonance coupling". In: *CPMT Symposium Japan*. IEEE, 2012, pp. 1–4. ISBN: 978-1-4673-2655-1. DOI: 10.1109/ICSJ.2012.6523439.

[Kou18] Konstantia Koulidou. "Why Should Jewellers Care About The "Digital" ?" In: *Journal of Jewellery Research* 1 (2018). ISSN: 2516-337X. URL: http://shura.shu.ac.uk/27954/.

[Kra+17] Marcus Kramer, Aaron Lobbestael, Emily Barten, John Eian, and Gregory Rausch. "Wearable Pulse Oximetry Measurements on the Torso, Arms, and Legs: A Proof of Concept". In: *Military Medicine* 182.suppl_1 (2017), pp. 92–98. ISSN: 0026-4075. DOI: 10.7205/MILMED-D-16-00129. URL: https://academic.oup.com/milmed/article-pdf/182/suppl_1/92/21873094/milmed-d-16-00129.pdf.

[Kus+19] Roman Kusche, Turner Adornetto, Paula Klimach, and Martin Ryschka. *A Bioimpedance Measurement System for Pulse Wave Analysis*. 2019. URL: https://arxiv.org/pdf/1902.11120.

[Kwo+22] Ju Hyeok Kwon, So Eui Kim, Na Hye Kim, Eui Chul Lee, and Jee Hang Lee. "Preeminently Robust Neural PPG Denoiser". In: *Sensors (Basel, Switzerland)* 22.6 (2022). DOI: 10.3390/s22062082.

[Kwo+15] Sungjun Kwon, Jeehoon Kim, Dongseok Lee, and Kwangsuk Park. "ROI analysis for remote photoplethysmography on facial video". In: *Annual International Conference of the IEEE Engineering in Medicine and Biology Society. IEEE Engineering in Medicine and Biology Society. Annual International Conference* 2015 (2015), pp. 4938–4941. DOI: 10.1109/EMBC.2015.7319499.

[KA21] Panicos A. Kyriacou and John Allen. "Photoplethysmography: Technology, Signal Analysis and Applications". In: 1 (2021).

[Lam78] Leslie Lamport. "Time, clocks, and the ordering of events in a distributed system". In: *Communications of the ACM* 21.7 (1978), pp. 558–565. ISSN: 0001-0782. DOI: 10.1145/359545.359563.

[LVH16] Tuomas Lappalainen, Lasse Virtanen, and Jonna Häkkilä. "Experiences with wellness ring and bracelet form factor". In: (2016). DOI: 10.1145/3012709.3016065. URL: http://dl.acm.org/ft_gateway.cfm?id=3016065&type=pdf.

[LC10] Sami M. Lasassmeh and James M. Conrad. "Time Synchronization in Wireless Sensor Networks: A Survey". In: *IEEE SoutheastCon 2010*. IEEE, 2010, pp. 242–245. ISBN: 978-1-4244-5854-7. DOI: 10.1109/SECON.2010.5453878.

[LL22] Kayhan Latifzadeh and Luis A. Leiva. "Gustav: Cross-device Cross-computer Synchronization of Sensory Signals". In: *The Adjunct Publication of the 35th Annual ACM Symposium on User Interface Software and Technology*. Ed. by Maneesh Agrawala. ACM Digital Library. New York,NY,United States: Association for Computing Machinery, 2022, pp. 1–3. ISBN: 9781450393218. DOI: 10.1145/3526114.3558723.

[Láz+19] Jesús Lázaro, Eduardo Gil, Michele Orini, Pablo Laguna, and Raquel Bailón. "Baroreflex Sensitivity Measured by Pulse Photoplethysmography". In: *Frontiers in Neuroscience* 13 (2019), p. 339. ISSN: 1662-453X. DOI: 10.3389/fnins.2019.00339. URL: https://www.frontiersin.org/articles/10.3389/fnins.2019.00339/pdf.

[Lee+19] Hooseok Lee, Heewon Chung, Jong-Woong Kim, and Jinseok Lee. "Motion Artifact Identification and Removal From Wearable Reflectance Photoplethysmography Using Piezoelectric Transducer". In: *IEEE Sensors Journal* 19.10 (2019), pp. 3861–3870. ISSN: 1530-437X. DOI: 10.1109/JSEN.2019.2894640.

[LKL16] Hooseok Lee, Hoon Ko, and Jinseok Lee. "Reflectance pulse oximetry: Practical issues and limitations". In: *ICT Express* 2.4 (2016), pp. 195–198. ISSN: 24059595. DOI: 10.1016/j.icte.2016.10.004.

[LYK06] Hyojung Lee, Wonpil Yu, and Youngmi Kwon. "Efficient RBS in Sensor Networks". In: *Third International Conference on Information Technology, New Generations*. Ed. by Shahram Latifi. Los Alamitos Calif.: IEEE Computer Society, 2006, pp. 279–284. ISBN: 0-7695-2497-4. DOI: 10.1109/ITNG.2006.61.

[Lee+21] Inho Lee, Nakkyun Park, Hanbee Lee, et al. "Systematic Review on Human Skin-Compatible Wearable Photoplethysmography Sensors". In: *Applied Sciences* 11.5 (2021), p. 2313. DOI: 10.3390/app11052313.

[LE04] Kang B. Lee and J. Eldson. "Standard for a Precision Clock Synchronization Protocol for Networked Measurement and Control Systems". In: (2004), pp. 98–105. DOI: 10.1109/SFICON.2002.1159815.

[LSH16] SeungMin Lee, HyunSoon Shin, and ChanYoung Hahm. "Effective PPG sensor placement for reflected red and green light, and infrared wristband-type photoplethysmography". In: IEEE ICACT, 2016, pp. 556–558. ISBN: 978-8-9968-6506-3. DOI: 10.1109/ICACT.2016.7423470.

[Lei+20] Charles E. Leiserson, Neil C. Thompson, Joel S. Emer, et al. "There's plenty of room at the Top: What will drive computer performance after Moore's law?" In: *Science (New York, N.Y.)* 368.6495 (2020). ISSN: 0036-8075. DOI: 10.1126/science.aam9744.

[Lew+11] Magdalena Lewandowska, Jacek Ruminski, Tomasz Kocejko, and Jedrzej Nowak. "Measuring pulse rate with a webcam — A non-contact method for evaluating cardiac activity". In: *2011 Federated Conference on Computer Science and Information Systems (FedCSIS 2011)*. Piscataway, NJ: IEEE, 2011. ISBN: 978-1-4577-0041-5. URL: https://www.infona.pl/resource/bwmeta1.element.ieee-art-000006078233.

[LS14] Dong Li and Prasun Sinha. "RBTP: Low-Power Mobile Discovery Protocol through Recursive Binary Time Partitioning". In: *IEEE Transactions on Mobile Computing* 13.2 (2014), pp. 263–273. ISSN: 1536-1233. DOI: 10.1109/TMC.2012.240.

[LT10] Huaming Li and Jindong Tan. "Heartbeat-driven medium-access control for body sensor networks". In: *IEEE Engineering in Medicine and Biology Society* 14.1 (2010), pp. 44–51. DOI: 10.1109/TITB.2009.2028136.

[Li+22] Jianzheng Li, Jialong Zhang, Yizhou Jiang, et al. “A Flexible and Miniaturized Chest Patch for Real-time PPG/ECG/Bio-Z Monitoring”. In: *Annual International Conference of the IEEE Engineering in Medicine and Biology Society* 2022 (2022), pp. 4312–4315. DOI: 10.1109/EMBC48229.2022.9872005.

[Li+10] Jin Li, Jie Jin, Xiang Chen, Weixin Sun, and Ping Guo. “Comparison of respiratory-induced variations in photoplethysmographic signals”. In: *Physiological Measurement* 31.3 (2010), p. 415. ISSN: 0967-3334. DOI: 10.1088/0967-3334/31/3/009. URL: http://iopscience.iop.org/article/10.1088/0967-3334/31/3/009/pdf.

[LRZ19] Kai Li, Heinz Rüdiger, and Tjalf Ziemssen. “Spectral Analysis of Heart Rate Variability: Time Window Matters”. In: *Frontiers in neurology* 10 (2019), p. 545. ISSN: 1664-2295. DOI: 10.3389/fneur.2019.00545.

[Lia+18] Yongbo Liang, Zhencheng Chen, Guiyong Liu, and Mohamed Elgendi. “A new, short-recorded photoplethysmogram dataset for blood pressure monitoring in China”. In: *Scientific Data* 5.1 (2018), p. 180020. ISSN: 2052-4463. DOI: 10.1038/sdata.2018.20. URL: https://www.nature.com/articles/sdata201820.

[Lin+10] Jiali Lin, R. Saunders, K. Schulmeister, et al. “ICNIRP Guidelines for limiting exposure to time-varying electric and magnetic fields (1 Hz to 100 kHz)”. In: *Health Physics* 99 (2010), pp. 818–836. URL: https://hal.archives-ouvertes.fr/hal-01019994/.

[Lin+21] Wenrui Lin, Berken Utku Demirel, Mohammad Abdullah Al Faruque, and G. P. Li. “Energy-efficient Blood Pressure Monitoring based on Single-site Photoplethysmogram on Wearable Devices”. In: *2021 43rd Annual International Conference of the IEEE Engineering in Medicine & Biology Society (EMBC)*. IEEE, 2021, pp. 504–507. ISBN: 978-1-7281-1179-7. DOI: 10.1109/EMBC46164.2021.9630488.

[Lin+98] D. P. Lindsey, E. L. McKee, M. L. Hull, and S. M. Howell. “A new technique for transmission of signals from implantable transducers”. In: *IEEE TBME* 45.5 (1998), pp. 614–619. ISSN: 0018-9294. DOI: 10.1109/10.668752.

[Liu+21] Haipeng Liu, John Allen, Syed Ghufran Khalid, Fei Chen, and Dingchang Zheng. “Filtering-induced time shifts in photoplethysmography pulse features measured at different body sites: the importance of filter definition and standardization”. In: *Physiological measurement* 42.7 (2021), p. 074001. ISSN: 0967-3334. DOI: 10.1088/1361-6579/ac0a34. URL: https://iopscience.iop.org/article/10.1088/1361-6579/ac0a34/meta.

[Liu+16] Jing Liu, Bryan Ping-Yen Yan, Wen-Xuan Dai, et al. “Multi-wavelength photoplethysmography method for skin arterial pulse extraction”. In: *Biomedical optics express* 7.10 (2016), pp. 4313–4326. ISSN: 2156-7085. DOI: 10.1364/BOE.7.004313.

[LPS17] Yuhao Liu, Matt Pharr, and Giovanni Antonio Salvatore. “Lab-on-Skin: A Review of Flexible and Stretchable Electronics for Wearable Health Monitoring”. In: *ACS nano* 11.10 (2017), pp. 9614–9635. DOI: 10.1021/acsnano.7b04898.

[Loh+22] Hui Wen Loh, Shuting Xu, Oliver Faust, et al. "Application of photoplethysmography signals for healthcare systems: An in-depth review". In: *Computer Methods and Programs in Biomedicine* 216 (2022), p. 106677. ISSN: 01692607. DOI: 10.1016/j.cmpb.2022.106677. URL: https://pubmed.ncbi.nlm.nih.gov/35139459/.

[LC22] Nguyen Mai Hoang Long and Wan-Young Chung. "Wearable Wrist Photoplethysmography for Optimal Monitoring of Vital Signs: A Unified Perspective on Pulse Waveforms". In: *IEEE Photonics Journal* 14.2 (2022), pp. 1–17. DOI: 10.1109/JPHOT.2022.3153506.

[Lon+19] Sally K. Longmore, Gough Y. Lui, Ganesh Naik, et al. "A Comparison of Reflective Photoplethysmography for Detection of Heart Rate, Blood Oxygen Saturation, and Respiration Rate at Various Anatomical Locations". In: *Sensors* 19.8 (2019), p. 1874. DOI: 10.3390/s19081874. URL: https://www.mdpi.com/1424-8220/19/8/1874/pdf.

[Lop+15] Matthew Loper, Naureen Mahmood, Javier Romero, Gerard Pons-Moll, and Michael J. Black. "SMPL: A Skinned Multi-Person Linear Model". In: *ACM Transactions on Graphics* 34.6 (2015), pp. 1–16. ISSN: 0730-0301. DOI: 10.1145/2816795.2818013.

[Lu+20] Yiqin Lu, Bingjian Huang, Chun Yu, Guahong Liu, and Yuanchun Shi. "Designing and Evaluating Hand-to-Hand Gestures with Dual Commodity Wrist-Worn Devices". In: *Proceedings of the ACM on Interactive, Mobile, Wearable and Ubiquitous Technologies* 4.1 (2020), pp. 1–27. DOI: 10.1145/3380984.

[Luc+17] Brandon Lucia, Vignesh Balaji, Alexei Colin, Kiwan Maeng, and Emily Ruppel, eds. *Intermittent Computing: Challenges and Opportunities: Schloss Dagstuhl - Leibniz-Zentrum fuer Informatik GmbH, Wadern/Saarbruecken, Germany*. 2017. DOI: 10.4230/LIPIcs.SNAPL.2017.8.

[Luk+09] Martin Lukac, Paul Davis, Robert Clayton, and Deborah Estrin. "Recovering Temporal Integrity with Data Driven Time Synchronization". In: (2009), pp. 61–72.

[LKK+17] Chu Luo, Henri Koski, Mikko Korhonen, et al. *Rapid clock synchronisation for ubiquitous sensing services involving multiple smartphones*. 2017. DOI: 10.1145/3123024.3124432.

[Lyo11] Richard G. Lyons. *Understanding Digital Signal Processing*. 3rd ed. Upper Saddle River, N.J.: Prentice Hall and London: Pearson Education, 2011. ISBN: 9780137027415.

[Mae+08] Y. Maeda, M. Sekine, T. Tamura, et al. "Comparison of Reflected Green Light and Infrared Photoplethysmography". In: *Conference proceedings : ... Annual International Conference of the IEEE Engineering in Medicine and Biology Society. IEEE Engineering in Medicine and Biology Society. Annual Conference* 2008 (2008), pp. 2270–2272. ISSN: 1557-170X. DOI: 10.1109/IEMBS.2008.4649649.

[MST11a] Yuka Maeda, Masaki Sekine, and Toshiyo Tamura. "Relationship Between Measurement Site and Motion Artifacts in Wearable Reflected Photoplethysmography". In: *Journal of Medical Systems* 35.5 (2011), pp. 969–976. ISSN: 0148-5598. DOI: 10.1007/s10916-010-9505-0. URL: https://doi.org/10.1007/s10916-010-9505-0.

[MST11b] Yuka Maeda, Masaki Sekine, and Toshiyo Tamura. "The Advantages of Wearable Green Reflected Photoplethysmography". In: *Journal of medical systems* 35.5 (2011), pp. 829–834. ISSN: 0148-5598. DOI: 10.1007/s10916-010-9506-z. URL: https://doi.org/10.1007/s10916-010-9506-z.

[Mae+13] Yuka Maeda, Masaki Sekine, Toshiyo Tamura, and Koichi Mizutani. "The effect of contact pressure to the photoplethysmographic sensor during walking". In: *Transactions of Japanese Society for Medical and Biological Engineering* 51.Supplement (2013), R-307-R–307. ISSN: 1881-4379. DOI: 10.11239/jsmbe.51.R-307.

[Mai+18] Shovan Maity, Debayan Das, Baibhab Chatterjee, and Shreyas Sen. "Characterization and Classification of Human Body Channel as a function of Excitation and Termination Modalities". In: *2018 40th Annual International Conference of the IEEE Engineering in Medicine and Biology Society (EMBC)*. 2018, pp. 3754–3757. DOI: 10.1109/EMBC.2018.8513332.

[Mai+17] Shovan Maity, Debayan Das, Xinyi Jiang, and Shreyas Sen. "Secure Human-Internet using Dynamic Human Body Communication". In: *2017 IEEE/ACM International Symposium on Low Power Electronics and Design (ISLPED)*. 2017, pp. 1–6. DOI: 10.1109/ISLPED.2017.8009190.

[Mai+20a] Shovan Maity, Nirmoy Modak, David Yang, et al. "A 415 nW Physically and Mathematically Secure Electro-Quasistatic HBC Node in 65nm CMOS for Authentication and Medical Applications". In: *CICC*. IEEE, 2020, pp. 1–4. ISBN: 978-1-7281-6031-3. DOI: 10.1109/CICC48029.2020.9075930.

[Mai+21] Shovan Maity, Nirmoy Modak, David Yang, et al. "Sub-μWRComm: 415-nW 1–10-kb/s Physically and Mathematically Secure Electro-Quasi-Static HBC Node for Authentication and Medical Applications". In: *IEEE JSSC* 56.3 (2021), pp. 788–802. ISSN: 0018-9200. DOI: 10.1109/JSSC.2020.3041874.

[MMS18] Shovan Maity, Kavian Mojabe, and Shreyas Sen. "Characterization of Human Body Forward Path Loss and Variability Effects in Voltage-Mode HBC". In: *IEEE Microwave and Wireless Components Letters* 28.3 (2018), pp. 266–268. ISSN: 1531-1309. DOI: 10.1109/LMWC.2018.2800529.

[Mai+20b] Shovan Maity, Mayukh Nath, Gargi Bhattacharya, Baibhab Chatterjee, and Shreyas Sen. "On the Safety of Human Body Communication". In: *IEEE TBME* 67.12 (2020), pp. 3392–3402. ISSN: 1558-2531. DOI: 10.1109/TBME.2020.2986464.

[Mai+19] Shovan Maity, David Yang, Baibhab Chatterjee, and Shreyas Sen. "A sub-nW Wake-up Receiver for Human Body Communication". In: *BioCAS 2019, Biomedical Circuits and Systems Conference*. IEEE, 2019, pp. 1–4. ISBN: 978-1-5386-3603-9. DOI: 10.1109/BIOCAS.2018.8584785.

[MC96] Marek Malik and A. John Camm. "Guidelines: Heart Rate Variability: Standards of Measurement, Physiological Interpretation, and Clinical Use". In: *European Heart Journal* 17 (1996), pp. 354–381.

[MP95] Jaakko Malmivuo and Robert Plonsey. *Bioelectromagnetism: Principles and applications of bioelectric and biomagnetic fields*. New York and Oxford: Oxford University Press, 1995. ISBN: 9780195058239. DOI: 10.1093/acprof:oso/9780195058239.001.0001.

[Man97] S. Mann. "Wearable computing: a first step toward personal imaging". In: *Computer* 30.2 (1997), pp. 25–32. ISSN: 00189162. DOI: 10.1109/2.566147.

[Man07] Paul D. Mannheimer. "The light-tissue interaction of pulse oximetry". In: *Anesthesia and analgesia* 105.6 Suppl (2007), S10–7. DOI: 10.1213/01.ane.0000269522.84942.54.

[MK10] Shrirang Mare and David Kotz. "Is Bluetooth the right technology for mHealth?" In: *USENIX Workshop on Health Security (HealthSec)* (2010). URL: https://digitalcommons.dartmouth.edu/facoa/3336.

[Mas+21] Giulio Masinelli, Fabio Dell'Agnola, Adriana Arza Valdés, and David Atienza. "SPARE: A Spectral Peak Recovery Algorithm for PPG Signals Pulsewave Reconstruction in Multimodal Wearable Devices". In: *Sensors* 21.8 (2021), p. 2725. DOI: 10.3390/s21082725.

[Mat+00] Nobuyuki Matsushita, Shigeru Tajima, Yuji Ayatsuka, and Jun Rekimoto. "Wearable Key: Device for Personalizing nearby Environment". In: *Digest of Papers. Fourth International Symposium on Wearable Computers*. 2000, pp. 119–126. DOI: 10.1109/ISWC.2000.888473.

[Maz08] Nafiseh Seyed Mazloum. "Body-Coupled Communications: Experimental characterization, channel modeling and physical layer design". MA thesis. 2008. URL: https://odr.chalmers.se/bitstream/20.500.12380/87937/1/87937.pdf.

[McC+16] Cameron McCarthy, Nikhilesh Pradhan, Calum Redpath, and Andy Adler. "Validation of the Empatica E4 Wristband". In: *IEEE EMBS ISC*. 2016, pp. 1–4. ISBN: 978-1-5090-0935-0. DOI: 10.1109/EMBSISC.2016.7508621.

[McC+18] Ryan McConville, Gareth Archer, Ian Craddock, et al. *Online Heart Rate Prediction using Acceleration from a Wrist Worn Wearable*. 2018. URL: http://arxiv.org/pdf/1807.04667.

[McD+15] Daniel J. McDuff, Justin R. Estepp, Alyssa M. Piasecki, and Ethan B. Blackford. "A Survey of Remote Optical Photoplethysmographic Imaging Methods". In: *Conference proceedings : ... Annual International Conference of the IEEE Engineering in Medicine and Biology Society. IEEE Engineering in Medicine and Biology Society. Annual Conference* 2015 (2015), pp. 6398–6404. ISSN: 1557-170X. DOI: 10.1109/EMBC.2015.7319857.

[Med+02] Mihály Medvegy, Gábor Duray, Arnold Pintér, and István Préda. "Body surface potential mapping: historical background, present possibilities, diagnostic challenges". In: *Annals of noninvasive electrocardiology : the official journal of the International Society for Holter and Noninvasive Electrocardiology, Inc* 7.2 (2002), pp. 139–151. ISSN: 1082-720X. DOI: 10.1111/j.1542-474x.2002.tb00155.x.

[MMK21] Elisa Mejia-Mejia, James M. May, and Panayiotis A. Kyriacou. "Effect of Filtering of Photoplethysmography Signals in Pulse Rate Variability Analysis". In: *Annual International Conference of the IEEE Engineering in Medicine and Biology Society. IEEE Engineering in Medicine and Biology Society. Annual International Conference* 2021 (2021), pp. 5500–5503. DOI: 10.1109/EMBC46164.2021.9629521.

[MK22] Elisa Mejía-Mejía and Panicos A. Kyriacou. "Spectral analysis for pulse rate variability assessment from simulated photoplethysmographic signals". In: *Frontiers in physiology* 13 (2022). ISSN: 1664-042X. DOI: 10.3389/fphys.2022.966130.

[MMK22] Elisa Mejía-Mejía, James M. May, and Panayiotis A. Kyriacou. "Effects of using different algorithms and fiducial points for the detection of interbeat intervals, and different sampling rates on the assessment of pulse rate variability from photoplethysmography". In: *Computer Methods and Programs in Biomedicine* 218 (2022), p. 106724. ISSN: 01692607. DOI: 10.1016/j.cmpb.2022.106724.

[Mej+20] Elisa Mejía-Mejía, James M. May, Robinson Torres, and Panayiotis A. Kyriacou. "Pulse rate variability in cardiovascular health: a review on its applications and relationship with heart rate variability". In: *Physiological measurement* 41.7 (2020), 07TR01. ISSN: 0967-3334. DOI: 10.1088/1361-6579/ab998c. URL: https://iopscience.iop.org/article/10.1088/1361-6579/ab998c.

[MA17] Geoff V. Merrett and Bashir M. Al-Hashimi. "Energy-driven computing: Rethinking the design of energy harvesting systems". In: *Proceedings of the 2017 Design, Automation & Test in Europe Conference & Exhibition (DATE)*. Piscataway, N.J.: IEEE, 2017, pp. 960–965. ISBN: 978-3-9815370-8-6. DOI: 10.23919/DATE.2017.7927130.

[Mil+06] Sandrine C. Millasseau, James M. Ritter, Kenji Takazawa, and Philip J. Chowienczyk. "Contour analysis of the photoplethysmographic pulse measured at the finger". In: *Journal of hypertension* 24.8 (2006), pp. 1449–1456. ISSN: 0263-6352. DOI: 10.1097/01.hjh.0000239277.05068.87.

[Mil91] David L. Mills. "Internet time synchronization: the network time protocol". In: *IEEE Transactions on Communications* 39.10 (1991), pp. 1482–1493. ISSN: 00906778. DOI: 10.1109/26.103043.

[Mil06] David L. Mills. *Computer Network Time Synchronization: The Network Time Protocol*. 1st. CRC Press, 2006. ISBN: 9780429114397. DOI: ttps://doi.org/10.1201/9781420006155.

[Mil11] David L. Mills. *Computer network time synchronization: The network time protocol on earth and in space*. 2nd. Boca Raton, Fla.: CRC Press, 2011. ISBN: 9781439814642.

[MSH16] Andreia V. Moço, Sander Stuijk, and Gerard de Haan. "Motion robust PPG-imaging through color channel mapping". In: *Biomedical optics express* 7.5 (2016), pp. 1737–1754. ISSN: 2156-7085. DOI: 10.1364/BOE.7.001737.

[MSH18] Andreia V. Moço, Sander Stuijk, and Gerard de Haan. "New insights into the origin of remote PPG signals in visible light and infrared". In: *Scientific Reports* 8.1 (2018), p. 8501. ISSN: 2045-2322. DOI: 10.1038/s41598-018-26068-2. URL: https://www.nature.com/articles/s41598-018-26068-2.pdf.

[MGR21] Charles Molnar, Jane Gair, and Connie Rye. *Concepts of Biology*. 1st Canadian edition. Victoria, B.C.: BCcampus, 2021. ISBN: 978-1-989623-99-2. URL: https://opentextbc.ca/biology/.

[Moo+85] George B. Moody, Roger G. Mark, Andrea Zoccola, and Sara Mantero. "Derivation of Respiratory Signals from Multi-lead ECGs". In: 12 (1985), pp. 113–116.

[Moo65] Gordon E. Moore. "Cramming more components onto integrated circuits". In: 38.8 (1965).

[MAK15] Miltiadis Moralis-Pegios, Pelagia Alexandridou, and Christos Koukourlis. "Applying Pulse Width Modulation in Body Coupled Communication". In: *Journal of Electrical and Computer Engineering* 2015 (2015), pp. 1–6. ISSN: 2090-0147. DOI: 10.1155/2015/378054. URL: https://www.hindawi.com/journals/jece/2015/378054/.

[Mor+19] Davide Morelli, Alessio Rossi, Massimo Cairo, and David A. Clifton. "Analysis of the Impact of Interpolation Methods of Missing RR-intervals Caused by Motion Artifacts on HRV Features Estimations". In: *Sensors (Basel, Switzerland)* 19.14 (2019). DOI: 10.3390/s19143163.

[Mor16] Ralph Morrison. *Grounding and Shielding: Circuits and Interference*. Sixth edition. John Wiley & Sons, Ltd, 2016. ISBN: 9781119183754.

[Nag+20] Genki Nagamatsu, Ewa Magdalena Nowara, Amruta Pai, Ashok Veeraraghavan, and Hiroshi Kawasaki. "PPG3D: Does 3D head tracking improve camera-based PPG estimation?" In: *Annual International Conference of the IEEE Engineering in Medicine and Biology Society. IEEE Engineering in Medicine and Biology Society. Annual International Conference* 2020 (2020), pp. 1194–1197. DOI: 10.1109/EMBC44109.2020.9176065.

[Nag+15] Jun-ichi Naganawa, Karma Wangchuk, Minseok Kim, Takahiro Aoyagi, and Jun-ichi Takada. "Simulation-Based Scenario-Specific Channel Modeling for WBAN Cooperative Transmission Schemes". In: *IEEE Journal of Biomedical and Health Informatics* 19.2 (2015), pp. 559–570. ISSN: 2168-2194.

[NAK07] Hiroya Nakao, Kensuke Arai, and Yoji Kawamura. "Noise-induced synchronization and clustering in ensembles of uncoupled limit-cycle oscillators". In: *Physical review letters* 98.18 (2007), p. 184101. ISSN: 0031-9007. DOI: 10.1103/PhysRevLett.98.184101.

[NPE15] Gabriel Nallathambi, Jose C. Principe, and Neil R. Euliano. "Pulse based signal processing for systolic peak recognition". In: *2015 IEEE 25th International Workshop on Machine Learning for Signal Processing (MLSP)*. [S.l.]: IEEE, 2015, pp. 1–6. ISBN: 978-1-4673-7454-5. DOI: 10.1109/MLSP.2015.7324322.

[Nar+18] David Naranjo-Hernández, Amparo Callejón-Leblic, Željka Lučev Vasić, MirHojjat Seyedi, and Yue-Ming Gao. "Past Results, Present Trends, and Future Challenges in Intrabody Communication". In: *Wireless Communications and Mobile Computing* 2018 (2018), pp. 1–39. ISSN: 1530-8669. DOI: 10.1155/2018/9026847.

[NDR17] Venkat Natarajan, Deeksha Dadhich, and Kumar Ranganathan. *Compressive Sensing Sparse Sampling Photoplethysmogram (PPG) Measurement*. US Patent US 2017/0281013 A1. Oct. 2017. URL: https://patents.google.com/patent/US20170281013.

[Nat+21] Mayukh Nath, Shovan Maity, Shitij Avlani, Scott Weigand, and Shreyas Sen. "Inter-body coupling in electro-quasistatic human body communication: theory and analysis of security and interference properties". In: *Scientific Reports* 11.1 (2021), p. 4378. ISSN: 2045-2322. DOI: 10.1038/s41598-020-79788-9. URL: https://www.ncbi.nlm.nih.gov/pmc/articles/PMC7902665/.

[NMS20] Mayukh Nath, Shovan Maity, and Shreyas Sen. "Toward Understanding the Return Path Capacitance in Capacitive Human Body Communication". In: *IEEE TCSII* 67.10 (2020), pp. 1879–1883. ISSN: 1558-3791. DOI: 10.1109/TCSII.2019.2953682.

[ESA20] NAVIPEDIA of the European Space Agency (ESA). *Time References in GNSS*. 2020. URL: https://gssc.esa.int/navipedia/index.php/Time%5C_References%5C_in%5C_GNSS (visited on 12/15/2022).

[NW78] Michael R. Neuman and John G. Webster. "Biopotential Amplifiers". In: *Medical Instrumentation: Application and Design* (1978), pp. 273–335.

[NDM81] J. A. Nijboer, J. C. Dorlas, and H. F. Mahieu. "Photoelectric plethysmography–some fundamental aspects of the reflection and transmission method". In: *Clinical physics and physiological measurement : an official journal of the Hospital Physicists' Association, Deutsche Gesellschaft fur Medizinische Physik and the European Federation of Organisations for Medical Physics* 2.3 (1981), pp. 205–215. ISSN: 0143-0815. DOI: 10.1088/0143-0815/2/3/004.

[NO21] Meir Nitzan and Zehava Ovadia-Blechman. "Physical and physiological interpretations of the PPG signal". In: *Photoplethysmography*. Ed. by Panicos A. Kyriacou and John Allen. Amsterdam: Academic Press, 2021, pp. 319–340. ISBN: 9780128233740. DOI: 10.1016/B978-0-12-823374-0.00009-8.

[NPP] Nordic Semiconductor. *Power Profiler Kit II, commercial product*. URL: https://www.nordicsemi.com/Products/Development-hardware/Power-Profiler-Kit-2 (visited on 05/12/2022).

[ND18] Gina M. Notaro and Solomon G. Diamond. "Simultaneous EEG, eye-tracking, behavioral, and screen-capture data during online German language learning". In: *Data in brief* 21 (2018), pp. 1937–1943. DOI: 10.1016/j.dib.2018.11.044. URL: https://www.sciencedirect.com/science/article/pii/S2352340918314379.

[Obi21] Amarachukwu Ikechukwu Obi. "An Overview of Wearable Photoplethysmographic Sensors and Various Algorithms for Tracking of Heart Rates". In: *Engineering Proceedings* 10.1 (2021), p. 77. DOI: 10.3390/engproc2021010077.

[Ohm+06] Ren Ohmura, F. Naya, H. Noma, and K. Kogure. "B-Pack: A Bluetooth-based Wearable Sensing Device for Nursing Activity Recognition". In: *Wireless Pervasive Computing (ISWPC)*. IEEE, 2006, pp. 1–6. ISBN: 0-7803-9410-0. DOI: 10.1109/ISWPC.2006.1613628.

[Ome+21] Aleksandr Ometov, Viktoriia Shubina, Lucie Klus, et al. "A Survey on Wearable Technology: History, State-of-the-Art and Current Challenges". In: *Computer Networks* 193 (2021), p. 108074. ISSN: 13891286. DOI: 10.1016/j.comnet.2021.108074.

[Ort+98] Maggie Orth, J. R. Smith, E. R. Post, J. A. Strickon, and E. B. Cooper. "Musical jacket". In: *SIGGRAPH 98*. Ed. by Joan. Ed Truckenbrod and Ines. Ed Hardtke. New York, NY, USA: ACM, 1998, p. 38. ISBN: 1581130457. DOI: 10.1145/281388.281456.

[Our22a] Ltd. Oura Health. *Heart Rate Graph*. 2022. URL: https://support.ouraring.com/hc/en-us/articles/4410651298963-Live-Heart-Rate (visited on 02/10/2023).

[Our22b] Ltd. Oura Health. *Heart Rate Graph*. 2022. URL: https://support.ouraring.com/hc/en-us/articles/4410656562579-Heart-Rate-Graph (visited on 02/10/2023).

[PLP20] David Pallier, Vincent Le Cam, and Sebastien Pillement. "Energy-efficient GPS synchronization for wireless nodes". In: *IEEE Sensors Journal* (2020), pp. 1–9. ISSN: 1530-437X. DOI: 10.1109/JSEN.2020.3031350.

[PT85] Jiapu Pan and Willis J. Tompkins. "A Real-Time QRS Detection Algorithm". In: *IEEE Transactions on Bio-Medical Engineering* 32.3 (1985), pp. 230–236. ISSN: 0018-9294. DOI: 10.1109/TBME.1985.325532.

[PM15] Jiwoong Park and Patrick P. Mercier. "Magnetic human body communication". In: *IEEE EMBC* 2015 (2015), pp. 1841–1844. DOI: 10.1109/EMBC.2015.7318739.

[Par+21] Junyung Park, Hyeon Seok Seok, Sang-Su Kim, and Hangsik Shin. "Photoplethysmogram Analysis and Applications: An Integrative Review". In: *Frontiers in physiology* 12 (2021), p. 808451. ISSN: 1664-042X. DOI: 10.3389/fphys.2021.808451.

[Pea95] Karl Pearson. "Note on Regression and Inheritance in the Case of Two Parents". In: *Proceedings of the Royal Society of London* 58.347-352 (1895), pp. 240–242. ISSN: 0370-1662. DOI: 10.1098/rspl.1895.0041.

[Per+19] Elena Peralta Calvo, Raquel Bailón Luesma, Jesús Lázaro Plaza, Eduardo Gil Herrando, and Vaidotas Marozas. "Optimal Fiducial Points for Pulse Rate Variability Analysis from Forehead and Finger PPG Signals". In: *Physiol. meas.* ART-2019-109892 (2019). DOI: 10.1088/1361-6579/ab009b.

[Pet+16] Juha Petäjäjärvi, Konstantin Mikhaylov, Risto Vuohtoniemi, Heikki Karvonen, and Jari Iinatti. "On the human body communications: wake-up receiver design and channel characterization". In: *EURASIP Journal on Wireless Communications and Networking* 2016.1 (2016), pp. 1–17. ISSN: 1687-1499. DOI: 10.1186/s13638-016-0674-5. URL: https://link.springer.com/article/10.1186/s13638-016-0674-5.

[PBG07] Michael T. Petterson, Valerie L. Begnoche, and John M. Graybeal. "The effect of motion on pulse oximetry and its clinical significance". In: *Anesthesia and analgesia* 105.6 Suppl (2007), S78–S84. DOI: 10.1213/01.ane.0000278134.47777.a5.

[Pfl+14] Maik Pflugradt, Igor Fritzsch, Steffen Mann, Timo Tigges, and Reinhold Orglmeister. "A novel pulseoximeter for bluetooth synchronized measurements in a body sensor network". In: *EDERC'14*. IEEE, 2014, pp. 21–25. ISBN: 978-1-4799-6843-5. DOI: 10.1109/EDERC.2014.6924351.

[Pha+08] D. H. Phan, S. Bonnet, R. Guillemaud, E. Castelli, and N. Y. Pham Thi. "Estimation of respiratory waveform and heart rate using an accelerometer". In: *Conference proceedings : ... Annual International Conference of the IEEE Engineering in Medicine and Biology Society. IEEE Engineering in Medicine and Biology Society. Annual Conference* 2008 (2008), pp. 4916–4919. ISSN: 1557-170X. DOI: 10.1109/IEMBS.2008.4650316.

[Phi+04] M. Philipose, K. P. Fishkin, M. Perkowitz, et al. "Inferring Activities from Interactions with Objects". In: *IEEE Pervasive Computing* 3.4 (2004), pp. 50–57. ISSN: 1536-1268. DOI: 10.1109/MPRV.2004.7.

[Pim+17] Marco A. F. Pimentel, Alistair E. W. Johnson, Peter H. Charlton, et al. "Toward a Robust Estimation of Respiratory Rate From Pulse Oximeters". In: *IEEE TBME* 64.8 (2017), pp. 1914–1923. ISSN: 0018-9294. DOI: 10.1109/TBME.2016.2613124.

[PGM21] N. de Pinho Ferreira, C. Gehin, and B. Massot. "A Review of Methods for Non-Invasive Heart Rate Measurement on Wrist". In: *IRBM* 42.1 (2021), pp. 4–18. ISSN: 19590318. DOI: 10.1016/j.irbm.2020.04.001.

[PGM20] Nicolas de Pinho Ferreira, Claudine Gehin, and Bertrand Massot. "Ambient Light Contribution as a Reference for Motion Artefacts Reduction in Photoplethysmography". In: *Proceedings of the 13th International Joint Conference on Biomedical Engineering Systems and Technologies*. SCITEPRESS - Science and Technology Publications, 2020, pp. 23–32. ISBN: 978-989-758-398-8. DOI: 10.5220/0008878800230032.

[PMV03] Josien P. W. Pluim, J. B. Antoine Maintz, and Max A. Viergever. "Mutual-information-based registration of medical images: a survey". In: *IEEE transactions on medical imaging* 22.8 (2003), pp. 986–1004. ISSN: 0278-0062. DOI: 10.1109/TMI.2003.815867.

[PSP10] Ming-Zher Poh, Nicholas C. Swenson, and Rosalind W. Picard. "Motion-tolerant magnetic earring sensor and wireless earpiece for wearable photoplethysmography". In: *IEEE transactions on information technology in biomedicine : a publication of the IEEE Engineering in Medicine and Biology Society* 14.3 (2010), pp. 786–794. DOI: 10.1109/TITB.2010.2042607.

[PENa] Ian Poole. *RFID Frequency Bands & Spectrum*. URL: https://www.electronics-notes.com/articles/connectivity/rfid-radio-frequency-identification/frequency-bands-spectrum.php (visited on 07/21/2022).

[PENb] Ian Poole. *RFID Frequency Bands & Spectrum*. URL: https://www.electronics-notes.com/articles/connectivity/rfid-radio-frequency-identification/standards-iec-iso-epcglobal.php (visited on 07/21/2022).

[Pop11] Cristian Pop. "AN1391: Introduction to the BodyCom Technology". In: *Microchip Technology Inc.* (2011).

[Pos+13] H. F. Posada-Quintero, D. Delisle-Rodríguez, M. B. Cuadra-Sanz, and R. R. La Fernández de Vara-Prieto. "Evaluation of pulse rate variability obtained by the pulse onsets of the photoplethysmographic signal". In: *Physiological Measurement* 34.2 (2013), pp. 179–187. ISSN: 0967-3334. DOI: 10.1088/0967-3334/34/2/179.

[PO97] E. Rehmi Post and Margaret Orth. “Smart Fabric, or "Wearable Clothing"”. In: *First international symposium on wearable computers*. IEEE Comput. Soc, 1997, pp. 167–168. ISBN: 0-8186-8192-6. DOI: 10.1109/ISWC.1997.629937.

[Pou+16] Ivan Poupyrev, Nan-Wei Gong, Shiho Fukuhara, et al. “Project Jacquard: Interactive Digital Textiles at Scale”. In: *CHI'16*. 2016, pp. 4216–4227.

[Pra+00] R. J. Prance, A. Debray, T. D. Clark, et al. “An ultra-low-noise electrical-potential probe for human-body scanning”. In: *Measurement Science and Technology* 11.3 (2000), pp. 291–297. ISSN: 0957-0233. DOI: 10.1088/0957-0233/11/3/318. URL: https://iopscience.iop.org/article/10.1088/0957-0233/11/3/318/meta.

[Qai+20] Waleed Bin Qaim, Aleksandr Ometov, Antonella Molinaro, et al. “Towards Energy Efficiency in the Internet of Wearable Things: A Systematic Review”. In: *IEEE Access* 8 (2020), pp. 175412–175435. ISSN: 2169-3536. DOI: 10.1109/ACCESS.2020.3025270.

[RC16] Vega Pradana Rachim and Wan-Young Chung. “Wearable Noncontact Armband for Mobile ECG Monitoring System”. In: *IEEE transactions on biomedical circuits and systems* 10.6 (2016), pp. 1112–1118. ISSN: 1932-4545. DOI: 10.1109/TBCAS.2016.2519523.

[Rag+18] Martin Ragot, Nicolas Martin, Sonia Em, Nico Pallamin, and Jean-Marc Diverrez. “Emotion Recognition Using Physiological Signals: Laboratory vs. Wearable Sensors”. In: Springer, Cham, 2018, pp. 15–22. DOI: 10.1007/978-3-319-60639-2_2. URL: https://link.springer.com/chapter/10.1007/978-3-319-60639-2_2.

[Ram+13] Prabhu Ramanathan, Sudha Ramasamy, Prateek Jain, et al. “Low value capacitance measurements for capacitive sensors-A review”. In: *Sensors & Transducers* (2013).

[RCP22] Daniel Ray, Tim Collins, and Prasad V. S. Ponnapalli. “DeepPulse: An Uncertainty-aware Deep Neural Network for Heart Rate Estimations from Wrist-worn Photoplethysmography”. In: *Annual International Conference of the IEEE Engineering in Medicine and Biology Society. IEEE Engineering in Medicine and Biology Society. Annual International Conference* 2022 (2022), pp. 1651–1654. DOI: 10.1109/EMBC48229.2022.9871813.

[Ray+21] Daniel Ray, Tim Collins, Sandra Woolley, and Prasad Ponnapalli. “A Review of Wearable Multi-wavelength Photoplethysmography”. In: *IEEE reviews in biomedical engineering* PP (2021). DOI: 10.1109/RBME.2021.3121476.

[RBA23] Maximilian Reiser, Andreas Breidenassel, and Oliver Amft. “Simulation framework for reflective PPG signal analysis depending on sensor placement and wavelength”. In: IEEE, 2023. DOI: 10.1109/BSN56160.2022.9928522. URL: https://www.cdh.med.fau.de/publications/?id=TP3K87FM.

[Rei+08] Andrew Reisner, Phillip A. Shaltis, Devin McCombie, and H. Harry Asada. “Utility of the photoplethysmogram in circulatory monitoring”. In: *Anesthesiology* 108.5 (2008), pp. 950–958. DOI: 10.1097/ALN.0b013e31816c89e1.

[Rei+19] Attila Reiss, Ina Indlekofer, Philip Schmidt, and Kristof Van Laerhoven. “Deep PPG: Large-Scale Heart Rate Estimation with Convolutional Neural Networks”. In: *Sensors (Basel, Switzerland)* 19.14 (2019).

[RN93] Jun Rekimoto and Katashi Nagao. "The World through the Computer: Computer Augmented Interaction with Real World Environments". In: *User interface software and technology*. Ed. by George Robertson. New York, NY: ACM, 1993, pp. 29–36. ISBN: 089791709X. DOI: 10.1145/215585.215639.

[Rel+18] Natasa Reljin, Gary Zimmer, Yelena Malyuta, et al. "Using support vector machines on photoplethysmographic signals to discriminate between hypovolemia and euvolemia". In: *PloS one* 13.3 (2018), e0195087. DOI: 10.1371/journal.pone.0195087.

[RYA01] S. Rhee, B. H. Yang, and H. H. Asada. "Artifact-Resistant Power-Efficient Design of Finger-Ring Plethysmographic Sensors". In: *IEEE transactions on bio-medical engineering* 48.7 (2001), pp. 795–805. ISSN: 0018-9294. DOI: 10.1109/10.930904.

[Rhe+98] Sokwoo Rhee, Boo-Ho Yang, Kuowei Chang, and H. H. Asada. "The ring sensor: a new ambulatory wearable sensor for twenty-four hour patient monitoring". In: *Proceedings of the 20th Annual International Conference of the IEEE Engineering in Medicine and Biology Society*. Ed. by H. K. Chang and Y. T. Zhang. Picatway NJ: IEEE Service Center, 1998, pp. 1906–1909. ISBN: 0-7803-5164-9. DOI: 10.1109/IEMBS.1998.746970.

[Rib+18] Gustavo Dos Santos Ribeiro, Victor Ribeiro Neves, Luís Fernando Deresz, et al. "Can RR intervals editing and selection techniques interfere with the analysis of heart rate variability?" In: *Brazilian journal of physical therapy* 22.5 (2018), pp. 383–390. DOI: 10.1016/j.bjpt.2018.03.008.

[RR07] Matthias Ringwald and Kay Romer. "Practical time synchronization for Bluetooth Scatternets". In: *4th International Conference on Broadband Communications, Networks & Systems, 2007*. 2007, pp. 337–345. ISBN: 978-1-4244-1432-1. DOI: 10.1109/BROADNETS.2007.4550453.

[Rob05] Hector J. Gracia Roberto Casas. "Synchronization in wireless sensor networks using bluetooth". In: *3rd International Workshop on Intelligent Solutions in Embedded Systems*. IEEE, 2005, pp. 79–88. ISBN: 3-902463-03-1. DOI: 10.1109/WISES.2005.1438715.

[Röd+22] Tobias Röddiger, Christopher Clarke, Paula Breitling, et al. "Sensing with Earables: A Systematic Literature Review and Taxonomy of Phenomena". In: *Proceedings of the ACM on Interactive, Mobile, Wearable and Ubiquitous Technologies* 6.3 (2022), pp. 1–57. DOI: 10.1145/3550314.

[Ron22] Shenyi Rong. "Quantifications and characteristics of dynamic soft tissue artifacts captured by wearable inertial measurement unit sensors". PhD thesis. University of British Columbia, Oct. 2022. URL: https://open.library.ubc.ca/soa/cIRcle/collections/ubctheses/24/items/1.0421332.

[Ros15] Joe Rossignol. *Some Tattoos Found to Interfere With Apple Watch's Sensors*. https://www.macrumors.com/2015/04/29/apple-watch-sensors-tattoogate/. Accessed: 2023-01-20. 2015.

[Rut+20] Parker S. Ruth, Jerry Cao, Millicent Li, et al. "Multi-Channel Facial Photoplethysmography Sensing". In: *Annual International Conference of the IEEE Engineering in Medicine and Biology Society. IEEE Engineering in Medicine and Biology Society. Annual International Conference* 2020 (2020), pp. 4179–4182. DOI: 10.1109/EMBC44109.2020.9176700.

[RK10] V. O. Rybynok and P. A. Kyriacou. "Beer-lambert law along non-linear mean light pathways for the rational analysis of Photoplethysmography". In: *Journal of Physics: Conference Series* 238.1 (2010), p. 012061. ISSN: 1742-6596. DOI: 10.1088/1742-6596/238/1/012061. URL: https://iopscience.iop.org/article/10.1088/1742-6596/238/1/012061/pdf.

[Sae+11] Mohammed Saeed, Mauricio Villarroel, Andrew T. Reisner, et al. "Multiparameter Intelligent Monitoring in Intensive Care II: a public-access intensive care unit database". In: *Critical care medicine* 39.5 (2011), pp. 952–960. DOI: 10.1097/CCM.0b013e31820a92c6.

[San+10] S. Sangiorgi, A. Manelli, M. Reguzzoni, et al. "The cutaneous microvascular architecture of human diabetic toe studied by corrosion casting and scanning electron microscopy analysis". In: *Anatomical record (Hoboken, N.J. : 2007)* 293.10 (2010), pp. 1639–1645. DOI: 10.1002/ar.21168.

[SPH12] Munehiko Sato, Ivan Poupyrev, and Chris Harrison. "Touché: Enhancing Touch Interaction on Humans, Screens, Liquids, and Everyday Objects". In: *Conference proceedings CHI 2012, it's the experience*. Ed. by Joseph A. Konstan, Ed H. Chi, and Kristina Höök. New York: Association for Computing Machinery, 2012, p. 483. ISBN: 9781450310154. DOI: 10.1145/2207676.2207743.

[SD14] Klemens Sattlegger and Uli Denk. "Navigating your way through the RFID jungle". In: *White Paper, Texas Instruments* (2014).

[SG64] Abraham. Savitzky and M. J. E. Golay. "Smoothing and Differentiation of Data by Simplified Least Squares Procedures". In: *Analytical Chemistry* 36.8 (1964), pp. 1627–1639. ISSN: 0003-2700. DOI: 10.1021/ac60214a047.

[SMZ17] Tim Schäck, Michael Muma, and Abdelhak M. Zoubir. "Computationally Efficient Heart Rate Estimation During Physical Exercise Using Photoplethysmographic Signals". In: *2017 25th European Signal Processing Conference (EUSIPCO)*. IEEE, 2017, pp. 2478–2481. ISBN: 978-0-9928626-7-1. DOI: 10.23919/EUSIPCO.2017.8081656.

[SGM00] A. Schmidt, H.-W. Gellersen, and C. Merz. "Enabling implicit human computer interaction: a wearable RFID-tag reader". In: *The fourth international symposium on wearable computers*. IEEE Comput. Soc, 2000, pp. 193–194. ISBN: 0-7695-0795-6. DOI: 10.1109/ISWC.2000.888497.

[Sch00] Albrecht Schmidt. "Implicit human computer interaction through context". In: *Personal Technologies* 4.2-3 (2000), pp. 191–199. ISSN: 1617-4917. DOI: 10.1007/BF01324126. URL: https://link.springer.com/article/10.1007/BF01324126.

[Sch+18] Philip Schmidt, Attila Reiss, Robert Duerichen, Claus Marberger, and Kristof Van Laerhoven. *Introducing WESAD, a Multimodal Dataset for Wearable Stress and Affect Detection*. 2018. DOI: 10.1145/3242969.3242985. URL: http://dl.acm.org/ft_gateway.cfm?id=3242985&type=pdf.

[SBW12] Felix Scholkmann, Jens Boss, and Martin Wolf. "An Efficient Algorithm for Automatic Peak Detection in Noisy Periodic and Quasi-Periodic Signals". In: *Algorithms* 5.4 (2012), pp. 588–603. DOI: 10.3390/a5040588.

[Sch17] Philipp C. Schönle. "A Power Efficient Spectrophotometry & PPG Integrated Circuit for Mobile Medical Instruments". In: (2017). DOI: 10.3929/ETHZ-A-010897884.

[SAS] Sciosense, B.V. *AS3930, commercial product.* URL: https://www.sciosense.com/products/wireless-sensor-nodes/as3930-lf-receiver-ic/ (visited on 05/12/2022).

[Seh+22] Jessica Sehrt, Bent Braams, Niels Henze, and Valentin Schwind. "Social Acceptability in Context: Stereotypical Perception of Shape, Body Location, and Usage of Wearable Devices". In: *Big Data and Cognitive Computing* 6.4 (2022), p. 100. DOI: 10.3390/bdcc6040100.

[Sel+22] Vinothini Selvaraju, Nicolai Spicher, Ramakrishnan Swaminathan, and Thomas M. Deserno. "Unobtrusive Heart Rate Monitoring using Near-Infrared Imaging During Driving". In: *Annual International Conference of the IEEE Engineering in Medicine and Biology Society. IEEE Engineering in Medicine and Biology Society. Annual International Conference* 2022 (2022), pp. 2967–2971. DOI: 10.1109/EMBC48229.2022.9871416.

[Sen16] Shreyas Sen. "SocialHBC: Social Networking and Secure Authentication using Interference-Robust Human Body Communication". In: *Proceedings of the 2016 International Symposium on Low Power Electronics and Design.* New York, NY: ACM, 2016, pp. 34–39. ISBN: 9781450341851. DOI: 10.1145/2934583.2934609.

[SG17] Fred Shaffer and J. P. Ginsberg. "An Overview of Heart Rate Variability Metrics and Norms". In: *Frontiers in public health* 5 (2017), p. 258. ISSN: 2296-2565. DOI: 10.3389/fpubh.2017.00258.

[SCL20] Eesha J. Shah, Jia Yi Chow, and Marcus J. C. Lee. "Anxiety on Quiet Eye and Performance of Youth Pistol Shooters". In: *Journal of sport & exercise psychology* (2020), pp. 1–7. DOI: 10.1123/jsep.2019-0174.

[Sha49] Claude E. Shannon. "Communication in the Presence of Noise". In: *Proceedings of the IRE* 37.1 (1949), pp. 10–21. ISSN: 0096-8390. DOI: 10.1109/JRPROC.1949.232969.

[She+90] A. Sherwood, M. T. Allen, J. Fahrenberg, et al. "Methodological guidelines for impedance cardiography". In: *Psychophysiology* 27.1 (1990), pp. 1–23. ISSN: 0048-5772. DOI: 10.1111/j.1469-8986.1990.tb02171.x.

[SH15] Yulia Silina and Hamed Haddadi. "New directions in jewelry". In: *Proceedings of the 2015 ACM International Symposium on Wearable Computers.* Ed. by Kenji Mase. New York, NY: ACM, 2015, pp. 49–56. ISBN: 9781450335782. DOI: 10.1145/2802083.2808410.

[Sjo+20] Michael W. Sjoding, Robert P. Dickson, Theodore J. Iwashyna, Steven E. Gay, and Thomas S. Valley. "Racial Bias in Pulse Oximetry Measurement". In: *The New England journal of medicine* 383.25 (2020), pp. 2477–2478. DOI: 10.1056/NEJMc2029240.

[Smi16] Suzanne Smiley. *Operating Principles: Coupling.* 2016. URL: https://www.atlasrfidstore.com/rfid-insider/operating-principles-coupling (visited on 07/21/2022).

[Smi+98] J. Smith, T. White, C. Dodge, et al. "Electric field sensing for graphical interfaces". In: *IEEE Computer Graphics and Applications* (1998). ISSN: 02721716. DOI: 10.1109/38.674972.

[SDH03] Marc Smith, D. Davenport, and H. Hwa. "AURA: A mobile platform for object and location annotation". In: UbiComp (2003).

[Son07] Seong-Jun et al. Song. "A 0.2-mW 2-Mb/s Digital Transceiver Based on Wideband Signaling for Human Body Communications". In: *IEEE Journal of Solid-State Circuits* 42.9 (2007), pp. 2021–2033.

[SM21] Andreas Spilz and Michael Munz. *Novel Approach To Synchronisation Of Wearable IMUs Based On Magnetometers*. 2021. URL: https://arxiv.org/pdf/2107.03147.

[Sta+22] Simon Stankoski, Ivana Kiprijanovska, Ifigeneia Mavridou, et al. "Breathing Rate Estimation from Head-Worn Photoplethysmography Sensor Data Using Machine Learning". In: *Sensors* 22.6 (2022), p. 2079. DOI: 10.3390/s22062079.

[Sta+97] Thad Starner, Steve Mann, Bradley Rhodes, et al. "Augmented Reality through Wearable Computing". In: *Presence: Teleoperators and Virtual Environments* 6.4 (1997), pp. 386–398. ISSN: 1054-7460. DOI: 10.1162/pres.1997.6.4.386.

[Ste22] Becky Stern. *Oura Ring Teardown (Gen 3 and Gen 2)*. 2022. URL: https://beckystern.com/2022/04/17/oura-ring-teardown-gen-3-and-gen-2/ (visited on 02/10/2023).

[SN12] Norbert Stuban and Masatsugu Niwayama. "Optimal filter bandwidth for pulse oximetry". In: *Rev. Sci. Instrum.* 83.10 (2012), p. 104708. DOI: 10.1063/1.4759491.

[Sug+20] Norihiro Sugita, Tomoya Matsuzaki, Makoto Yoshizawa, et al. "Comparison of Visible and Infrared Video Plethysmography Captured from Different Regions of the Human Face". In: *Annual International Conference of the IEEE Engineering in Medicine and Biology Society. IEEE Engineering in Medicine and Biology Society. Annual International Conference* 2020 (2020), pp. 4187–4190. DOI: 10.1109/EMBC44109.2020.9176138.

[SYZ12] Xuxue Sun, Ping Yang, and Yuan-Ting Zhang. "Assessment of photoplethysmogram signal quality using morphology integrated with temporal information approach". In: *Conference proceedings : ... Annual International Conference of the IEEE Engineering in Medicine and Biology Society. IEEE Engineering in Medicine and Biology Society. Annual Conference* 2012 (2012), pp. 3456–3459. ISSN: 1557-170X. DOI: 10.1109/EMBC.2012.6346709.

[SY16] Ye Sun and Xiong Bill Yu. "Capacitive Biopotential Measurement for Electrophysiological Signal Acquisition: A Review". In: *IEEE Sensors Journal* 16.9 (2016), pp. 2832–2853. ISSN: 1530-437X. DOI: 10.1109/JSEN.2016.2519392.

[SBK05] Bharath Sundararaman, Ugo Buy, and Ajay D. Kshemkalyani. "Clock synchronization for wireless sensor networks: a survey". In: *Ad Hoc Networks* 3.3 (2005), pp. 281–323. ISSN: 1570-8705. DOI: 10.1016/j.adhoc.2005.01.002.

[SHI16] Kenji Suzuki, Taku Hachisu, and Kazuki Iida. "EnhancedTouch: A Smart Bracelet for Enhancing Human-Human Physical Touch". In: *CHI 2016*. Ed. by Jofish Kaye, Allison Druin, Cliff Lampe, Dan Morris, and Juan Pablo Hourcade. New York, New York: The Association for Computing Machinery, 2016, pp. 1282–1293. ISBN: 9781450333627. DOI: 10.1145/2858036.2858439.

[Svi+18] Nina Sviridova, Tiejun Zhao, Kazuyuki Aihara, Kazuyuki Nakamura, and Akimasa Nakano. "Photoplethysmogram at green light: Where does chaos arise from?" In: *Chaos, Solitons & Fractals* 116 (2018), pp. 157–165. ISSN: 09600779. DOI: 10.1016/j.chaos.2018.09.016.

[SS16] Timo Sztyler and Heiner Stuckenschmidt. "On-body localization of wearable devices: An investigation of position-aware activity recognition". In: *IEEE International Conference 2016*. 2016, pp. 1–9. DOI: 10.1109/PERCOM.2016.7456521.

[Tak+11] Masato Takahashi, Charith Lasantha Fernando, Yuto Kumon, et al. "Earthlings Attack!: A Ball Game Using Human Body Communication". In: *Proceedings of the 2nd Augmented Human International Conference*. Ed. by Masahiko Inami, Jun Rekimoto, Hideki Koike, and Hideo Saito. New York, New York, USA: ACM Digital Library, 2011, pp. 1–4. ISBN: 9781450304269. DOI: 10.1145/1959826.1959843.

[Tak+98] K. Takazawa, N. Tanaka, M. Fujita, et al. "Assessment of vasoactive agents and vascular aging by the second derivative of photoplethysmogram waveform". In: *Hypertension (Dallas, Tex. : 1979)* 32.2 (1998), pp. 365–370. ISSN: 0194-911X. DOI: 10.1161/01.hyp.32.2.365.

[TMS+14] Toshiyo Tamura, Yuka Maeda, Masaki Sekine, et al. "Wearable Photoplethysmographic Sensors—Past and Present". In: *Electronics* 3.2 (2014), pp. 282–302. DOI: 10.3390/electronics3020282.

[Tar+14] L. Tarassenko, M. Villarroel, A. Guazzi, et al. "Non-contact video-based vital sign monitoring using ambient light and auto-regressive models". In: *Physiological measurement* 35.5 (2014), pp. 807–831. ISSN: 0967-3334. DOI: 10.1088/0967-3334/35/5/807.

[TDK] TDK. *B82450A7204A, commercial product*. URL: https://www.tdk-electronics.tdk.com/inf/30/db/ind_2008/b82450a_a.pdf (visited on 05/12/2022).

[Tem17] Andriy Temko. "Accurate Heart Rate Monitoring During Physical Exercises Using PPG". In: *IEEE TBME* 64.9 (2017), pp. 2016–2024. ISSN: 0018-9294. DOI: 10.1109/TBME.2017.2676243.

[TT04] Jun-Nosuke Teramae and Dan Tanaka. "Robustness of the noise-induced phase synchronization in a general class of limit cycle oscillators". In: *Physical review letters* 93.20 (2004), p. 204103. ISSN: 0031-9007. DOI: 10.1103/PhysRevLett.93.204103.

[MSPb] Texas Instruments, Inc. *MSP430FR5969, commercial product*. URL: https://www.ti.com/product/MSP430FR5969 (visited on 06/16/2021).

[MSPa] Texas Instruments, Inc. *MSP430G2553, commercial product*. URL: https://www.ti.com/product/MSP430G2553 (visited on 06/16/2021).

[OPA3] Texas Instruments, Inc. *OPA320S, commercial product*. URL: https://www.ti.com/product/OPA320 (visited on 04/15/2017).

[TRF] Texas Instruments, Inc. *TRF7970A, commercial product.* URL: https://www.ti.com/product/TRF7970A (visited on 05/12/2022).

[Tho+16] Simi Susan Thomas, Viswam Nathan, Chengzhi Zong, et al. "BioWatch: A Noninvasive Wrist-Based Blood Pressure Monitor That Incorporates Training Techniques for Posture and Subject Variability". In: *IEEE Journal of Biomedical and Health Informatics* 20.5 (2016), pp. 1291–1300. ISSN: 2168-2194. DOI: 10.1109/JBHI.2015.2458779.

[TA19] Francisco Tirado-Andrés and Alvaro Araujo. "Performance of clock sources and their influence on time synchronization in wireless sensor networks". In: *International Journal of Distributed Sensor Networks* 15.9 (2019), p. 16. ISSN: 1550-1477. DOI: 10.1177/1550147719879372.

[Toc+22] Guillaume Tochou, Robin Benarrouch, David Gaidioz, et al. "A Sub-100-µW 0.1-to-27-Mb/s Pulse-Based Digital Transmitter for the Human Intranet in 28-nm FD-SOI CMOS". In: *IEEE Journal of Solid-State Circuits* 57.5 (2022), pp. 1409–1420. ISSN: 1558-173X. DOI: 10.1109/JSSC.2022.3140905.

[Tom+19] William J. Tomlinson, Stella Banou, Christopher Yu, Milica Stojanovic, and Kaushik R. Chowdhury. "Comprehensive Survey of Galvanic Coupling and Alternative Intra-Body Communication Technologies". In: *IEEE Communications Surveys & Tutorials* 21.2 (2019), pp. 1145–1164. DOI: 10.1109/COMST.2018.2879643.

[TB90] D. M. Trujillo and H. R. Busby. "A mathematical method for the measurement of bone motion with skin-mounted accelerometers". In: *Journal of Biomechanical Engineering* 112.2 (1990), pp. 229–231. ISSN: 0148-0731. DOI: 10.1115/1.2891176.

[Tur+83] Ethel Tur, Moshe Tur, Howard I. Maibach, and Richard H. Guy. "Basal Perfusion of the Cutaneous Microcirculation: Measurements as a Function of Anatomic Position". In: *Journal of Investigative Dermatology* 81.5 (1983), pp. 442–446. ISSN: 0022202X. DOI: 10.1111/1523-1747.ep12522619.

[Tur19] Victoria Turk. *This sleep-tracking ring can detect when you've drunk too much.* 2019. URL: https://www.wired.co.uk/article/oura-ring-uk-sleep-tracking (visited on 02/10/2023).

[UA22] Lena Uhlenberg and Oliver Amft. "Comparison of Surface Models and Skeletal Models for Inertial Sensor Data Synthesis". In: *2022 IEEE-EMBS International Conference on Wearable and Implantable Body Sensor Networks (BSN)*. IEEE, 2022, pp. 1–5. ISBN: 978-1-6654-5925-9. DOI: 10.1109/BSN56160.2022.9928504.

[Umm+20] Jason D. Ummel, Orlando S. Hoilett, Benjamin D. Walters, et al. "Kick Ring LL: A Multi-Sensor Ring Capturing Respiration, Electrocardiogram, Oxygen Saturation, and Skin Temperature1". In: *Annual International Conference of the IEEE Engineering in Medicine and Biology Society. IEEE Engineering in Medicine and Biology Society. Annual International Conference* 2020 (2020), pp. 4394–4397. DOI: 10.1109/EMBC44109.2020.9176654.

[TPN] Unexpected Maker. *TinyPICO NANO, commercial product.* URL: https://www.tinypico.com/tinypico-nano (visited on 05/12/2022).

[van+89] M. J. van Gemert, S. L. Jacques, H. J. Sterenborg, and W. M. Star. "Skin optics". In: *IEEE transactions on bio-medical engineering* 36.12 (1989), pp. 1146–1154. ISSN: 0018-9294. DOI: 10.1109/10.42108.

[vGe+19] Paul van Gent, Haneen Farah, Nicole van Nes, and Bart van Arem. "Analysing Noisy Driver Physiology Real-Time Using Off-the-Shelf Sensors: Heart Rate Analysis Software from the Taking the Fast Lane Project". In: *JORS* 7 (2019). ISSN: 2049-9647. DOI: 10.5334/jors.241.

[vR03] Jana van Greunen and Jan Rabaey. "Lightweight time synchronization for sensor networks". In: *Proceedings of the 2nd ACM International Conference on Wireless sensor networks and Applications*. Ed. by C. S. Raghavendra, Krishna M. Sivalingam, Ramesh Govindan, and Parmesh Ramanathan. New York, N.Y.: ACM Press, 2003, p. 11. ISBN: 1581137648. DOI: 10.1145/941350.941353.

[VG04] Kristof Van Laerhoven and Hans-Werner Gellersen. "Spine versus Porcupine: A Study in Distributed Wearable Activity Recognition". In: *Eighth International Symposium on Wearable Compuiters*. Los Alamitos: IEEE Computer Society, 2004, pp. 142–149. ISBN: 0-7695-2186-X. DOI: 10.1109/ISWC.2004.40.

[VVG03] Kristof Van Laerhoven, Nicolas Villar, and H-W Gellersen. "A Layered Approach to Wearable Textile Networks". In: IET, 2003, pp. 61–66.

[Var+18a] Virag Varga, Gergely Vakulya, Alanson Sample, and Thomas R. Gross. "Enabling Interactive Infrastructure with Body Channel Communication". In: *Proceedings of the ACM on Interactive, Mobile, Wearable and Ubiquitous Technologies* 1.4 (2018), pp. 1–29. DOI: 10.1145/3161180.

[Var+18b] Virag Varga, Marc Wyss, Gergely Vakulya, Alanson Sample, and Thomas R. Gross. "Designing Groundless Body Channel Communication Systems: Performance and Implications". In: *Proceedings of the 31st Annual ACM Symposium on User Interface Software and Technology*. Ed. by Patrick Baudisch. ACM Conferences. New York, NY: ACM, 2018, pp. 683–695. ISBN: 9781450359481. DOI: 10.1145/3242587.3242622.

[Vaz+15] P. Vaz, V. Almeida, L. R. Ferreira, C. Correia, and J. Cardoso. "Signal (Stream) synchronization with White noise sources, in biomedical applications". In: *Biomedical Signal Processing and Control* 18 (2015), pp. 394–400. DOI: 10.1016/j.bspc.2015.02.015. URL: https://www.sciencedirect.com/science/article/pii/S174680941500035X.

[VSN08] Wim Verkruysse, Lars O. Svaasand, and J. Stuart Nelson. "Remote plethysmographic imaging using ambient light". In: *Optics express* 16.26 (2008), pp. 21434–21445. DOI: 10.1364/oe.16.021434.

[Ver+15] Johan Vertens, Fabian Fischer, Christian Heyde, et al. "Measuring Respiration and Heart Rate using Two Acceleration Sensors on a Fully Embedded Platform". In: *Proceedings of the 3rd International Congress on Sport Sciences Research and Technology Support*. SCITEPRESS - Science and and Technology Publications, 2015, pp. 15–23. ISBN: 978-989-758-159-5. DOI: 10.5220/0005604000150023.

[Vig92] John R. Vig. "Introduction to quartz frequency standards". In: *NASA STI/Recon Technical Report N* 92 (1992), p. 29498.

[VME19] Angel Villegas, David McEneaney, and Omar Escalona. "Arm-ECG Wireless Sensor System for Wearable Long-Term Surveillance of Heart Arrhythmias". In: *Electronics* 8.11 (2019), p. 1300. DOI: 10.3390/electronics8111300.

[Vol+17] Mikhail V. Volkov, Nikita B. Margaryants, Andrey V. Potemkin, et al. "Video capillaroscopy clarifies mechanism of the photoplethysmographic waveform appearance". In: *Scientific Reports* 7.1 (2017), p. 8. ISSN: 2045-2322. DOI: 10.1038/s41598-017-13552-4. URL: https://www.nature.com/articles/s41598-017-13552-4.pdf.

[Vu+12] Tam Vu, Akash Baid, Simon Gao, et al. "Distinguishing users with capacitive touch communication". In: *MobiCom*. Ed. by Özgür B. Akan, Eylem Ekici, Lili Qiu, and Alex C. Snoeren. New York: ACM, 2012, pp. 197–208. ISBN: 9781450311595. DOI: 10.1145/2348543.2348569.

[WFA15] Florian Wahl, Martin Freund, and Oliver Amft. "WISEglass: Smart eyeglasses recognising context". In: *Proceedings of the 10th EAI International Conference on Body Area Networks*. Ed. by Giancarlo Fortino, Junichi Suzuki, Yiannis Andreopoulos, et al. ICST, 2015. ISBN: 978-1-63190-084-6. DOI: 10.4108/eai.28-9-2015.2261470.

[Wal88] Augustus D. Waller. "On the electromotive changes connected with the beat of the mammalian heart, and of the human heart in particular". In: *Proceedings of the Royal Society of London* (1888). DOI: 10.1098/rspl.1888.0048.

[Wan+19] Chaofan Wang, Zhanna Sarsenbayeva, Chu Luo, Jorge Goncalves, and Vassilis Kostakos. "Improving Wearable Sensor Data Quality Using Context Markers". In: UbiComp/ISWC '19. ACM, 2019. ISBN: 978-1-4503-6869-8. DOI: 10.1145/3341162.3349334.

[Wan+07] Shiaokai Wang, William Pentney, Ana-Maria Popescu, Tanzeem Choudhury, and Matthai Philipose. "Common Sense Based Joint Training of Human Activity Recognizers". In: *IJCAI* (2007). URL: https://openreview.net/forum?id=B1bbmQM_bH.

[Wan+17] Wenjin Wang, Albertus C. den Brinker, Sander Stuijk, and Gerard de Haan. "Algorithmic Principles of Remote PPG". In: *IEEE transactions on biomedical engineering* 64.7 (2017), pp. 1479–1491. ISSN: 0018-9294. DOI: 10.1109/TBME.2016.2609282.

[WSH16] Wenjin Wang, Sander Stuijk, and Gerard de Haan. "A Novel Algorithm for Remote Photoplethysmography: Spatial Subspace Rotation". In: *IEEE Transactions on Biomedical Engineering* 63.9 (2016), pp. 1974–1984. ISSN: 1558-2531. DOI: 10.1109/TBME.2015.2508602.

[Wan+99] Roy Want, Kenneth P. Fishkin, Anuj Gujar, and Beverly L. Harrison. "Bridging physical and virtual worlds with electronic tags". In: *CHI 99*. Ed. by Marian G. Williams and Steven Pemberton. Conference on human factors in computing systems. New York: ACM Press and Harlow : Pearson Education, 1999, pp. 370–377. ISBN: 0201485591. DOI: 10.1145/302979.303111.

[Weg+07] Marc Simon Wegmueller, Andreas Kuhn, Juerg Froehlich, et al. "An Attempt to Model the Human Body as a Communication Channel". In: *IEEE TBME* 54.10 (2007), pp. 1851–1857. ISSN: 0018-9294. DOI: 10.1109/TBME.2007.893498.

[Wei+22] Wenchuan Wei, Korosh Vatanparvar, Li Zhu, Jilong Kuang, and Alex Gao. "Remote Photoplethysmography and Heart Rate Estimation by Dynamic Region of Interest Tracking". In: *Annual International Conference of the IEEE Engineering in Medicine and Biology Society. IEEE Engineering in Medicine and Biology Society. Annual International Conference* 2022 (2022), pp. 3243–3248. DOI: 10.1109/EMBC48229.2022.9871722.

[Wei93] Mark Weiser. "Some Computer Science Issues in Ubiquitous Computing". In: *Communications of the ACM* 36.7 (1993), pp. 75–84. ISSN: 0001-0782. DOI: 10.1145/159544.159617.

[Wel67] Peter D. Welch. "The Use of Fast Fourier Transform for the Estimation of Power Spectra: A Method Based on Time Averaging Over Short, Modified Periodograms". In: *IEEE Transactions on Audio and Electroacoustics* 15.2 (June 1967), pp. 70–73. ISSN: 1558-2582. DOI: 10.1109/TAU.1967.1161901.

[WMG93] Pierre Wellner, Wendy Mackay, and Rich Gold. "Back to the Real World". In: *Communications of the ACM* 36.7 (1993), pp. 24–26. ISSN: 0001-0782. DOI: 10.1145/159544.159555.

[Wel+20] Kaylie Welykholowa, Manish Hosanee, Gabriel Chan, et al. "Multimodal Photoplethysmography-Based Approaches for Improved Detection of Hypertension". In: *Journal of clinical medicine* 9.4 (2020). ISSN: 2077-0383. DOI: 10.3390/jcm9041203.

[Wes+09] Tracy Westeyn, Peter Presti, Jeremy Johnson, and Thad Starner. "A Naive Technique Correcting Time-Series Data for Recognition Applications". In: *ISWC 2009*. Los Alamitos Calif.: IEEE Computer Society, 2009, pp. 159–160. ISBN: 978-0-7695-3779-5. DOI: 10.1109/ISWC.2009.19.

[Wij+12] Ralph W. C. G. R. Wijshoff, Massimo Mischi, Jeroen Veen, Alexander M. van der Lee, and Ronald M. Aarts. "Reducing motion artifacts in photoplethysmograms by using relative sensor motion: phantom study". In: *Journal of Biomedical Optics* 17.11 (2012), p. 117007. DOI: 10.1117/1.JBO.17.11.117007.

[Wik22] Wikimedia Commons. *Schematic diagram of normal sinus rhythm for a human heart as seen on ECG*. File: SinusRhythmLabels.svg. 2022. URL: https://commons.wikimedia.org/wiki/File:SinusRhythmLabels.svg (visited on 02/24/2023).

[Wil+14] Erik Wilde, Stefan Lüder, Jack Hodges, Florian Michahelles, and Mareike Kritzler. "A Web of Wearables". In: *UbiComp '14 adjunct : proceedings of the 2014 ACM International Joint Conference on Pervasive and Ubiquitous Computing : September 13-17, 2014, Seattle, WA, USA*. Ed. by A. J. Brush. ACM, 2014, pp. 1063–1068. ISBN: 9781450330473. DOI: 10.1145/2638728.2659393.

[Wil+54] Frank N. Wilson, Charles E. Kossmann, Ashton Graybiel, and Eugene Lepeschkin. "Recommendations for Standardization of Electrocardiographic and Vectorcardiographic Leads". In: *Circulation* 10.4 (1954), pp. 564–573. DOI: 10.1161/01.cir.10.4.564.

[Win+20] Jasper de Winkel, Vito Kortbeek, Josiah Hester, and Przemysław Pawełczak. "Battery-Free Game Boy". In: *Proceedings of the ACM on Interactive, Mobile, Wearable and Ubiquitous Technologies* 4.3 (2020), pp. 1–34. DOI: 10.1145/3411839.

[WW83] B. B. Winter and J. G. Webster. "Driven-Right-Leg Circuit Design". In: *IEEE transactions on bio-medical engineering* 30.1 (1983), pp. 62–66. ISSN: 0018-9294. DOI: 10.1109/tbme.1983.325168.

[WP20] Marek Wójcikowski and Bogdan Pankiewicz. "Photoplethysmographic Time-Domain Heart Rate Measurement Algorithm for Resource-Constrained Wearable Devices and its Implementation". In: *Sensors* 20.6 (2020), p. 1783. DOI: 10.3390/s20061783.

[WMa16] **Florian Wolling**. "Body-Coupled Communication in Intra-Body Sensor Networks". MA thesis. University of Freiburg, 2016.

[Woo22] Emma Woollacott. *Apple Sued Over 'Racial Bias' Of Apple Watch*. https://www.forbes.com/sites/emmawoollacott/2022/12/29/apple-sued-over-racial-bias-of-apple-watch/. Accessed: 2023-01-20. 2022.

[WHO] World Health Organization (WHO). *Drinking Water*. URL: https://www.who.int/water%5C_sanitation%5C_health/monitoring/water.pdf (visited on 11/09/2021).

[Wor] WorldTimeServer. *One-For-All Internet Time Zone: Does It Exist?* https://www.worldtimeserver.com/learn/one-for-all-internet-time-zone-does-it-exist/. Accessed: 2023-12-14.

[Wu+16] Lyndia C. Wu, Vaibhav Nangia, Kevin Bui, et al. "In Vivo Evaluation of Wearable Head Impact Sensors". In: *Annals of Biomedical Engineering* 44.4 (2016), pp. 1234–1245. ISSN: 1573-9686. DOI: 10.1007/s10439-015-1423-3.

[XDH22] Ran Xiao, Cheng Ding, and Xiao Hu. "Time Synchronization of Multimodal Physiological Signals through Alignment of Common Signal Types and Its Technical Considerations in Digital Health". In: *Journal of Imaging* 8.5 (2022), p. 120. ISSN: 2313-433X. DOI: 10.3390/jimaging8050120. URL: https://www.mdpi.com/2313-433X/8/5/120.

[Xie+18] Qingsong Xie, Qirui Zhang, Guoxing Wang, and Yong Lian. "Combining Adaptive Filter and Phase Vocoder for Heart Rate Monitoring Using Photoplethysmography During Physical Exercise". In: *IEEE EMBC* (2018), pp. 3568–3571. ISSN: 1557-170X. DOI: 10.1109/EMBC.2018.8512925.

[Xu+17] Tongtong Xu, Ao Guo, Jianhua Ma, and Kevin I-Kai Wang. "Feature-Based Temporal Statistical Modeling of Data Streams from Multiple Wearable Devices". In: *DASC'17*. Piscataway, NJ: IEEE, 2017, pp. 119–126. ISBN: 978-1-5386-1956-8. DOI: 10.1109/DASC-PICom-DataCom-CyberSciTec.2017.34.

[Xue+17] Jiguo Xue, Cheng Quan, Chunyong Li, Jingwei Yue, and Chenggang Zhang. "A crucial temporal accuracy test of combining EEG and Tobii eye tracker". In: *Medicine* 96.13 (2017), e6444. DOI: 10.1097/MD.0000000000006444. URL: https://www.ncbi.nlm.nih.gov/pmc/articles/PMC5380258/.

[Yam+22] Nithya Yamasinghe, Yohan Ranasinghe, Yasmika Dissanayake, Janaka L. Wijekoon, and Rrubaa Panchendrarajan. "iMask: An IoT-based Intelligent Mask to Identify and Track COVID-19 Suspects". In: *2022 IEEE International Conference on Smart Internet of Things (SmartIoT)*. IEEE, 2022, pp. 7–14. ISBN: 978-1-6654-7952-3. DOI: 10.1109/SmartIoT55134.2022.00011.

[Yan+17] Liangwen Yan, Sijung Hu, Abdullah Alzahrani, Samah Alharbi, and Panagiotis Blanos. "A Multi-Wavelength Opto-Electronic Patch Sensor to Effectively Detect Physiological Changes against Human Skin Types". In: *Biosensors* 7.2 (2017), p. 22. DOI: 10.3390/bios7020022. URL: https://www.mdpi.com/2079-6374/7/2/22/pdf.

[Yan+20] Liangwen Yan, Yue Yu, Sijung Hu, et al. "Illumination Adaptation in a Multi-Wavelength Opto-Electronic Patch Sensor". In: *Sensors (Basel, Switzerland)* 20.17 (2020), p. 4734. DOI: 10.3390/s20174734. URL: https://www.mdpi.com/1424-8220/20/17/4734.

[Yiz+16] Zhong Yizhou, Pan Yun, Zhang Ling, and Cheng Kwang-Ting. "A wearable signal acquisition system for physiological signs including throat PPG". In: *Conference proceedings : ... Annual International Conference of the IEEE Engineering in Medicine and Biology Society. IEEE Engineering in Medicine and Biology Society. Annual Conference* 2016 (2016), pp. 603–606. ISSN: 1557-170X. DOI: 10.1109/EMBC.2016.7590774.

[YH17] Lee Yongsu and Yoo Hoi-Jun. "A 274μW clock synchronized wireless body area network IC with super-regenerative RSSI for biomedical ad-hoc network system". In: *IEEE EMBC* 2017 (2017), pp. 710–713. DOI: 10.1109/EMBC.2017.8036923.

[YFM19] Kristina Yordanova, Jesus Favela, and Gabriela Marcu. "Challenges Providing Ground Truth for Pervasive Healthcare Systems". In: *IEEE Pervasive Computing* 18.2 (2019), pp. 100–104. ISSN: 1536-1268. DOI: 10.1109/MPRV.2019.2912261.

[Zea17] Clint Zeagler. "Where to wear it". In: *Proceedings of the 2017 ACM International Symposium on Wearable Computers*. Ed. by Seungyon "Claire." Lee. [Place of publication not identified]: ACM, 2017, pp. 150–157. ISBN: 9781450351881. DOI: 10.1145/3123021.3123042.

[Zha+11] Boying Zhang, Jin Teng, Xiaole Bai, Zhimin Yang, and Dong Xuan. "P 3 - coupon: A probabilistic system for Prompt and Privacy-preserving electronic coupon distribution". In: *2011 IEEE International Conference on Pervasive Computing and Communications (PERCOM)*. Piscataway NJ: IEEE, 2011, pp. 93–101. ISBN: 978-1-4244-9530-6. DOI: 10.1109/PERCOM.2011.5767599.

[Zha+22] Ying Zhang, Huaiyu Zhu, Haipeng Liu, et al. "A Wearable Swallowing Recognition System Based on Motion and Dual Photoplethysmography Sensing of Laryngeal Movements". In: *Annual International Conference of the IEEE Engineering in Medicine and Biology Society. IEEE Engineering in Medicine and Biology Society. Annual International Conference* 2022 (2022), pp. 13–16. DOI: 10.1109/EMBC48229.2022.9871902.

[Zha+18] Yu Zhang, Tao Gu, Chu Luo, Vassilis Kostakos, and Aruna Seneviratne. "FinDroidHR: Smartwatch Gesture Input with Optical Heartrate Monitor". In: *Proceedings of the ACM on Interactive, Mobile, Wearable and Ubiquitous Technologies* 2.1 (2018), pp. 1–42. DOI: 10.1145/3191788.

[ZPL15] Zhilin Zhang, Zhouyue Pi, and Benyuan Liu. "TROIKA: A General Framework for Heart Rate Monitoring Using Wrist-Type Photoplethysmographic Signals During Intensive Physical Exercise". In: *IEEE Transactions on Bio-Medical Engineering (TBME)* 62.2 (2015), pp. 522–531. ISSN: 0018-9294. DOI: 10.1109/TBME.2014.2359372.

[Zhe+08a] Jia Zheng, Sijung Hu, Vince Azorin-Peris, et al. "Remote simultaneous dual wavelength imaging photoplethysmography: a further step towards 3-D mapping of skin blood microcirculation". In: *Multimodal Biomedical Imaging III*. Ed. by Fred S. Azar and Xavier Intes. SPIE Proceedings. SPIE, 2008, 68500S. DOI: 10.1117/12.761705.

[Zhe+08b] Jia Zheng, Sijung Hu, Vassilios Chouliaras, and Ron Summers. "Feasibility of Imaging Photoplethysmography". In: *BMEI 2008*. Los Alamitos, California: IEEE, 2008, pp. 72–75. ISBN: 978-0-7695-3118-2. DOI: 10.1109/BMEI.2008.365.

[Zhe+14] Ya-Li Zheng, Xiao-Rong Ding, Carmen Chung Yan Poon, et al. "Unobtrusive Sensing and Wearable Devices for Health Informatics". In: *IEEE transactions on bio-medical engineering* 61.5 (2014), pp. 1538–1554. ISSN: 0018-9294. DOI: 10.1109/TBME.2014.2309951.

[Zhe+12] Yali Zheng, Billy Leung, Stanley Sy, Yuanting Zhang, and Carmen C. Y. Poon. "A clip-free eyeglasses-based wearable monitoring device for measuring photoplethysmograhic signals". In: *Conference proceedings : ... Annual International Conference of the IEEE Engineering in Medicine and Biology Society. IEEE Engineering in Medicine and Biology Society. Annual Conference* 2012 (2012), pp. 5022–5025. ISSN: 1557-170X. DOI: 10.1109/EMBC.2012.6347121.

[Zim+09] Patrick H. Zimmerman, J. Elizabeth Bolhuis, Albert Willemsen, Erik S. Meyer, and Noldus, Lucas P. J. J. "The Observer XT: a tool for the integration and synchronization of multimodal signals". In: *Behavior Research Methods* 41.3 (2009), pp. 731–735. ISSN: 1554-3528. DOI: 10.3758/BRM.41.3.731. URL: https://link.springer.com/article/10.3758/BRM.41.3.731.

[Zim96] Thoams Guthrie Zimmerman. "Personal Area Networks: Near-Field Intra-Body Communication". In: *IBM systems Journal* 35.3.4 (1996), pp. 609–617.

[Zim95] Thomas Guthrie Zimmerman. "Personal Area Networks (PAN): Near-Field Intra-Body Communication". MA thesis. Massachusetts Institute of Technology, 1995.

[Zon+03] W. Zong, T. Heldt, G. B. Moody, and R. G. Mark. "An Open-Source Algorithm to Detect Onset of Arterial Blood Pressure Pulses". In: *Computers in Cardiology*. IEEE, 2003, pp. 259–262. ISBN: 0-7803-8170-X. DOI: 10.1109/CIC.2003.1291140.

[Zum11] Hank Zumbahlenas. *Linear Circuit Design Handbook*. Analog Devices, Inc., Newnes, 2011. ISBN: 9780080559155.

Acknowledgements

This dissertation and the research presented have been supervised by Professor Kristof Van Laerhoven, head of the Ubiquitous Computing lab of the University of Siegen in Germany. Therefore, I would like to start by thanking Kristof for the opportunity to follow him to Siegen and to become his first PhD candidate there. Without his inexhaustible pool of knowledge and inspiration, this dissertation would not have been possible. I have appreciated the close collaboration in establishing the research team and am grateful to have been given the chance of going abroad and connecting with international universities.

Second, I would like to thank Professor Oliver Amft from the University of Freiburg in Germany who agreed on being my second, external examiner. Our research has repeatedly shown points of contact, so I am glad that he agreed to take on this role.

Equally, I would like to thank Professor Roman Obermaisser and Professor Roland Wismüller from the University of Siegen in Germany for agreeing on being my third and fourth examiners as well as taking over the chairing duties within the committee.

I would also like to thank Professor Florian Michahelles from the Vienna University of Technology for his trust in me and the patience during the transition from Siegen to Vienna, simultaneously finishing this thesis and starting my PostDoc position there.

My research visit at the University of Oulu in Finland was a very inspiring time. Many thanks to Heli Koskimäki, Juha Röning, and Pekka Siirtola for hosting and welcoming me at the Biomimetics and Intelligent Systems Group. Likewise, many thanks to Denzil Ferreira and Elina Kuosmanen for co-hosting, guiding, and letting me participate in their exciting research. Moreover, Henna Mönttinen, Henna Tiensuu, Gunjan Chandra, and Matti Huotari, thank you all for being great office mates and the exciting time in Oulu!

I want to thank my colleagues and friends Benjamin Völker, Christian Marschall, Onofre Martorell, Philipp Marcel Scholl, and Wendy Wlasak for proofreading this dissertation. In this course, I would also like to mention my closest friends Ramona Sayeed and Sebahattin Akdemir. To all of you, thank you for your constant support throughout the entire PhD period, the valuable advice, and the fruitful topic-related as well as refreshing off-topic discussions. Thank you for standing by me with your feedback until the last minute!

Last but not least, the dearest thanks go to my family: Danke, dass ihr mich in den Jahren, mit all ihren Höhen und Tiefen, unterstützt und mir Mut zugesprochen habt!

Þetta reddast

"In the end, everything will be fine."

Icelandic motto